

**TU**

TECHNISCHE UNIVERSITÄT WIEN

DISSERTATION

**Self-Assembly, Hierarchical Structure and Mechanical  
Properties of (Organo-)Silica Monoliths**

ausgeführt zum Zweck der Erlangung des akademischen Grades  
eines Doktors der technischen Wissenschaften unter der Leitung von

Privatdoz. Dr.rer.nat. Helga Lichtenegger

E308

Institut für Werkstoffwissenschaft und Werkstofftechnologie  
und

Prof. Dr. Nicola Hüsing

Institut für Anorganische Chemie I, Universität Ulm  
(vormals E165, Institut für Materialchemie, TU Wien)

eingereicht an der Technischen Universität Wien

**Fakultät für Maschinenwesen und Betriebswissenschaften**

von

Dipl.-Ing. Christina Fritscher

9525335

Johann Straußgasse 36/16, A-1040 Wien

Wien, am 22.07.2008

# Kurzfassung der Dissertation

Ziel dieser Arbeit war, die Selbstorganisation in mesostrukturierten, lyotropen flüssigkristallinen Tensid/Wasser- sowie Tensid/Wasser/Silica-Precursor-Mischungen zu untersuchen und die mechanischen Eigenschaften der resultierenden hierarchisch strukturierten (Organo-)Silica-Materialien zu bestimmen. Ordnungsprozesse wurden mit Hilfe von Synchrotron-Röntgenkleinwinkelstreuung zeitaufgelöst gemessen.

Amphiphile Moleküle wie Tenside oder Blockcopolymere organisieren sich in geeigneten Lösungsmitteln zu sogenannten Mesophasen. Diese finden weithin Anwendung in der Herstellung von biomimetisch inspirierten Werkstoffen. Die Ausrichtung der Domänen in den Mesophasen erlaubt eine zusätzliche Kontrolle in der Herstellung von Nanomaterialien. In dieser Arbeit wird der Einfluss von Magnetfeldern und Oberflächeneffekten auf die Selbstorganisation von amphiphilen Molekülen in Heiz- und Kühlzyklen beschrieben. Weiters wurden verschiedene, teils polymerisierbare Moleküle auf ihre Fähigkeit hin untersucht, in wässriger Phase geordnete Strukturen auszubilden. Das spätere Vernetzen der organischen Phase erlaubt die (relativ) einfache Herstellung von Nanokomposit-Materialien mit einer hohen strukturellen Ordnung der Bauelemente auf Nanometerebene.

Eine wichtige Anwendung finden amphiphile Moleküle als Struktur gebende Template in der Sol-Gel-Synthese. Die resultierenden periodisch mesoporösen Materialien finden bereits vielfältige Anwendungen in der Industrie, wie z.B. in der Chromatographie oder in der Katalyse. Zumeist werden Filme oder Pulver hergestellt. Die Synthese von monolithischem Material ist noch immer die Ausnahme, verspricht jedoch eine Erweiterung des Anwendungsfensters dieser Materialien besonders im ‚Life-Science‘-Bereich.

Glykolmodifizierte Silica-Vorstufen ermöglichen aufgrund ihrer guten Verträglichkeit mit flüssigkristallinen Templaten die Fabrikation von monolithischem Material mit hoch geordneten Mesoporen. Zusätzlich zu der Strukturierung auf Nanometerebene entsteht während der Synthese mit einem auf Polyethylenoxid basierendem Blockcopolymer durch Phasenseparation eine komplexe Makromorphologie. *In-situ* Untersuchungen mithilfe von Synchrotron-Röntgenkleinwinkelstreuung erlauben Rückschlüsse auf die Formationsmechanismen sowohl auf der Nanometerebene, als auch auf der Mikrometerebene. Die hier beschriebenen Experimente ergänzen die bisher in der Literatur veröffentlichten Studien, die bis auf wenige Ausnahmen an Filmen und Pulvern

durchgeführt wurden, um einen Syntheseweg mit vorgeformter flüssigkristalliner Phase. Wie in dieser Arbeit nachgewiesen wird, handelt es sich hier trotz alledem nicht um einen ‚True liquid crystal templating‘-Prozess, bei dem eine flüssigkristalline Mesophase 1:1 abgeformt wird. Die Experimente zeigen, dass nach der Zugabe des Precursors bis zur Gelierung kooperative Umordnungsprozesse stattfinden. Neben der Ethylenglykol-modifizierten Silica-Vorstufe wurde zum Vergleich auch ein Ethylenglykol-modifizierter, phenylverbrückter Precursor untersucht.

Mit dem zunehmenden Interesse an mesoporösen monolithischen Materialien steigt auch das Interesse an deren mechanischen Eigenschaften. Druckversuche und instrumentierte Härteprüfungsuntersuchungen wurden an rein anorganischen und an phenylverbrückten monolithischen (Organo-)Silica-Gelen durchgeführt und verglichen.

Die bisherigen Versuche, mesoporöse Materialien makroskopisch zu strukturieren, beschränken sich zumeist auf einfache Formen, die durch den jeweiligen Probenbehälter bestimmt werden. Im letzten Kapitel wird beschrieben, wie unter Verwendung neuer Photopolymere mithilfe von Rapid Prototyping nahezu beliebig strukturierte, lösliche Gussformen hergestellt werden können. Die polymerischen Gussformen können im Anschluss an den Sol-Gel-Prozess problemlos bei Raumtemperatur entfernt werden. Daher eignet sich das Verfahren dazu, Hybridmaterialien, wie z.B. organisch verbrückte Silica-Materialien mit einer komplexen Architektur auf der Millimeter- bis Centimeter-Ebene zu erzeugen.

## Abstract

The aim of this work was to investigate the self-assembly process in mesostructured lyotropic liquid crystalline surfactant/water and surfactant/water/silica precursor mixtures and to determine the mechanical properties of the resulting hierarchically structured (organo-)silica materials. Ordering processes were measured *in-situ* using synchrotron small angle X-ray scattering.

Amphiphilic molecules such as surfactants and block copolymers self-assemble in suitable solvents to so-called mesophases, which are widely used in the design of biomimetically inspired materials. The orientation of the mesophase domains provides additional control in the fabrication of nanomaterials. Part of this work deals with the influence of magnetic fields and surface effects on reordering of amphiphilic molecules during heating and cooling cycles. Additionally, various, partly polymerizable molecules were examined with regard to their ability to form ordered structures in aqueous media. Later crosslinking of the organic phase allows the (relatively) easy fabrication of nanocomposites of high structural order of the building blocks at the nanometer scale.

An important application of amphiphilic molecules is their use as structure-directing agents in sol-gel synthesis. The resulting periodically ordered mesoporous materials are already widely used in industry, e.g., in chromatography or catalysis. Currently, mostly films and powders are being produced. The synthesis of monolithic material is still the exception, but significantly widens the possible applications within the area of the life sciences.

Due to their good compatibility with liquid crystal templates, glycol-modified silica precursors allow the fabrication of monolithic material with highly ordered periodic mesopores. In addition to the structuring on the mesoscale, polyethylene oxide based block copolymers lead to a phase separation during synthesis resulting in complex macromorphologies. *In-situ* synchrotron small angle X-ray scattering experiments give clues on the formation mechanism on the nanometer (meso-)scale as well as on the micrometer scale. The experiments performed in this work provide information on the structure formation mechanism in the presence of pre-assembled liquid crystal templates, adding to the studies previously described in literature, which mostly describe the formation mechanism for films and powders. Nevertheless, as will be shown in the thesis, the synthesis still does not account for a ‘True liquid crystal templating’ route. The resulting structure of the (organo-)silica materials is not a 1:1 replica of the employed liquid crystalline template, but evolves due to a cooperative reordering of the molecules

after the addition of the precursor. Structure evolution was investigated for the ethylene glycol-modified silane and a phenylene-bridged ethylene glycol-modified precursor.

With growing interest in periodically ordered mesoporous (organo-)silica monoliths, the need for information on the mechanical properties of these complex materials increases, as well. Compression and instrumented indentation tests were performed on pure inorganic and phenylene-bridged monolithic samples.

Up to now, the structure of mesoporous silica monoliths on the macroscale were more or less restricted to simple shapes, determined by the sample container in which gelation took place. The last part of this work deals with the fabrication of sacrificial molds of complex design by means of rapid prototyping, using new soluble resins. Since these photopolymeric molds are easily removed at room temperature after gelation, the process is very well suited for the production of hybrid (e.g. organically-bridged silica) materials with a complex architecture on the millimeter and centimeter scale.

# Acknowledgement

I would like to thank my supervisors Helga Lichtenegger\* (Institute of Materials Science and Technology, IMST, TU-Vienna) and Nicola Hüsing (Department of Inorganic Chemistry I, University of Ulm) who, despite the distances and schedules involved, have been unceasingly supportive during research and writing. I would also like to extend my gratitude to Prof. Sabine Seidler and Prof. Ulrich Schubert for the working space and resources, as well as their patience and support over the years. I would like to thank Jürgen Stampfl for providing me with the opportunity to work with rapid prototyping.

My heartfelt thanks go out to all members of the Institute of Materials Science and Technology and the Institute of Material Chemistry, TU Vienna for their help and the enjoyable working atmosphere. Foremost, I would like to thank Thomas Koch\*\*\* and Dieter Holzinger for their helpfulness and being the best laboratory colleagues I could think of. I owe my gratitude to Doris Brandhuber\*\*\* and Ralf Supplit\* for being great company as well as big help in chemical matters, to Vassiliki-Maria Archodoulaki, Annette Danninger, Denise Dragan, Doris Eibinger, Claudia Feldgitscher, Dagmar Fischer, Rüdiger Haas, Philipp Heinz, Johannes Homa, Sorin Ivanovici, Melitta Kirl, Ruppert Kleinl, Heidemarie Knoblich, Jana Knoblich, Rene Kogler, Sigrid Lüftl, Mirka Malenovska, Christian Martschitsch, Thomas Papst, Robert Potzmann, Michael Puchberger (for NMR-experiments and discussion), Christoph Rill, Harald Schauer, Roman Stoiber, Christian Zaruba, Stefan Zellhofer and others.

Special thanks go to Herwig Peterlik for his help and support with the small angle X-ray scattering experiments and evaluation and for all his enthusiasm and good ideas, Stephan Puchegger (python expert and whodunit borrower), Dieter Loidl (oven specialist) and Rüdiger Reitinger\*, all from the Group “Dynamics of Condensed Systems”, University of Vienna.

Robert Liska, Christine Maier, Robert Inführ and Adi Zimmermann I would like to thank for chemical support, their cool new resins for rapid prototyping and the multifunctional surfactants. Dominique Farnik I would like to thank for being a comrade in arms.

Of the working group in Ulm I want to thank Steffi Geist\*\* (for her cheer and helpfulness), Conny Egger, Jürgen Holzbock, Sarah Hartmann\*, Jasmin Geserick\*, Petra Kaiser and Manuel Weinberger. For TEM measurements, I want to express my gratitude to Ute Hörmann (Electron Microscopy Group of Materials Science, University of Ulm) whose TEM studies and inputs really made a difference, as well as to Johannes Bernardi.

I would especially like to thank to Anna Roig, Elena Taboada and Raul Solanas from the Institut de Ciència de Materials de Barcelona. Not only did I have a wonderful time in Barcelona, but also most wonderful, scd-dried samples afterwards.

I am much obliged to Sigrid Bernstorff of Elettra Synchrotron, Trieste and Pierre Panine of ESRF, Grenoble. Naturally, a big ‘thank you’ goes to the people who supported me during the synchrotron beamtimes (marked with \* in the text above).

I gratefully acknowledge financial support of the Austrian Science Fund (FWF) under grant no. P15852 and of the European Union for financing Elettra and ESRF synchrotron experiments.

Special thanks to my best friends and family for encouragement, understanding and patience, in particular to Ellen, Tobias, Franz and Markus for proofreading and to Martin for overall support and being there.

## Abbreviations and Symbols

$2\theta$	scattering angle
a, c	lattice constants
A, G, P	amplitudes (standard, Guinier, Porod)
a.u.	arbitrary units
<b>B</b>	magnetic field
BET	Brunauer, Emmet, Teller
BJH	Barrett, Joyner, Halenda
C	C-parameter (nitrogen sorption)
CAD	computer aided design
$\chi$	azimuthal angle (SAXS) or magnetic susceptibility
CP	cross polarization
cpp	critical packing parameter
d	<i>d</i> -spacing
<b>D</b>	(LLC) domain vector
$\delta^2$	parameter to correlate RHS and Rmicelle
DBJH	BJH pore diameter
$\delta$	chemical shift (NMR)
$\Delta G$	free energy (of self-assembly)
DLP	digital light processing
E	Young's modulus (elastic modulus)
EISA	evaporation induced self-assembly
F	coloidal surface free energy
FCC	face centered cubic
FFT	fast Fourier transform
FWHM	full width at half maximum
H	hardness
<b>H</b>	magnetic field strength
HCPS	hexagonally closed packed spheres
HMBC	heteronuclear multiple bond correlation
HPLC	high performance liquid chromatography
I	intensity
IASC	Institute of Applied Synthetic Chemistry, TU Vienna, Austria
ICMAB	Institut de Ciència de Materials de Barcelona
IIT	instrumented indentation testing



IUPAC	International Union of Pure and Applied Chemistry
L	coherence length
$\lambda$	wavelength
(L)LC	(lyotropic) liquid crystal
<b>M</b>	magnetization
MAS-NMR	magic angle spinning NMR
$m_{hkl}$	multiplicity
MW	molecular weight
NMR	nuclear magnetic resonance
P(q)	form factor
$p/p_0$	relative pressure
$p_c$	critical pressure
PMO	periodic mesoporous organosilica
POM	polarized optical microscopy
ppm	parts per million
PSD	position sensitive detector
q	scattering vector
R, R'	alkyl/aryl group
R, r	radius
$R_C$	radius of hydrophobic core (micelles)
$R_S$	thickness of hydrophilic shell (micelles)
$R_{HS}$	hard sphere radius
$R_{micelle}$	radius of the micelle
$R_g$	Guinier radius
$\rho$	density
$\rho_S, \rho_M, \rho_C$	electron density (of shell, core, dilute hydrochloric acid)
ROH	alcohol
RP	rapid prototyping
RT	room temperature
<b>S</b>	beam axis
S(q)	structure factor
SANS	small angle neutron scattering
SAXS	small angle X-ray scattering
$S^{BET}$	BET surface area
scd, scf	supercritically dried, supercritical fluid
SEM	scanning electron microscopy
surfmer	polymerizable surfactants
$t^{wall}$	thickness

$T_c$	critical temperature
TEM	transmission electron microscopy
TGA	thermogravimetric analysis
$t_g$	gelation time
TLCT	true liquid crystal templating
tms	surface silylated with trimethylchlorosilane
$t_{pm}$	time at which periodic mesostructure evolves in the SAXS pattern
$t_{ps}$	time at which phase separation occurs
USAXS	ultra small angle X-ray scattering
v/v	volume fraction
w/w	weight fraction
WAXS	wide angle X-ray scattering
XRD	X-ray diffraction

### **Precursor abbreviations and chemicals:**

AIBN	azobisisobutyronitrile
BEA	acrylic acid 2-butyl-carbamoyloxy-ethyl ester
BMA	1,4-butanediol dimethacrylate
bPh	phenylene -bridged 1,4-bis[tris-(2-hydroxyethoxy)silyl]benzene ethylene glycol-modified
bPhGMS	phenylene-bridged silane
Brij 56	polyoxyethylene 10 cetylether
Brij 97	polyoxyethylene 10 oleyl ether
CTAB	cetyltrimethylammonium bromide
EGMS	tetrakis-(2-hydroxyethyl)-orthosilicate
LA	lauryl acrylate
MPS	methacryloxy propyltrimethoxy-silane
P123	block copolymer Pluronic P123, PEO <sub>20</sub> PPO <sub>70</sub> PEO <sub>20</sub>
PE	petroleum ether
(P)EO, (P)PO	(poly)ethylene oxide, (poly)propylene oxide
Span 40	sorbitan monopalmitate
TEOS, TMOS	tetraethyl orthosilicate, tetramethyl orthosilicate
THF	tetrahydrofurane
tms	trimethylchlorosilane
Triton X-45	polyethylene glycol 4-tert-octylphenyl ether
TTA	trimethylolpropane triacrylate

# Table of contents

<b>TABLE OF CONTENTS</b> .....	<b>1</b>
<b>1 INTRODUCTION</b> .....	<b>4</b>
1.1 <b>Bioinspired materials processing</b> .....	<b>4</b>
1.2 <b>Self-assembly</b> .....	<b>7</b>
1.2.1 Lyotropic liquid crystals.....	7
1.2.2 Preferential orientation.....	8
1.3 <b>Sol-gel chemistry</b> .....	<b>9</b>
1.3.1 Basics.....	9
1.3.2 Liquid crystal templating.....	11
1.3.3 Phase separation and multimodal pore size distribution.....	14
1.3.4 Drying of the monolithic material.....	16
1.4 <b>Silica-based mesoporous hybrid materials</b> .....	<b>18</b>
1.5 <b>Mechanical properties</b> .....	<b>21</b>
1.6 <b>Structuring on the macroscopic level</b> .....	<b>22</b>
1.6.1 Macroscopic shape of periodic mesoporous materials.....	22
1.6.2 Rapid prototyping/stereolithography.....	23
<b>2 EXPERIMENTAL</b> .....	<b>25</b>
2.1 <b>Structural design on the nanometer level</b> .....	<b>25</b>
2.1.1 Employed surfactants.....	25
2.1.1.1 Cetyltrimethylammonium bromide (CTAB).....	25
2.1.1.2 PEO <sub>20</sub> PPO <sub>70</sub> PEO <sub>20</sub> (Pluronic P123).....	26
2.1.1.3 Brij 56 and Brij 97.....	27
2.1.1.4 Polyethylene glycol 4-tert-octylphenyl ether (Triton X-45).....	27
2.1.1.5 Preparation of the LC-phases.....	27
2.1.2 Employed precursors.....	28
2.1.2.1 Q <sup>8</sup> M <sup>8</sup> -cube precursor solution.....	28
2.1.2.2 Ethylene glycol-modified silane (EGMS).....	29
2.1.2.3 Phenylene-bridged ethylene glycol-modified silane (bPhGMS).....	30
2.1.2.4 Preparation of monolithic gels.....	31
2.1.3 Drying of the wet monoliths.....	31

2.1.3.1	Supercritical drying .....	31
2.1.3.2	Ambient pressure drying after surface silylation with trimethylchlorosilane .....	32
2.1.4	Addition of polymerizable species to LC templates .....	32
<b>2.2</b>	<b>Structural design on the macroscopic level .....</b>	<b>34</b>
2.2.1	Employed resins .....	34
2.2.2	Fabrication of sacrificial cellular molds .....	35
2.2.3	Casting of gels .....	35
2.2.4	Dissolution of molds .....	35
<b>2.3</b>	<b>Analytical methods .....</b>	<b>36</b>
2.3.1	X-ray scattering .....	36
2.3.2	Thermogravimetric analysis .....	45
2.3.3	Nuclear magnetic resonance (NMR) spectroscopy .....	45
2.3.4	Polarized optical microscopy .....	45
2.3.5	Nitrogen sorption .....	46
2.3.6	Scanning- and transmission electron microscopy .....	46
<b>2.4</b>	<b>Mechanical testing .....</b>	<b>47</b>
2.4.1	Instrumented indentation testing .....	47
2.4.2	Compression tests .....	49
<b>3</b>	<b>RESULTS AND DISCUSSION.....</b>	<b>50</b>
<b>3.1</b>	<b>Ordering effects in lyotropic liquid crystal systems.....</b>	<b>50</b>
3.1.1	Lamellar LC structure of Triton X-45 .....	51
3.1.2	Hexagonal LC structure of CTAB .....	54
3.1.3	Alignment of silica-surfactant mesophases .....	57
<b>3.2</b>	<b>Investigation of novel “multifunctional” surfactants.....</b>	<b>60</b>
3.2.1	Aqueous solutions of a benzoic acid derivative .....	60
3.2.2	Aqueous solutions of a perylene derivative .....	62
3.2.3	Aqueous solutions of an alkylpolyethylene oxide derivative .....	63
3.2.4	Brij 97 as structure directing agent .....	65
<b>3.3</b>	<b>Addition of polymerizable species to P123 in water .....</b>	<b>67</b>
3.3.1	Phase diagram of P123/water/monomer mixtures .....	67
3.3.2	Gels prepared with P123/monomer mixtures .....	70
<b>3.4</b>	<b><i>In-situ</i> synchrotron SAXS/XRD study on silica/surfactant self-assembly.....</b>	<b>73</b>
3.4.1	Pluronic P123 as structure directing agent .....	73
3.4.1.1	LC phase of Pluronic P123 in water .....	74

3.4.1.2	Core-Shell model for P123 micelles in water.....	76
3.4.2	Mesostructure formation in monolithic mesoporous gels.....	80
3.4.3	Extending the q-region in the scattering experiments: The hybrid network.....	87
3.4.4	Extending the q-region in the scattering experiments: The pure silica network.....	94
3.4.5	Interpretation.....	98
3.4.6	Development of macromorphology in the phenylene-bridged network.....	101
<b>3.5</b>	<b>Interplay of mesostructure and macromorphology.....</b>	<b>108</b>
3.5.1	Morphology derived from the ethylene glycol-modified precursor.....	108
3.5.2	Morphology in the phenylene-bridged systems.....	110
3.5.3	Proposed growth model.....	113
<b>3.6</b>	<b>Mechanical properties of the hierarchically structured monolithic material.....</b>	<b>115</b>
3.6.1	Instrumented indentation tests.....	115
3.6.1.1	Bimodal porous silica monoliths prepared from EGMS.....	116
3.6.1.2	Bimodal porous organosilica monoliths prepared from bPhGMS.....	120
3.6.2	Compressive tests on supercritically dried monoliths.....	123
<b>3.7</b>	<b>Macroscopic Templating.....</b>	<b>127</b>
3.7.1	Water-soluble photopolymer molds.....	127
3.7.2	Organo-soluble photopolymer molds.....	129
3.7.2.1	Design of the sacrificial molds and templating process.....	129
3.7.2.2	Surface texture resulting from contact to the photopolymeric mold.....	132
3.7.2.3	Ambient pressure drying of the macroscopically shaped gels.....	134
<b>4</b>	<b>CONCLUSIONS.....</b>	<b>138</b>
<b>5</b>	<b>REFERENCES.....</b>	<b>141</b>
<b>APPENDIX.....</b>		<b>150</b>
<b>A.</b>	<b>Considerations on the limitations of the obtained numerical values.....</b>	<b>150</b>
<b>B.</b>	<b>Experimental details on supercritical drying.....</b>	<b>153</b>
<b>C.</b>	<b>Samples for mechanical testing.....</b>	<b>154</b>
<b>CURRICULUM VITAE.....</b>		<b>157</b>

# 1 Introduction

## 1.1 Bioinspired materials processing

Many natural materials such as nacre, bone or wood exhibit a complex architecture over several length scales. Starting with a bottom-up formation, living organisms grow their tissue taking advantage of biologically controlled self-assembly processes. This is in strong contrast to man-made materials, which are fabricated mostly in a top-down approach. Where to the human engineer the whole periodic system is more or less open, biomaterials have to be optimized for functional use taking into account restricted resources such as elements, materials consumption and energy. This can only be achieved by a sophisticated hierarchical structure, where the resulting material is tuned by a composite structure mostly in the nanometer to micrometer range and a cellular structure mostly in the micrometer to millimeter range [1].

A beautiful example is shown in Figure 1.1.1; The glass sponge skeleton of *Euplectella*, a deep-sea sponge found in the Western Pacific, consists of at least seven hierarchical levels, with each level contributing to the mechanical stability and the toughness of the final product [2]. In natural materials the cellular structure is important for mechanical reasons, offering stability at minimal mass consumption (light weight) and for biological reasons, allowing for the passage of cellular fluids.

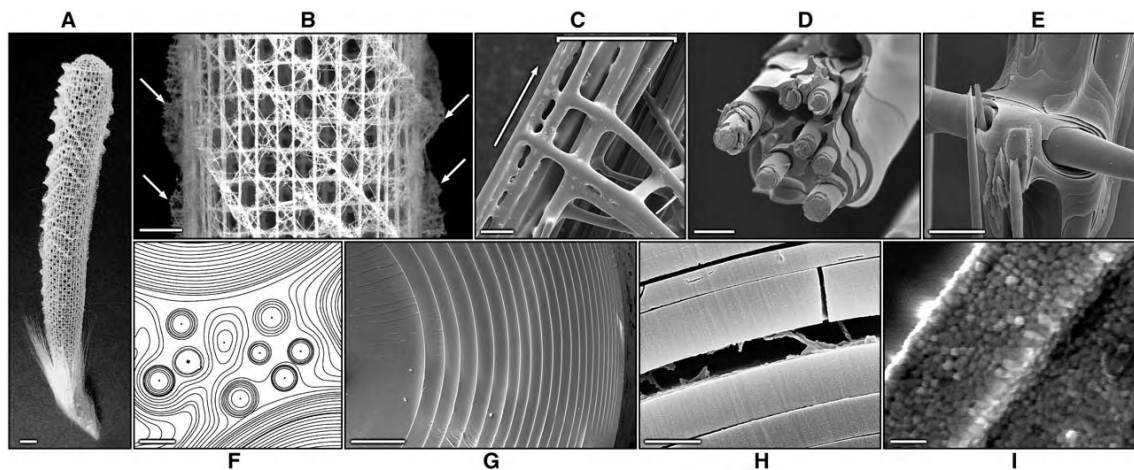


Figure 1.1.1. (A) Biosilica sponge skeleton of *Euplectella* (scale bar 1 cm). (B-I) Structure of the different hierarchical levels: The lattice is made up of vertical and horizontal struts with diagonal elements, each strut consists of bundled multiple spicules. In the micrometer range the material has a ceramic fiber-composite structure, where the lattice is cemented with laminated silica layers connected by an organic interlayer. The lamellae are built of nanoparticles (taken from [2]).

Synthetic cellular materials have become very popular in industrial applications for the same reasons, i.e., light weight and high surface area. The latter is especially important in chromatography and catalysis, as well as in tissue engineering and implants. Porosity and pore structure influence many physical properties such as density, thermal conductivity, strength and the possibility for interaction of the material with liquids and gases. In nature porosity is achieved by subsequently organizing the smallest building blocks in a sophisticated way up to the macroscale. In this complex synthesis-construction pathway, different driving forces such as molecular interactions or surface forces have to act at different hierarchical levels in parallel and/or in sequence. Diatoms, for example, are microscopically small marine algae with different sizes and overall shapes, consisting of a complex nanoporous skeleton made from amorphous silica. The highly periodic porous structure has been found to be templated by vesicles as shown in Figure 1.1.2.

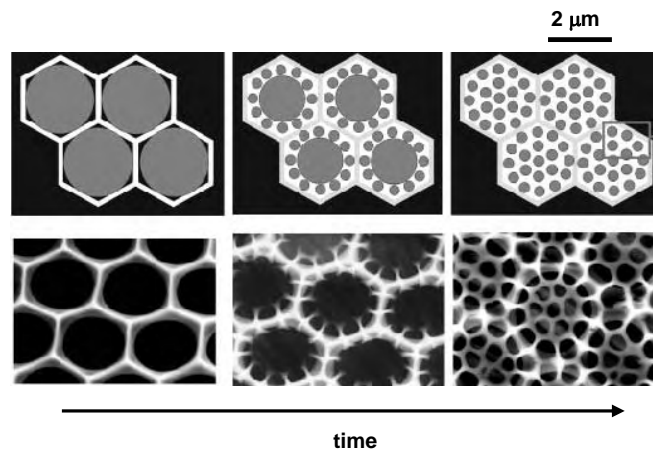


Figure 1.1.2. Templating mechanism in the formation of porous silica of the diatom species *coscinodiscus wailesii* as reported by Sumper [3].

For a long time mankind did not have the appropriate tools to engage in nanoscale architecture. This has changed dramatically in recent years with the emergence of structuring and characterization techniques with nanometer resolution. Chemical methods have leveraged the fabrication of nanomaterials, offering spontaneous long-range organization and transformation of building blocks across multiple length scales. *Organized-matter* chemistry of inorganic materials now includes the use of self-assembled organic templates, cooperative assemblies of templates and building blocks, spatially restricted reaction fields and combinations thereof [4].

Among the many attempts undertaken by materials scientists to mimic the controlled organization over several hierarchical levels of cellular materials, soft chemistry methods, i.e., chemistry at ambient temperatures and pressures, offer a high degree of control over

structure as well as chemical composition. In certain sol-gel chemistry silica materials structural organization on at least four levels, from the molecular range to the macroscopic scale has been achieved [5]. This was realized by interconnected synthesis processes, during which chemical and physical forces act on each of the components, leading to a sophisticated overall material architecture. The resulting morphology and composition can be adjusted by the careful choice of precursors, pH, concentration, temperature and additives. The obtained materials consist of highly porous inorganic or organic-inorganic hybrid networks templated by organized supramolecular assemblies on the nanometer scale (2-100 nm).

This work takes a closer look at the self-assembly process of amphiphilic molecules in solution and at their role as structure-directing agents in the fabrication of hierarchically structured mesoporous (organo-)silica materials. These materials are of great interest in size- and shape-selective processes (e.g., such as catalysis), in sensors, chromatography, fuel storage and, recently in the fabrication of nanocomposites as well as in tissue engineering. Whereas periodic mesoporous materials are still mostly realized in films and powders several routes to monolithic materials have been reported in the literature, providing an additional hierarchical level on the macroscale. Currently, however, with the exception of a few studies, the macroscopic level is constricted to simple shapes like cylinders and platelets. Expanding the hierarchical architecture to a cellular structure in the millimeter range (0.1-10 mm) is a promising step in the direction of new applications in the area of the life sciences. With growing interest in mesoporous monoliths, the mechanical properties of these materials become more and more important. Similar to the mechanical properties of biomaterials, the final materials properties result from the chemical and structural interplay at the different hierarchical levels.



## 1.2 Self-assembly

Control over the structure at nanometer scale, as commonly found in nature, can in principle be achieved by various processes, such as molecular recognition, self-assembly and templating. Typical interactions found in self-assembly processes are hydrogen bonding, van der Waals, electrostatic, capillary and hydrophobic forces.

### 1.2.1 Lyotropic liquid crystals

One way to mimic the self-organization in nature leading to structural and chemical ordering is the self-assembly of amphiphilic molecules in a solvent. Above a certain concentration (the critical micelle concentration) amphiphilic molecules in water form a variety of self-assembled structures, so-called lyotropic liquid crystalline (LLC) phases. Structures obtained at adequate concentrations range from hexagonal, bicontinuous cubic, lamellar to more complex structures [6]. In a simple geometrical model of chain packing, the favourable aggregate structures of the amphiphile system can be derived from the critical packing parameter (cpp) [7]. The cpp can be calculated from the volume,  $v$ , and the extended length,  $l_{\max}$ , of the hydrophobic part and the head group area according to Figure 1.2.1.

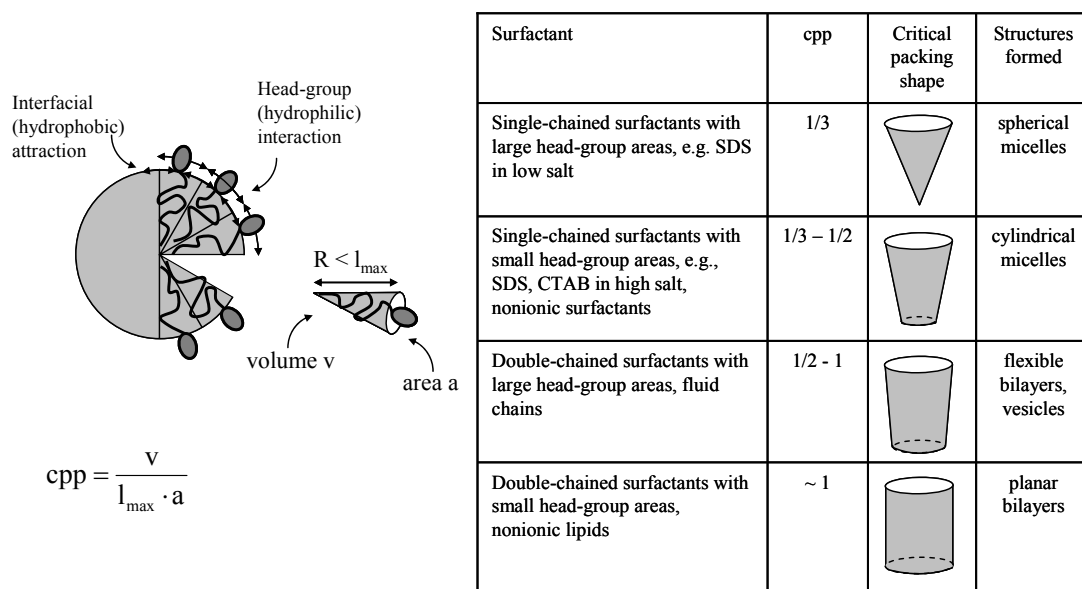


Figure 1.2.1. Critical packing parameter (cpp), critical packing shape and preferred aggregate structures of surfactant molecules (adopted and modified from [7]).

LLCs combine properties of a crystal and a melt, i.e., partial order/disorder of the system. In the case of mesoscale ordering, the material may be non-crystalline on the atomic scale,

but exhibits a collective order of molecular aggregates leading to a well-defined structure on a larger length-scale. The resulting assembly of the molecules depends on the nature, structure and concentration of the surfactant and the solvents and co-solvents. It is also well known that temperature and processing play important roles in the aggregation behaviour of a lyotropic crystal [6, 8-16].

### 1.2.2 Preferential orientation

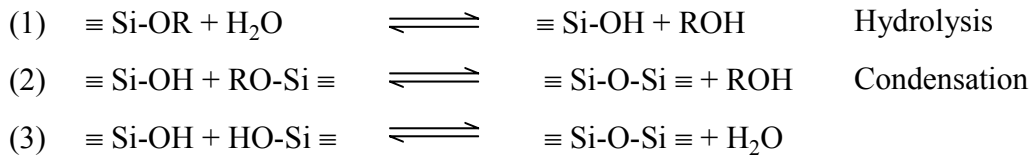
In the absence of external forces lyotropic liquid crystalline domains tend to be oriented randomly in the mixture. Different methods have been reported to align these domains through external influences such as shear [17, 18], magnetic [19, 20] or electric fields [21], or surface effects [22]. The orientation of the LC surfactant/silica phase in the fabrication of periodic mesoporous silica materials is a special challenge. Potential applications are found in nanoscale engineering, separation technology, microelectronics, biomaterials engineering and catalysis. Few attempts at aligning the periodic mesopores with the goal to produce monolithic monodomain samples have been reported in the literature [18-20].

Magnetic effects in “non-magnetic” materials, such as employed by Tolbert and co-workers [19, 20], are small and rely on the diamagnetic properties of the components. Diamagnetism is the result of the induced magnetization caused by the motion of electrons under an applied field. The magnetization  $\mathbf{M}$  induced in a material is proportional to the applied field strength  $\mathbf{H}$ ,  $\mathbf{M}=\chi\mathbf{H}$ .  $\chi$  is the magnetic susceptibility and in case of a diamagnetic material ( $\chi<0$ ) typically in the order of  $-10^{-6}$  to  $-10^{-5}$ . In case a material/molecule exhibits anisotropic diamagnetism, a magnetic torque acts on it, resulting in rotation. The reason for diamagnetic anisotropy can be traced back to the chemical bonds. E.g.,  $\chi$  of C-C bonds is smaller in the direction of the bond ( $\parallel$ ) than normal to the bond ( $\perp$ ) ( $\chi_{\parallel} < \chi_{\perp} < 0$ ). Therefore, the anisotropic diamagnetic susceptibility defined by  $\Delta\chi = \chi_{\parallel} - \chi_{\perp}$  is negative and the C-C bond tends to align in a direction perpendicular to the field [23]. An aromatic ring has a large diamagnetic susceptibility due to the ring current induced by a magnetic field. For this reason, aromatic rings tend to align with the ring plane parallel to the applied field. Since the magnetic interaction energy associated with  $\Delta\chi$  of a particle is proportional to the volume of the particle, the energy to align one single molecule is too small compared to the thermal energy  $k_{\text{B}}T$ . The size has to be large enough to exceed thermal energy. As Firouzi et al. have shown, the  $\Delta\chi^{\text{m}}$  of single molecules, assembled in uniaxial LC domains, contribute to an overall domain susceptibility  $\Delta\chi^{\text{d}}$ . This effect allows an orientation of the domains in high magnetic fields, if thermal disordering and viscoelastic forces can be overcome [19]. One way known to overcome the viscosity of LC phases is heating the mixture above its anisotropic-isotropic phase transition temperature.

## 1.3 Sol-gel chemistry

### 1.3.1 Basics

Amorphous silica can be derived from molecular alkoxide precursors  $\text{Si}(\text{OR})_4$  by acid or base catalysed hydrolysis and condensation reactions:



Most commonly, tetramethoxysilanes (TMOS,  $\text{R}=\text{Me}$ ) and tetraethoxysilanes (TEOS,  $\text{R}=\text{Et}$ ) are used as silica source. Depending on the synthesis and processing parameters, films, xerogels, aerogels, particles or fibers can be produced (Figure 1.3.1).

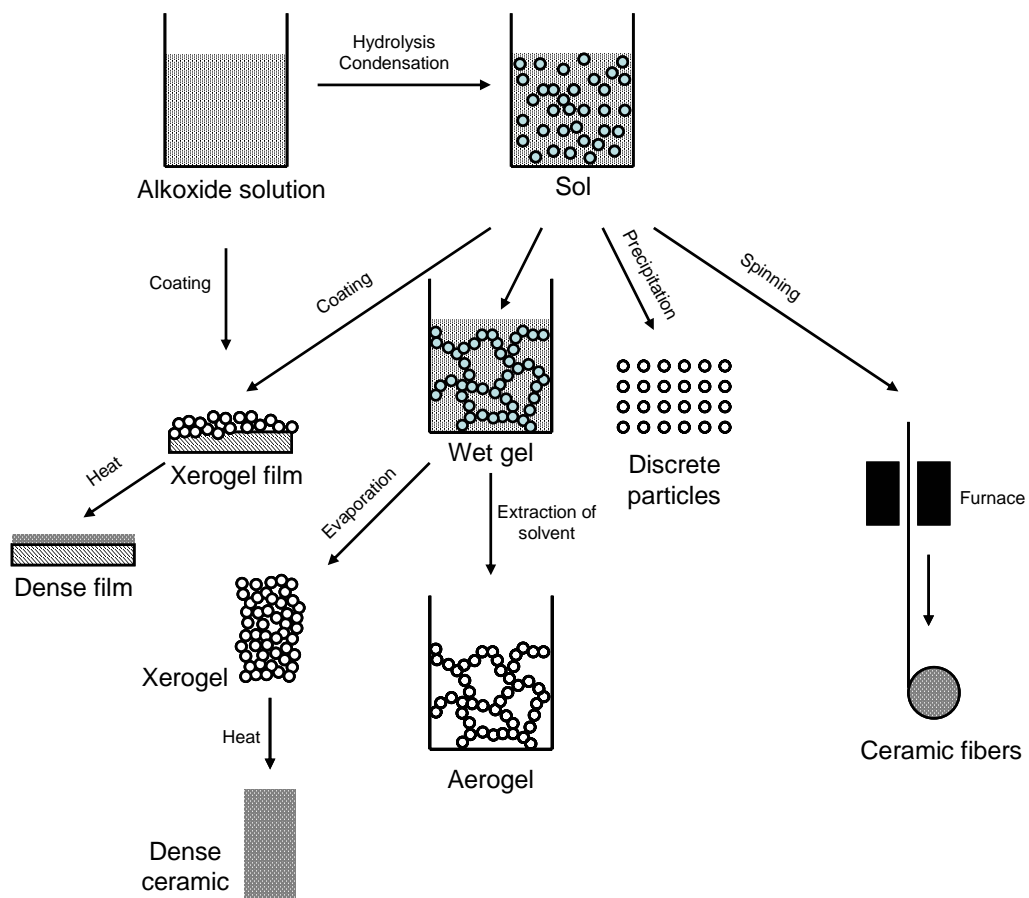


Figure 1.3.1. Sol-gel synthesis processing options (modified from [24]).

In principle sol-gel synthesis leads to the creation of an oxide network by progressive polycondensation reactions of a molecular precursor in a liquid medium. Here, the sol is defined as a stable suspension of colloidal solid particles or polymers in a liquid and the gel is defined as a three-dimensionally continuous solid network surrounding and supporting a continuous liquid or gaseous phase. At the beginning of the reaction, small three-dimensional oligomeric particles are formed, with Si-OH groups on their outer surface. Depending on the experimental conditions those particles grow or agglomerate leading to a stable suspension or the formation of a three-dimensional network. In the latter case the point of gelation is reached, when a continuous network is formed (time until then is denoted gelation time  $t_g$ ). At the same time the viscosity of the gel increases sharply and a form-stable, elastic body is obtained, the wet gel. Typically, the wet gels are aged after gelation for hours to days. Although a particular network is frozen in at the gel point, the chemical reactions are still in progress. Structural rearrangements remain possible in gels, as long as there are still condensable particles or monomers present in the pore liquid. The established network is flexible, allowing neighbouring M-OH or M-OR groups to bend towards each other and undergo condensation reactions. In principle, at this point of synthesis, the hydrolysis and condensation reactions establishing the network are still reversible. This enables mass transport from thermodynamically unfavourable regions to thermodynamically more favourable regions. This process of ripening (coarsening) leads to a reduction in the net curvature. Due to these activities the stiffness of the gel body increases during aging. The most important factor for the resulting network is the relative rate of hydrolysis to condensation reactions. Under acidic conditions hydrolysis of silicon alkoxides is much faster than condensation. Therefore, nearly all species are hydrolyzed at a very early stage of the synthesis and thus, can condense to form small clusters with reactive Si-OH groups. Reactions on the surface of these clusters are favoured for electronic reasons. This gives a polymer-like network with small pores and is called reaction-limited cluster aggregation (RLCA).

There are many other parameters that influence the network formation and change perpetually as polycondensation proceeds, making the system a very complex one [24]:

- the kind of precursor
- the alkoxy group to water ratio
- the kind of solvent
- the kind of catalyst
- the pH and temperature
- the relative and absolute concentrations of the components in the mixture

In addition, the presence of surfactants, block copolymers, lipids, swelling agents, proteins, etc., may change the hydrolysis and condensation rates. Such molecules are often added to influence the structural properties of the resulting gels, as will be explained in the next sections.

Aerogels, xerogels and films as depicted in Figure 1.3.1 are porous materials. Many physical properties such as penetrability, density, thermal conductivity, strength, etc. are controlled by the porosity and pore structure of a solid. Roughly three pore-size regimes can be distinguished (defined by IUPAC):

- micropores: smaller than 2 nm
- mesopores: between 2 and 50 nm
- macropores: larger than 50 nm

Porosity is defined as the ratio of the pore Volume  $V_p$  to the total volume  $V$  occupied by the porous material. An important term in describing a cellular solid is the surface area, which is the accessible area of solid surface per unit mass of material. Besides porosity and surface area, the properties of porous materials are often related to the apparent density, which is defined as the ratio between the density of the cellular solid and the density of the material.

### **1.3.2 Liquid crystal templating**

As described in the Chapter 1.2.1 amphiphilic molecules such as surfactants or block copolymers in water form lyotropic liquid crystalline (LLC) phases. In 1992, a group of Mobil scientists reported the fabrication of inorganic periodic mesoporous materials using ionic surfactant template molecules, known as the M41S phase [25, 26]. Like microporous crystalline zeolites, this class of materials exhibits very large specific surface areas, ordered pore systems and a narrow pore size distribution. However, unlike zeolites, mesoporous materials exhibit amorphous pore walls and pore sizes ranging from 2-50 nm. In 1995, the first synthesis of mesoporous silica using non-ionic surfactants was reported by Bagshaw et al. [27].

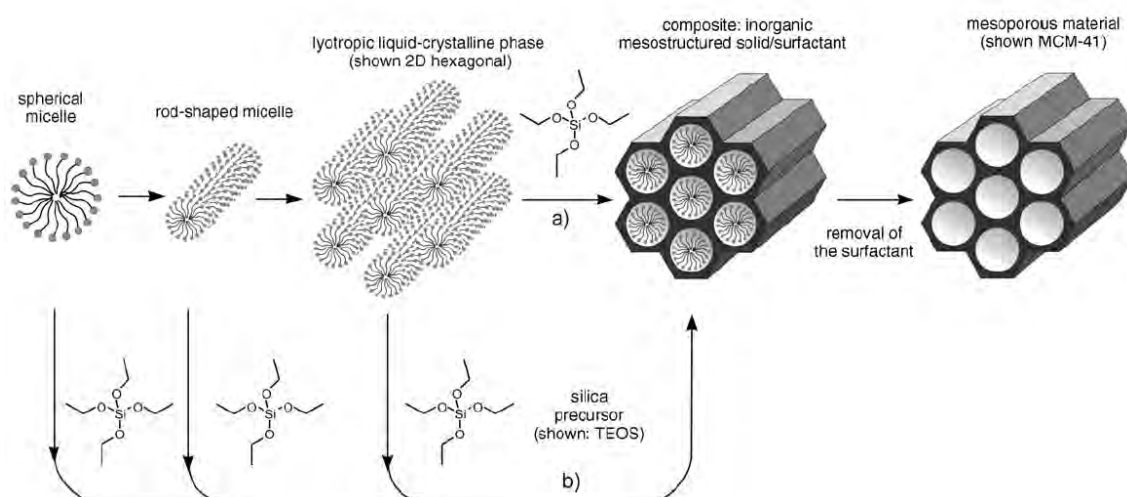


Figure 1.3.2. Formation of mesoporous materials by structure-directing agents: a) true liquid crystal template mechanism, b) cooperative liquid crystal template mechanism [28].

In the meantime, non-ionic block copolymers, especially Pluronic-type triblock copolymer templates,  $(EO)_x-(PO)_y-(EO)_x$  ( $EO = \text{ethylene oxide}$ ;  $PO = \text{propylene oxide}$ ), are widely used for the creation of highly ordered mesostructures under acidic conditions (so-called SBA silica phases) [29-33].

While the fabrication of mesoporous materials through liquid crystal templating (classified as endotemplate method, respectively “soft-matter templating”) in the sol-gel process is by now well established and a multitude of systems using different ionic and non-ionic surfactants have been reported [31, 34], there are still questions and discrepancies concerning the formation mechanism. In the literature a distinction is made between two main pathways to synthesize ordered mesostructures (Figure 1.3.2 [35]). One is the so-called “true” liquid crystal templating (TLCT) pathway. The other one is described as surfactant-templating assembly with inorganic oligomers or nanoparticles. In TLCT synthesis, true or semi-liquid crystal phases are used as templating structures; e.g., Attard et al. [36] synthesized mesoporous silica by using high concentrations of non-ionic surfactants and obtained a cast of the organic mesophase. Another example for TLCT is the evaporation-induced self-assembly (EISA) process for the fabrication of mesostructured films [35, 37]. One crucial step in TLCT is to get rid of the alcohol, which would otherwise destroy the LC phase.

Surfactant-templating assembly with inorganic oligomers or nanoparticles is based on the interaction between surfactants and silicates and their ability to form inorganic-organic mesostructure assemblies. Here, the inorganic oligomers/nanoparticles can be either preformed or formed in the synthesis. Stucky and co-workers reported a cooperative

formation mechanism [38, 39], where the interaction between inorganic and organic species at a molecular scale governs the formation of 3D-ordered arrangements (Figure 1.3.3).

The condensation of the silica species at the interface changes the charge density of the oligomers and with it the arrangement of the surfactants. Matching of the charge density at the interface controls the assembly process. Both  $S^0I^0$  ( $N^0I^0$ ) and  $S^0H^+XI^+$  interaction in non-ionic-surfactant templating systems are possible (S: surfactant, I: inorganic species, see Figure 1.3.3 e, f).

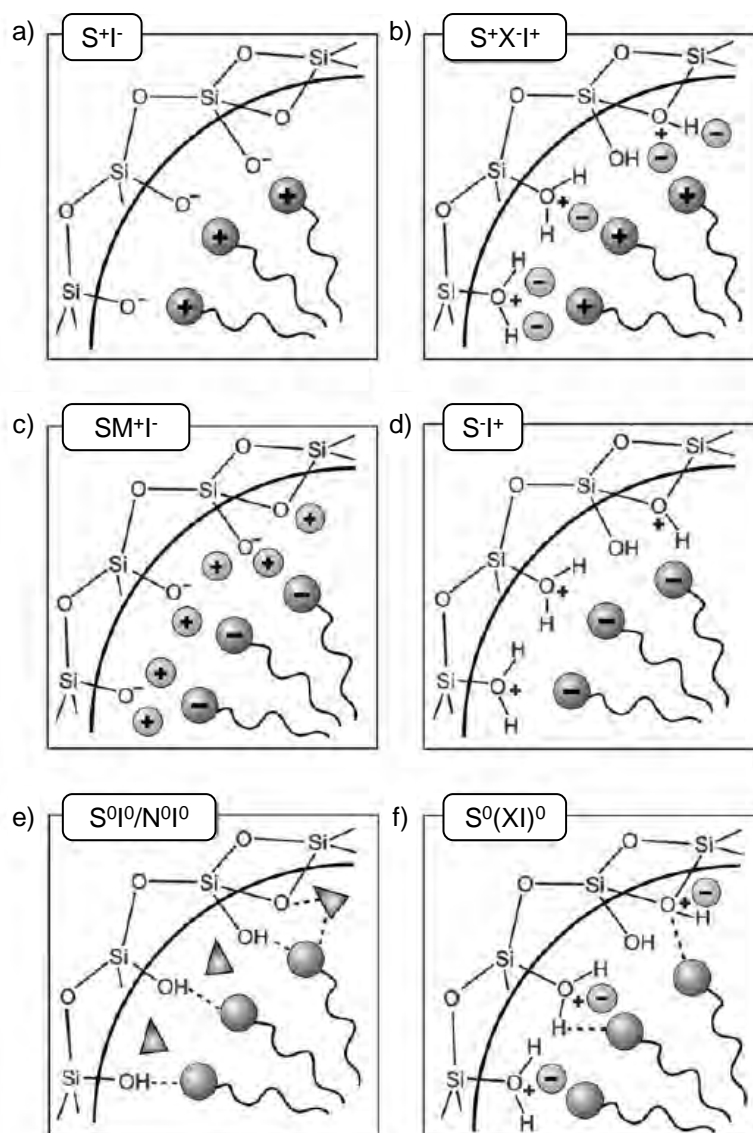


Figure 1.3.3. Interactions between the inorganic species and the head group of ionic (a-d) and non-ionic (e, f) surfactants with consideration of the possible synthetic pathway in acidic, basic, or neutral media. Electrostatic:  $S^+I^-$ ,  $S^+XI^+$ ,  $SM^+I^-$ ,  $S^-I^+$ ; through hydrogen bonds:  $S^0I^0/N^0I^0$ ,  $S^0(XI)^0$  (taken from [28]).

Many methods, such as SAXS/XRD and SANS, NMR or Cryo-TEM, have been used to gain detailed information on the evolution of the mesostructure [33, 37, 40-47]. These investigations were mostly focussed on mesostructured films or powders.

The last step in the synthesis of periodic mesoporous silica-materials is the removal of the template, either by solvent extraction after surface silylation, supercritical drying or calcination (Section 1.3.4).

### **1.3.3 Phase separation and multimodal pore size distribution**

For many applications materials with more than one kind of pores are necessary, e.g., the combination of micro- and mesopores or meso- and macropores for high performance liquid chromatography (HPLC). Different fabrication methods have been applied to achieve such systems.

In alkoxy-derived sol-gel systems, macroporous morphologies can be achieved by inducing a phase separation parallel to the sol-gel transition. An easy one-step synthesis method was introduced by Nakanishi and co-workers in which they use water-soluble organic polymers such as poly(ethylene oxide) (PEO) to induce a macroscopic phase separation parallel to the sol-gel transition [48, 49]. This approach was refined by Lindén and Nakanishi by simultaneously applying ionic or non-ionic surfactants as structure directing agents for the mesopores. The resulting materials exhibit an interconnected porosity on several length scales. The macroporosity is controlled via PEO-nanoparticle interactions, whereas the diameter of the mesopores is controlled by the surfactant. Long-range ordering of the mesopores was eventually achieved using conventional alkoxy silane precursors in combination with Pluronic P123 as template and 1,3,5-trimethylbenzene as swelling agent [50, 51].

Typically, the hydrolysis and polycondensation of alkoxy silanes under acidic conditions gives a relatively narrow molecular weight distribution of the polymerizing oligomers. The average molecular weight of the polymerizing species in solution increases with time due to polycondensation reactions. Following the thermodynamics of a solution containing polymerizable species, the mutual solubility of the constituents therefore becomes lower. This is due to the loss of entropy of mixing, which increases the free energy of mixing ( $\Delta G = \Delta H - T\Delta S$ ) of the system. As a result, the multi-component system becomes less stable, as the absolute value of  $T\Delta S$  decreases. When  $\Delta G$  becomes positive, the thermodynamic driving force for phase separation is generated. Several kinds of additives such as water-soluble polymers, surfactants or poor solvents of the oligomers can start to phase separate during the sol-gel process.



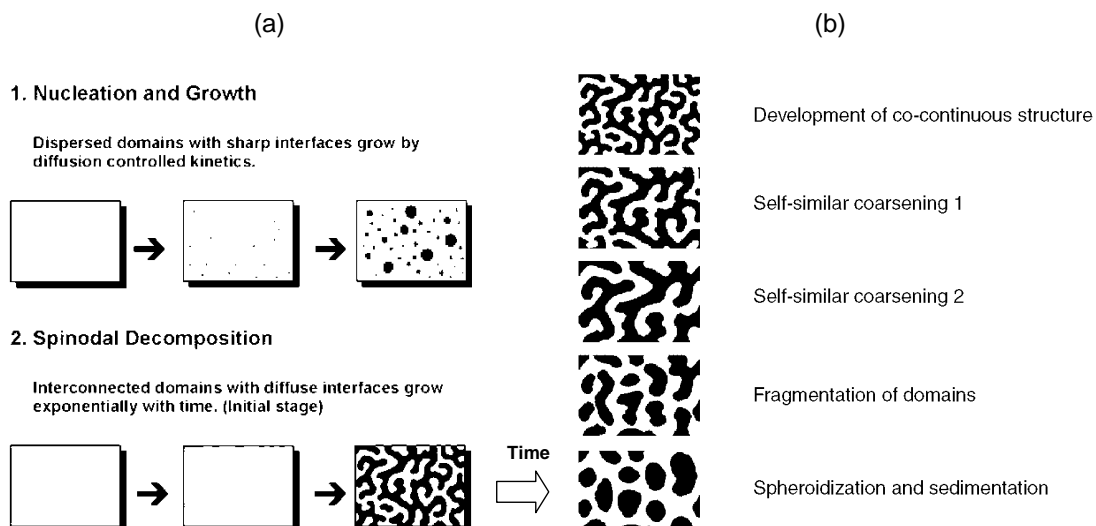


Figure 1.3.4. a) Schematic mechanism of (1) nucleation and growth and (2) spinodal decomposition. b) Self-similar coarsening of the decomposed phase (taken from [52]).

E.g., surfactants that contain poly(oxyethylene) units such as for Pluronic, form hydrogen-bonds with the silanol sites of the oligomers by their ether oxygens. In the further course of the process, a phase rich in surfactant/polymer together with siloxane oligomers evolves. The ongoing polycondensation reactions in the sol are similar to the continuous cooling of a glass-forming liquid into a miscibility gap that means a two-phase region.

In principle, there are two different processes for phase separation: In the metastable region, between binodal and spinodal line, any infinitesimal fluctuation of the composition is energy-consuming and finite activation energy is required to develop phase separated domains. The typical phase-separation mechanism in this region is called “nucleation and growth, as” shown in Figure 1.3.4. Within the spinodal line, in the unstable region, any infinitesimal fluctuation gains energy and the system starts to separate. In case of spinodal decomposition the phase domains have no clear interface at the initial stages of the process, but the contrast increases with time.

Typical structures for sol gel materials derived by spinodal phase separation are co-continuous macromorphologies. The resulting structure is strongly dependent on the interfacial energy. If the system has time to reduce the interfacial energy, it reorganizes the domain structure towards less interfacial area, which results in a (self-similar) coarsening of the structure. With both processes resulting from “irreversible” polycondensation reactions, the sol-gel transition at some point freezes the heterogeneity induced by the phase separation. The frozen structure depends on the onset of phase separation relative to the gelation time. The earlier phase separation is induced in the system, the coarser the

macromorphology of the resulting network will be. Parameters that influence the solubility of the constituents or change the hydrolysis-polycondensation reaction rates such as, e.g., temperature, also have an influence on the final phase-separated domains. Additionally, the reaction rates are dependent on the volume fraction of the solvent.

### 1.3.4 Drying of the monolithic material

The removal of the pore liquid is a difficult step in the fabrication of monolithic gel bodies. With conventional drying methods (evaporation) the network deforms heavily, due to the surface tension of the liquid retreating from the interior of the gel body to the outside. New siloxane bridges are formed due to the approaching of inner surfaces. At the point where the surface tension is no longer capable of deforming the network, which becomes too stiff for further shrinkage, the gel is most likely to crack and in the worst case to collapse, resulting in powders or strongly shrunken monoliths. In the fabrication of aerogels, where the pore liquid has to be removed without strongly altering the network structure and volume, more sophisticated ways of drying have to be applied. In addition, in mesoporous materials gained by liquid crystalline templating, it is necessary to remove the amphiphilic molecules filling the mesopores.

Supercritical drying is one method of avoiding strong capillary forces that arise at liquid-vapour interfaces. In a first step the pore liquid is exchanged with a suitable solvent (e.g. methanol).

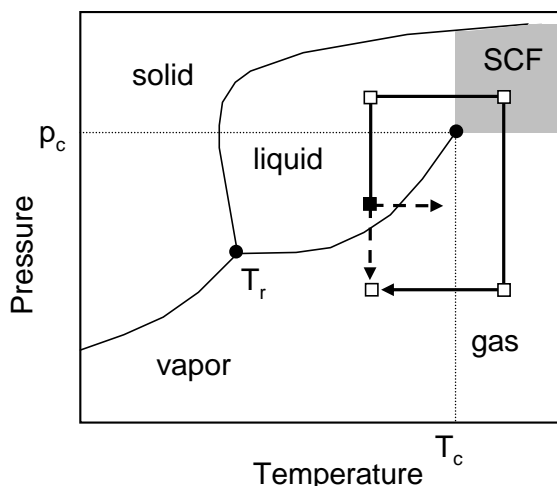


Figure 1.3.5 shows the detour compared to normal drying (dashed arrow) that is taken during the supercritical extraction of a solvent (full-line-arrow). The shaded area represents the supercritical fluid region (SCF) and  $T_r$  is the triple point (modified from [24]). Various stages during drying are represented by empty squares ( $\square$ ), the starting point is marked by a full square ( $\blacksquare$ ).

The solvent-covered gel is put into an autoclave. Then, the solvent is transferred into the supercritical state by slowly raising the temperature, resulting in a pressure increase. As soon as temperature and pressure are at values above the critical point ( $T_c$ ,  $p_c$ ) of the corresponding solvent, the gel is kept there for a certain time so that the sample, as well as the autoclave, are filled completely with the supercritical fluid. Subsequently, the supercritical fluid is removed slowly. Figure 1.3.5 shows the pathway in the phase diagram taken by supercritical fluid extraction.

In the mid-nineties, a novel route for drying large silica monoliths was reported relying on a surface modification treatment with trimethylchlorosilane [53-56]. In the meantime the process of surface-silylation with trimethylchlorosilane and subsequent drying at ambient pressure has been established as alternative to supercritical drying, combining both modification of the network and simultaneous extraction of the surfactant molecules [57, 58].

## 1.4 Silica-based mesoporous hybrid materials

Hybrid organic-inorganic materials can be defined as nanocomposites made of organic and inorganic components combined over length scales ranging from a few Ångstroms to a few tens of nanometres [59]. In case of silica-based mesoporous organic-inorganic hybrid materials, the positioning of organic and inorganic building blocks on a molecular level allows one to profit from the functional variation of organic chemistry, with the advantage of both thermally stable and robust inorganic compounds. There are different pathways reported in the literature to obtain silica-based mesoporous organic-inorganic hybrid materials on a molecular level: (1) The co-condensation of condensable inorganic silica species and silylated organic compounds; (2) The post-synthetic functionalization of the pore surface of a preformed, silica-based network (grafting), and (3) the usage of bisilylated single-source organosilica precursors such as organo-bridged trialkoxysilane precursors, leading to periodic mesoporous organosilicas, PMOs [28]. One advantage of the sol-gel processing is the possibility to combine inorganic and organic species on a very small level. The distribution and interplay between soft and hard matter can be controlled with a high accuracy by variation of the synthesis conditions.

### (1) Co-condensation

The co-condensation of tetraalkoxysilanes,  $(RO)_4Si$ , with terminal trialkoxy-organosilanes of the type  $(R'O)_3SiR$  in the presence of structure-directing agents leads to materials with organic residues anchored covalently to the pore walls. Problems encountered with this method are the sometimes inhomogeneously distributed residues, the loss of mesoscopic order with increasing concentration of  $(R'O)_3SiR$  in the synthesis and problems to remove the template without destroying the organic functionality.

### (2) Surface modification through postsynthetic functionalization of silica (“grafting”)

In this method, inner surfaces of preformed mesostructured silica gels are modified with organic components, primarily by reaction of organosilanes of the type  $(R'O)_3SiR$ , chlorosilanes  $ClSiR_3$  or silazanes  $HN(SiR_3)_2$  with the silanol groups on the pore surfaces. Such modification influences the optical, electronic, separation, chemical or biochemical properties and leads to a wide range of applications [60]. Disadvantages are the possible blocking of the pores, e.g., if the organosilanes react preferentially at the pore opening.

### (3) Periodic mesoporous organosilicas (PMOs)

The sol-gel synthesis of organic-inorganic hybrid materials by reaction of bridged organosilica precursors of the type  $(R'O)_3Si-R-Si(OR')_3$  has been known for a long time.

The combination with liquid crystal templating allows the fabrication of PMOs. Here, the organic moieties are an inherent part of the network. One advantage of this method is that the organic moiety is homogeneously distributed in the hybrid network. The covalently bonded organic spacer allows varying properties of the final gel framework, such as flexibility, hydrophobicity, tunable refractive index or catalytic activity. In the meantime the fabrication of PMO's has been widely investigated [61-72] and PMOs with crystal-like pore walls have been reported [45, 73, 74]. The latter ones exhibit a long-range order of the organic bridges within the pore walls of the mesoporous material. An *in-situ* SAXS investigation with synchrotron radiation published by Morell et al [45] shows that mesostructure formation and organization of the molecular precursor species take place simultaneously. The employment of non-ionic triblock copolymers such as Pluronic P123 permits the synthesis of large-pore PMOs and was first published in 2001 [66].

### Nanocomposites

Besides the combination of organic-inorganic building blocks on a molecular level several attempts have been reported to take advantage of sol-gel-derived materials in the fabrication of composites, e.g., as reinforcing particles [75]. The combination of soft and hard matter to form nanocomposites is a sophisticated way of tuning the mechanical properties of a material, as is done by many biological systems. Artificial nanocomposites consisting of silica and polymer can be derived by different approaches. The first involves mixing polymer with silica particles or silica precursors. In the second synthesis approach polymerizable monomers are mixed with silica particles followed by polymerization. The third method involves mixing both silica precursors and polymer monomers. Both species are simultaneously or consecutively polymerized. Since the interface of the organic and inorganic building blocks plays a crucial role in the final material properties, mesoporous silica materials with their high surface area provide interesting scaffolds for the fabrication of hybrid organic-inorganic nanocomposites [76-78]. Improvements of the material properties are found in thermal stability, tensile strength, modulus and toughness [77].

The use of polymerizable surfactants (surfmers) [79] in the LC-templating process represents a special case. In 1958, Freedman et al. [80] reported the first synthesis of a monomer which was also an emulsifying agent. Since this time a wide variety of surfmers have been studied [81-88]. The combination of monomer self-assembly and condensation of inorganic species was, e.g., employed by Gray et al. [89] They used an inverse hexagonal phase around a hydrophilic solution containing an inorganic precursor. They postulated three criteria for success: The amphiphile must (1) contain a readily polymerizable group, (2) be compatible with the inorganic precursor and form the desired LC phase over a definable range of compositions and (3) the polymerization of the

monomer must proceed with retention of overall phase architecture. The use of surfmers as structure directing agents in the templating process of periodic mesoporous materials leads to a nanocomposite material with a geometrically confined, permanent organic phase inside the mesopores or vice versa [89, 90].

Another possibility to combine inorganic and organic building blocks is the addition of polymerizable species to the synthesis mixture (precursor, surfactant, solvent + monomer) [91-94]. Sellinger et al [93] report the fabrication of nanocomposite films mimicking nacre by a simple dip-coating process (evaporation-induced self-assembly, EISA) of a silica/surfactant/monomer mixture. Subsequent polymerization of the monomeric species, induced by light or heat, completes the nanocomposite assembly process. A coupling agent such as an organofunctional silane, e.g., methacryloxy propyltrimethoxy silane, covalently binds the organic phase to the silica framework.

## 1.5 Mechanical properties

Cellular materials allow producing materials with low weight and at the same time good mechanical properties. Polymeric, ceramic or metallic foams are employed in different fields such as light weight structures, insulation, crash protection and implant tissue. The latter, especially, is inspired from the fact, that most natural material such as (trabecular) bone, exhibit cellular structure. For cellular materials the primary factors controlling the mechanical properties are the apparent (relative) density  $\rho^* / \rho_s$  (where  $\rho^*$  is the density of the material and  $\rho_s$  is the density of the solid, non-porous framework), the architecture and the underlying material properties.

For three-dimensional elastic open-cell foams the elastic modulus,  $E^*$ , as well as the failure stress under compression,  $\sigma^*$ , scale with the square of the apparent density [95, 96]:

$$\frac{E^*}{E_s} = C_1 \left( \frac{\rho^*}{\rho_s} \right)^2 \quad \text{Eq. 1.1}$$

Here (\*) again refers to the properties of the overall cellular solid and the subscript s refers to the corresponding bulk material. This relation has been found for artificial open cell foams as well as for many natural porous materials such as bone or wood. Besides the apparent density, the micro- and nanoarchitecture of the cellular structure have been shown to play a significant role due to different modes of deformation.

In the field of light but mechanically robust materials periodic surfactant templated silica materials are interesting, since their structural mechanical properties may be tailored by nanoscale architecture as well as chemical tuning over the atomic and nanoscale structure. Several studies have been performed on the stability and the mechanical properties of these materials [97-99], reporting that nanostructured silicas can be stiffer and more elastic than the non-porous solid. As for disordered porous materials such as bulk aerogels, the Young's moduli are known to scale with the material density and are normally in the range of several MPa to 1-2 GPa [100, 101]. New methods such as, e.g., the resonant beam technique allows the simultaneous determination of Young's and shear modulus in highly porous materials [102, 103].

Most investigations on the mechanical properties of periodic mesoporous silica materials have been undertaken on thin films [104, 105]. A recent report by Brinker and co-workers examines the modulus-density scaling behaviour of nanostructured porous silica materials [106]. Based on the quadratic scaling of the modulus with relative density in natural porous materials, they investigate the modulus density-scaling relationship for cubic (C), hexagonal (H) and worm-like disordered (D) nanoporous silica films. The resulting scaling

exponent  $n$  follows the relation  $n_{(C)} < n_{(H)} < n_{(D)} < 2$ , indicating a less pronounced sensitivity to porosity than natural cellular solids. The explanation given for this insensitivity is that an increase in the modulus of the framework compensates for decreasing density as the wall thickness decreases. The underlying reason is that the nanoconfinement of the wall structure gives rise to an increasing population of three- and four-membered siloxane rings instead of the larger and weaker siloxane rings found in conventional amorphous silica.

The effects of meso- and macroporosity in monolithic carbons and carbon-carbon nanocomposites, nanocasted from monolithic silica with hierarchical pore structure, were studied by depth-sensing indentation measurements by Wang et al. [107]. They report an increase in the mechanical strength for the nanocomposites. The bending strength of bimodal porous silica gels with different macropore morphologies derived from water glass, with a porosity ranging from 30-90%, were investigated by Takahashi et al. [108, 109]. They affirm that a power law function applies to the relation between bending strength or Young's modulus and the bulk density of the gels with same macromorphology. Furthermore, they report a higher strength and elastic modulus compared with other porous materials of the same porosity.

## 1.6 Structuring on the macroscopic level

### 1.6.1 Macroscopic shape of periodic mesoporous materials

There have been several attempts to shape mesostructured monolithic material in the past, since the new hierarchical level significantly widens the application of sol-gel derived materials in the direction of the life sciences (cellular tissue engineering). In biological/biomedical research the development of scaffold structures, on which cells are able to adhere, is required. The crucial requirements of such a tissue engineering scaffold are that a) its surface chemistry favours cellular attachment, differentiation and proliferation, b) it is biodegradable, bioresorbable or inert, c) it exhibits similar mechanical properties to the replaced tissue, d) it can be easily fabricated in individual shapes and sizes and e) it has interconnecting porosity, so as to facilitate tissue integration [110-112]. Moreover, the presence of silanol groups at the surface and the textural properties are crucial for apatite formation which makes it only logical to use mesoporous silica [113-116]. Additional advantages of the sol-gel route are the mild synthesis conditions, the high purity of the obtained materials, the small pore size distribution, the low density and the possibility of implementing organic entities not only in the pores of the inorganic network but also into the walls (Chapter 1.3.2 and 1.4).



Until now few reports have been made on expanding the structural organization up to the macroscale [117-120]. Most of the time, monolithic mesoporous materials are restricted to simple geometries determined by the size and shape of the vessel used, resulting in cylinders, platelets, etc. Theoretically there are several methods to obtain complex structured parts, such as localized deposition/hardening of material as done in stereolithography and 3D-printing, selective removal/carving of material or casting. Selective gelation/polymerization of silica material has been achieved for thin films, allowing only a 2D-patterning [121]. Popall et al. report the 3D-patterning of organic-inorganic hybrid materials by two-photon polymerization processes using femtosecond lasers [122]. Conventional casting methods aiming at complex or undercut structures use high temperatures to get rid of the sacrificial molds [123]. Therefore, these methods cannot be applied in the fabrication of organic-inorganic hybrid materials. Another problem that arises during casting of sol-gel materials is the alcohol release during the gelation process, the shrinkage of the SiO<sub>2</sub>-network and the capillary forces that are acting on the network during drying.

### 1.6.2 Rapid prototyping/stereolithography

Rapid Prototyping (RP) is a suitable manufacturing method for fabricating structures with high geometric complexity and heavily undercut features, which cannot easily be fabricated with traditional manufacturing methods.

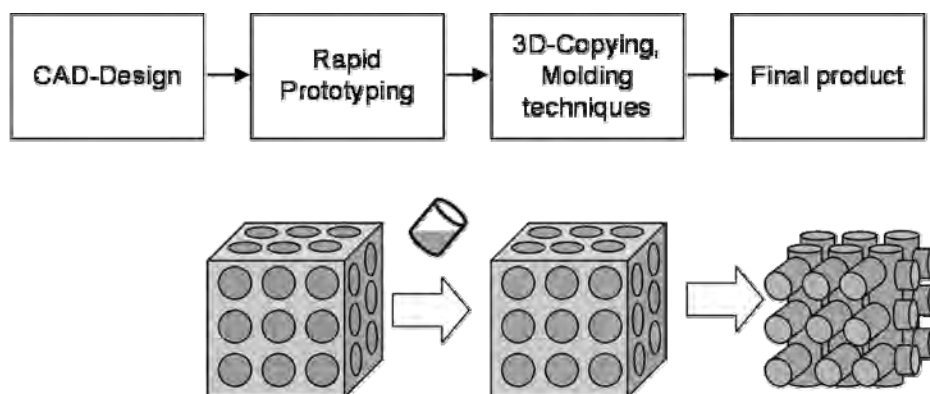


Figure 1.6.1. Rapid prototyping typically starts with a CAD-model which is fabricated by different methods.

In a first step, the three dimensional prototype is designed by CAD (computer aided design). Once the 3D-model of the desired part has been correctly set up, the input data is sliced into layers of a constant thickness. Manufacturing of the part is then done by adding material layer by layer until the desired shape is achieved. RP techniques are limited in the

number of materials that can be processed (photopolymers, thermoplastics, powder-based materials). There is the possibility to use the RP part as mold for the final material, introducing an additional step in the fabrication of the desired part. Nevertheless, this method of 3D-copying is still a fast and easy way to obtain complex structured parts without the need of machining or tooling. E.g., molding based on powder filled slurries in combination with wax molds made by RP (gelcasting) offer an easy route for the fabrication of metallic and ceramic parts, where the limiting factor is the shrinkage during sintering.

Stereolithography is an RP technique based on the solidifying of a liquid photosensitive monomer with a laser or light source. The final polymeric part is manufactured layer by layer.

In Figure 1.6.2 (b) the principle of a digital light processing (DLP) based machine is shown. For fabrication of the 3D-parts a CAD model (e.g., Figure 1.6.2 (a)) is designed and sliced up into thin layers. Layer by layer the model then is projected on to the bottom layer of the resin tank by a micro-mirror array. Where the light sensitive resin is irradiated, it is cured in a few seconds. The polymer adheres on the z-stage which is moved up 30 to 50  $\mu\text{m}$  in z-direction (thickness of one layer). Then the next layer is cured and so on. The final part is separated from the z-stage and residual unpolymerized resin is washed away in acetone. Currently used systems achieve resolutions in the xy-plane down to 5  $\mu\text{m}$  and a minimal layer thickness of 10  $\mu\text{m}$ . Far higher accuracy is possible with two-photon-stereolithography.

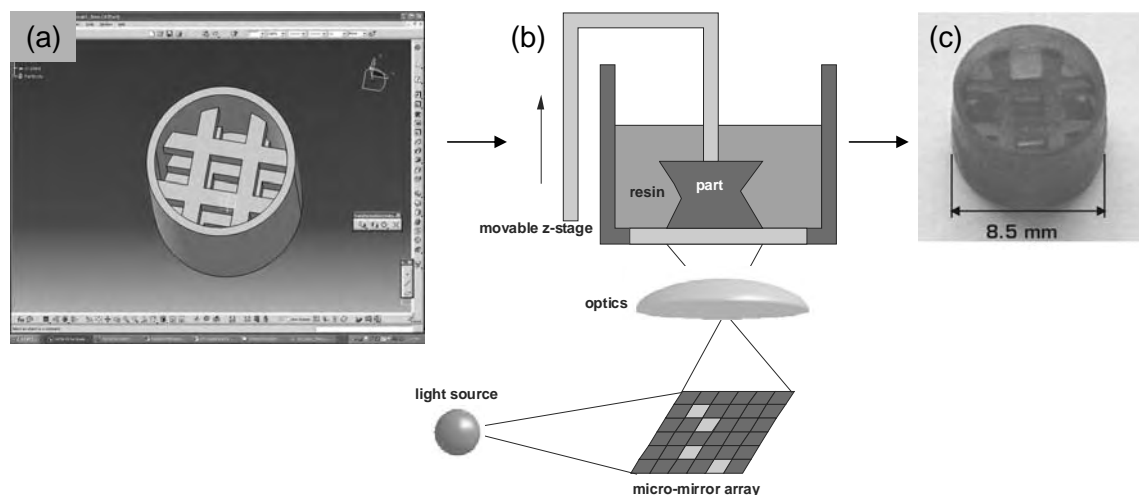


Figure 1.6.2. Working principle for RP systems based on digital micro-mirrors.

## 2 Experimental

### 2.1 Structural design on the nanometer level

#### 2.1.1 Employed surfactants

In this work several ionic and non-ionic surfactants were employed as structure directing agents in the formation of silica monoliths with periodic mesoporosity. Others were studied regarding their phase behavior as well as their alignment at interfaces and in low magnetic fields.

##### 2.1.1.1 Cetyltrimethylammonium bromide (CTAB).

CTAB is a cationic surfactant that consists of a hydrophobic alkyl chain with a hydrophilic trimethylammonium bromide headgroup (Figure 2.1.1).

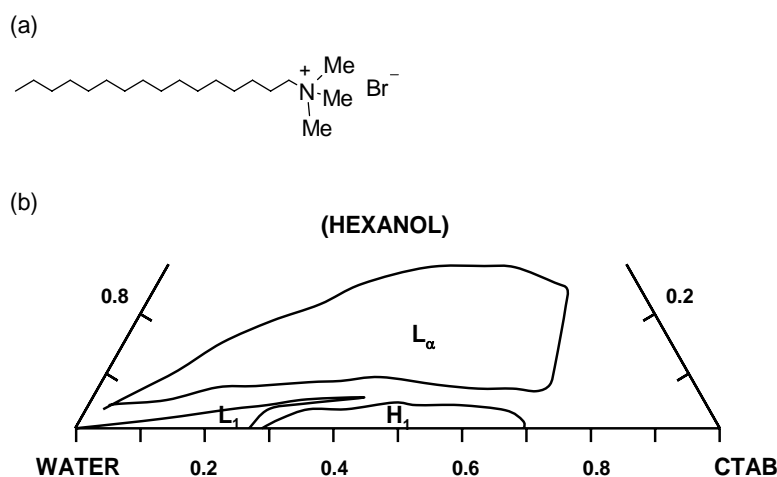


Figure 2.1.1. (a) Molecular structure of cetyltrimethylammonium bromide. (b) Ternary phase diagram of CTAB/water/hexanol (simplified from [8]).

The phase diagram is shown in Figure 2.1.1 (b).  $L_1$  denotes the normal micellar phase. In  $H_1$  the basic structural units of the system are rod-like cylindrical micelles. These micelles are arranged in a hexagonal pattern within the aqueous region.  $L_\alpha$  indicates the lamellar micellar region [8]. CTAB is commonly used in the synthesis of mesostructured silica gels and leads mostly to 2D hexagonal structure of the mesopores.

### 2.1.1.2 $PEO_{20}PPO_{70}PEO_{20}$ (Pluronic P123)

The non-ionic ABA block copolymer P123 was bought from Aldrich and used as received with a specific average molecular weight of 5800. It consists of two hydrophilic polyethylene oxide blocks and a more hydrophobic polypropylene oxide block.

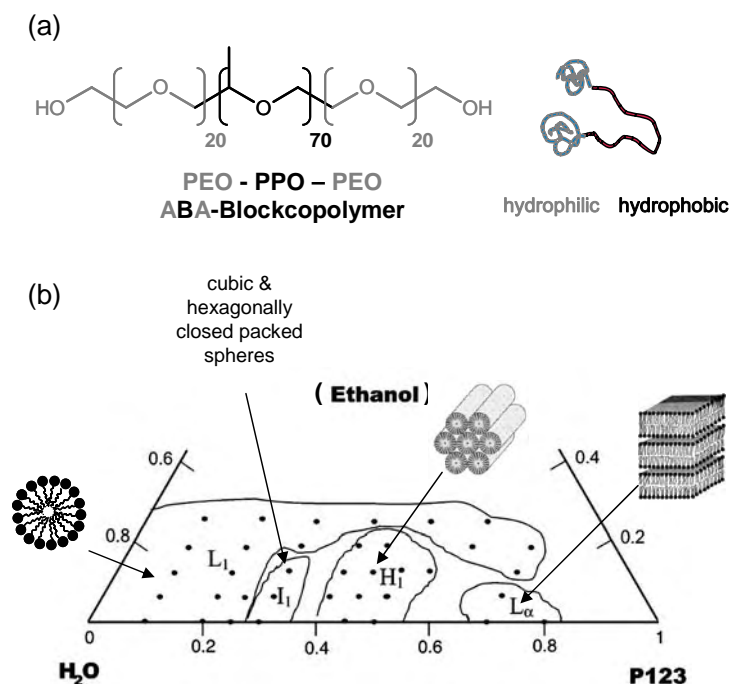


Figure 2.1.2. (a) Molecular structure of Pluronic P123. (b) Ternary phase diagram of P123/water/ethanol at T=23 °C (modified from[13]).

In the ternary phase diagram of P123/water/ethanol shown in Figure 2.1.2 (b), L<sub>1</sub> denotes the region with isotropic solution (water rich), I<sub>1</sub> denotes the clear isotropic gels and mixture of cubic and HCPS (hexagonally close packing of spheres) lattice, H<sub>1</sub> denotes cylindrical micelles arranged in a 2D hexagonal lattice, and L<sub>α</sub> denotes the lamellar phase. P123 was mainly used in concentrations of 30%(w/w) and 40%(w/w) in water or aqueous solution of HCl. As depicted in Figure 2.1.2 at 30%(w/w) cubic  $Fm3m$  and  $P6_3mmc$  (HCPS) phases coexist (I<sub>1</sub>). To promote the easy dissolution of the surfactant, P123 was heated at 50 °C prior to mixing with water. The mixture was then stirred in a sealed vessel at 50-60 °C until homogeneous and afterwards stored at 4 °C, where it became transparent and liquid due to the increased hydrophilicity of the PPO-blocks at low temperatures.

Block copolymers have been used successfully for the fabrication of mesoporous materials. The resulting periodic mesoporous gels exhibit large pores and thick walls [29]. In addition to its role as structure directing agent the polyethylene oxide blocks of P123 also induce a liquid-liquid phase separation leading to the formation of macropores (described in Chapter 1.3.3).

### 2.1.1.3 Brij 56 and Brij 97

Polyoxyethylene 10 cetylother (Brij 56,  $C_{16}E_{10}$ ) and polyoxyethylene 10 oleyl ether (Brij 97,  $C_{18}H_{35}E_{10}$ ) are AB-block copolymers consisting of a hydrophobic alkyl block and a hydrophilic polyethylene oxide block. In addition Brij 97 comprises a double-bond in the alkyl block.

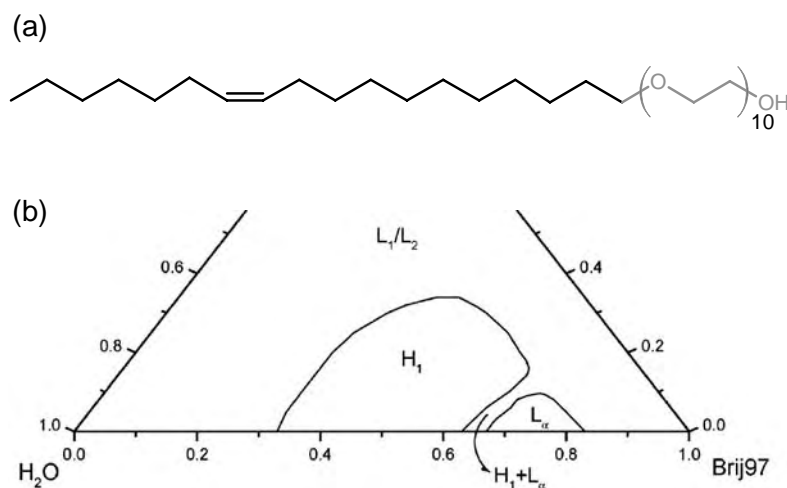


Figure 2.1.3. (a) Molecular structure of Brij 97. (b) Ternary phase diagram of Brij 97/1-butyl-3-methylimidazolium tetrafluoroborate/water at 25 °C (taken from [14]). The L-regions denote isotropic solutions (water-rich or Brij 97-rich);  $L_{\alpha}$  lamellar liquid crystal phase;  $H_1$ , hexagonal liquid crystal phase.

### 2.1.1.4 Polyethylene glycol 4-tert-octylphenyl ether (Triton X-45).

Triton X-45 is a liquid non-ionic surfactant and has been reported to give mesoporous solids at very high acid concentrations [124].

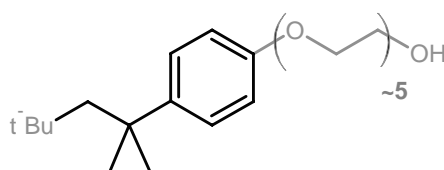


Figure 2.1.4. Molecular structure of Triton X-45.

### 2.1.1.5 Preparation of the LC-phases

Surfactant and distilled water/aqueous solution of hydrochloric acid were mixed in the desired concentrations and homogenized in a sealed container. Homogenization was achieved through mechanical stirring (magnetic stirrer) of the heated or, in case of P123, the cooled mixture and also through exposure to ultrasound.

## 2.1.2 Employed precursors

### 2.1.2.1 $Q^8M^8$ -cube precursor solution

**Synthesis:** (modified from [125]) An aqueous alkaline silicate solution was prepared by mixing 0.0448 mol 25% tetramethylammonium hydroxide (TMAOH in  $CH_3OH$ ) + 0.224 mol  $CH_3OH$  + 0.392 mol  $H_2O$  + 0.0448 mol tetramethyl orthosilicate (TMOS). The solution was stirred overnight under argon atmosphere and afterwards kept at 4 °C. Due to the highly alkaline conditions the silica does not polymerize but reacts to double four rings (see Figure 2.1.5).

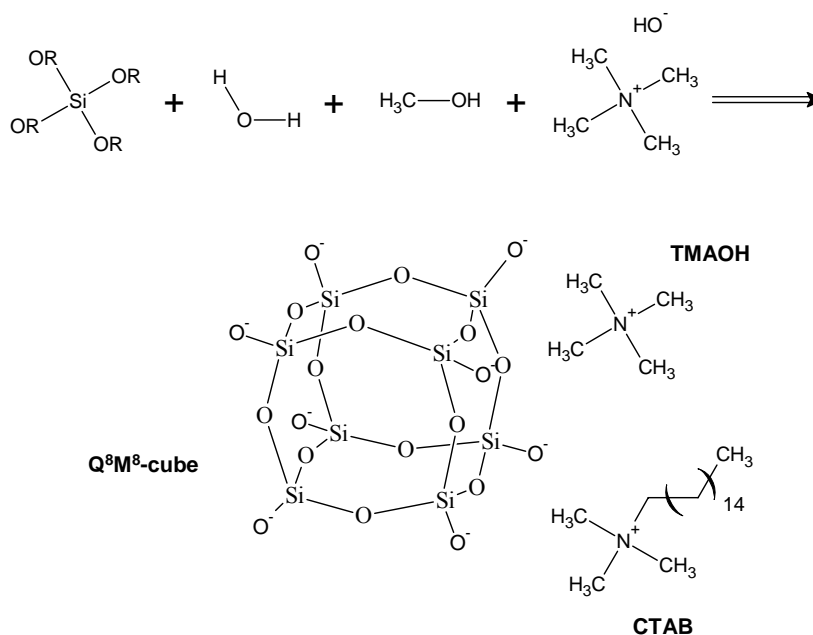


Figure 2.1.5. Synthesis of the  $Q^8M^8$  Si-precursor and the further preparation of a silica/surfactant liquid crystal. The solution is stabilized through the highly alkaline conditions.

#### Processing of a highly alkaline silica/surfactant liquid crystal:

A silicate/surfactant liquid crystal was prepared by adding a 7-12%(w/w) aqueous solution of the cationic surfactant cetyltrimethylammonium bromide (CTAB) to the aqueous alkaline silicate solution ( $Q^8M^8$ ) at RT. The mixture separates into a viscous silicate/surfactant-rich LC phase with hexagonal or lamellar structure and a water-rich phase. The highly alkaline conditions (pH=12.5) prevent the polymerization of the double-four-ring silicate oligomers.

### 2.1.2.2 Ethylene glycol-modified silane (EGMS)

A main problem in the fabrication of monolithic silica materials derived from conventional alkoxy silanes is the release of alcohols due to hydrolysis and condensation reactions during the process. In the presence of methanol or ethanol the solvent phase becomes more lipophilic. Therefore, the hydrophobic interactions of the surfactant molecules are destabilized. As a consequence, the formation of a lyotropic mesophases is in many cases prohibited. To overcome this, the conventional silica precursor tetraethylorthosilicate (TEOS) was modified with ethylene glycol.

#### Synthesis of ethylene glycol-modified silane:

In a synthesis described by Mehrotra [126] the ethoxy groups of TEOS were substituted with ethylene glycol at 413 K under argon atmosphere (Figure 2.1.6). Ethanol, which is produced during the transesterification reaction, was continuously removed by distillation over a Vigreux column. At the end of the reaction excess ethanol was removed in vacuo. The final product, a transparent viscous liquid was analysed by  $^{29}\text{Si}(\text{H})\text{-HMBC-NMR}$  using  $\text{CDCl}_3$  as solvent and revealed one peak at about -83 ppm. TGA measurements were performed to determine the Si-content.

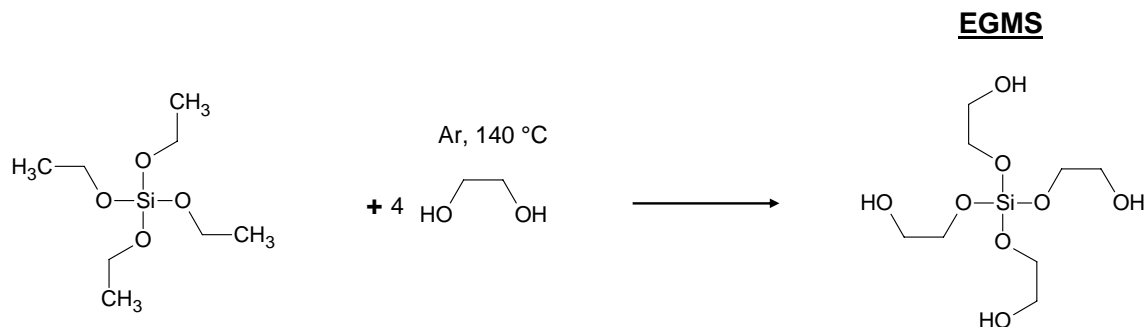


Figure 2.1.6. Synthesis of the ethylene glycol modified precursor.

Table 2.1. Theoretical  $\text{SiO}_2$ - and Si-content of ethylene glycol-modified silane (EGMS).

	MW / $\text{g mol}^{-1}$ (% $(\text{w/w})$ )	$\text{SiO}_2$ -content / % $(\text{w/w})$	Si-content / % $(\text{w/w})$
theroretical	272.31 (100)	22.1	10.3
experimental	-	20.8	9.7

### 2.1.2.3 Phenylene-bridged ethylene glycol-modified silane (*bPhGMS*)

1,4-Bis(triethoxysilyl)benzene was synthesized via Grignard reaction from dibromobenzene as described by Shea et al [68]. TEOS (450 mL, 2 mol), dry tetrahydrofuran (THF, 250 mL), and a few crystals of iodine were added in a flame-dried Ar-purged three-necked round-bottomed flask with a magnetic stirrer and magnesium turnings (15 g, 0.62 mol). The solution was brought to reflux (65 °C) and 1,4-dibromobenzene (48 g, 0.2 mol) in dry THF (125 mL) was added dropwise during a 2 h period. The reaction was allowed to reflux for another 1.5 h, becoming greyish yellow. While cooling to room temperature the THF was removed by vacuum evaporation. The precipitated MgBr was removed by vacuum filtration. Subsequently, about 200 mL petroleum ether were added to precipitate the residual MgBr, which was again removed by filtration.

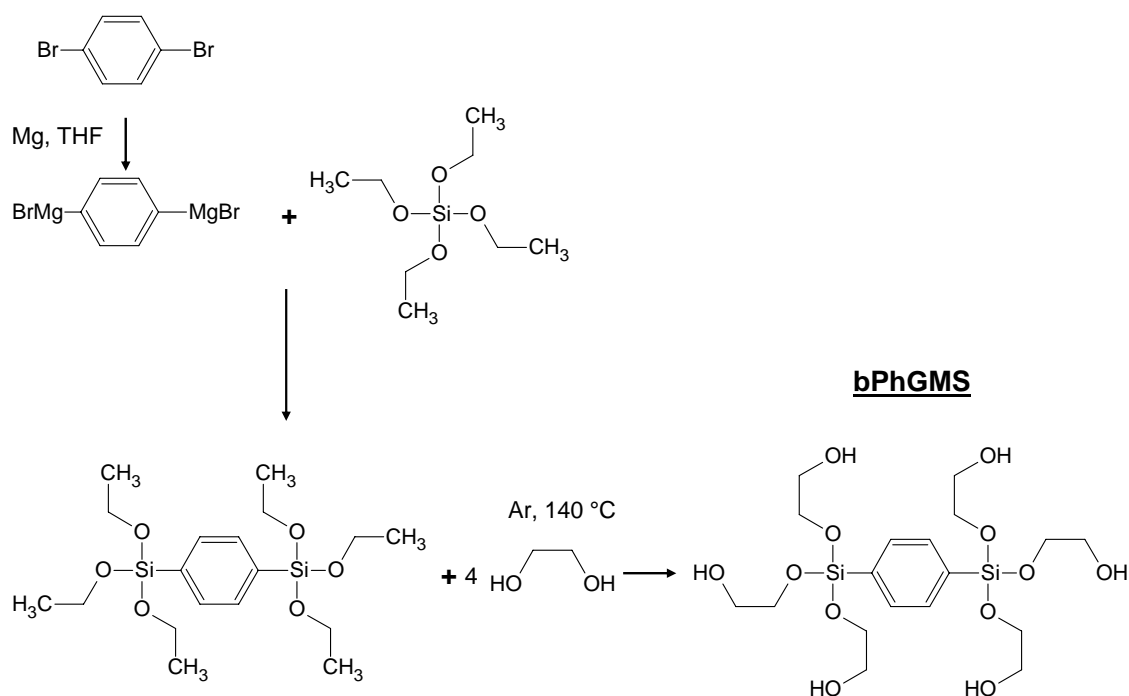


Figure 2.1.7 Synthesis of the phenylene-bridged ethylene glycol modified precursor.

The final product was obtained after removing excess TEOS (65 °C, 0.5 Torr) and appeared as colourless oil. The product was analyzed by <sup>1</sup>H NMR (1.26 ppm (t, J=6.97 Hz, CH<sub>3</sub>), 3.89 ppm (q, J=6.97 Hz, OCH<sub>2</sub>), 7.69 ppm (s, CH); Si: -59.0 ppm). Recovery yield was between 19 and 42% compared to the theoretical value (80.53 g).



In a second step 1,4-b(triethoxysilyl)benzene was reacted with ethylene glycol in a molar ratio of 1:6, otherwise the same procedure was followed as described for EGMS. The final product, this time consisting of transparent solid grains, was characterized with TGA to determine the Si-content (see Table 2.2). No NMR-measurements could be performed due to the low solubility of the precursor in other solvents than alcohol or water.  $^{13}\text{C}$  and  $^{29}\text{Si}$  CP MAS NMR studies were performed on the final dried gels.

Table 2.2: Theoretical  $\text{SiO}_2$ - and Si-content of phenylene-bridged ethylene glycol-modified silane (bPhGMS).

	MW / $\text{g mol}^{-1}$ (%(w/w))	$\text{SiO}_2$ -content / %(w/w)	Si-content / %(w/w)
theoretical	498.64 (100)	24.1	11.3
experimental	bPhGMS01	24	11
	bPhGMS02	22	10
	bPhGMS03	15	7

#### 2.1.2.4 Preparation of monolithic gels

Gels were made with different surfactants as structure directing agents and at various pH values. Other parameters that were changed in the experiments are the weight-ratio of Si/surfactant, Si/solvent and the temperature. As will be demonstrated, these parameters (type of precursor and surfactant, pH-value, temperature, dilution) have a strong influence on the formation of the mesostructure and the macromorphology, and therefore allow to some extent a control over the pore structure.

In a typical procedure, a given amount of surfactant was homogeneously dissolved in an aqueous solution of hydrochloric acid (pH=0-7). For the sol-gel synthesis the resulting LC-phase was added to the precursor under stirring at RT. After homogenization using a vortex stirrer, ultrasound or a centrifuge, the resultant liquid mixture was poured into containers. The container was sealed and kept at 313 K (unless denoted otherwise) for gelation. After gelation, the wet gels were kept at a temperature of 313 K for another 7 days for aging.

The denotation of samples prepared with the glycol-modified precursors in the presence of Pluronic P123 is explained in Figure 2.1.8.

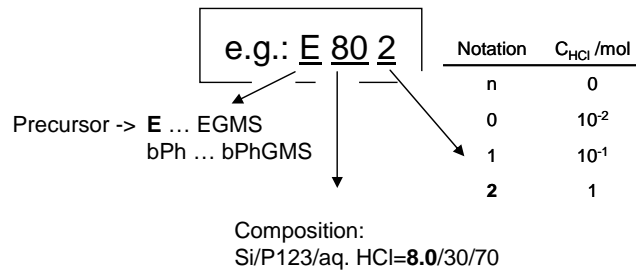


Figure 2.1.8. Denotation of the samples prepared with ethylene glycol-modified silane (EGMS) and bridged-phenylene glycol-modified silane (bPhGMS) and Pluronic P123 as structure directing agent. The weight ratio of P123/HCl (aq.) was kept constant at 30/70 unless denoted.

## 2.1.3 Drying of the wet monoliths

### 2.1.3.1 Supercritical drying

Samples prepared with EGMS/P123, bPhGMS/P123 and EGMS/Brij 97, were dried with carbon dioxide or methanol as supercritical fluids. The critical parameters of the two solvents are shown in Table 2.3. As obvious, the gels dried with methanol are exposed to higher temperatures throughout the process. In both cases the pore fluid first was exchanged to methanol (washing for 4 times).

CO<sub>2</sub> Supercritical drying was performed at the planta pilota at the MATGRAS (Barcelona, Spain), as well as in a laboratory autoclave. The aged and washed monoliths were carefully put into the autoclave and covered with methanol. The sealed container was flushed with liquid CO<sub>2</sub> (p=60-100 bar). After complete solvent exchange (for details see appendix), the system was sealed again and the temperature was increased above  $T_c$ , simultaneously leading to a pressure rise above  $p_c$ . The supercritical CO<sub>2</sub> was then removed carefully.

Supercritical drying with methanol has the advantage of being a fast process because no time-consuming solvent exchange to CO<sub>2</sub> has to be performed. Of course, the high pressure and temperature applied have more influence on the network so that a restructuring of the network may occur. Also functional organic groups may react, be replaced or destroyed. The supercritical drying was performed in a high-temperature and high-pressure plant. Therefore, the samples were covered with methanol and subsequently the pressure was increased to 52 bar. After that the temperature was increased over  $T_c$  within ~2 h (see appendix), while the pressure increased to 140 bar. After 4 h in the supercritical state, methanol was removed within 70 min and the autoclave with the samples was subjected to natural cooling. Crack-free monoliths were obtained.

Table 2.3 The two different supercritical fluids employed in the supercritical drying of the monolithic gels.

Solvent	Notation	T <sub>c</sub> / °C	p <sub>c</sub> / bar	Advantage	Disadvantage
CO <sub>2</sub>	-scd(CO <sub>2</sub> )	31.3	73	low T <sub>c</sub> not flammable	time-consuming solvent exchange
CH <sub>3</sub> OH	-scd(MeOH)	240	81	fast	high temperatures and pressures flammable solvent

Whereas gels dried with CO<sub>2</sub> are known to be rather hydrophilic, gels dried with methanol are more hydrophobic (surface covered with methoxy groups) [127].

### ***2.1.3.2 Ambient pressure drying after surface silylation with trimethylchlorosilane***

The liquid crystalline template was removed by surface silylation with trimethylchlorosilane. Therefore the wet gel was reacted by immersing the gel body in a solution of 10 (v/v) trimethylchlorosilane in petroleum ether (PE) for 12 h and afterwards washed 3 times with PE and 5 times with ethanol to remove unreacted silane species (samples are denoted as -tms). The surface modified samples were dried by slowly heating to 55 °C, 70 °C and 120 °C (up to 60 °C the heating rate was 3 °C/2 h, after that 10 °C/2 h).

### **2.1.4 Addition of polymerizable species to LC templates**

For the sol-gel system combining the ethylene glycol-modified silane with a liquid crystal templating approach using the poly(ethylene oxide)-based block copolymer P123 in acidic aqueous media the composition and pH-range for well ordered meso- and macropores is well known. Therefore, this system was chosen to introduce polymerizable species to the templating process, with the intention to incorporate monomers into the hydrophobic regions of the final mesopores. Further polymerization should allow the fabrication of composite material with a well defined spatial confinement of organic and inorganic components. Two different monomer-crosslinker combinations were investigated: (1) lauryl acrylate (LA) together with 1,4-butandiol dimethacrylate (BMA) and methacryloxy propyltrimethoxy silane (MPS) as coupling agent ; (2) acrylic acid 2-butyl-carbamoyloxy-ethyl ester (BEA) in combination with ethoxylated trimethylolpropane triacrylate (TTA). The combinations and compositions are listed in Table 2.4. BEA and TTA were chosen due to their high biocompatibility [128]. All materials were obtained from Sigma Aldrich, except TTA, which was obtained from Rahn.

## 2.1 STRUCTURAL DESIGN ON THE NANOMETER LEVEL

Table 2.4 lists the formulations of polymerizable additives investigated in this work.

Nomenclature	Monomer	Crosslinker	Coupling agent	Weight ratio (molar ratio)
<b>LB</b>	lauryl acrylate (LA)	1,4-butanediol dimethacrylate (BMA)	-	89.5:10.5:0 (1:0.12:0)
<b>LBM</b>	lauryl acrylate (LA)	1,4-butanediol dimethacrylate (BMA)	methacryloxy propyltrimethoxy-silane (MPS)	89.5:10.5:46.2 (1:0.12:0.48)
<b>AT</b>	acrylic acid 2-butyl-carbamoyloxy-ethyl ester (BEA)	trimethylolpropane triacrylate (TTA)	-	80:20:0 (1:0.18:0)

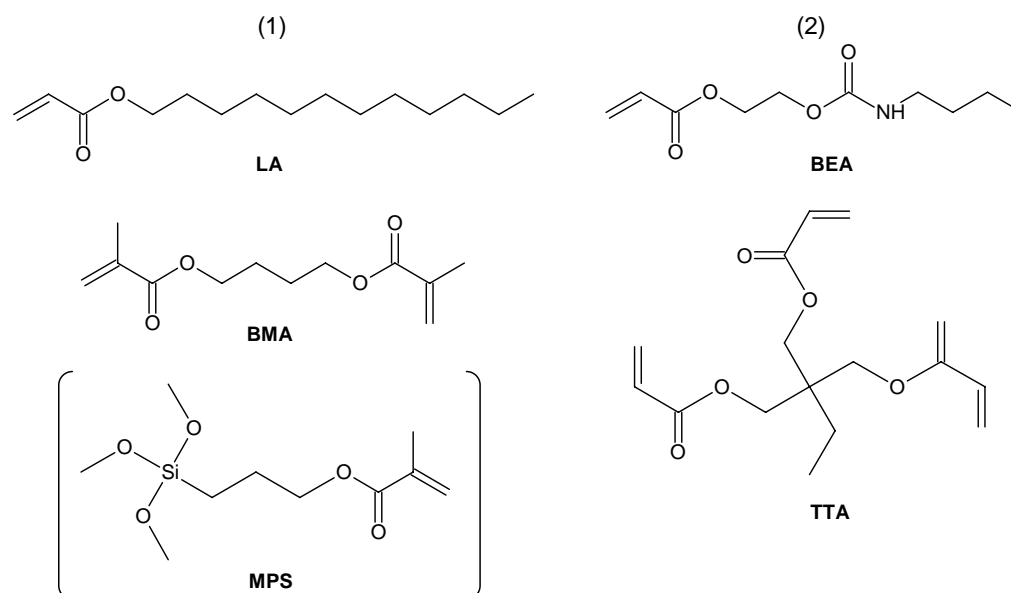


Figure 2.1.9. Monomers, crosslinkers and coupling agent added to the LLC phase of the non-ionic poly(ethylene oxide)-based block copolymeric surfactant P123 in acidic aqueous media.

MPS was distilled under vacuum for purification. All other components were used as received. Initiators used in this work were the photoinitiator Irgacure 819 (bis(2,4,6-trimethylbenzoyl)-phenylphosphine oxide) which was received from Ciba SC as a gift and the thermal initiator AIBN.

In a typical procedure polymerizable species were homogenized with the LLC phase of Pluronic P123 in water or aqueous hydrochloric acid. Samples were prepared with P123/water concentrations of 30/70 and 40/60 (w/w) and increasing amount of additives. The resulting mixtures were investigated by SAXS (Chapter 3.3.1) and in further investigations replaced the pure P123/HCl (aq.) phase in the sol-gel synthesis (Chapter 3.3.2).

## 2.2 Structural design on the macroscopic level

Rapid Prototyping (RP) was used to build sacrificial molds for the macroscopic casting of periodic mesoporous gels. The cellular 3D-structures were designed with CATTIA and printed using a stereolithography method as described in Chapter 1.6.2.

### 2.2.1 Employed resins

Commercially available RP resins lead to highly cross-linked polymers which can only be removed by high temperatures, e.g., 550 °C for conventional epoxy molds [123]. The templating of organic/inorganic nanocomposites is a general challenge because of the temperature sensitivity of the organic phase that does not allow for calcination as a method for template removal. In this work recently developed organo-soluble [129, 130] as well as water-soluble photopolymerizable [112, 131] resins for stereolithography RP were used.

Table 2.5. Components of the water-soluble [129, 130] and b) the organo-soluble [112, 131] resin-formulations which were investigated in this work.

Function	Components for water-soluble resin	%(w/w)	Components for organo-soluble resin	%(w/w)
Base monomer	DMAA (N,N-dimethyl-acrylamide)	40.0	DIBA (N,N-diisobutyl acrylamide)	72.0
Crosslinking agent	MAA (methacrylic anhydride)	8.0	MAA (methacrylic anhydride)	11.0
Comonomer	MA (methacrylic acid)	40.0	DAA (diacetone acrylamide)	9.9
Filler	NVP (N-vinyl pyrrolidon)	13.0	CAB (cellulose acetate butyrate)	4.1
Photoinitiator	Irgacure 819	3.0	Irgacure 819	3.0
Dye			OR1	0.09

The new resins are dissolvable at ambient temperature and therefore allow for the macroscopic shaping of organic-inorganic hybrid materials as derived from soft chemistry methods. This will be shown in Chapter 3.7. Since gelation of the gels derived from ethylene glycol modified silanes was performed in aqueous media, it was necessary to assure that the sacrificial molds were stable during the process. A photopolymerizable resin formulation based on highly reactive acrylamides has proven suitable for processing in water or polar solvents. The organo-soluble resin used in this work contains less DAA

(for %(w/w) see Table 2.5) to provide stability throughout the aging of the gel for one week in aqueous media [129, 130].

### **2.2.2 Fabrication of sacrificial cellular molds**

The soluble polymer structures used as sacrificial molds for the templating of the mesostructured silica material in this work were built by direct light processing (DLP) on a Perfactory® (Envisiontec). In a typical procedure the sacrificial molds were built with a layer thickness of 70  $\mu\text{m}$  and an exposure time of 10 s per layer. The power of the light source was 550  $\text{mW}/\text{dm}^2$ .

### **2.2.3 Casting of gels**

In a typical procedure, the vessel containing the sacrificial RP part was filled with the homogenized sol and sealed. Bubbles were avoided by short centrifugation or ultrasound, respectively. Gelation and aging (one week) took place at 313 K (standard procedure for sol-gel-processing of the glycol-modified precursors).

### **2.2.4 Dissolution of molds**

The organo-soluble molds were dissolved in n-butylamine/THF or n-ethylamine/THF in a volume ratio of 1:9 at RT under constant stirring.

## 2.3 Analytical methods

### 2.3.1 X-ray scattering

Elastic scattering of X-rays is a method commonly used to investigate structures on the atomic or mesoscopic level. In this work small angle X-ray scattering (SAXS) investigations were performed on liquid crystalline samples as well as wet and dried mesoporous gels. From these measurements it is possible to gain information on the structural features in the nanometer regime. Additionally, wide angle X-ray scattering (WAXS) measurements were carried out to get information on the molecular structure of the walls of the porous gels.

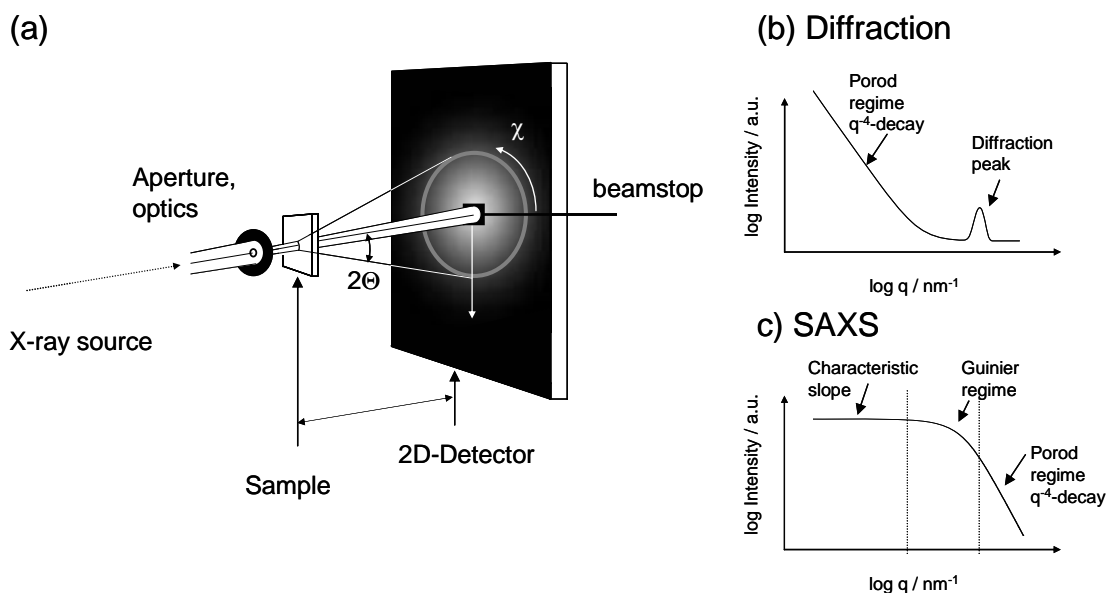


Figure 2.3.1. a) Schematic setup for a 2D SAXS experiment. b) Example for a scattering pattern consisting of a Porod regime (see Eq. 2.4) and a Bragg reflection.

Depending on the setup, it is possible to investigate particles of different size with scattering experiments. For example, sample-detector distance, size of the detector, wavelength of the incident beam ( $\lambda$ ) and size of the utilized beam stop determine the accessible  $q$ -range (and therefore the investigable size range in real space,  $r \propto 1/q$ ). Typically, SAXS techniques provide information on structures in the size region from 1 to 100 nm. The simplified experimental setup of a SAXS experiment is shown in Figure 2.3.1. The data obtained with a 2D detector can be analysed by radial and azimuthal integration. The latter gives information on the size and shape of the scattering units or the periodic structure if present (Figure 2.3.1 b)): averaging over concentric circles round the primary beam with  $\chi$  as the azimuthal angle). Additionally to size and structure,

information on the orientation of anisotropic particles can be derived from a  $2\theta$  integration (averaging over scattering angle  $2\theta$ ).

**Small Angle X-ray Scattering (SAXS) theory.** In the following the theory of X-ray scattering will be presented very shortly, including the models and equations relevant in this work. For deeper insight, the theory of SAXS was treated in detail, for example, by Guinier & Fournet (1955) [132]. Applications of scattering methods on soft condensed matter are described, e.g., in Kasai & Kakudo [133] and Lindner & Zemb (1991) [134]. Analysis and modelling of SAXS data from polymer solutions was discussed by Pedersen [135] and a review on SAXS as characterization method for nanostructures in inorganic and hybrid materials was given by Peterlik & Fratzl [136]. Detailed analysis of scattering curves of ordered mesoscopic materials was described by Förster et al. [137]. Possibilities and advantages of synchrotron SAXS have recently been summarized by Narayanan [138].

Since in elastic scattering no energy is transferred to the system, the norm of the wave vector of the incoming beam ( $|\vec{k}|$ ) and the scattered beam ( $|\vec{k}'|$ ) are identical ( $|\vec{k}| = |\vec{k}'| = 2\pi/\lambda$ ). The transferred momentum (scattering vector  $\vec{q}$ ) can be written as

$$\vec{q} = \vec{k} - \vec{k}', \quad q = \frac{4\pi \sin \theta}{\lambda} \quad \text{Eq. 2.1}$$

where  $2\theta$  is the scattering angle between incoming and scattered beam. For diffuse scattering near the direct beam (small angle scattering) and distances large compared to atomic distances, the intensity of a system composed of two different locally separated phases (2 phase model, see e.g., Glatter & Kratky [139]) with sharp interface can be described by

$$I(\vec{q}) = C(\rho_\alpha - \rho_\beta)^2 \left| \int_{V_\alpha} e^{i\vec{q}\vec{r}} d\vec{r} \right|^2 \quad \text{Eq. 2.2}$$

Here,  $\rho$  is the electron density of phase  $\alpha$ , respectively  $\beta$ , and the integral only extends over the volume of the  $\alpha$ -phase ( $\alpha$  and  $\beta$  are exchangeable).

Each maximum in the scattering curve and every change in slope may be correlated with a characteristic length (particle size, particle distance) of the material (see Figure 2.3.1 (b)) and (c)). In small angle scattering, typical patterns show power-law decays in intensity as shown in Figure 2.3.1 (c). The region where the decay starts or ends is visible in the log intensity versus log  $q$ -plot as knee. From the position of the knee in reciprocal space, a characteristic size of the system in real space is obtained.



In principle the scattering intensity from a system composed of particles can be expressed by  $I(q) = A \cdot P(q) \cdot S(q)$  [140], where  $A$  is a parameter depending on the total volume of the particles,  $P(q)$  is the form factor of the individual particles, and  $S(q)$  the structure factor, describing the packing of the particles.  $S(q)$  approaches 1 for uncorrelated particles (e.g., dilute systems). For small  $q$ , the form factor has a general form which depends only on the radius of gyration of the electron density,  $R_g$  (Guinier radius) of the particle. This is the so-called Guinier's law (Eq. 2.3), which is valid for dilute and isolated particles.

$$\text{Guinier's law: } I(q) \sim G \cdot \exp\left(-\frac{(qR_g)^2}{3}\right) \quad (qR_g \leq 1) \quad \text{Eq. 2.3}$$

For spherical particles with radius  $r$  the following relation applies:  $R_g^2 = 3/5 \cdot r^2$  (Svergun & Feigin [141]).  $R_g$  can be derived from the linear slope of a so-called Guinier plot ( $\log I(q)$  plotted against  $q^2$ ). At very small  $q$ , the intensity is constant in the case of spherical particles. For asymmetric particles, dependent on their dimensionality, the intensity follows a characteristic power law, e.g.,  $q^{-1}$  for rods/cylinders (1D) and  $q^{-2}$  for discs/bilayers (2D). This is valid for  $qD \gg 1$  (with  $D$  being the largest dimension of the particle).

The behaviour towards large  $q$ -values is generally described by Porod's law:

$$I(q) \propto P \cdot q^{-4} \quad \text{Eq. 2.4}$$

Eq. 2.4 is only valid for sharp interfaces between particles and surrounding, but independent of morphology and dilution. Analytical expressions for the form factor of particles with different morphology are given in the following equations (taken from [134]):

$$\text{Spherical particles: } I(q) = \phi(\Delta\rho)^2 P(q) = V\phi(\Delta\rho)^2 \left(3 \frac{\sin qR - qR \cos qR}{(qR)^3}\right)^2 \quad \text{Eq. 2.5}$$

$$\text{Cylindrical particles: } I(q) = \phi(\Delta\rho)^2 P(q) = \frac{\pi^2}{q} a^2 \phi(\Delta\rho)^2 \left(2 \frac{J_1(qa)}{qa}\right)^2 \quad \text{Eq. 2.6}$$

$$\text{Bilayers: } I(q) = \phi(\Delta\rho)^2 P(q) = \frac{2\pi}{q^2} H \phi(\Delta\rho)^2 \left(\frac{\sin(qH/2)}{qH/2}\right)^2 \quad \text{Eq. 2.7}$$

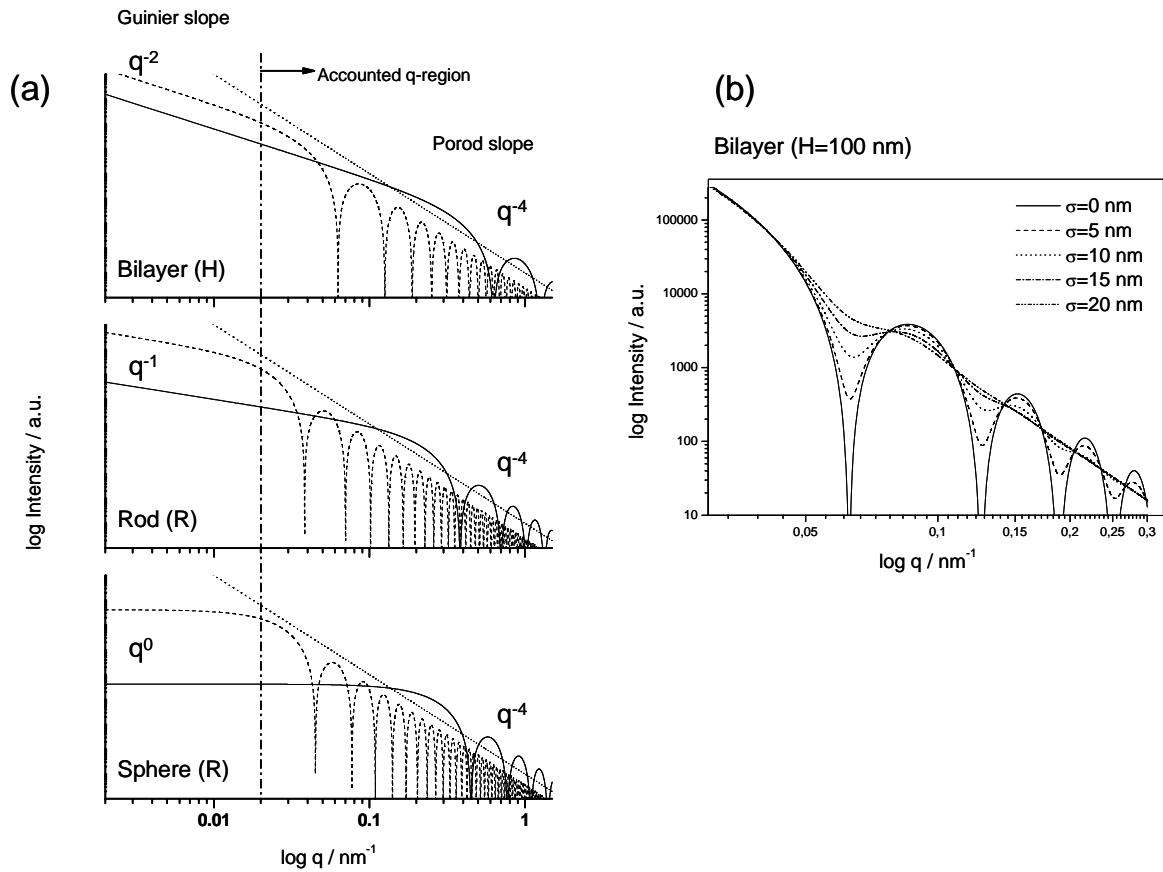


Figure 2.3.2. (a) Scattering functions for homogeneous spherical, cylindrical (length infinite) and disc-shaped (radius infinite) particles in a log-log plot with different radii ( $R$ ,  $a$ ), respectively, thickness ( $H$ ) (full line:  $R$ ,  $a$ ,  $H=10$  nm; dotted line:  $R$ ,  $a$ ,  $H=100$  nm). The intensity increases with a shape-characteristic power towards small  $q$ -values. The following Porod regime towards high  $q$ -values is indicated as dashed line. The vertically drawn line indicates the  $q$ -range, which was accessible in the kinetic measurements.

(b) Scattering curves of discs with mean thickness  $D=300$  nm and varying polydispersity (Gaussian size distribution, standard deviation  $\sigma$ ).

$R$  is the radius of the spherical particle,  $V$  is the volume of each sphere ( $V = \frac{4}{3}\pi R^3$ );  $a$  is the radius of the cylindrical particle and  $H$  is the thickness of one bilayer.  $\Delta\rho$  is the electron contrast of the particle and the solvent. Eqs. 2.5-2.7 yield curves with characteristic minima and maxima (Figure 2.3.2 (a)). In case of polydispersity of  $R$ ,  $a$  and  $H$ , the oscillations are smeared out depending on the size distribution. This can be easily simulated by including a particle size distribution,  $N(R)$ , leading to an expression for the intensity of isolated, polydisperse particles:

$$I(q) = \phi(\Delta\rho)^2 \int P(q, R)N(R)dR, \quad \text{Eq. 2.8}$$

where  $N(R)$  is, e.g., a Gaussian distribution (Figure 2.3.2 (b)).

In the case of polydisperse (no oscillations observed in the Porod regime) and disordered and dilute spherical particles ( $S(q)=1$  which is valid under the assumption of negligible particle interference) a Debye function is suitable to approximate the particle form factor [136, 140].

$$\text{Debye approximation: } P(q) = \left( 1 + \frac{\sqrt{2}}{3} q^2 R^2 \right)^{-2} \quad \text{Eq. 2.9}$$

This function describes the form factor of spheres with the radius  $R$  in the limiting case towards high values of  $q$  and corresponds to an extremely wide size distribution. Its quality as fit function in the case of forming particles will be discussed in detail in the appendix (page 150).

**X-ray diffraction (XRD).** For materials with long range order, such as crystalline phases or gels with periodically arranged mesopores, correlations between the positions of the micelles/pores become strong enough to produce diffraction peaks if Bragg's law is fulfilled.

$$\text{Bragg's law: } \lambda = 2 \cdot d_{hkl} \cdot \sin \theta_{hkl} \quad \text{Eq. 2.10}$$

The sequence of Bragg reflections defined by their Miller indices ( $hkl$ ) is used to identify the nature of each phase. Structures relevant in this work are listed in Table 2.6.

The periodic distance,  $d$ , can be calculated in a first approximation from the peak maximum,  $q_{\max}$ , according to:

$$d = \frac{2\pi}{q_{\max}} \quad \text{Eq. 2.11}$$

The lattice parameters of the different structures can be derived from the equations given in Table 2.6.

Estimation of the domain size: In case the peak intensity follows a Gaussian distribution, an estimate for the size of the contributing domains, respectively the size of coherently scattering regions, can be derived from the full-width at half-maximum (FWHM) of the first reflection of the periodical structure. This may be done by calculating the coherence length ( $L$ ), according to Scherrer's formula (Eq. 2.12). Observed broadening of the peaks is a consequence of the finite domain size.

$$L = \frac{2\pi K}{\sqrt{FWHM_{\text{exp}}^2 - FWHM_{\text{ref}}^2}} \quad \text{Eq. 2.12}$$

$L$  corresponds to the crystallite size and  $K$  is a constant close to 1 that depends on the shape of the crystallite.  $FWHM_{\text{exp}}$  is the full-width at half-maximum of the measured

diffraction peak ( $FWHM_{\text{exp}} = 2.35 \cdot \sigma$  with  $\sigma$  being the Gaussian half width from fitting the intensities with a Gaussian function) and  $FWHM_{\text{ref}}$  is the width of the detector/equipment resolution. For the application of Scherrer's formula it is important that  $FWHM_{\text{ref}}$  has to be significantly smaller than  $FWHM_{\text{exp}}$ . Since in this work, experiments were carried out at synchrotron radiation sources (ESRF, Elettra), a very good q-resolution could be achieved and L was therefore approximated (lower limit,  $K=1$ ) by:

$$L = \frac{2\pi K}{FWHM_{\text{exp}}} \quad \text{Eq. 2.13}$$

Table 2.6 lists the characteristic parameters for different types of lattices relevant in this work.

Structure	Position of reflections	Sequence of Bragg reflections	Multiplicity $m_{hkl}$
Hexagonal (P6mm)	$q_{hk} = \frac{4\pi\sqrt{(h^2 + k^2 + hk)}}{a\sqrt{3}}$	(10), (11), (20), (21), (30), (22), (31), ...	$m_{h0} = 6$ $m_{hh} = 6$ $m_{hk} = 12$
Lamellar	$q_h = \frac{2\pi h}{a}$	(100), (200), (300), ...	$m_h = 1$
FCC* (Fm3m)	$q_{hkl} = \frac{2\pi\sqrt{(h^2 + k^2 + l^2)}}{a}$	(111), (200), (220), (311), (222), (400), (331), (420), ...	$m_{h00} = 6$ $m_{hh0} = 12$ $m_{hhh} = 8$ $m_{hk0} = 24$ $m_{hhk} = 24$ $m_{hkl} = 48$
HCPS* (P6 <sub>3</sub> mmc)	$q_{hkl} = \frac{2\pi\sqrt{\frac{4}{3}(h^2 + hk + k^2) + \frac{3}{8}l^2}}{a}$	(100), (002), (101), (102), (110), (200), (112), ...	$m_{h00} = 6$ $m_{00l} = 2$ $m_{hh0} = 6$ $m_{hk0} = 12$ $m_{0kl} = 12$ $m_{hhl} = 12$ $m_{hkl} = 48$

\* FCC ... face centered cubic; HCPS ... hexagonally close-packed spheres

a) Laboratory equipment

SAXS and WAXS measurements were performed with a rotating anode generator and a 2D position sensitive detector (Bruker SAXS, Karlsruhe and Vantec 2000), equipped with a pinhole camera (Nanostar, Bruker AXS, Karlsruhe), and Cu-K $\alpha$  radiation collimated and monochromatized from crossed Göbel mirrors. All obtained 2D-SAXS patterns were radially averaged and background corrected to obtain the scattering intensity in dependence on the scattering vector  $q$ , where  $q=4\pi\sin\theta/\lambda$  with  $2\theta$  being the scattering angle and  $\lambda=0.1542$  nm the X-ray wavelength. The sample-detector distance was varied to obtain information on the  $q$ -region of interest. The smallest sample-detector distance was 2.8 cm for the WAXS measurements, the largest  $\sim 105$  cm (SAXS). This corresponds to a total  $q$ -range of  $0.2\text{--}33$  nm $^{-1}$  (Table 2.7). A special sample holder allowed heating of the samples inside quartz capillaries.

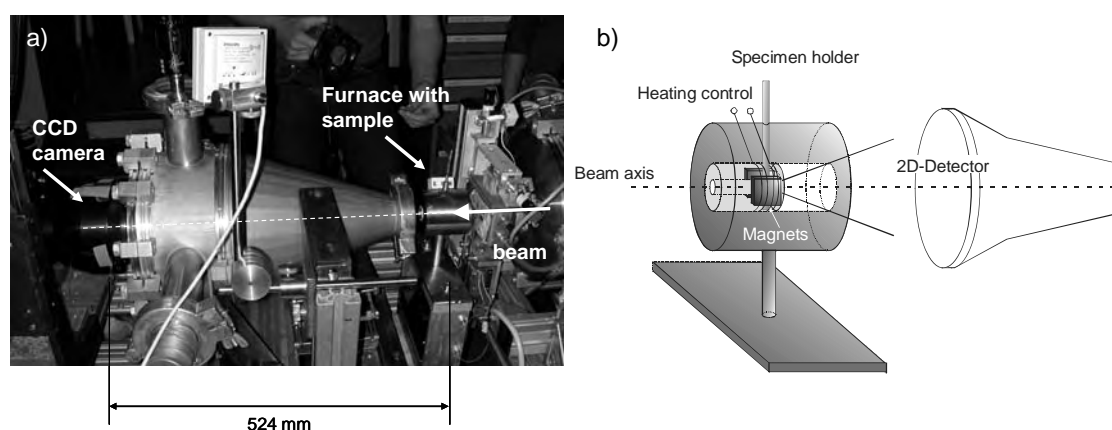


Figure 2.3.3. a) Shows the experimental setup for *in-situ* time- and position resolved SAXS at the synchrotron Trieste. The sample was placed in a specially adapted furnace equipped with magnets that could be fitted in the beam on a moveable stage. 2D scattering patterns were recorded with a CCD camera. b) Sketch of the oven

Table 2.7. Employed camera lengths and the corresponding accessible regimes in reciprocal and real space used with the laboratory equipment.

Sample-detector distance / mm	Designated $q$ -regime / nm $^{-1}$ (real space / nm)	Investigated systems
1052.5	0.2–2.2 (2.9–31.4)	Pluronic P123, Brij 56, Brij 97
209.5	0.5–9.5 (0.7–12.6)	CTAB, polyethylene glycol derivate, perylene derivate, Brij 97
28 (WAXS)	5.7–33 (0.2–1.1)	bPhGMS/P123-gels

### b) Synchrotron SAXS/WAXS

In case of time-resolved measurements of self-assembly processes of LLC phases and to gain detailed information on the formation of network and mesophase in the synthesis of surfactant templated mesoporous materials, laboratory sources usually require measurement times at least in the order of minutes due to their limited intensity. Therefore they are not suitable for *in-situ* studies of fast reacting systems. High brilliance synchrotron sources allow a high time resolution without loss of statistics (e.g., recording of 10 scattering patterns per second). This allows a thorough investigation of the self-assembly process and the gelation mechanism with a time resolution on a second or minute scale. Furthermore, the brilliance of the beam allows focussing with high intensity resulting in a high spatial resolution. *In-situ* measurements on the ordering of lyotropic liquid crystalline phases (Chapter 3.1) and gel kinetics (Chapter 3.4) were performed at the small angle X-ray scattering (SAXS) beamline BL 5.2 L at the synchrotron research centre Elettra in Trieste/Italy and at the ID02 High Brilliance Beamline at the European Synchrotron Radiation Facility (ESRF) in Grenoble/France.

**BL 5.2 L Elettra, Trieste, Italy.** The beamline optics consist of a flat, asymmetric-cut double crystal monochromator and a double focusing toroidal mirror. Data obtained by the 2D CCD-detector for small angle scattering (Photonic Science, Oxford) were analysed using the software fit2d [142]. Curves were background corrected and normalized.

Setup 1: For *in-situ* measurements on re-ordering effects of lyotropic liquid crystal phases an oven was built that could be positioned in the beam. The oven was mounted on a movable stage. Temperature was controlled using a temperature sensor at the sample and a heating wire, both connected to an external temperature control unit that was operated from outside the experimental hutch. The principle of the oven is depicted in Figure 2.3.3. To investigate the influence of small magnetic fields on domain orientation of different LLC mixtures permanent magnets consisting of  $\text{Sm}_2\text{Co}_{17}$  could be mounted inside the oven to either side of the sample. The gap between the magnets was 4 mm, resulting in a magnetic field of 0.3 T which was verified by Hall sensor measurements. The applied field (**B**) was perpendicular to the beam axis (**S**) as well as the long axis of the capillary. To investigate re-ordering effects of LLC domains position-resolved, the monochromatic X-ray beam (wavelength  $\lambda=0.154$  nm) was focused to a diameter of 0.5 mm. A 2D CCD-detector for small angle scattering (Photonic Science, Oxford) was placed in a distance of 524 mm to the sample (Figure 2.3.3).

Setup 2: SAXS measurements were carried out using a fixed wavelength of 0.077 nm and a camera length of 2092 mm. SAXS data were acquired with a 2D CCD-detector for small

angle scattering (Photonic Science, Oxford). Gelation of different surfactant templated systems without/with polymerizable additives was recorded. After gelation, samples were exposed to heat to induce polymerization of the organic additives.

**Setup 3:** Time-resolved combined SAXS and WAXS measurements were carried out using a fixed wavelength of 0.154 nm. A 150 mm linear wire PSD (Gabriel-type gas detector) was placed at a distance of 1520 mm to the sample. An additional 1D PSD was used for recording diffraction in the wide angle regime. The setup provided an effective  $q$ -range of  $0.2\text{--}3.5\text{ nm}^{-1}$  (SAXS) and  $8\text{--}17.5\text{ nm}^{-1}$  (WAXS). The SAXS/WAXS measurements were carried out during the gelation process, thus continuously following network and mesophases formation.

**ID02 High Brilliance Beamline ESRF, Grenoble, France.** SAXS measurements were carried out at the ID02 with an incident X-ray wavelength of 0.1 nm and a beam diameter of 0.3 mm. The scattered intensity was recorded by an image intensified CCD detector. Two different sample detector distances were employed, 1.5 m, leading to a scattering vector ( $q$ ) range of  $0.18 < q < 4\text{ nm}^{-1}$  and 10 m, leading to  $q$ -range of  $0.018 < q < 0.6\text{ nm}^{-1}$ . The typical acquisition time was in the range of 0.01–0.1 s. The 2D SAXS patterns were normalized and regrouped to 1D scattering curves. The data were dark image subtracted, distortion corrected, flat field divided, point spread function corrected and normalized by time and intensity.

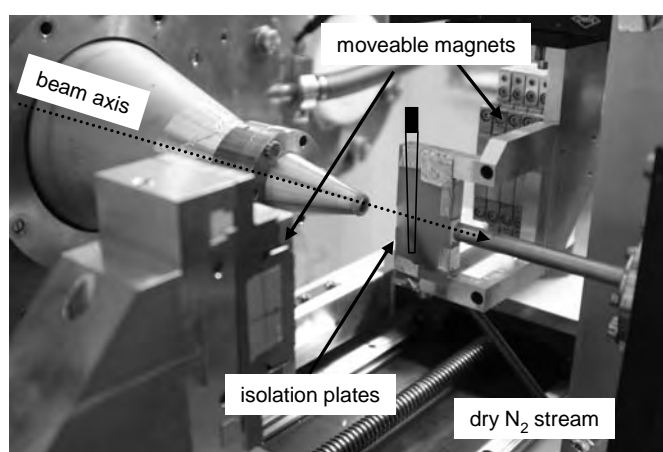


Figure 2.3.4. Experimental setup at ID02 High Brilliance Beamline ESRF. Permanent magnets were mounted on a remotely controlled motor. Temperature was adjusted with a stream of dry nitrogen.

The temperature of the samples was controlled by a dry nitrogen stream with a measured equilibration time for water of approximately 240 s. Permanent magnets were mounted on a remotely controlled motor on either side of the sample (Figure 2.3.4). Two different

distances for the magnets were employed in the investigations: a gap of 240 mm (no magnetic field) and a gap of 12.57 mm leading to a magnetic field of 1 T at the position of the sample. The applied field (**B**) was again perpendicular to the beam axis (**S**) as well as the long axis of the capillary.

### 2.3.2 Thermogravimetric analysis

The silicon-content of the glycol-modified precursors was determined by thermogravimetric analysis (TGA) on a Netzsch TG 209c with a heating rate of 5 °C/ min under a flow of synthetic air from 40 °C-800 °C. The silicon content was calculated from the residual weight at 800 °C, which was assumed to be pure SiO<sub>2</sub> (for reference see Table 2.1). The data were processed using Netzsch Proteus Analysis Software.

### 2.3.3 Nuclear magnetic resonance (NMR) spectroscopy

**Solution.** <sup>1</sup>H- and <sup>29</sup>Si-NMR spectra of the liquid precursors were recorded on a Bruker DRX Avance 300 DPX spectrometer equipped with a 5 mm broadband inverse probe head, at a <sup>1</sup>H frequency of 300.13 and a <sup>29</sup>Si frequency 59.62 MHz, respectively. For the ethylene glycol-modified silane additional <sup>1</sup>H/<sup>29</sup>Si-HMBC-NMR measurements were carried out.

**Solid State.** <sup>13</sup>C and <sup>29</sup>Si CP (cross polarizing)/MAS NMR spectra were measured at a Bruker Avance 300 spectrometer, equipped with a 4 mm broadband MAS probe head and an operating frequency of 75.39 MHz (<sup>13</sup>C) and 59.57 MHz (<sup>29</sup>Si). The spectra were measured on dried samples derived from EGMS as well as from bPhGMS in order to obtain information on the presence of residual surfactant in the porous structure, the crosslinking of the silica network and the condition of the organic moieties covalently linked to the silica network via Si-C bonds. For amorphous silica three overlapping broad peaks are expected in the <sup>29</sup>Si CP/MAS NMR spectrum with chemical shifts  $\delta$  of -91, -101, -109 ppm. These correspond to Q<sup>n</sup> (Si-(OSi)<sub>n</sub>(OR)<sub>4-n</sub>, n=2,3,4) species in the material. In case of the phenylene-bridged precursor the organosiloxane units T<sup>m</sup> (R'-Si-(OSi)<sub>m</sub>(OR)<sub>3-m</sub>, m=1,2,3) result in three overlapping broad peaks in the spectrum with the exchange of one Si-O bond for a Si-C bond (Q → T units) causing a shift of approximately 45 ppm to lower fields.

### 2.3.4 Polarized optical microscopy

Polarized optical microscopy (POM) was used to examine different surfactant/water systems with regard to their lyotropic liquid crystalline phase behaviour. Media with anisotropic long-range order (this excludes cubic symmetry) such as LLCs exhibit birefringence. This leads to characteristic highlighted textures with crossed polarizers.



Investigations were performed on a Zeiss Axiolab, equipped with polarization filters, a digital camera and an additional heating and cooling stage.

### 2.3.5 Nitrogen sorption

Nitrogen adsorption and desorption measurements were performed to provide information on the surface area, pore volume as well as pore size distribution in the micro-, meso- and lower macropore size regime (0.5-100 nm) [143]. The measurements on samples investigated in Chapter 3.6.2 were performed on an ASAP 2010 (Micromeritics) instrument. The samples were outgassed for 6 h in the degas unit of the desorption apparatus at 473 K under vacuum prior to analysis. All other N<sub>2</sub>-sorption measurements were performed at 77.4 K on a Nova 400e and an Autosorb-1 (Quantachrome). The samples were degassed under vacuum at 100 °C for at least 3 hours prior to analysis. The surface area was calculated by the 5 point method according to Brunauer, Emmett and Teller (BET); the pore size distribution according to Barrett, Joyner, and Halenda (BJH) from the adsorption branch of the isotherms. The pore wall thickness for 2D hexagonal mesophases was calculated by  $2d_{10}^{SAXS} / \sqrt{3} - D^{BJH}$ , where  $D^{BJH}$  is the BJH pore diameter.

### 2.3.6 Scanning- and transmission electron microscopy

Electron microscopy was carried out in order to obtain information on the macro- and mesoporous structure of the inorganic and hybrid networks. The macromorphology was investigated predominantly with scanning electron microscopy (SEM). Therefore pieces of monolithic material were thinly coated with gold. Measurements were performed on a Philips XL 30. Transmission electron microscopy (TEM) was performed on a Tecnai F20 S-TWIN operated at 200 kV (USTEM, TU Vienna). Detailed investigations on selected samples were carried out within cooperation with the Electron Microscopy Group of Materials Sciences at the University of Ulm. These measurements were obtained on a Philips CM20 equipped with a LaB<sub>6</sub>-cathode and operated at 200 kV in bright field mode. Two sample preparation techniques for the TEM specimens were applied. The standard procedure is to grind the monolithic material carefully, disperse the resulting powder in ethanol and deposit it on carbon-coated copper grids. In a second procedure the material is embedded in epoxy resin interdispersed with TiN. Subsequently, the sample is face-ground mechanically and further thinned in the ion-mill. This method offers the possibility to study the mesopore structure with respect to the macromorphology.

## 2.4 Mechanical testing

### 2.4.1 Instrumented indentation testing

Instrumented indentation testing (IIT) uses a high-resolution actuator to force an indenter into a test surface, and a high-resolution sensor to continuously measure the resulting penetration. The most commonly measured parameters by IIT are hardness ( $H$ ) and elastic modulus ( $E$ ).

During loading, both plastic and elastic deformations contribute to the formation of a hardness impression conforming with the shape of the indenter to some contact depth ( $h_c$ ). As the indenter is withdrawn, only the elastic portion of the displacement is recovered. From the recovery, information on the elastic properties of the material is obtained.

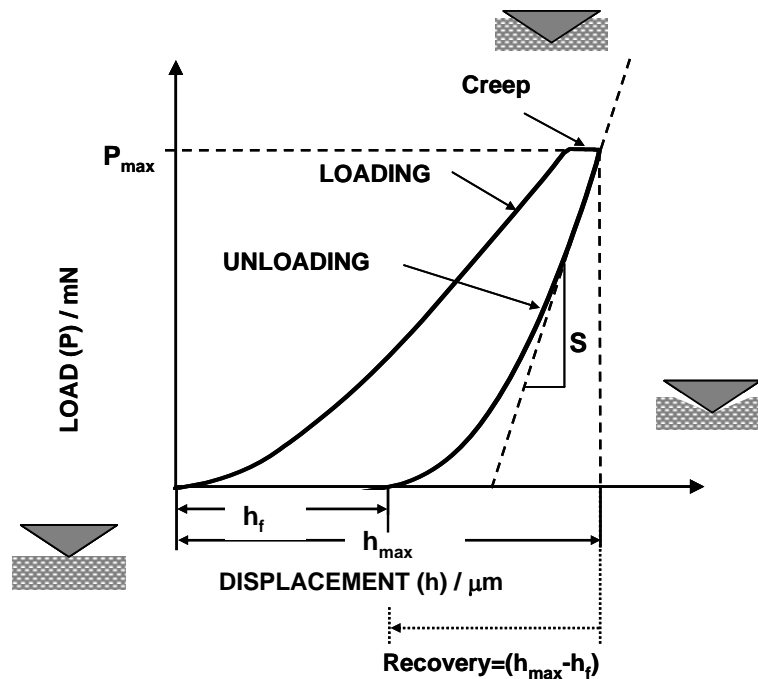


Figure 2.4.1. Load versus indenter displacement (modified from [144]).

Figure 2.4.1 shows the sketch of a load versus indenter displacement for an indentation experiment;  $P_{\max}$  is the peak indentation load;  $h_f$  the final depth of the contact impression after unloading of the indenter;  $h_{\max}$  is the indenter displacement at the peak load;  $S$  is the unloading stiffness (modified from [144]).

The hardness ( $H$ ) of the surface is determined using the equation  $H = \frac{P}{A}$ ; where  $P$  is the applied load and  $A$  is the projected contact area at that load. The elastic modulus ( $E$ ) is determined from the reduced modulus ( $E_r$ ), given by:

$$S = \frac{dP}{dh} = \frac{2E_r \sqrt{A}}{\sqrt{\pi}}; E_r = \frac{\sqrt{\pi} \cdot S}{2\beta \cdot \sqrt{A}} \text{ and } \frac{1}{E_r} = \frac{(1-\nu^2)}{E} + \frac{(1-\nu_i^2)}{E_i} \quad \text{Eq. 2.14}$$

$\beta$  is a constant that depends on the geometry of the indenter,  $\nu$  is the Poisson's ratio for the test material and  $E_i$  and  $\nu_i$  are the elastic modulus and the Poisson's ratio, respectively, of the indenter (diamond indenter,  $E_i=1141$  GPa,  $\nu_i=0.07$ ). Eq. 2.14 is founded in elastic contact theory. For a triangular cross section of the indenter like the Berkovich that was used for the experiments,  $\beta=1.034$ .

The recovery was calculated, by  $R = \frac{h_{\max} - h_f}{h_{\max} / 100}$  and is given therefore in percent of the maximum displacement.

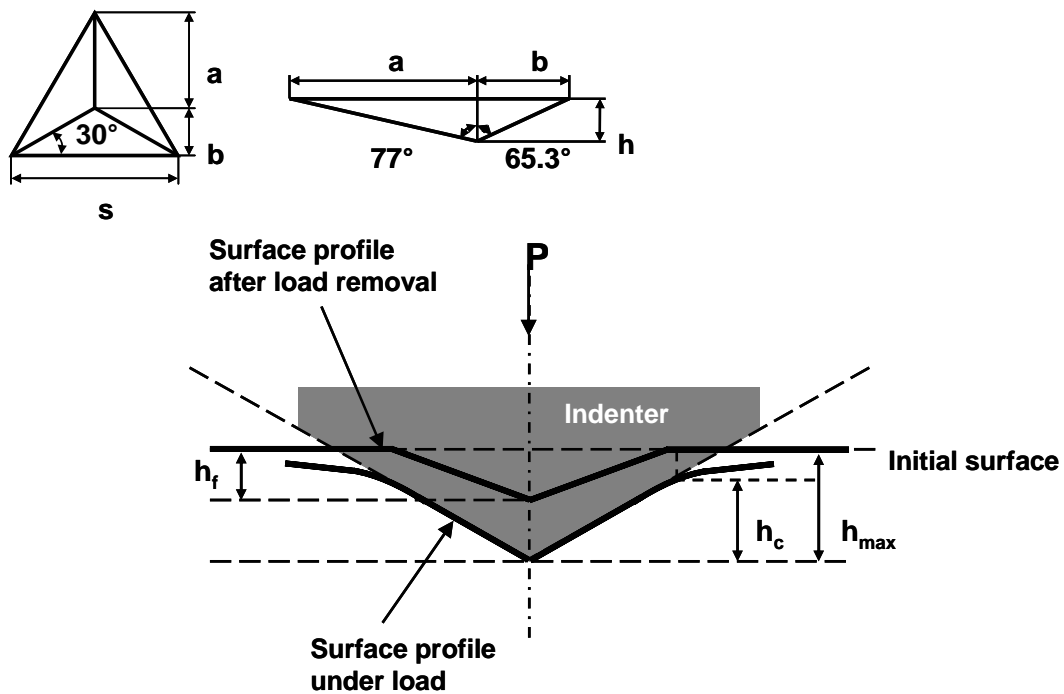


Figure 2.4.2 Schematic map of the indentation experiment [144].

The instrumented indentation measurements were performed on a Nanoindenter XP (Nano Instruments, Oak Ridge, USA). The temperature was kept at  $23 \pm 0.5$  °C. A Berkovich indenter as depicted in Figure 2.4.2 was used for all measurements. Maximum load was reached in 20 s, followed by holding of the maximum load for 30 s. A fixed maximum penetration depth of 12  $\mu\text{m}$  was employed in all measurements to guarantee that the indenter catches a significant part of the porous network and to gain information from a comparable volume. For the material a Poisson's ratio  $\nu$  of 0.2 was assumed. Hardness and

modulus were determined following Eq. 2.14. Every result represents the average value of 4 to 12 single measurements.

### 2.4.2 Compression tests

Compression tests were performed on a Zwick Z050. The base areas of cylindrically shaped, monolithic samples were first ground parallel and then mounted between two steel blocks. Two different experimental setups were employed which are depicted in Figure 2.4.3. The samples were loaded in compression and stress and strain were recorded. Typically five tests for each material and each setup were evaluated.

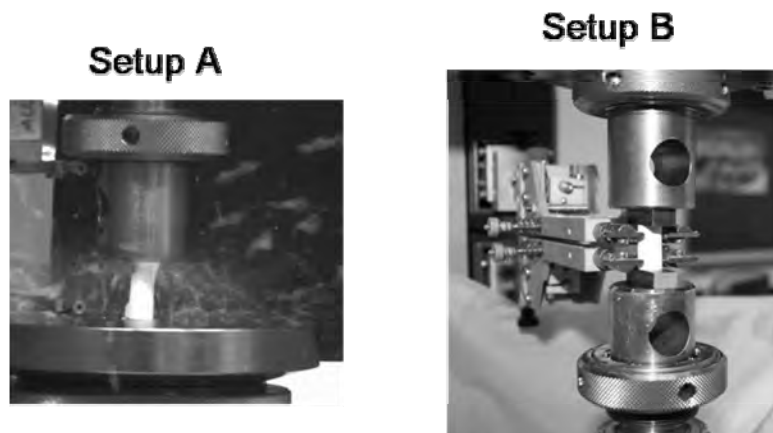


Figure 2.4.3 Two different setups on the Zwick Z050 were employed in the experiments.

To minimize errors due to friction and start-up behaviour, the samples in setup B were additionally mounted between pincers and preloaded with 3 N. The forceps were removed as soon as a compression of 0.3 mm was reached. This should allow a better determination of the modulus. Young's modulus was determined from the obtained (compressive) stress-strain curves following the relation:

$$E = \frac{\Delta F}{\Delta L} \cdot \frac{L}{A} \quad \text{Eq. 2.15}$$

Here  $\Delta F/\Delta L$  is the slope derived from the compressive stress-compressive strain curve,  $L$  is the length of the sample body and  $A$  is the base area.

## 3 Results and Discussion

### 3.1 Ordering effects in lyotropic liquid crystal systems

At ambient temperatures, the LLC domains are randomly distributed and the high viscoelasticity of the LLC aggregates usually counteracts further orientational ordering. Heating the mixture over its anisotropic-isotropic phase transition and gradually cooling allows the molecules to rearrange with a higher degree of orientational order. *In-situ* SAXS measurements on the rearrangement of different LC systems were carried out at the synchrotron research centers Elettra (Trieste, Italy, BL5.2L) and at ESRF (Grenoble, France, ID02). Therefore, aqueous surfactant solutions were homogenized for several hours to days at 50 to 60 °C and sealed in 2 mm quartz capillaries. An external weak magnetic field ( $\leq 1$  T) was applied in part of the measurements during heating-cooling cycles. The surfactant/water systems investigated are summarized in Table 3.1.

For most surfactants a domain orientation was observed prior to the first heating-cooling cycle due to sample preparation, namely, pressing the mixture into the 2 mm-diameter quartz capillaries with a syringe. In order to get rid of this shear-induced ordering the samples were heated up to 60 °C and kept at this temperature for at least 10 min to equilibrate. Isotropy was checked in the scattering pattern. To allow reorientation of domains after being heated over their order/disorder transition temperature the samples were cooled down slowly at a rate of 1 K min<sup>-1</sup>. SAXS patterns were recovered *in-situ* at several temperatures. For the analysed surfactants no measurable influence of a weak magnetic field could be observed during the involved exposure times.

The investigated surfactant/water-systems in the given compositions (Table 3.1) exhibit lamellar morphology with the exception of CTAB that shows a hexagonal structure in accordance with literature [8] with a  $d_{10}$ -spacing of 6.74 – 6.76 nm. For mixtures of 60%(w/w) sorbitan monopalmitate (Span 40) in water, the scattering pattern exhibits four reflections which can be indexed according to a lamellar structure with  $q_{100}=0.98$  nm<sup>-1</sup> corresponding to a repeating unit distance of 6.4 nm. One additional peak is located at  $q=1.3$  nm<sup>-1</sup> which could not be assigned to the lamellar structure. During cooling the LLC phase down from 333 K to room temperature a hexagonal structure with  $d_{10}=4.8$  nm ( $q=1.45$  nm<sup>-1</sup>) was observed in the temperature regime between 333 K > T > 313 K (see Figure 3.1.1 (c)). Below 313 K the system exhibits a pure lamellar structure with a distance of 6.4 nm between the lamellae.

Table 3.1 Structures of investigated LC systems and the effects due to heating above the anisotropic-isotropic transition followed by slow cooling (1 K/min).

Surfactant	Molecular formula	Conc. % (w/w)	Structure	Change in $d$ -spacing after heating	Alignment (through shear or/and border effects)
Triton X-45	$C_8H_{17}C_6H_4EO_5$	20	lam.	no	yes
Triton X-45	$C_8H_{17}C_6H_4EO_5$	50	lam.	yes	yes
Triton X-45	$C_8H_{17}C_6H_4EO_5$	60	lam.	yes	yes
Span 40	$C_{22}H_{42}O_6$	60	lam./hex.	-	-
CTAB	$C_{16}H_{33}N(CH_3)_3Br$	30	hex.	no	yes

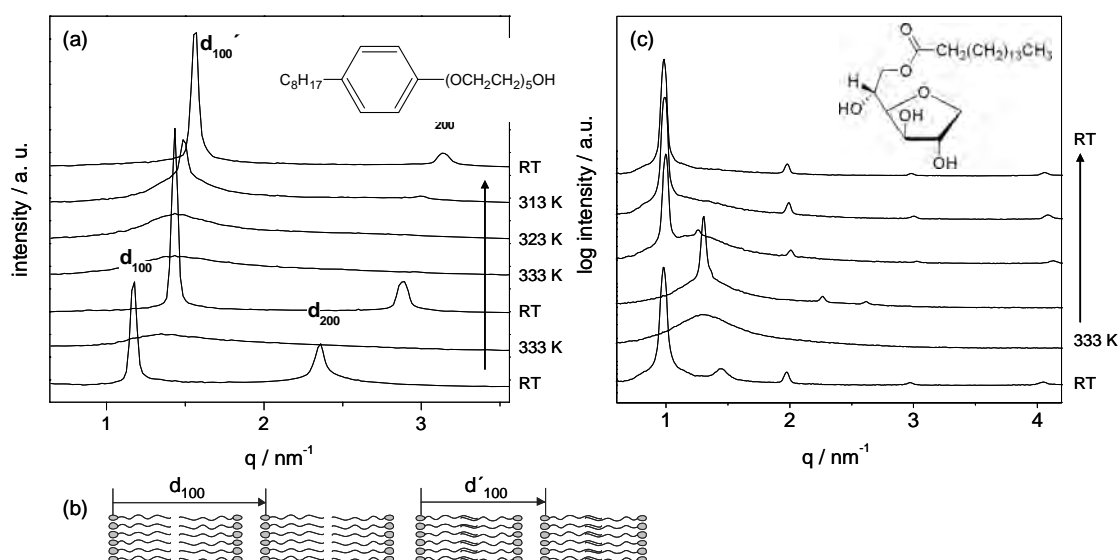


Figure 3.1.1. (a) Change in  $d$ -spacing after heating and cooling in the LLC-system Triton X-45/H<sub>2</sub>O. (b) Model for the decrease in repeating unit distance in case of Triton X-45: the long hydrophobic molecule tails stack with increasing degree of overlap. (c) Structure change in the LLC Span 40/H<sub>2</sub>O during heating and cooling.

### 3.1.1 Lamellar LC structure of Triton X-45

The system Triton X-45 in water was studied in three different concentrations (20%(w/w), 50%(w/w) and 60%(w/w) surfactant), all of them yielding transparent homogeneous viscous liquids. For this surfactant in water, a change of  $d$ -spacing was observed following subsequent heating and cooling cycles as illustrated in Figure 3.1.1 (a) and (b). In the scattering pattern the peak positions can be indexed according to a lamellar LC phase, with the  $d_{100}$  and  $d_{200}$  reflections clearly visible. The curves are ordered from bottom to top, with

the lowest curve recorded at room temperature before heating and giving an initial  $d$ -spacing of 5.38 nm. Upon heating the sample up to 333 K, the long-range order vanished and the diffraction peaks disappeared (second curve from bottom), indicating that the order–disorder transition was passed at this temperature.

Upon slow cooling of the system, the lamellar phase was restored, but with a smaller  $d$ -spacing of 4.41 nm (decrease by 18%). A second heating-cooling cycle resulted in a further decrease of the  $d$ -spacing by another 7% to  $d=4.01$  nm (four top curves in Figure 3.1.1 (a)). In the case of 60%(w/w) Triton X-45 in water the observed decrease in  $d$ -spacing was around 13.5% from 5.03 nm to 4.35 nm. Since no additional peaks evolved, a formation of ripple phases can be excluded. A possible explanation for the observed effect is that upon heating and cooling for several times, the surfactant molecules get the opportunity to stack with their tails closer together, such that they start to partly overlap (see Figure 3.1.1 (b)). The length of a single Triton X-45 molecule (see Figure 3.1.1 (a)) is about 3.23 nm. If the molecules were to stack in a lamellar morphology with no overlap and no bending of the molecule (which is highly unlikely in practice), the  $d$ -spacing would be 6.46 nm, thus representing the theoretical maximum value. The re-ordering mechanism appears to be highly dependent on the processing history as well as on the surfactant concentration. Whereas heating and slow cooling of 50%(w/w) and 60%(w/w) Triton X-45 in water showed a considerable decrease of the  $d$ -spacing, no decrease of the  $d$ -spacing upon heating and cooling was observed in the samples with 20% Triton X-45 in water. Here, the  $d$ -spacing was constantly as small as  $d=4.55$  nm from the beginning. Faster cooling of externally heated samples for comparison showed no decrease of the  $d$ -spacing ( $d$  is constant with a value of 5.2 nm).

Moreover, the Triton X-45/water system exhibited strong preferential alignment of the LC-lamellae at the sample/glass-capillary interface. Scanning of the 2 mm capillary through a 0.5 mm beam in steps of 0.1 mm allowed a clear distinction between the regions close to the capillary wall and the bulk material. In the bulk, no preferential orientation of the liquid crystalline domains was observed (thus excluding also effects of the weak magnetic field applied to the sample), whereas the liquid crystalline domains tended to align parallel to the walls of the glass capillary. The scattering patterns of Triton X-45 in water are shown in Figure 3.1.2 (a). In the bulk the diffraction rings exhibit constant intensity (a-II), whereas close to the sample/glass interface strong intensive spots were observed at the equator of the SAXS pattern, indicating a preferential orientation of the lamellae parallel to the walls (a-III). Figure 3.1.2 (b) shows the intensity of the 100-reflection ring integrated over the scattering angle  $2\theta$  and plotted versus the azimuth. SAXS curves from either side of the capillary (I and III) exhibit a strong peak at the equator, contrary to the scattering curves from the bulk (II) which show constant intensity (random orientation).

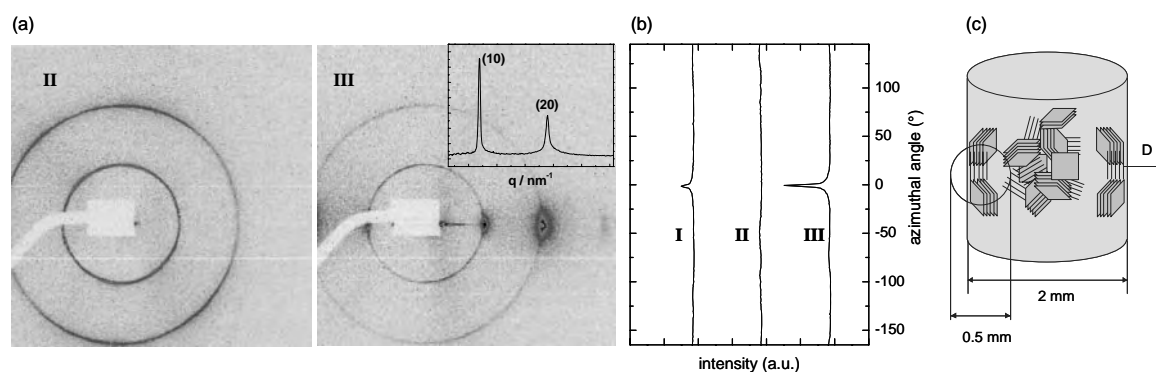


Figure 3.1.2. 50%(w/w) of Triton X-45 in water after heating up to 60 °C and subsequently cooling down to room temperature without magnets. The lamellar crystalline domains close to the sample/glass interface tend to orient parallel to the capillary wall. (a-II) 2D-scattering pattern from the middle of the capillary and (a-III) close to the glass wall;

(b) Intensity of the 100-reflection integrated over  $2\theta$  and displayed versus the azimuth: I and III show signals close to the capillary wall (left and right, respectively), II from the centre. (c) Schematic representation of the preferential alignment at the interface, **D** is the director of the lamellar domains. The size of the beam was 0.5 mm and is shown schematically.

In Figure 3.1.2 (c) a model of the arrangement is displayed. The lamellar liquid crystalline domains orient parallel to the capillary walls, since a parallel alignment is the energetically most favourable arrangement. Close to the interface the domain director **D** is perpendicular to the glass wall. Similar observations were reported by Jager-Lezer et al. [145] and for hexagonal structures by Raimondi et al. [22].

Due to the high viscosity of the system at room temperature, the system cannot adopt this arrangement fully without heating (thus lowering the viscosity) and cooling down slowly (providing time for re-ordering). The reason for the strong alignment of liquid crystalline Triton X-45 in water may be the formation of particularly large lamellar domains, and therefore considerable lowering of energy for parallel alignment with the glass surface. The presence of large LC domains would also explain the shear sensitivity of Triton X-45 in water that often led to a weak preferential alignment of the system due to the processing of the liquid when filling the capillary, often in different directions than the eventual alignment at the interface. The shear-induced orientation, however, vanished completely after heating, leading way to the sharp, parallel orientation along the walls. This interface induced alignment does not seem to be as strongly dependent on the heating and cooling history of the sample as change in the  $d$ -spacing, and was observed also in externally treated samples subjected to faster cooling.



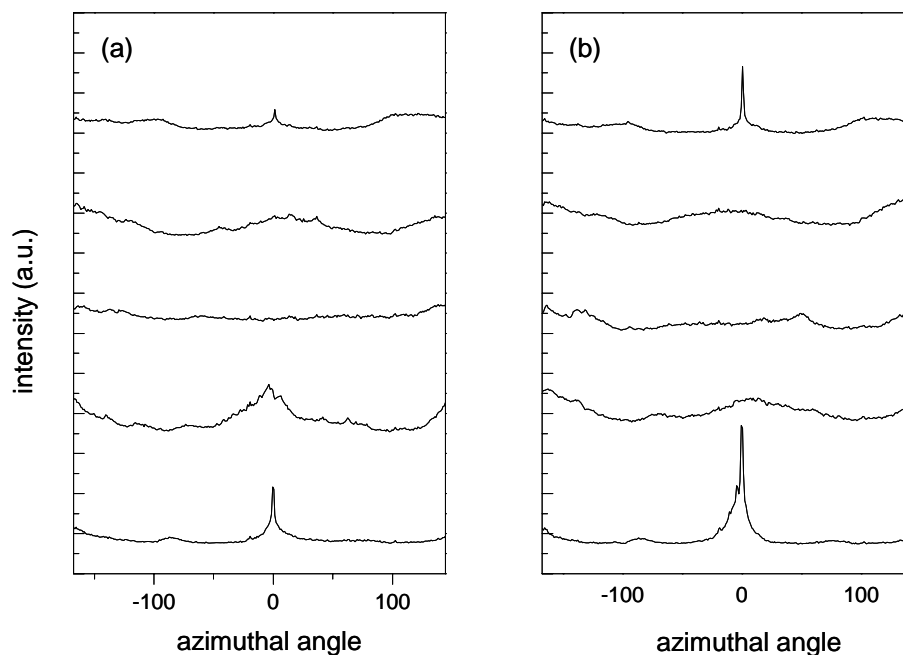


Figure 3.1.3. 20%(w/w) Triton X-45: Scan through the capillary before heating (a) and after heating to 60 °C (b). The domains are already aligned at the beginning of the experiment. After heat-treatment the orientation at the capillary walls has increased.

The preferential alignment became much more pronounced after heating and cooling, most likely due to reordering processes in the sample enhancing the alignment. This is shown in Figure 3.1.3 for 20%(w/w) Triton X-45. At this concentration alignment of the lamellar liquid crystal domains parallel to the capillary walls was observed right from the beginning, presumably due to lower viscosity of the mixture at lower concentration. The lower viscosity of 20%(w/w) Triton X-45 in water as compared to higher concentrations may also account for easier re-arrangement of the molecules with respect to each other already at room temperature and therefore a closer stacking reflected by the small  $d$ -spacing observed in these samples right from the start.

### 3.1.2 Hexagonal LC structure of CTAB

CTAB is a cationic surfactant commonly used in the fabrication of ordered mesoporous silica materials. Detailed measurements on a 30%(w/w) solution of CTAB in water were performed at the ID02 High Brilliance Beamline ESRF, Grenoble, France.

As already described at the beginning of this chapter the given composition results in a LC phase of hexagonally ordered elongated cylindrical micelles, where the molecular director (**M**) points along the long axis of the molecule and the domain director (**D**) points along the long axis of the cylindrical micelles ( $\mathbf{M} \perp \mathbf{D}$ ).

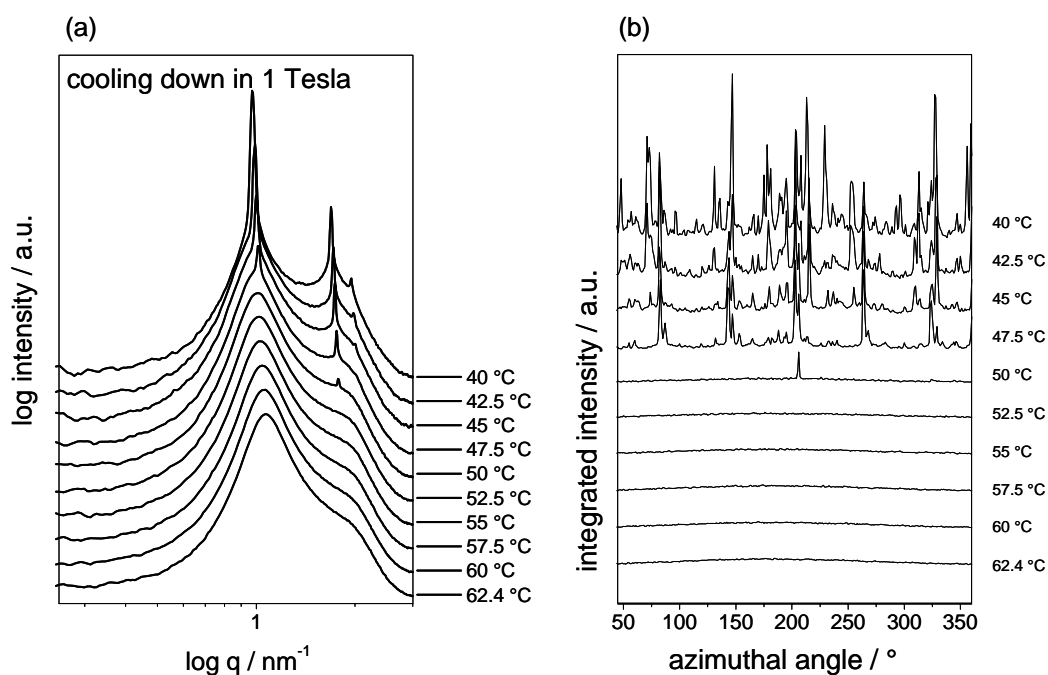


Figure 3.1.4. (a) *In-situ* synchrotron SAXS pattern during the first cooling cycle inside a magnetic field of 1 T. (b) Radial integration of the  $(100)_{\text{hex}}$  diffraction peak of (a) plotted as integrated scattering intensity over the radial position.

Three distinct peaks could be observed in the scattering pattern corresponding to a periodic distance of  $d_{100}=6.73$  nm. No scattering from crystalline CTAB ( $d_{100}=2.6$  nm) was observed. As shown in Figure 3.1.5 for the unheated sample (I), alignment of the LC domains was observed in the radial integration of the  $(100)_{\text{hex}}$  diffraction peak. The one fully visible peak is situated at approximately  $180^\circ$  which correlates with an orientation of the domain vector parallel to the capillary walls (and perpendicular to the beam). By calculating the coherence length according to Eq. 2.13 a rough estimate of the domain size of 220 nm is obtained. The sample was first heated to  $62^\circ\text{C}$  and kept there for 20 min and then slowly cooled down to  $40^\circ\text{C}$  inside a magnetic field of 1 Tesla. The isotropic-anisotropic phase transition was found to be at  $50^\circ\text{C}$  as can be seen in Figure 3.1.4 (a). Therefore the sample was heated and cooled several times in steps of  $2.5^\circ\text{C}/5$  min between  $40$  and  $55^\circ\text{C}$ . In Figure 3.1.4 (b) the radial integration of the  $(100)_{\text{hex}}$  reflection is depicted for the first cooling cycle inside the magnetic field. At  $50^\circ\text{C}$  an oriented structure starts to evolve at a position of  $205^\circ$ , which means the domains have been tilted by  $25^\circ$  by the treatment. At  $47.5^\circ\text{C}$  six intensity peaks are obtained from the radial integration with a distance of  $60^\circ$  each ( $(23^\circ)-83^\circ-143^\circ-203^\circ-263^\circ-323^\circ$ ). This corresponds to the signal from hexagonally ordered cylinders oriented with their long axis parallel to the beam. Note, however, that this arrangement was only intermediate and changed upon further cooling.

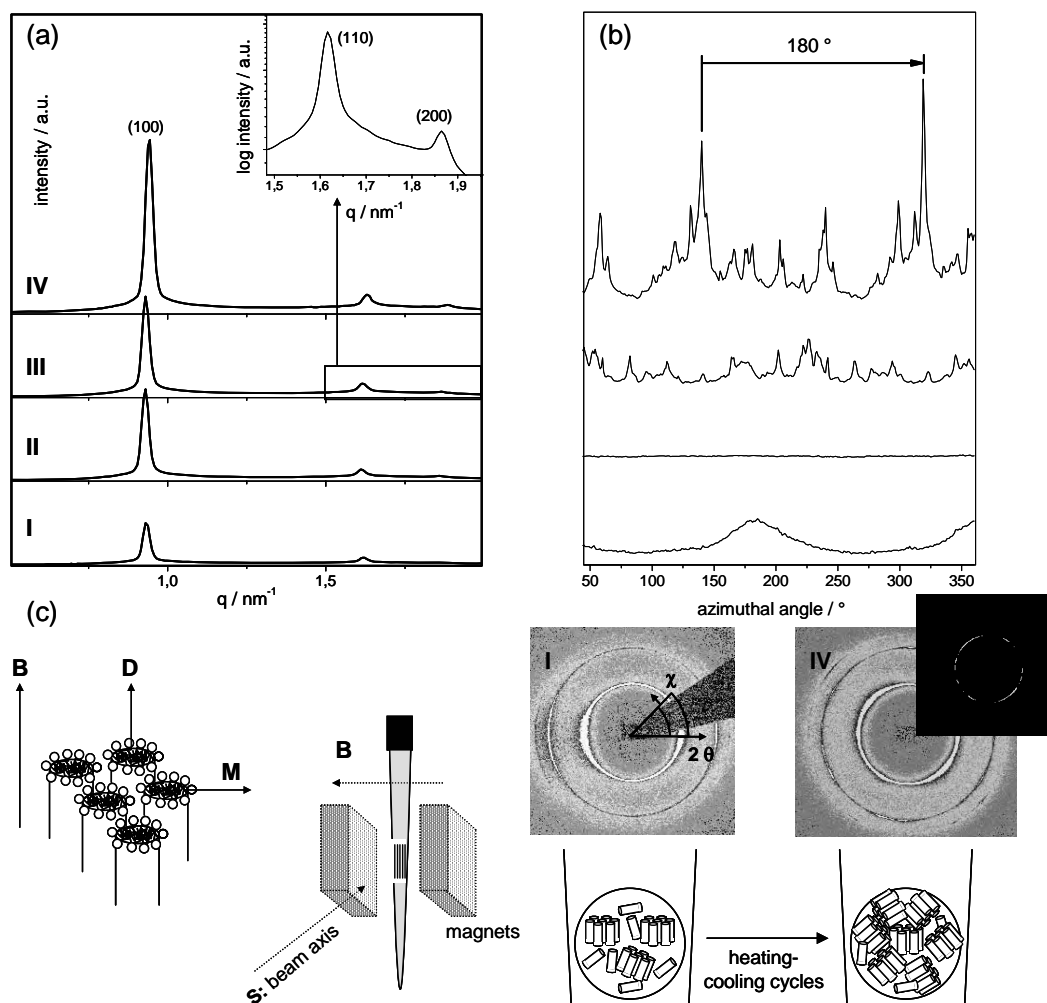


Figure 3.1.5. (a+b) *In-situ* scattering curves and the corresponding results from the radial integration over the  $(100)_{\text{hex}}$  reflection. The curves were obtained after heating and cooling a hexagonal liquid crystal phase formed by 30%(w/w) CTAB in water. Measurements were performed in a magnetic field of 1 Tesla ( $\mathbf{B} \perp \mathbf{S} \perp$  long axis of the capillary) (III) and with removed magnets (IV). An orientation of the domains with their domain vector ( $\mathbf{D}$ ) pointing along the long axis of the capillary was found due to sample preparation (I). After (external) heating over the isotropic-anisotropic transition temperature (fast cooling) all domains are randomly distributed (II). (c) Schematic of the setup and the alignment of the LC domains.

Moreover, magnetic ordering effects would lead to an orientation perpendicular and not parallel to the beam. Since other measurement series on the same mixture showed different orientation, it is concluded that the oriented hexagonal scattering pattern is due to the presence of large domains with the above described orientation in the beam. The individual  $\text{CTA}^+$  molecules have negative diamagnetic susceptibility ( $\Delta\chi_m < 0$ ) [19] the condition  $\mathbf{M} \perp \mathbf{D}$  for the hexagonal structure gives an overall positive diamagnetic domain susceptibility ( $\Delta\chi^d > 0$ ). Therefore, the hexagonal domains should align with their domain director on average parallel to the magnetic field.

In the experimental setup the magnetic field was perpendicular to the beam axis (**S**) and the long axis of the capillary (see schematics in Figure 3.1.5 (c)). As a result the influence of the applied magnetic field should lead to orientation of the hexagonal domains with their domain directors on average perpendicular to the walls of the capillary. In Figure 3.1.5 the results after several heating-cooling cycles in the magnetic field (**III**) and with removed magnets (**IV**) is summarized. A direct influence of the magnetic field could not be proven. The intensity peaks found for the integrated intensity of the  $(100)_{\text{hex}}$  reflection plotted versus the azimuth suggest a reorientation of the domains away from alignment along the capillary walls. The complex reflection pattern suggests that the domains contributing are neither fully oriented nor fully randomly distributed. For the domain size a lower limit of  $\sim 220$  nm can be estimated from the FWHM of the  $(100)_{\text{hex}}$  reflection. However, the beam size of approximately 0.3 mm and the observed diffraction patterns suggests that domains are much larger. For the  $(100)_{\text{hex}}$  reflection an increase of the amplitude after each cycle was observed. This can be explained by an increase of the domain size contributing to the scattering. Neither  $d$ -spacing or FWHM was changed significantly by heating and cooling the mixture, probably due to the fact, that the peak width is covered by the resolution function.

### 3.1.3 Alignment of silica-surfactant mesophases

Once hydrolysis/condensation reactions in the sol-gel synthesis have started, it is very difficult to influence, respectively, align the meso-phase. Tolbert et al. have reported a system that overcomes this problem by hindering silica condensation through highly alkaline conditions [19, 20]. The system consists of an aqueous-rich and a viscous silicate-surfactant-rich phase at room temperature. By slowly cooling the alkaline lyotropic silicate-surfactant liquid crystal through its isotropic-anisotropic phase transition in a 11.7 T magnetic field they succeeded to macroscopically orient the liquid crystals.

A highly alkaline silica/surfactant liquid crystal was prepared by adding 10%(w/w) aqueous solution of the cationic surfactant cetyltrimethylammonium bromide to a  $Q^8M^8$ -cube precursor solution as described in Chapter 2.1.2. Polarized optical microscopy (POM) and SAXS were used to verify the lyotropic liquid crystalline character of the viscous phase. The measurements of the ungelled samples were performed in sealed quartz capillaries. Gelation was induced by leaving the samples in concentrated HCl-vapor up to 48 h. Dependent on composition lamellar, hexagonal or mixed structures were observed prior to gelation. Mostly hexagonal structure with repeating unit distance of 4.1 nm was found after exposure to HCl.

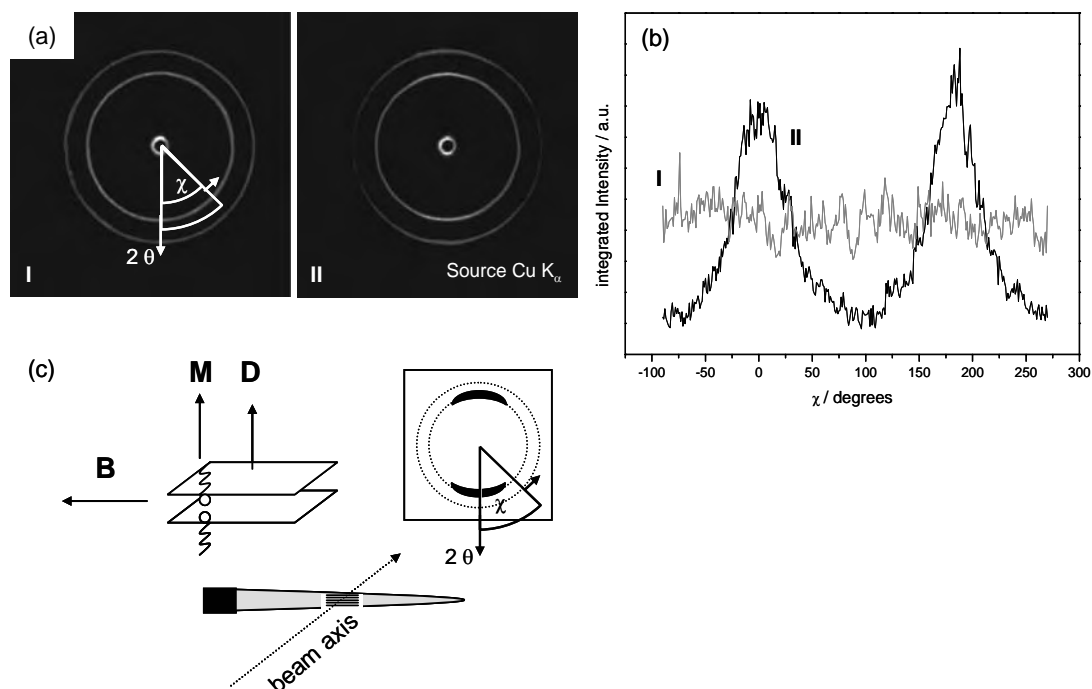


Figure 3.1.6. Highly alkaline silica/surfactant liquid crystal (TMOS/CTAB/TMAOH/H<sub>2</sub>O/CH<sub>3</sub>OH=1/0.31/1/130/14 in molar ratio) without orientation (I, reference) and oriented in a strong magnetic field (II).

To confirm possible alignment in a magnetic field experiments were performed by heating a solution of the molar overall ratio of TMOS:TMAOH:H<sub>2</sub>O:CH<sub>3</sub>OH:CTAB=1:1:130:13.9:0.3 up to 363 K followed by slow cooling (5 K/h) inside a 7 T magnetic field of a NMR. The high viscosity of the oriented silicate-surfactant liquid crystals at room temperature allows them to be removed from the magnetic field without loss of orientational order. SAXS-measurements of the magnetically aligned and the unaligned sample show indeed anisotropy in the scattering pattern (Figure 3.1.6(a)). In Figure 3.1.6 (b) the difference in the integrated radial intensity over the width of the scattering-signal of the primary peak ( $q=1.49 \text{ nm}^{-1}$ ) is plotted for the reference (I) and the magnetically aligned material (II). The reflection at  $q=1.97 \text{ nm}^{-1}$  belongs to a second lamellar structure with a smaller periodic distance of 3.2 nm. Both observed lamellar structures show the same anisotropy in the SAXS measurements. The system is strongly birefringent in POM. In Figure 3.1.6 (c) the reason for the alignment is drawn schematically. CTAB is known to have a negative magnetic susceptibility ( $\Delta\chi=\chi_{\parallel}-\chi_{\perp}<0$ ). Therefore the molecular director (M) and the domain director (D) are perpendicular to the magnetic field. This leads to vertical alignment of the lamellae.

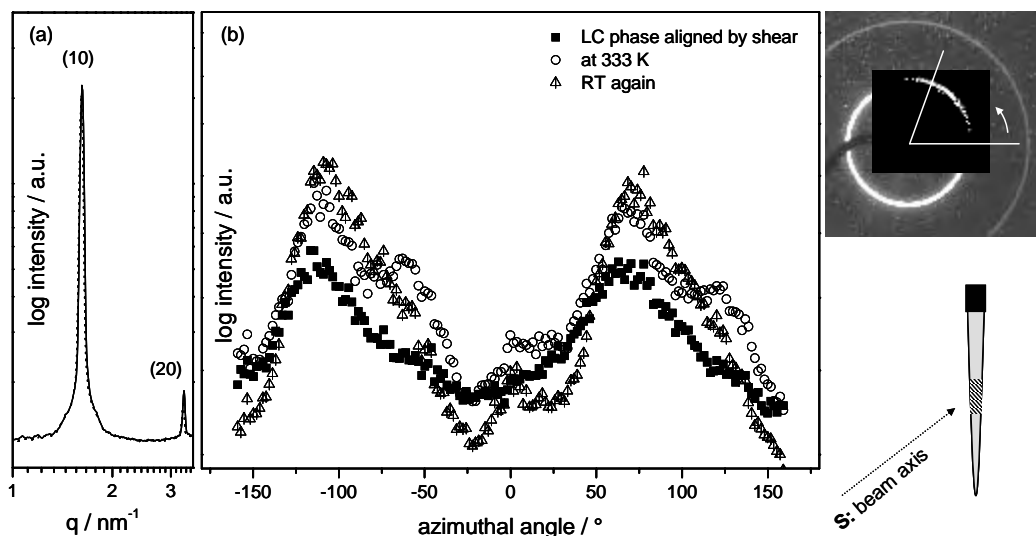


Figure 3.1.7. (a) SAXS curve of the viscous LC phase showing the lamellar structure. (b) Corresponding results from the radial integration over the (100) reflection. The lamellae can easily be oriented by shear. Heating to 333 K inside a quartz capillary leads to a small increase of ordering.

*In-situ* SAXS investigations on the rearrangement of the highly alkaline silica/surfactant liquid crystal phase were carried out at the synchrotron research center Elettra. Again, the samples were treated by heating and cooling inside and outside of a weak magnetic field. For the silica-surfactant-rich phase two distinct peaks were observed in the SAXS pattern (Figure 3.1.7 (a)) which can be indexed according to a lamellar structure with the  $d_{100}$  and  $d_{200}$  reflections clearly visible and a repeating unit distance of 3.9 nm. The viscous LLC phase can easily be aligned by shear. In Figure 3.1.7 (b) the intensity versus the azimuth illustrates the observed alignment after filling the capillary (diameter=1 mm). In contrast to the ordering effect observed for other LLC systems the lamellae are not oriented along the wall of the capillary. Only after heating and cooling a small increase of ordering can be seen at  $0^\circ$ . A possible explanation for the different orientation of the structure lies in the sample preparation. Due to the high viscosity of the system the lamellae are oriented while being pressed into the capillary through a syringe.

All the investigated systems proved to be highly sensitive to shear. Orientation due to domain diamagnetic susceptibility could only be verified for high magnetic fields such as provided by NMR and only with very slow cooling rates. A highly alkaline lamellar silicate-surfactant phase modified from [19] was aligned in a magnetic field of 7 T. For the surfactant Triton X-45 a decrease in periodic distance of the lamellae could be found after heating and cooling over the anisotropic-isotropic phase transition temperature at high surfactant concentrations. Furthermore, a strong alignment of the lamellae along the walls of the quartz capillaries was observed.

### 3.2 Investigation of novel “multifunctional” surfactants

In close cooperation with the Institute of Applied Synthetic Chemistry (IASC) two amphiphilic molecules were investigated with regard to their ability to form anisotropic LC phases. The molecules were designed with respect to a further possible alignment in magnetic fields and crosslinking of the organic phase.

#### 3.2.1 Aqueous solutions of a benzoic acid derivative

The introduction of polymerizable groups to surfactant molecules allows an additional cross-linking in the hydrophobic region of the network. The thus stabilized organic phase in the mesopores should enhance the mechanical properties of the resulting material.

A polyethylene glycol derivative (compound (1), Figure 3.2.1) was developed at the IASC [146] and received as yellowish oil.

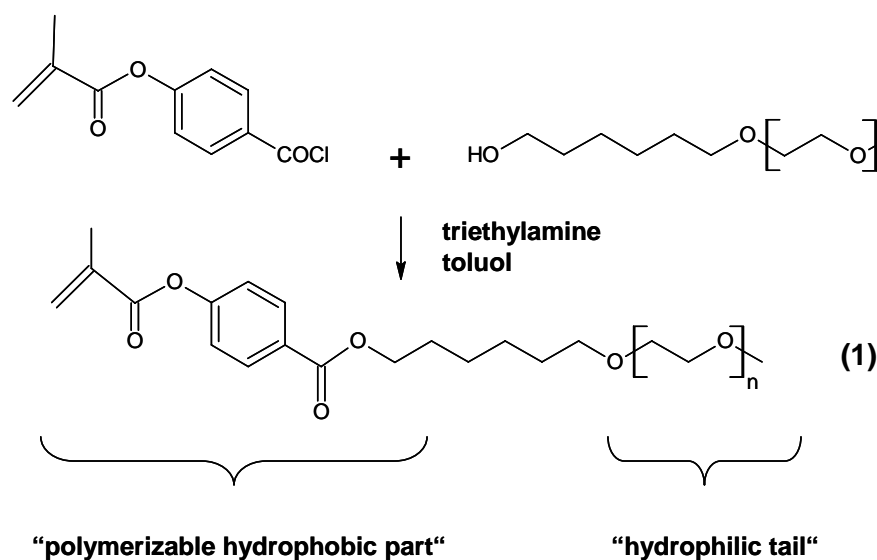


Figure 3.2.1. Synthesis path and molecular structure of the investigated benzoic acid derivative compound (1).

Mixtures of concentrations of 95%(w/w) to 25%(w/w) of compound (1) in water were produced by stirring in an ice bath. The resulting substances were filled in 2 mm-capillaries and further examined with SAXS at 21 °C. Down to surfactant concentrations of 40%(w/w), macroscopically homogeneous, transparent samples were obtained. At more dilute solutions ( $\leq 35\%$ (w/w)) the systems developed 2 phases on a macroscopic scale.

For the homogeneous mixtures a change from transparent to turbid (white) was observed at temperatures higher than 30 °C. This effect was also visible under the light microscope

### 3.2 INVESTIGATION OF NOVEL “MULTIFUNCTIONAL” SURFACTANTS

with crossed polarized filters for the 1 mm-diameter capillaries (change from dark to white). Since investigations on thin films did not show birefringence, the effect is most likely due to a phase separation starting with small droplets. Upon cooling below 30 °C the samples changed again to transparent. SAXS measurements did not show any liquid crystalline structure at 21 °C.

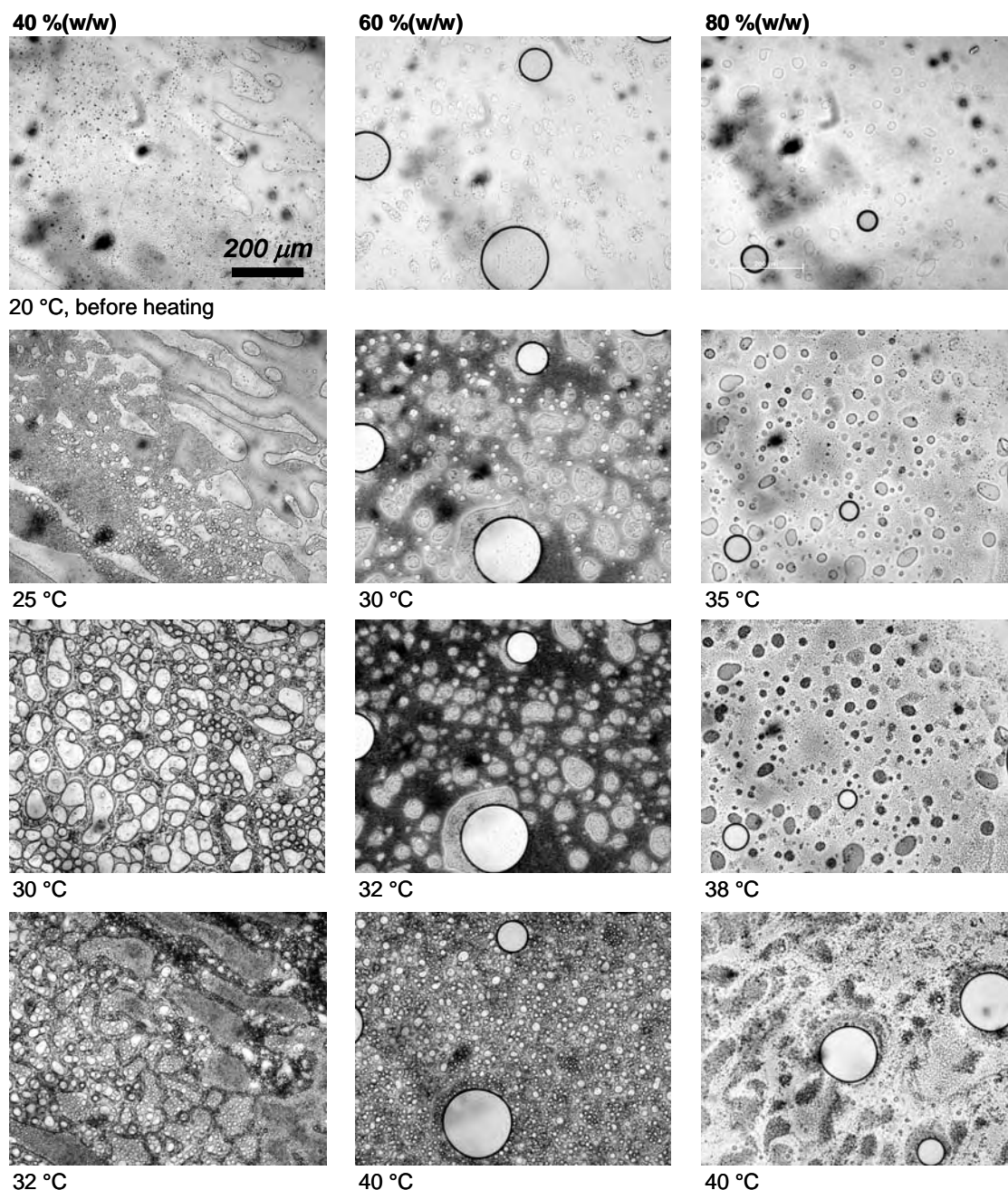


Figure 3.2.2. Microscopic phase separation during heating of 40, 60 and 80%(w/w) of  $C_{28}H_{44}O_{10}$  in water under the light microscope. No anisotropic liquid crystalline phase was observed at any temperature with crossed polarizing filters.



DSC-measurements for concentrations of 20, 40, 60 and 80%(w/w) did not show any phase transition. This result was confirmed by SAXS-measurements at the temperatures 40 °C and 60 °C, respectively. Microscopic images of the 20, 40, 60 and 80%(w/w) of the heated samples show that the mixtures undergo a phase separation into surfactant-rich and water-rich phases, in which both phases each consist of an isotropic liquid. Since no liquid crystalline region could be found by varying surfactant concentration and temperature, the molecule was not further investigated.

### 3.2.2 Aqueous solutions of a perylene derivative

The synthesis of an amphiphilic perylene derivative was performed mainly following the report of Arnaud et al. [147] and is described in detail elsewhere [146]. The molecule consists of a large aromatic core surrounded by four hydrophilic arms (see Figure 3.2.3). This design should enforce a one-dimensional supramolecular assembly in water through intermolecular  $\pi$ -stacking and/or hydrophobic interactions (as was reported by [147] for  $n=2$  and dilute concentration). The four hydrophilic arms hinder a possible aggregation of the assemblies and provide good water solubility. The perylene derivate with  $n=3$  (Figure 3.2.3, compound (2)) was received as orange viscous liquid.

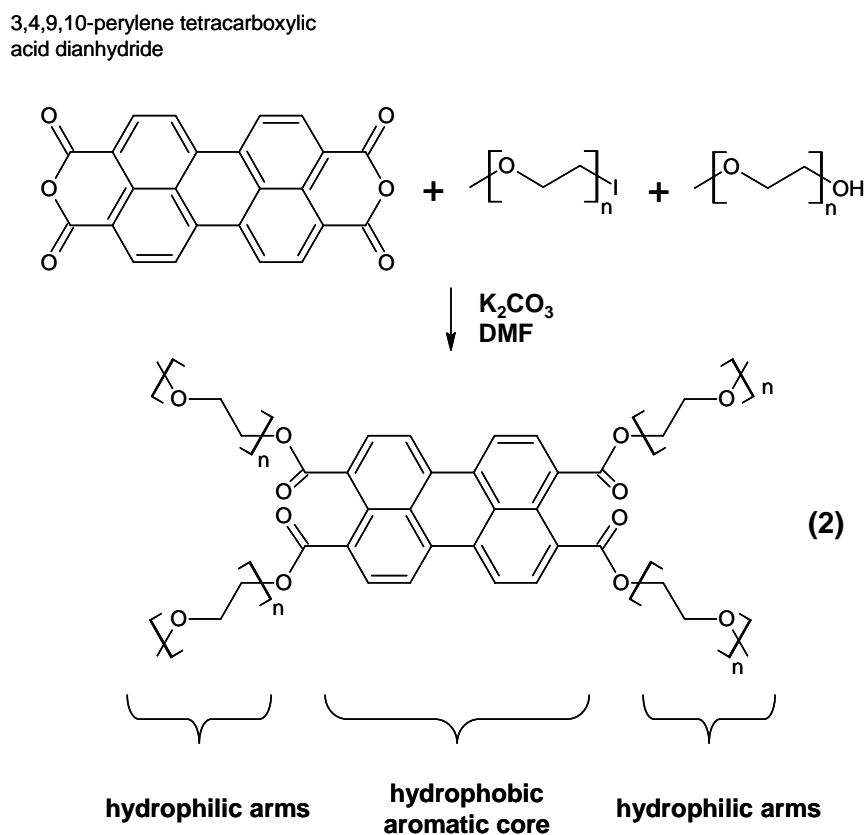


Figure 3.2.3. Synthesis path and molecular structure of the perylene derivate: compound (2) with  $n=3$ .

Concentrations of compound (2) of 10 up to 95%(w/w) in water were examined. The substance is highly soluble in water as well as in toluol and also butanol. POM investigations were performed by studying the phase behaviour depending on temperature and concentration, but did not show any anisotropic phases. SAXS measurements performed in a  $q$ -range of 1 to 8  $\text{nm}^{-1}$  revealed only a broad peak characteristic for short-range order in solutions. The observed distances are depending on surfactant concentration and correspond to mean distances of 3.2 nm for 40%(w/w) to 1.6 nm for 88%(w/w) of compound (2) in water.

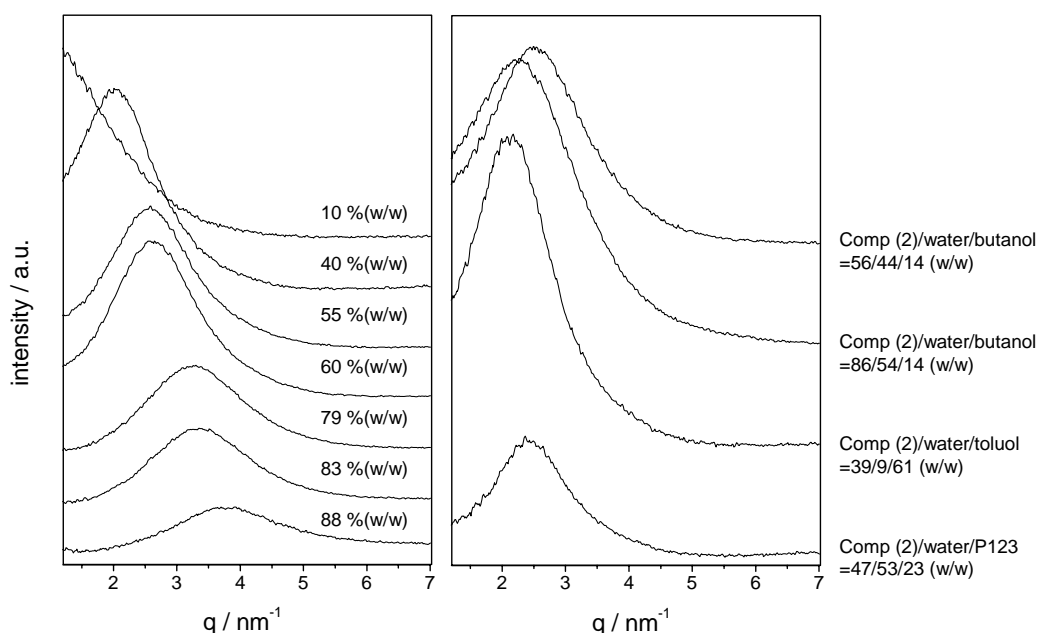


Figure 3.2.4. Short-range order of the amphiphilic perylene derivative in different concentrations.

Rheology experiments also could not confirm any stacking of the large hydrophobic aromatic core. Most likely, the four hydrophilic arms hinder the aggregation.

### 3.2.3 Aqueous solutions of an alkylpolyethylene oxide derivative

Non-ionic polyethylene oxide-based surfactants are commonly used in the templating of sol-gel derived mesoporous materials. By varying the length of the polyethylene glycol chain, properties such as pore diameter or lyotropic liquid crystal structure may be controlled to some extent. Investigations were carried out on the non-ionic surfactant Brij 97 (polyoxyethylene 10 oleyl ether) and a very similar newly designed molecule with up to three double bonds in the hydrophobic alkyl chain. Both molecules are depicted in Figure 3.2.5. The positioning of unsaturated fatty alcohols in the non-commercial molecule should allow oxidative as well as photochemical crosslinking in the hydrophobic region of the

surfactant micelles. The fabrication of the modified molecule is described in detail in [146]. Investigations with POM show at least two different liquid crystalline phases between the isotropic surfactant-rich and the water-rich phase. In a first experiment a drop of water and a drop of amphiphile were put on a slide side by side and allowed to mix. The result is shown in Figure 3.2.6. Hereby, the fan-like texture at higher water concentration suggests a hexagonal arrangement, whereas the Maltese crosses at high surfactant concentration indicate a lamellar ordering. This is in accordance with the phase diagram of Brij 97 as reported in [14] (see Figure 2.1.3).

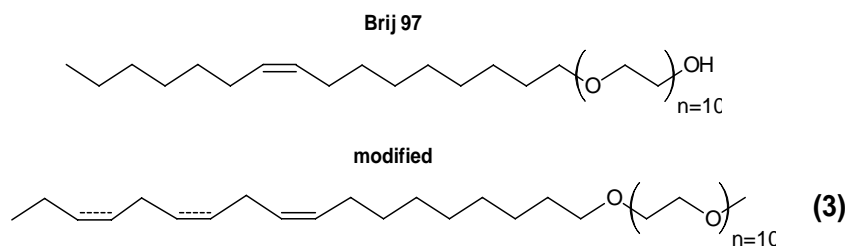


Figure 3.2.5. Molecular structure of polyoxyethylene 10 oleyl ether (Brij 97) and the polymerizable alkylpolyethylene glycol (compound (3)) with up to three double bonds in the hydrophobic alkyl chain.

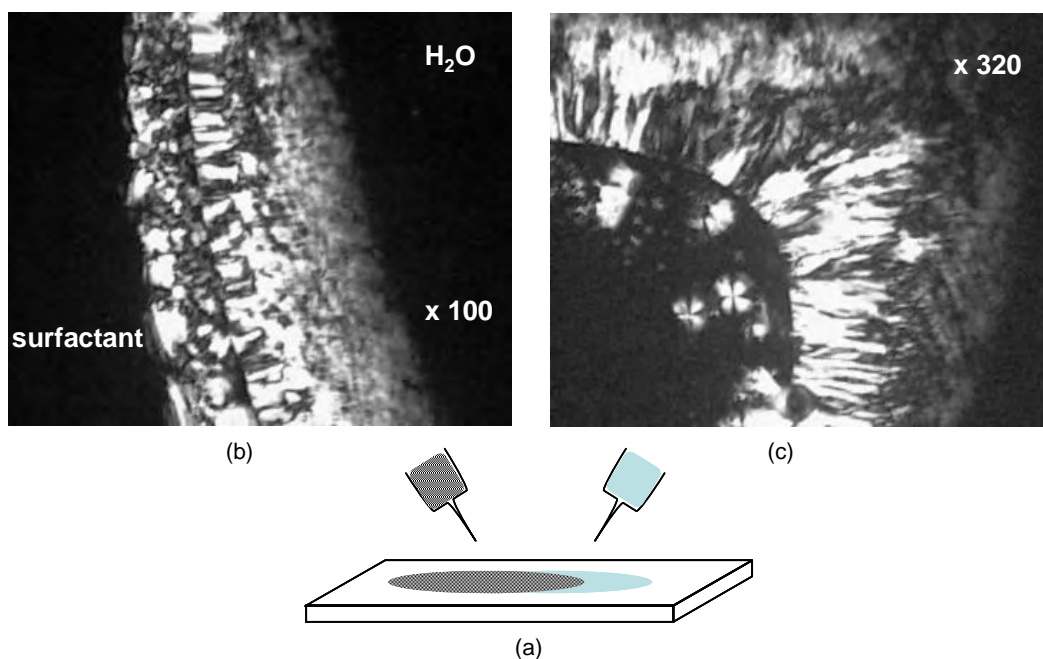


Figure 3.2.6. a) Schematic setup for a drop experiment. (b) and (c): Texture of the mixed region under crossed polars with fan-like structure characteristic for hexagonal arrangement and Maltese crosses at high surfactant concentration, characteristic for lamellar structure.

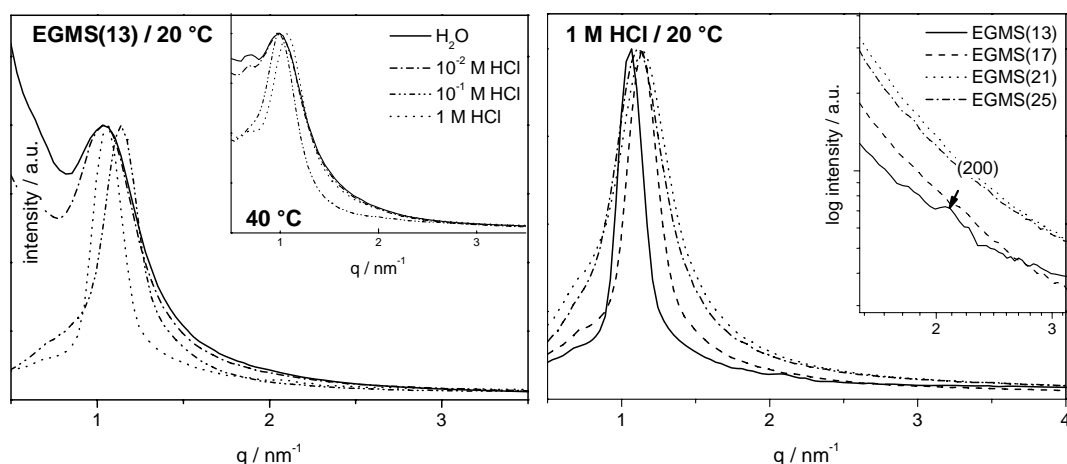


Figure 3.2.7. Small-angle X-ray scattering profiles for vacuum-dried gels prepared from EGMS, for starting composition of EGMS(13) at different HCl concentrations (left) and for increasing EGMS concentrations at an acid concentration of 1 M HCl (right).

Further POM investigations show that hexagonal LLC phases are existent between 38 to 60%(w/w) surfactant in water with anisotropic to isotropic phase transitions around 36 °C. This temperature decreases with increasing amphiphile concentration. Above 60%(w/w) a lamellar structure is indicated by the POM investigations up to a concentration of 75%(w/w). The phase behaviour of the newly synthesized amphiphile is qualitatively similar to the commercially available Brij 97 with slightly narrower phase regions and lower thermal boundaries. Therefore, experiments on the commercially available Brij 97 were carried out to investigate the possibilities of the molecule as structure directing agent in the gel synthesis with glycol-modified silanes. Brij 97 has already been reported as structure directing agent in the fabrication of periodic mesoporous silica using conventional tetraalkoxysilanes [31, 148, 149], employed surfactant concentrations ranging from 4-10%(w/w) resulting in regions with highly ordered pores of hexagonal symmetry.

### 3.2.4 Brij 97 as structure directing agent

Small-angle X-ray scattering results for wet gels prepared from EGMS as silica source and Brij 97 (in a concentration of 30%(w/w) in aq. HCl) as templating surfactant are shown in Figure 3.2.7. Four concentrations of EGMS, ranging from 10 to 25 (w/w) SiO<sub>2</sub>-content, to lyotropic liquid crystalline phase (30/70 (w/w)) have been examined at different pH. Therefore, the gels were prepared with H<sub>2</sub>O, 10<sup>-2</sup> M, 10<sup>-1</sup> M and 1 M hydrochloric acid. The series of gels show that the long-range order improves at lower pH.

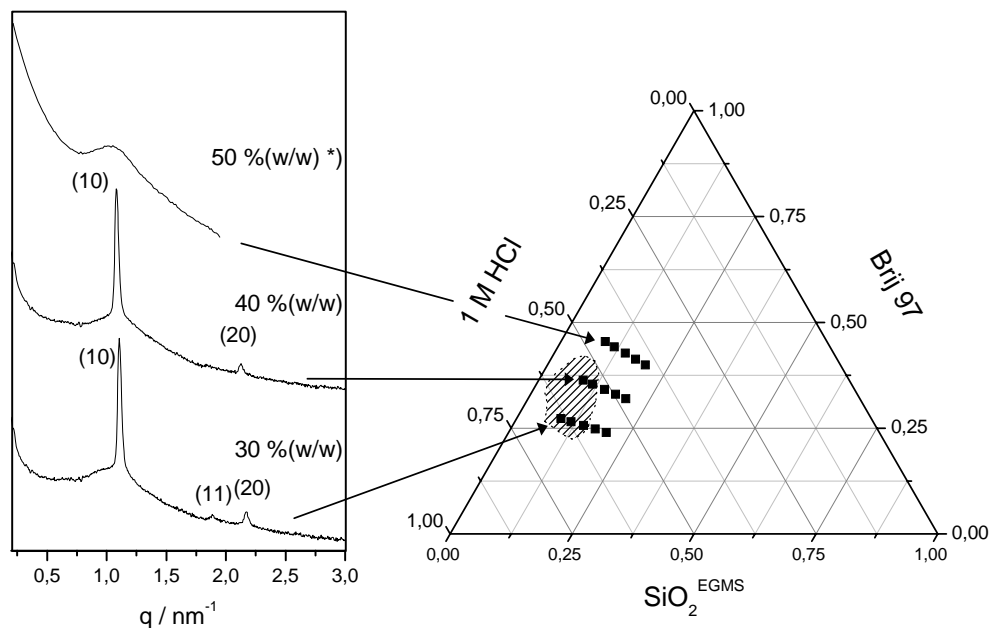


Figure 3.2.8. SAXS profiles for gels mixed from  $\text{SiO}_2(\text{EGMS})/(\text{Brij } 97+1 \text{ M HCl})$  equal to 10/100 and changing Brij 97/1M HCl ratios of 30:70, 40:60 and 50:50 (w/w) (\*SAXS curve for 50%(w/w) Brij 97 was measured with laboratory equipment, the other two curves were measured at the synchrotron facility Elettra). Results for all prepared gels are depicted in the ternary phase diagram (right). The encircled points indicate the region with pronounced periodic mesostructure.

The SAXS profiles in Figure 3.2.7 have been standardised to depict the decreasing FWHM with increasing acid concentration and decreasing  $\text{SiO}_2$ -content. The peaks are situated at  $q=1.1 \text{ nm}^{-1}$  which corresponds to a periodic distance of 5.7 nm. From the SAXS patterns it can be concluded that the order becomes more pronounced with decreasing silica concentration. Aging of the gels was performed at 20 °C, 30 °C and at 40 °C with the 20 °C-aged samples leading to higher periodic ordering proved by SAXS measurements. As known from the phase diagram of Brij 97 in water (Figure 2.1.3), a hexagonal phase is found in a concentration range of ~33-63%(w/w) surfactant in water. Therefore, Brij 97 in concentrations of 40 and 50%(w/w) in aq. HCl was additionally investigated in the sol-gel process. In Figure 3.2.8 scattering curves for different starting concentrations of EGMS/surfactant/1 M HCl are depicted. Results from all gels have been summarized in the ternary phase diagram. From the measurements it is clearly visible that periodic mesostructure could only be achieved at relatively low  $\text{SiO}_2$  concentrations. Gelation times of gels prepared at 20 °C and with 1 M HCl amount to approximately 48 h, independent of surfactant/water ratio. At elevated temperatures gelation takes place about twice as fast. Gels with ordered mesopores at low  $\text{SiO}_2$  content were very soft and collapsed into powders after ambient pressure drying. Samples were also dried with supercritical fluid extraction with MeOH as supercritical fluid, leading to monolithic material with less pronounced peaks in the SAXS curves and a periodic distance of approximately 5.3 nm.

### 3.3 Addition of polymerizable species to P123 in water

One attempt to produce nanocomposite materials with mesostructured silica as the inorganic matrix is to include polymerizable species to the template phase as, e.g., introduced by Sellinger et al. for nanolaminated films [93]. The poly(ethylene oxide)-based block copolymeric surfactant P123 in aqueous media has proven to be an excellent structure directing agent in sol-gel synthesis of ethylene glycol-modified precursors. Additional polymerizable species in the hydrophobic parts of the template (mesopores) should allow crosslinking of the organic at a later stage of the process, resulting in nanocomposite materials with a well defined spatial distribution of organic and inorganic moieties throughout the monolith. To prove the possibility of modifying the known and well-working system EGMS/P123/aq. HCl, three different monomer mixtures were added to P123 in water and aqueous hydrochloric acid, respectively. The three deployed monomer mixture are composed as follows (see also Table 2.4): **LB** consists of lauryl acrylate (LA) and 1,4-butanediol dimethacrylate (BMA) in a composition of 89.5:10.5 (w/w); **LBM** consists of LA, BMA and methacryloxy propyltrimethoxy-silane (MPS) as coupling agent with LA:BMA:MPS = 89.5:10.5:46.2 (w/w); **AT** is made of acrylic acid 2-butyl-carbamoyloxy-ethyl ester (BEA) and trimethylolpropane triacrylate (TTA) in a composition of 80:20 (w/w).

#### 3.3.1 Phase diagram of P123/water/monomer mixtures

In a first step the new LLC phases of polymerizable species and P123 in water were investigated. The amount of monomer mixture was increased, whereas the P123/water ratio was kept constant. Study of the structure was carried out using small angle X-ray scattering. The samples were sealed in quartz capillaries. Results for increasing amount of organic additives in 30 and 40%(w/w) P123 in water are shown in Figure 3.3.1. The investigated molar ratios of monomer to P123 molecules covered 1:1 up to at least 40:1.

**P123/water = 30/70 (w/w).** Thirty %(w/w) P123 in water without additives consists of a mixture of two liquid crystalline structures, namely hexagonally close-packed spheres, HCPS (P6<sub>3</sub>mmc) and cubic arrangement of micelles (Fm3m) [13] (compare also Chapter 3.4.1). Since this concentration was mainly used for the fabrication of gels described in this work, it was taken as a starting point. Increasing amounts of LB, LBM or AT were homogenized with the block copolymer water phase. The resulting small angle X-ray scattering patterns are depicted in Figure 3.3.1 (a). The number above each scattering curve shows the corresponding amount of monomer mixture to 30 (w/w) P123. At low amounts of additives (monomer mixture/P123/water = 1 to 10/30/70 (w/w)) the curves for the LLC

phases modified with LB and LBM are characteristic for (not-well resolved) mixed structure of 30%(w/w) P123 in water. The overlapping peaks can be assigned to a cubic (Fm3m) and a HCPS (P6<sub>3</sub>mmc) phase with  $q_{111}^{cub} \sim 0.41 \text{ nm}^{-1}$  and  $q_{100}^{hcps} \sim 0.385 \text{ nm}^{-1}$  in case of LB30 and  $q_{111}^{cub} \sim 0.44 \text{ nm}^{-1}$  and  $q_{100}^{hcps} \sim 0.39 \text{ nm}^{-1}$  in case of LBM30. This corresponds to a lattice parameter of  $a \sim 26 \text{ nm}$  for the cubic lattice and  $a \sim 19 \text{ nm}$  for the HCPS structure. For LB /P123/water = 10 to 30 /30/70 (w/w) and LBM/P123/water = 15 to 30/30/70 (w/w) the SAXS pattern changed significantly. A broad peak, which most likely still consists of overlapping peaks from Fm3m and HCPS ordering, but with a different ratio and form of the micelles, was found at  $q=0.31 \text{ nm}^{-1}$  (LB) and  $q=0.28 \text{ nm}^{-1}$  (LBM), respectively. The change towards smaller  $q$  indicates an increase in periodic distances due to micelle swelling. The SAXS pattern obtained for system AT30 in principle show the same results. Here,  $q_{111}^{cub}$  and  $q_{100}^{hcps}$  are weakly developed already at low monomer concentrations. From the SAXS curves it is concluded that the system stays liquid crystalline up to concentrations of monomer mixture/P123/H<sub>2</sub>O = 30/30/70 (w/w), but with changes in the initial distribution of cubic to HCPS phase and swelling of the micelles.

**P123/water = 40/60 (w/w).** Forty %(w/w) P123 in water without additives exhibits hexagonal ordering of cylindrical micelles (P6mm) [13]. At least three distinct peaks are visible in the SAXS curves, which can be assigned to the (10), (11) and (20) reflection.  $q_{100}^{hex}$  at low monomer concentration is positioned at  $0.44 \text{ nm}^{-1}$  (periodic distance  $d_{10}=14.3 \text{ nm}$ ) for systems LB40 and AT40 and at  $0.43 \text{ nm}^{-1}$  ( $d_{10}=14.6 \text{ nm}$ ) for system LBM40. With increasing amount of additives, the (10) reflection was shifted to lower  $q$  and became broader. At concentrations larger than 15/40/60 the (11) reflection was no longer visible. In the lauryl acrylate/1,4-butanediol dimethacrylate system structure was found up to a composition of 40/40/60 (w/w) with a resulting periodic distance of  $\sim 20.9 \text{ nm}$ . It can not be excluded that the structure has changed to lamellar.

For the system with methacryloxy propyltrimethoxy-silane as additional crosslinker (LBM) peaks were observed in the SAXS patterns up to compositions of 60 (and even more)/40/60 (w/w). Here, a resulting periodic distance of  $\sim 19.6 \text{ nm}$  is derived from the measurements. The system AT40 starts with a periodic distance of  $14.3 \text{ nm}$  at a composition of 1/40/60 (w/w) and displays a periodic distance of  $16.1 \text{ nm}$  at a composition of 30/40/60 (w/w). No comparable swelling as in the samples prepared with lauryl acrylate was observed. At high monomer concentrations, the SAXS curves become very similar to the curves obtained at low monomer concentrations in 30%(w/w) P123 in water.

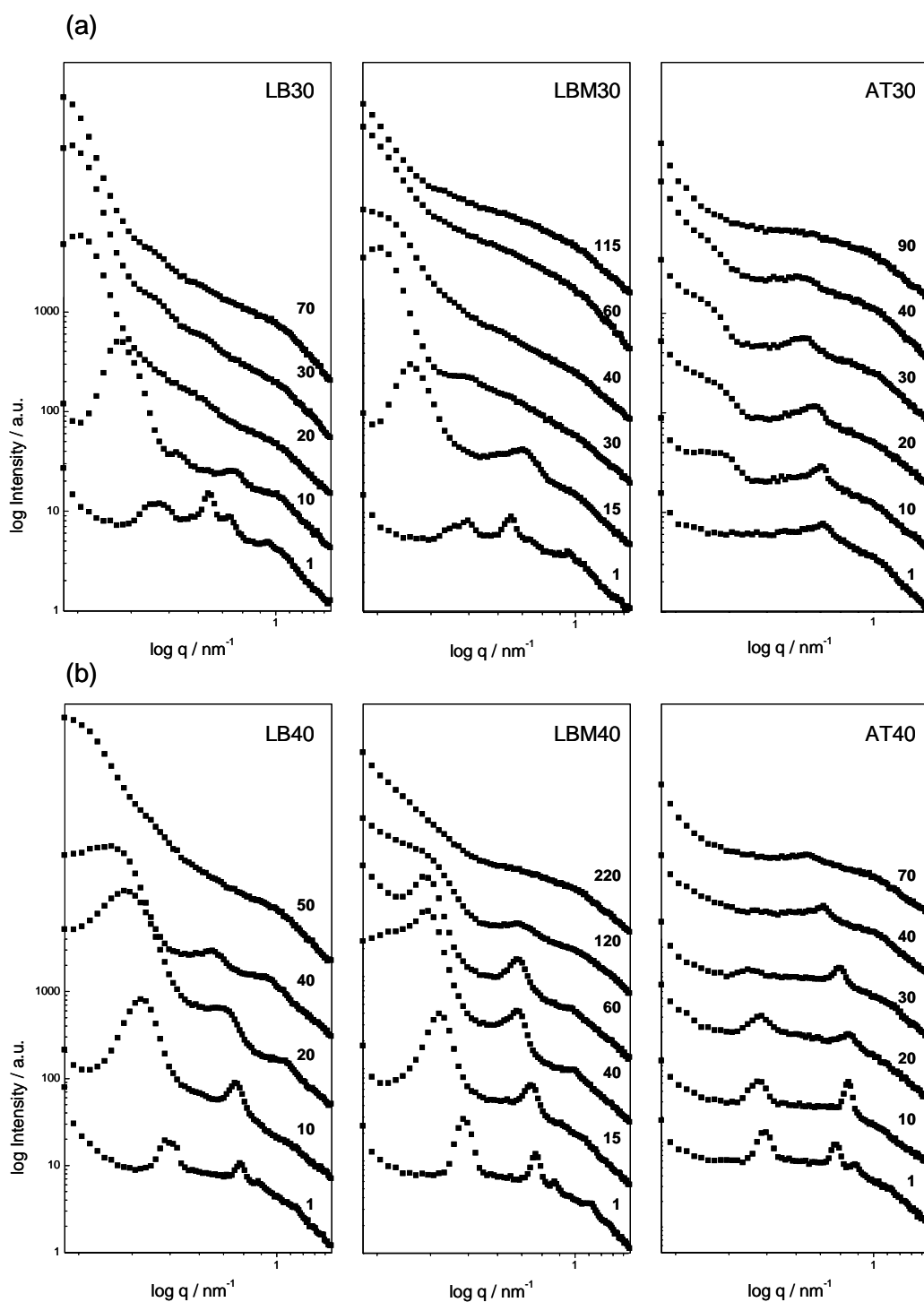


Figure 3.3.1. Small angle X-ray scattering patterns of the non-ionic block copolymer surfactant P123 in water in concentrations of (a) 30:70 and (b) 40:60 (w/w) with increasing amount of polymerizable additives. The amount of monomer mixture (LB, LBM, AT) to 100 g P123/H<sub>2</sub>O is depicted for each curve.



### 3.3.2 Gels prepared with P123/monomer mixtures

Sellinger et al. reported the use of polymerizable species in addition to surfactant (CTAB) in the fabrication of nanolaminated organic-inorganic films at very high concentration (47%(w/w) monomer) [93]. In contrast to the monolithic gels prepared from glycol-modified precursors described in this work, these films are prepared with evaporation-induced self-assembly starting with very dilute compositions rendering a high mobility of the system during the process. With regard to the investigations on LLC mixtures of different monomers and non-ionic poly(ethylene oxide)-based block copolymeric surfactant P123 in water described in the previous chapter, gels were prepared from EGMS in combination with a liquid crystal templating approach in acidic aqueous media, including polymerizable species as listed in Table 2.4 following the standard procedure.

Table 3.2. Components and composition of monomer/surfactant LLC phases investigated in a liquid crystal templating approach combined with sol-gel processing of a siliceous precursor (EGMS). The ratio of surfactant to aq. HCl was kept constant (30/70%(w/w)).

Components			Monomer (%(w/w))	Crosslinker (%(w/w))	Surfactant (%(w/w))
<u>Monomer:</u>	a	LB	2.2	0.3	97.5
L ... lauryl acrylate		AT	2.0	0.5	97.5
A ... acrylic acid 2-butyl-carbamoyloxy-ethyl ester	b	LB	4.5	0.5	95.0
<u>Crosslinker:</u>		AT	4.0	1.0	95.0
B ... 1,4-butanediol dimethacrylate	c	LB	9.0	1.0	90.0
T ... trimethylolpropane triacrylate		AT	8.0	2.0	90.0
<u>Surfactant:</u> Pluronic P123	d	LB	13.4	1.6	85.0
		AT	12.0	3.0	85.0

The two monomer formulations LB and AT were added to P123/aq. HCl in amounts of 2.5 to 15%(w/w) of polymerizable species to surfactant concentration (Table 3.2). The ratio of precursor to surfactant to aqueous hydrochloric acid were kept constant with  $\text{Si}^{\text{EGMS}}/\text{P123}/\text{aq. HCl} = 7.9/30/70$ . Gels were prepared at two different pH values, namely pH=0 (denoted as 1) and pH=2 (denoted as 2). As observable in the SAXS-profiles depicted in Figure 3.3.2 only small amounts of the investigated monomers can be added to the given system without loss of highly ordered periodic mesostructure.

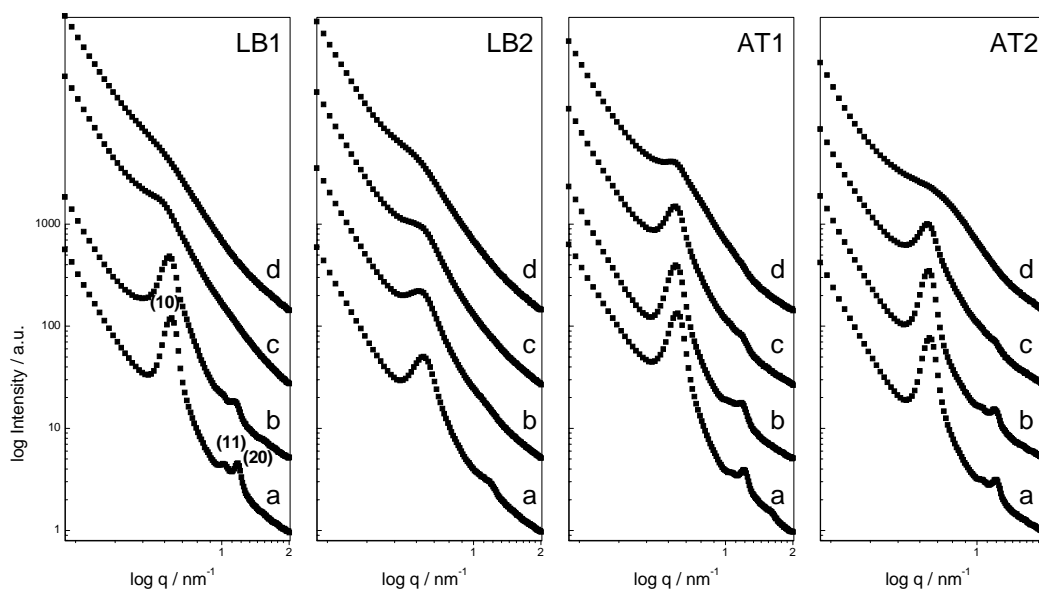


Figure 3.3.2. Small angle X-ray curves derived from gels with additional organic monomers added to the LLC template during synthesis. The ratio  $\text{Si}^{\text{EGMS}}/\text{P123}/\text{aq. HCl}$  was kept constant with 7.9/30/70 for all gels. pH was changed by deploying 1 M HCl (denoted as 1) and  $10^{-2}$  M HCl (denoted as 2).

Gels prepared with additional polymerizable species (LB, LBM, AT) and thermal or photo-initiators in the template were also measured at the synchrotron research center Elettra (Trieste, Italy, BL5.2L), monitoring the self-assembly process during gel-formation *in-situ*. Results were compared to measurements of a reference gel without additives.

To obtain a nanocomposite material, e.g., acrylic acid 2-butyl-carbamoyloxy-ethyl ester and trimethylolpropane triacrylate as polymerizable species (AT) were added to the primary formulation in a ratio of  $\text{AT}/\text{P1235}/1 \text{ M HCl} = 1.6/30/70$  (w/w) which is consistent with system AT1-b (Figure 3.3.2). Furthermore AIBN as thermal initiator was added to the sol. Gelation and mesostructure formation was followed *in-situ* after 80 min of external aging at 313 K. The evolution of the mesostructure started only after 130 min. After 210 min a periodic structure of hexagonally ordered cylindrical micelles had evolved with a periodic distance  $d_{10}=14$  nm. Twenty-four hours later the structure had shrunk further to a value for  $d_{10}=12.4$  nm. Both the reference system and system AT1-b showed similar behaviour.

This leads to the conclusion that the gelation process and the mesostructure formation in the system were not influenced by the addition of small amounts of organic monomers. Nevertheless, the amount of organic species added to this particular sol-gel system has to be kept low, since the degree of mesoscopic ordering decreases with increasing amount of monomers. Formation of the organic polymer was induced at 14 hours after formation of the periodic mesostructure by heating the sample to 343 K. After heating the sample for 20

min, the *d*-spacing had decreased by 2% (0.6% smaller than the reference system after 24 hours), indicating additional shrinkage, partly due to aging and polymerization of the organic phase. Further experiments were carried out with lauryl acrylate and 1,4-butanediol dimethacrylate (LB, LBM) as monomers leading to similar results.

### 3.4 *In-situ* synchrotron SAXS/XRD study on silica/surfactant self-assembly

Ethylene glycol-modified silane (EGMS) [150, 151] or ethylene glycol-modified phenylene-bridged organosilane (bPhGMS) [72] were used as precursors in the presence of Pluronic P123 as structure directing agent. The modification of the precursors with ethylene glycol allows gel formation in purely aqueous media, resulting in highly porous materials with a bimodal pore arrangement and monolithic structure.

The formation of periodically ordered mesostructures, and in the case of phenylene-bridged silica materials also the formation of lamellar arrangements of organic and inorganic moieties within the pore walls [45] has already been studied for powder synthesis with conventional ethoxy- or methoxy silane precursors by time-resolved SAXS/WAXS measurements [32, 33, 37, 40-42, 45]. Powder formation from conventional alkoxysilanes normally starts from very dilute acidic ethanol/water solutions of the surfactant (~2.5%(w/w)) and silane (~5%(w/w)). In this work, synthesis was started with a lyotropic liquid crystalline phase of surfactant in purely aqueous (acidic) medium, resulting in high concentrations of surfactant (15-20%(w/w)) and precursor (32-45%(w/w)). This is only possible due to the water solubility of the modified silanes and their compatibility with LLC surfactant phases in water [151]. The aim of the studies, described in the following, was to gain information on the formation of the inorganic or hybrid network in the presence of a pre-formed liquid crystalline phase. Evolution of the periodic arrangement, as well as sol-gel transition, were monitored *in-situ* with SAXS and partly with WAXS.

#### 3.4.1 Pluronic P123 as structure directing agent

The use of ethylene glycol modified precursors in the fabrication of mesoporous materials, in principle should allow for a true liquid crystalline templating (TLCT), without great disturbance of the LLC phases by the creation of alcohol. Therefore, high surfactant concentrations, with the mixture already in the LC regime of the phase diagram, are employed in the synthesis. It should be noted, however, that the hydrophobic/hydrophilic properties of a given system continuously change during polymerization of the inorganic species. At the beginning of the synthesis, also the temperature changes due to exothermic condensation of the precursor. These changes in parameters may be expected to influence also the mesophases. The results show that the starting liquid crystalline structure of the pure surfactant/water mixture and the periodic structure of the final mesopores are not the same, thus demonstrating the limitations of the concept of TLCT.

### 3.4.1.1 LC phase of Pluronic P123 in water

Pluronic P123 in the given concentration of 30%(w/w) (or below) in water or in dilute HCl, respectively, consists of a mixture of two liquid crystalline structures, namely hexagonally close-packed spheres, HCPS ( $P6_3mmc$ ) and cubic arrangement of micelles ( $Fm\bar{3}m$ ) [13]. The characteristics of the associated Bragg reflections are listed in Table 2.6. The broad peak at  $q \sim 0.37 \text{ nm}^{-1}$  observed at the beginning of the *in-situ* measurement (7-9 min after addition of the silane) is usually associated with micellar scattering of P123 aggregated in flocks by the polymerizing silica [152]. In our case of a liquid crystalline phase as starting point for the synthesis, the shape of the corresponding scattering curve still indicates a structural relation. The broad peaks observed (see Figure 3.4.1) resemble to some extent the diffraction pattern of 30%(w/w) P123 in  $H_2O$  after a loss in periodic structure and domain size with distances shifted to lower values of  $q$  (slightly swollen and smeared). The scattering pattern of 30%(w/w) P123 in water is shown in Figure 3.4.1 together with the curves of the sol and the final mesoporous gel for comparison. The peaks can be assigned to a mixture of a cubic ( $Fm\bar{3}m$ ) and a HCPS ( $P6_3mmc$ ) phase with a lattice parameter of  $a=26.9 \text{ nm}$  for the cubic lattice and  $a=19.1 \text{ nm}$  and  $c=31.2 \text{ nm}$  (with  $c=(8/3)^{1/2}a$ ), for the HCPS structure. This is in accordance with the literature [13]. The lattice parameters give some clue about the radii of the surfactant micelles, since they allow the calculation of maximal radii under the assumption of hard spheres, as described in Table 3.3.

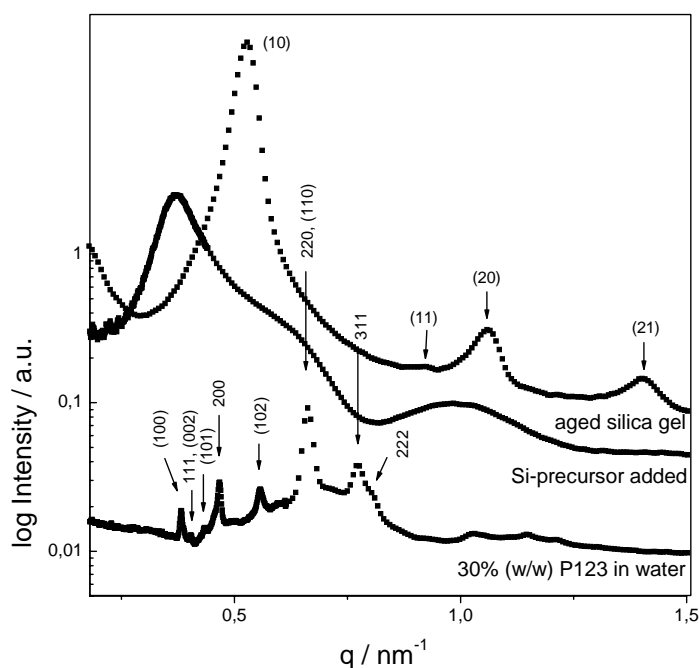


Figure 3.4.1. Scattering pattern of 30%(w/w) P123 in water (bottom curve). The middle scattering curve corresponds to the LLC phase after addition of the silica precursor. The top curve shows the diffraction pattern of the final mesoporous gel, with the resulting hexagonally arranged cylindrical mesopores.

Pluronic P123 in a concentration of 40%(w/w) in water forms cylindrical micelles, which are hexagonally ordered (P6mm). This corresponds to the final structure in the investigated mesoporous materials. As shown in the results in Table 3.3, the maximum radius of the micelles is smaller for the elongated than for the spherical micelles.

Table 3.3. Structure and the corresponding lattice parameters for the crystalline phases observed for 30 and 40%(w/w) Pluronic P123 in water. The lattice parameters give a limit for the radii of the surfactant micelles (R).

P123 %(w/w)	Phase	$q / \text{nm}^{-1}$	Lattice const. / nm	Limit
30	<u>intermediate:</u> Fm3m P6 <sub>3</sub> mmc	(111) 0.404 (100) 0.38	a = 26.9 a = 19.1 c = (8/3) <sup>1/2</sup> a = 31.2	$R \leq \frac{\sqrt{2}}{4}a \Rightarrow R \leq 9.5$ $R \leq \frac{a}{2} \Rightarrow R \leq 9.55$
40	hexagonal	(10) 0.466	a = 15.6	$R \leq \frac{a}{2} \Rightarrow R \leq 7.8$

It is well known, that PEO interacts with the surface of colloidal silica through hydrogen bonding with silanols by its ether oxygens [153, 154]. To gain more information on the behaviour of the LLC phase prior to the addition of the inorganic precursor, experiments on the initial concentration of surfactant in water were carried out. Therefore, the liquid crystalline structure of the employed P123 concentration (30%(w/w)) at different temperatures and for different pH was examined by small angle X-ray scattering.

The SAXS curves measured for the binary P123/water system at different pH and temperatures are shown in Figure 3.4.2. With increasing temperature, a loss of the periodic structure can be observed for all three systems. This loss is least pronounced for the sample at pH=0. The pH of the mixture has an influence on the obtained scattering curves. Whereas there are only small deviations between P123 in water and P123 in 10<sup>-2</sup> M HCl, the scattering pattern of the surfactant dissolved in 1 M HCl looks quite different. This is most likely due to a change in the form of the micelles, i.e. the radius of the hydrophobic core, R<sub>C</sub>, and the thickness of the hydrophilic shell, R<sub>S</sub>. Both parameters may be deduced from the form factor of spherical micelles as shown in the following.

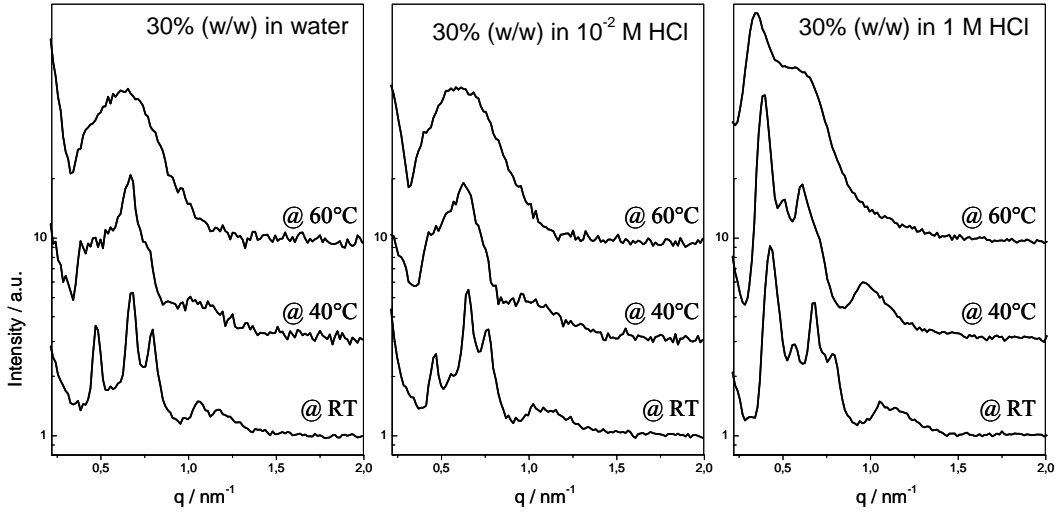


Figure 3.4.2. Scattering patterns of 30%(w/w) P123 in aqueous solution at different temperatures and pH.

### 3.4.1.2 Core-Shell model for P123 micelles in water

Assuming, that the micelles consist of a hydrophilic shell (PEO) and a hydrophobic core (PPO), the following model was applied:

For the crystalline phases of P123 in dilute HCl at RT, the scattering cross section of monodisperse micelles is proportional to the micellar form factor,  $P(q)$ , times the structure factor  $m_{hkl}|S_{hkl}(q)|^2$  ( $m_{hkl}$  is the multiplicity of the respective reflection) and the polarization factor. The scattering intensity from the mixed liquid crystalline phase, consisting of cubic and hexagonally close-packed arranged spheres (HCPS) was therefore calculated using the following relation:

$$I(q) = \langle P(q) \rangle \left[ A^{cub} m_{hkl}^{cub} |S_{hkl}^{cub}(q)|^2 + A^{hcps} m_{hkl}^{hcps} |S_{hkl}^{hcps}(q)|^2 \right] \exp(-q^2 \sigma^2) (1 + \cos^2(2\theta)) / \cos \theta$$

Eq. 3.1

with

$$P(q, R_C, R_S) = \left[ (4\pi/3)(\rho_S - \rho_M)(R_C + R_S)^3 F(q, R_C + R_S) + (4\pi/3)(\rho_C - \rho_S)R_C^3 F(q, R_C) \right]^2$$

Eq. 3.2

where  $F(q, R) = 3[(\sin qR - qR \cos qR)/(qR)^3]$  is the normalized scattering amplitude of a sphere (see Eq. 2.5). The electron density of the dilute hydrochloric acid,  $\rho_M$ , was calculated according to:

$$\rho_M = \frac{n_W Z_W + n_{HCl} Z_{HCl}}{V_M}$$

Eq. 3.3

Here,  $n_W$  and  $n_{HCl}$  are the number of moles of water and HCl in the volume  $V_M$  (volume of the aqueous medium) and  $Z_W$  and  $Z_{HCl}$  are the number of electrons in one mole of water, respectively HCl.  $N_A$  is the Avogadro number. In this model the P123 micelles are assumed to be of same size for both phases and, furthermore, monodisperse. Therefore, a hard sphere radius,  $R_{HS}$ , was introduced in the fit.  $R_{HS}$  is calculated according to the terms given in Table 3.3 and is assumed to be the same for the cubic and the HCPS structure. The lattice parameters of the two structures,  $a_{Fm3m}$  and  $a_{HCPS}$ , are then calculated from  $R_{HS}$ . The final radius of the micelles,  $R_{micelle}$ , is correlated to  $R_{HS}$  via a parameter  $\delta^2 = R_{HS} - R_{micelle}$  (by definition  $R_{HS} > R_{micelle}$ ). Fitting was performed following Eq. 3.1. The electron density for the hydrophobic PPO-core,  $\rho_C$ , was taken as  $337 \text{ e}^-/\text{nm}^3$ , which is slightly smaller than the calculated value for the PPO melt ( $337.5 \text{ e}^-/\text{nm}^3$ ) as reported by Soni et al [13]. The electron density of the hydrophilic shell,  $\rho_S$ , is a fit parameter.  $\rho_M$ , the electron density of the dilute HCl, was calculated according to Eq. 3.3. The obtained values are given in Table 3.4. In the fits  $R_{HS}$ ,  $\delta$ , amplitudes of the cubic and HCPS structure, FWHM of the Bragg reflections,  $\rho_S$  and  $R_C$  were left free. In a second attempt  $R_C$  was kept constant at 4.75 nm.

The obtained SAXS curves of the four different pH-values (water: pH~6,  $10^{-2}$  M HCl: pH~2,  $10^{-1}$  M HCl: pH~1, 1 M HCl: pH~0; measured at RT) were fitted according to Eq. 3.1.

#### a) Fit-results for $R_C$ as free parameter

In Figure 3.4.3 the resulting fit-curves together with the measured SAXS-curves and the resulting form factor are shown. Whereas the experimental curves for P123/ $H_2O$ ,  $10^{-2}$  M HCl and  $10^{-1}$  M HCl display more or less the same characteristic reflections, the system changes when 1 M HCl is used. This is also reflected in the differing form factor (dashed line) obtained by the fit. Fit results are listed in Table 3.4. Whereas  $R_C$  becomes larger with higher acidity,  $R_S$  increases at first but decreases significantly in the system P123/1 M HCl. The obtained radii of the core and the shell thicknesses at different pH are illustrated in detail in Figure 3.4.4 (a) and (b). Starting from the surfactant/water mixture, therefore,  $R_{micelle}$  starts to increase up to a pH of 1 but becomes significantly smaller at high acidity, whereas  $R_{HS}$  is similar to the value in the neutral mixture. At the same time  $\rho_S$  increases and reaches a value very close to the calculated electron density for 1 M HCl ( $338.2 \text{ e}^-/\text{nm}^3$ ) used in the mixture (see Table 3.4).



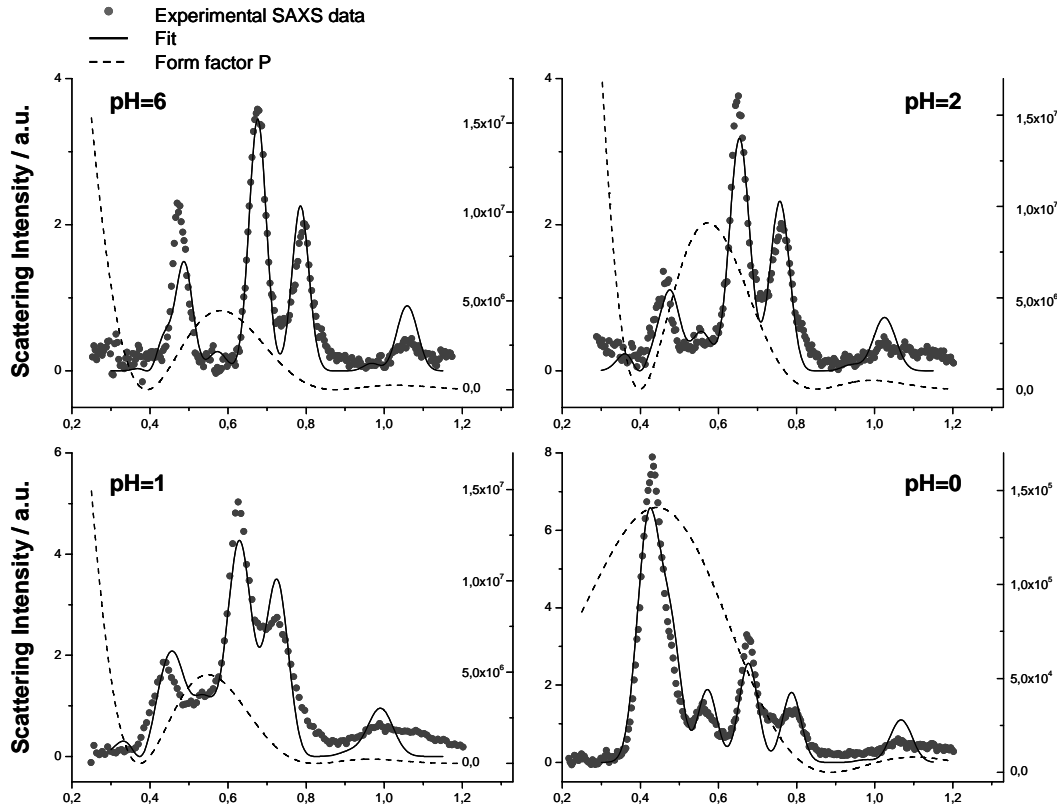


Figure 3.4.3. Diffraction pattern of the liquid crystalline structure of 30%(w/w) P123 at different pH. Solid lines depict the calculated intensity using a core-shell model with  $R_C$  a free parameter. The inserted dashed lines show the form factor  $P(q)$  resulting from the corresponding fit (right axes).

Table 3.4. 30 % (w/w) P123-solutions (22 °C) at different pH: Electron densities of solvent ( $\rho_M$ ), core ( $\rho_C$ ), shell ( $\rho_S$ ), radius of the spherical micelles ( $R_{\text{micelle}}$ ), core radius ( $R_C$ ), thickness of the shell ( $R_S$ ), ratio of the fraction of cubic to HCPS phase ( $I_{\text{Fm3m}}/I_{\text{HCPS}}$ ), parameter for the distance of the micelles ( $\delta$ ), FWHM of the Bragg reflections ( $\sigma$ ), lattice parameter of the cubic ( $a_{\text{Fm3m}}$ ) and the HCPS ( $a_{\text{HCPS}}$ ) structure.

		Parameters in form factor $F(q)$						Parameters in structure factor $S(q)$					
		Fixed		Fitted		Calc.		Fitted			Calc. ***		
P123	pH	$\rho_M^*$	$\rho_C^{**}$	$\rho_S$	$R_{\text{micelle}}$	$R_C /$	$R_S /$	$I_{\text{Fm3m}}/I_{\text{HCPS}}$	$\delta^2$	$\sigma /$	$a_{\text{Fm3m}}$	$a_{\text{HCPS}}$	
%(w/w)		$e/\text{nm}^3$	$e/\text{nm}^3$	$e/\text{nm}^3$	$(R_{\text{HS}}) / \text{nm}$	$\text{nm}$	$\text{nm}$			$\text{nm}^{-1}$	$/ \text{nm}$	$/ \text{nm}$	
30	6	333.95	337	330.5	9.2 (9.2)	4.7	4.5	20	$1 \cdot 10^{-3}$	0.022	26.1	18.5	
	2	334.04	337	329.0	9.5 (9.5)	4.7	4.8	8	$2 \cdot 10^{-3}$	0.027	26.9	19.0	
	1	334.42	337	331.4	9.9 (9.9)	4.9	5	5	$1 \cdot 10^{-5}$	0.032	27.9	19.7	
	0	338.2	337	338.4	8.5 (9.2)	5.1	3.4	2	0.67	0.025	26.0	18.4	

\*  $\rho_M$  was calculated following Eq. 3.3; \*\*  $\rho_C$  was kept fixed during fitting; \*\*\* lattice parameter of the cubic (Fm3m), respectively the HCPS (P6<sub>3</sub>mmc) structure calculated according to the relations given in Table 3.3; The values differ slightly from the given values in Table 3.3, due to a different experimental setup and the fitting conditions.

From the change in the amplitudes of the cubic, respectively the HCPS phase, one can deduce that the fraction of HCPS phase becomes larger with increasing acidity of the system.  $\delta$  is very small for pH=6, 2 and 1 and becomes only relevant at high acidity (1 M HCl). The size of the domains tends to become smaller in the acidic systems as seen by the change in  $\sigma$  (Table 3.4).

**b) Fit-results for  $R_C$  as fixed parameter ( $R_C = 4.75$  nm)**

When the radius of the core is kept fixed throughout the fit as demonstrated in Figure 3.4.4 (c), most of the obtained values differ only slightly from the values given in Table 3.4 ( $R_C$  left free). The same trends as before are observable for the  $R_{\text{micelle}}$ , which initially becomes larger at lowering the pH, but has its minimum at high acidity (1 M HCl). The change in  $\rho_s$  and the relation of cubic and HCPS phase show again the same trend as in the case of  $R_C$  as free parameter.  $\delta$  can be neglected for all four systems meaning that  $R_{\text{HS}}$  and  $R_{\text{micelle}}$  are equivalent.

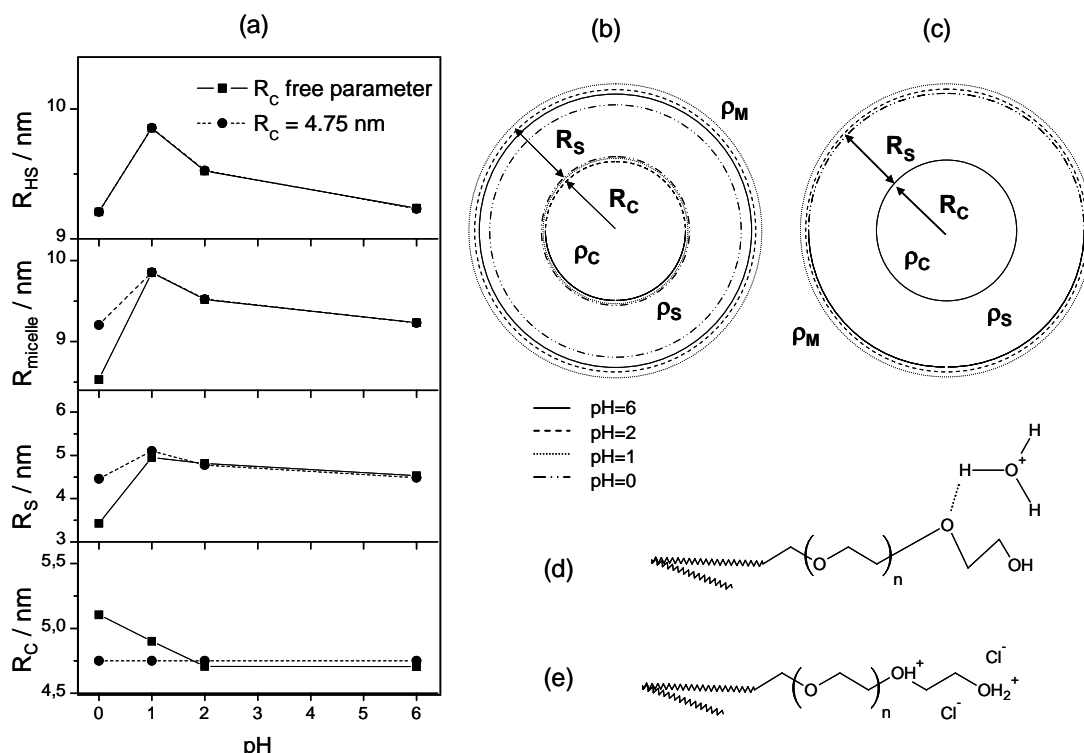


Figure 3.4.4. (a) Fit results of  $R_C$ ,  $R_S$ ,  $R_{\text{micelle}}$ ,  $R_{\text{HS}}$  plotted against pH. Schematic representation of the core-shell built-up of the micelles (with a hydrophobic core made of PPO and a hydrophilic shell consisting of PEO) and the changes of  $R_{\text{micelle}}$  and  $R_S$  with  $R_C$  first treated as free parameter (b) and then fixed at 4.75 nm (c). (d) Increase diameter due to increased hydrogen bonding. (e) Possible explanation for the increase of electron density in the shell at different pH.

In conclusion the fit results strongly suggest an increase of fraction of the HCPS phase ( $I_{Fm3m}/I_{HCPS}$  see Table 3.4) with increasing polarity of the system. The lattice parameters, as well as  $R_{micelle}$  of the moderate acidic solutions slightly increase, but at high acidity drop to or below the initial values observed at neutral pH. The reason for this is found in a decrease in shell thickness,  $R_S$  at pH=0. At the same time, the electron density of the shell,  $\rho_S$ , increases and becomes very similar to the calculated electron density of the surrounding media ( $\rho_M$ ). Yang et al [155] have investigated the influence of temperature and pH on micellar solutions of P123 (4%(w/w)). They report an increase in effective diameter of the micelles with increasing HCl concentration, due to stretching of the EO-chains by increased hydrogen bonding with the protonated water molecules Figure 3.4.4 (d). Furthermore, hydronium ions are incorporated in the shell and lead to swelling of the micelles. Our results show the same trend for more concentrated, LLC mixtures of P123, but only up to HCl concentrations of  $10^{-1}$  M.

A possible explanation for the observed decrease of  $R_{HS}$  in a solution of 1 M HCl is shown in Figure 3.4.4 (e). At very low pH, the PEO chains are protonated. Without the counteracting  $Cl^-$ -ions, the protonated PEO-units repel each other because of the same charge. Therefore, the smaller radius at high acidity or the higher electron density of the shell is likely due to the fact, that the protonated polyether fractions are closely packed with the  $Cl^-$  as counter ions in between them to hinder repulsion.

At 40%(w/w) of P123 in water the liquid crystalline structure is 2D hexagonal with the (100)-reflection at  $q=0.4688 \text{ nm}^{-1}$  (corresponding to a lattice constant of 15.48 nm). Thus, with a higher concentration of the polymer, the system shifts into a hexagonal phase, with the micelles no longer being spherical, but cylindrical. This transition from spherical micelles to cylinders can be described roughly by a simple geometrical model of chain packing, using the critical packing parameter (cpp) which was already introduced in Chapter 1.2.1. For spherical micelles, cpp is smaller than 1/3, whereas for cylinders the value of cpp lies between 1/3 and 1/2. In this model the transition is either due to an increase of the volume of the hydrophobic core or the decrease of the head group area [6, 7]. Soni et al [13] describe a decrease in the interfacial area per PEO block as well as a decrease in the lattice parameter, when increasing the copolymer concentration. This is a result of higher packing of the copolymer molecules, while the water content and its availability decrease.

### 3.4.2 Mesostructure formation in monolithic mesoporous gels

The *in-situ* measurements described in this section were performed at the SAXS beamline at Elettra. Information on the experimental setup is given in Chapter 2.3.1.

Combined SAXS/WAXS measurements were carried out on bPhGMS- and EGMS-derived systems, with the sample kept constant at 40 °C, beginning as soon as the LLC phase and precursor were completely homogenized. A temperature of 40 °C is important for the optimal self-assembly of the block copolymer molecules. Table 3.5 summarizes the investigated systems together with the composition and the observed parameters of the developing network.

Table 3.5. Overview of the different systems investigated *in-situ* at the SAXS beamline Elettra/Triest. The table gives the gel time ( $t_g$ ), the time at which the periodic mesostructure starts to evolve ( $t_{pm}$ ) together with the corresponding  $d$ -spacing ( $d$ ), the time of phase separation ( $t_{ps}$ ) and the observed Bragg reflections.

Sample	Silane	Composition / weight fractions (w/w)			$C_{HCl}$ / M	$t_g$ / min	$t_{ps}$ / min	$t_{pm}$ / min	Reflections	$d^{**}$ / nm
		silane (Si)	P123	aq. HCl						
E800	EGMS	82 (8)	30	70	$10^{-2}$	240*	240	~240	(10), (20)	14.6
E802	EGMS	82 (8)	30	70	1	70	95	110-120	(10), (20), (21), (30)	14.0
E80n	EGMS	82 (8)	30	70	0	1-3	1-3	1-3	(10), (20)	14.0
E47n	EGMS	48 (4.7)	30	70	0	3	3	3	(10), ((11)), (20)	13.5
bPh530	bPhGMS	48 (5.3)	30	70	$10^{-2}$	220	220	240	(10), (11), (20), (21)	13.9
bPh420	bPhGMS	38(4.2)	30	70	$10^{-2}$	125	145	145	(10), (11), (21)	13.9

\*) significant increase in viscosity after 60-75 min; \*\*) with which mesostructure starts to form

All compositions listed in Table 3.5 resulted in periodic mesoporous materials. The reflections can be indexed according to a 2D hexagonal structure (P6mm). In most cases, long range order of the mesostructure was only observed in the SAXS curves after gelation (0-40 min). A change in colour from transparent to opaque, as indication for phase separation ( $t_{ps}$ ), took place between gelation ( $t_g$ ) and long-range order formation ( $t_{pm}$ ).

***EGMS (E800)- and bPhGMS (bPh530)-gels synthesised with 10<sup>-2</sup> M HCl.*** In Figure 3.4.5 the *in-situ* SAXS pattern of the gelation kinetics of samples (a) E800 and (b) bPh530 are shown as function of time. The measurements start with the homogenized sol and follow the systems until gelation and mesostructure evolution have been accomplished.

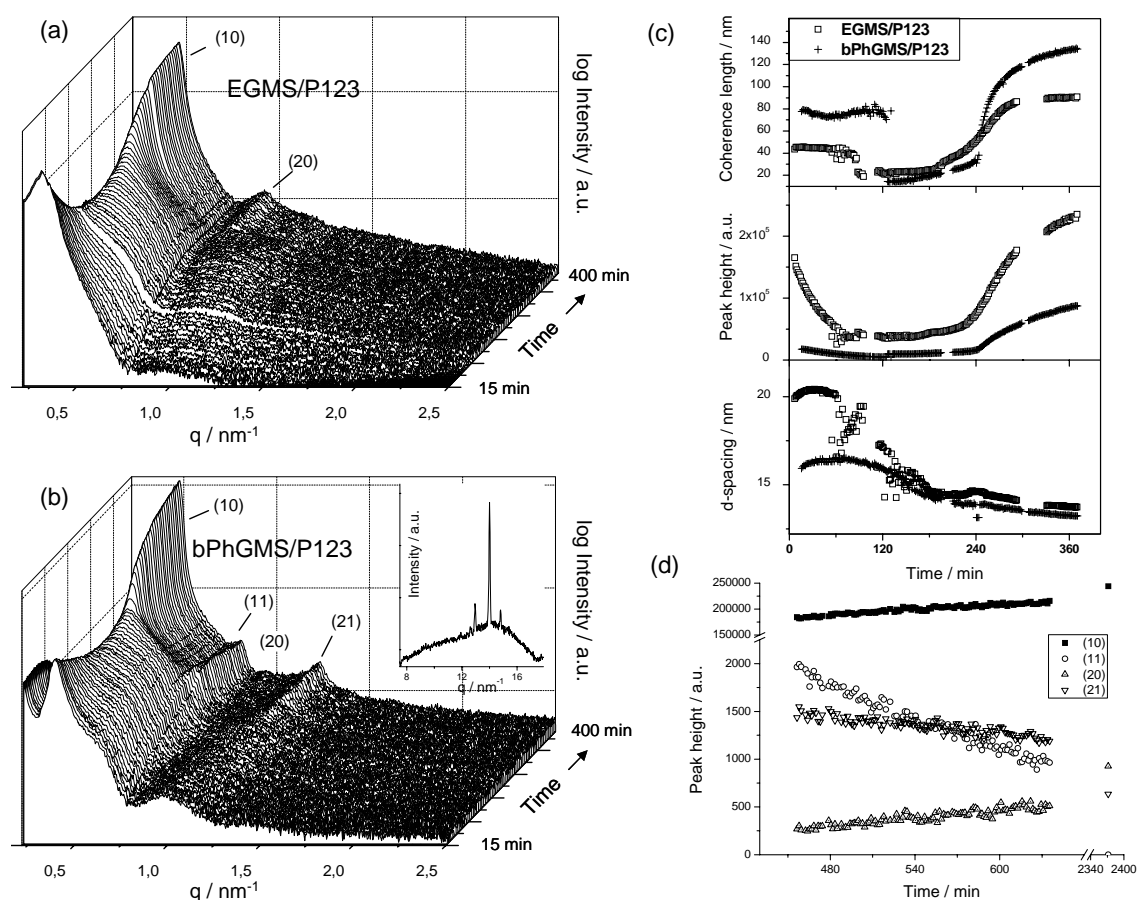


Figure 3.4.5. *In-situ* measurement of the sol-gel transition using (a) ethylene glycol-modified silane (E800) and (b) ethylene glycol-modified phenylene-bridged organosilane (bPh530) as the precursor. The insert in (b) shows the WAXS region at an early stage of the synthesis. (c) The evolution of the observed peaks as a function of time, described by the coherence length (Eq. 2.13), the intensity and the  $d$ -spacing. (d) Further evolution of the Bragg intensities of the bPhGMS system with time.

In both systems the addition of the silane significantly disturbs the long range order of the supramolecular arrangement described in Chapter 3.4.1. Nevertheless, some structural order is observed in the scattering pattern. This is more pronounced in case of the organically bridged precursor. Results for the fitted (10) reflection are depicted in Figure 3.4.5 (c) for both systems.

At this pH and for the given concentration of the constituents, gelation takes place after approximately 220-240 min, although a significant increase in viscosity could be observed in the EGMS system already after the first 70 minutes. A colour change from transparent to turbid, denoting phase separation occurs parallel to gelation. The periodic mesostructure starts to form, characterized by a rise of intensity and decrease of FWHM of the (10) reflection at  $q=0.429 \text{ nm}^{-1}$  and the appearance of the (20) reflection for the EGMS system. In the bPhGMS system, the intensity of the (10) reflection at  $q=0.45 \text{ nm}^{-1}$  starts to increase

rapidly ~20 min after gelation. Shortly afterwards, two additional distinct Bragg peaks emerge, corresponding to (11) and (21) of a periodic structure of hexagonally arranged cylinders. The detailed development of the peak intensities for the bPhGMS-system can be seen in Figure 3.4.5 (d). After 460 min the (20) reflection becomes visible. After 540 min this reflection exceeds the (11) reflection, due to the progression of the wall thickness of the mesopores.

In case of the phenylene-bridged precursor, three sharp peaks can be observed in the WAXS region at the beginning of the synthesis. Those reflections can be ascribed to d-spacings of 0.43 nm, 0.45 nm and 0.48 nm. However, the intensities of all 3 peaks decrease continuously until they vanish prior to the formation of the periodic mesostructure. This effect was observed only for two different *in-situ* measurements of the phenylene-bridged organosilane and always with the same, rather high, concentration of organosilane. A possible explanation lies in the preparation of the bridged precursor. The glycol modification implies a removal of ethanol, resulting in a solid material consisting of grains, which are partly crystalline. The vanishing of the sharp peaks correlates to a consumption of residual precursor grains in the synthesis and was not observed in a more dilute system. During further progress of the gelation, no change in the WAXS-pattern could be observed that would confirm formation of periodic order within the walls of the hybrid mesophase parallel to the formation of the mesostructure, as it was reported by Morell et al [45]. Since the final material exhibits lamellar ordering in the walls [72], the ordering effect was either too small to be observed in the WAXS data or takes place at a later stage.

By comparing the time resolved properties of the first reflections (Figure 3.4.5 (c) of samples E800 and bPh530, the pure silica network seems to develop more continuously than the organically-bridged material. A slightly larger periodic distance from the evolving long-range order was found for the EGMS-derived gels.

If the concentration of Si<sup>bPhGMS</sup> in the synthesis is slightly decreased, gelation and structure evolution proceeds faster. For sample, in sample bPh420, the gelation time is reduced from 220 min, as observed for sample bP580, to 125 min (see Table 3.5). Evolution of the periodic mesostructure starts already after approximately 140 min. The progress of the (10) reflection with time is plotted in Figure 3.4.6 (b). Again the behaviour of the intensity at  $q=0.22 \text{ nm}^{-1}$  is shown as dashed line.

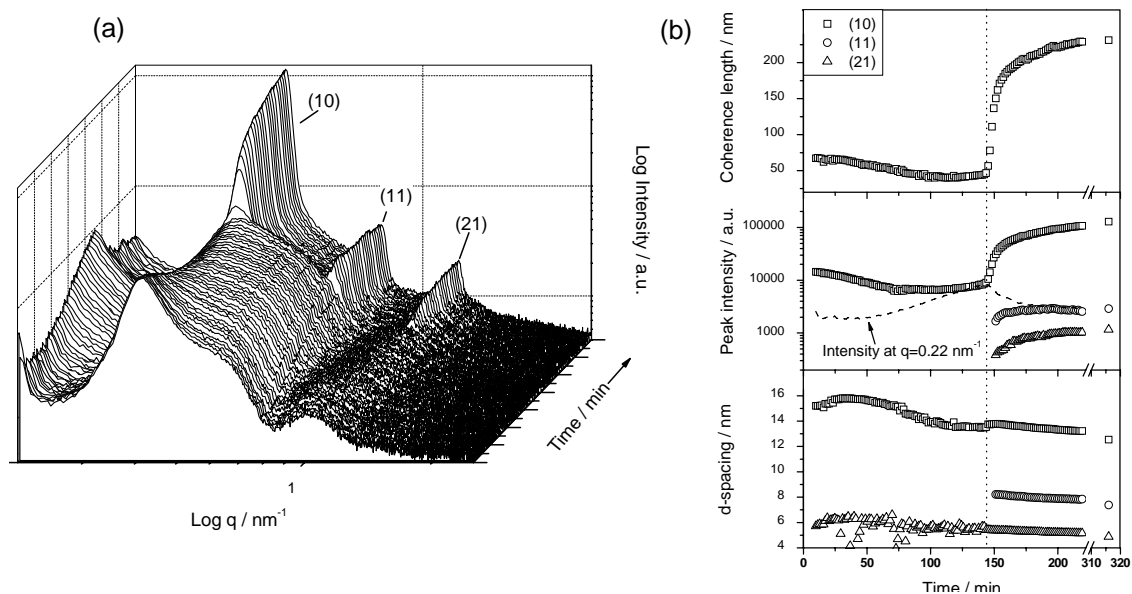


Figure 3.4.6. (a) *In-situ* SAXS measurement on phenylene-bridged system with lower Si-concentration; (b) Evolution of intensity, repeating unit distance and coherence length of the (10) (additional: (11) and (21)) reflection. Again an increase in intensity in the low  $q$ -range is observable prior to evolving of the Bragg reflections.

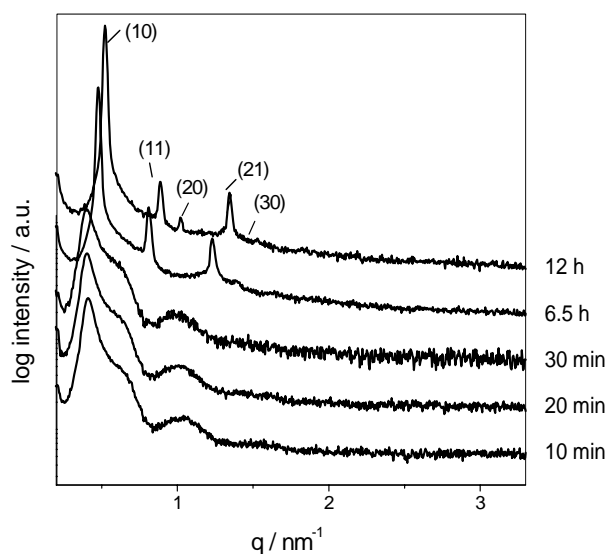


Figure 3.4.7. Single scattering profiles for bPh420 during synthesis and aging process.

In Figure 3.4.7 scattering curves measured at different stages of network formation are plotted for comparison. From the Bragg reflections the shrinkage of the  $d$ -spacing is clearly visible. Even after 6 hours of aging, the structure, namely, the wall thickness is not fully completed.

**EGMS gel with 1 M HCl (E802).** Temporal evolution of the periodic mesostructure in case of E802 is shown in Figure 3.4.8. In comparison to the previously described system of EGMS/P123 with  $10^{-2}$  M HCl, gelation was observed already after 70 min, prior to the colour change to turbid. Bragg reflections from the periodic arrangement of mesopores become visible in the SAXS pattern after 110 min. The peak at  $q=0.449 \text{ nm}^{-1}$  can be indexed according to (10). Further evolving peaks are (20), (21) and (30) which indicate the formation of highly ordered 2D hexagonal mesostructures with a repeating unit distance of 14 nm. Interestingly, in the low  $q$ -region of the measurements the scattering intensity first increased and then decreased parallel to mesostructure formation. For a better understanding, the intensity at  $q=0.22 \text{ nm}^{-1}$  is plotted in Figure 3.4.8 together with the intensity of the (10) reflection. The progress of the scattering intensity at low  $q$  indicates the evolution and dissolution of additional particles and was found in most systems. Detailed SAXS measurements of the considered  $q$ -region were undertaken at the ID02 beamline at ESRF, Grenoble and will be discussed in the following section.

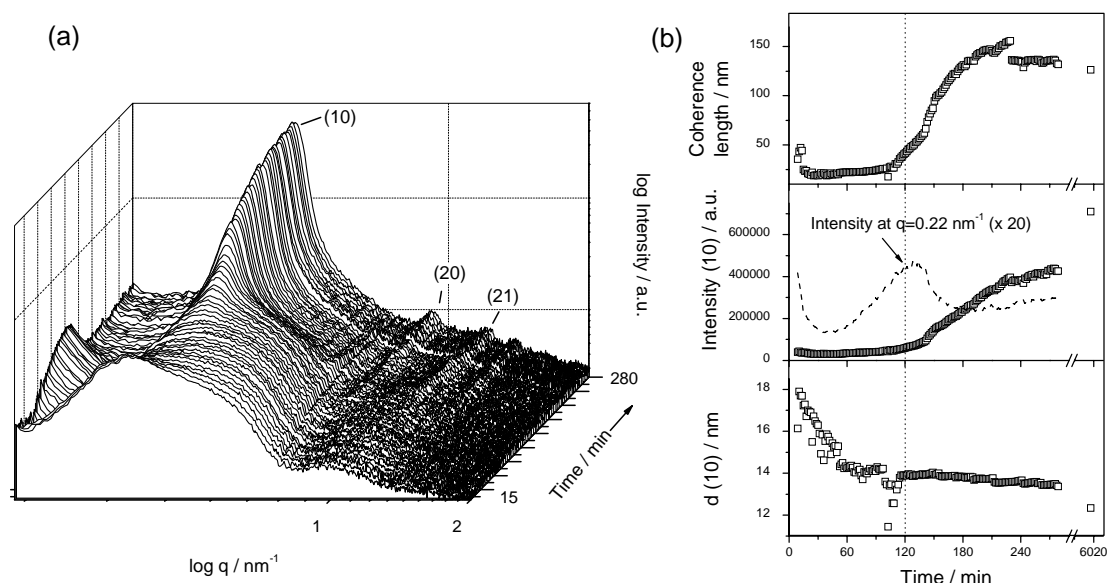


Figure 3.4.8. (a) Temporal evolution of the SAXS/XRD pattern for E802. (b) Fit values for the first Bragg reflection (10) of the periodic mesostructure. Periodic arrangement becomes visible after approximately 120 min, indicated by the dotted vertical line. Comparing the change and the increase in intensity of the first Bragg reflection with the intensity at  $q=0.22 \text{ nm}^{-1}$ , a maximum is observed around the point of mesostructure formation.

During aging of the gel (Figure 3.4.9) the repeating unit distance decreased to 12.38 nm, which corresponds to a lattice parameter of  $a=14.3 \text{ nm}$  of the hexagonal structure. Due to the formation of the walls the (21) reflection disappeared whereas the (11) reflection, which is not visible at the beginning of the kinetic measurements, appeared 10 to 15 h after synthesis.



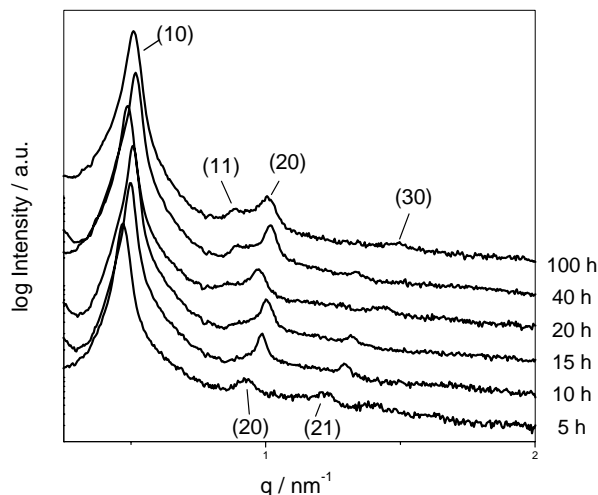


Figure 3.4.9 Small angle X-ray scattering profiles for EGMS/P123/1 M HCl at different stages of aging.

**Neutral pH (E80n).** As reported in [156], very short gelation times of only a few minutes can be observed at neutral pH ( $\sim 6$ ) for EGMS. The synthesis of two EGMS gels with different Si/P123 ratio was followed *in-situ*, sample E80n having a composition of Si/P123/H<sub>2</sub>O of 8/30/70 and sample E47n a composition of 4.7/30/70. Corresponding  $t_g$  and structure information are given in Table 3.5. The fitted values from the (10) reflections are depicted in Figure 3.4.10 (a).

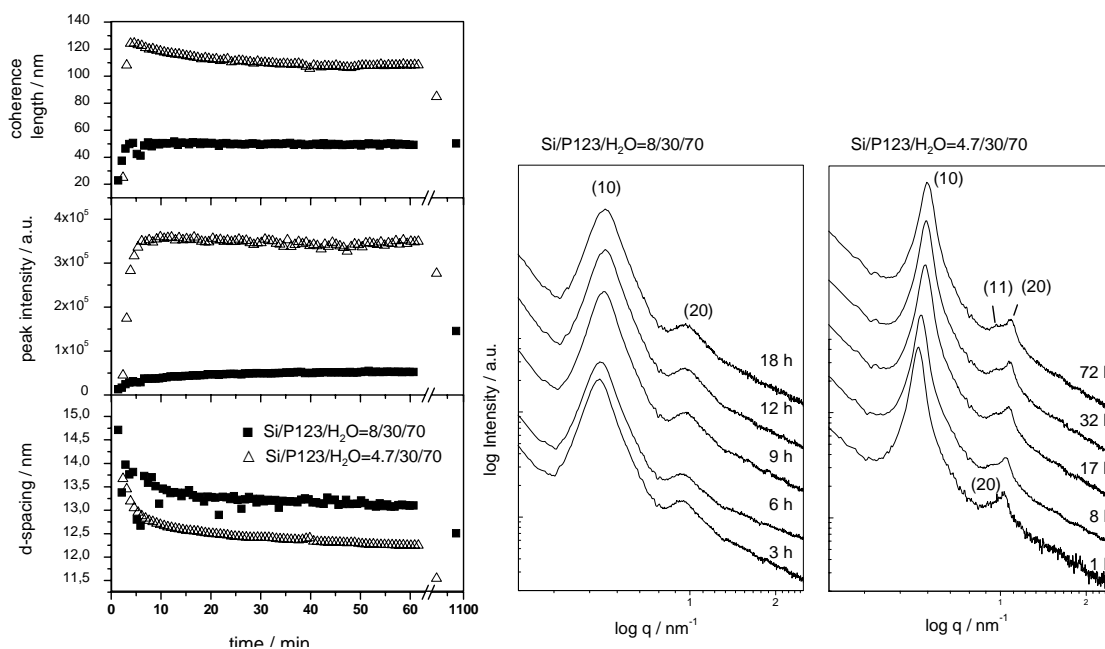


Figure 3.4.10 Left: Values obtained from the fit of the first reflection during the synthesis of EGMS/P123 gels in neutral media, where gelation, as well as mesostructure formation, take place quickly ( $\leq 3$  min). For this reason no transition is observed in the time-dependent scattering profiles. Right: Gels at different stages of the aging process.

System E47n has a slightly higher  $t_g$  ( $\sim 3$  min) and the characteristic increase in intensity and coherence length due to formation of the mesostructure is observed. The structural order is enhanced, leading to a lower limit for the coherence length  $L$  of approximately 105 nm (50 nm for sample E80n), with three peaks visible in the scattering profiles. However, contrary to E80n, the size of the domains exhibiting periodical order decreases during aging ( $L \sim 90$  nm).

### 3.4.3 Extending the $q$ -region in the scattering experiments: The hybrid network

Time-resolved *in-situ* SAXS studies described in the following were undertaken at the European Synchrotron Radiation Facility in Grenoble, France (for setup details see Chapter 2.3.1). Besides the  $q$ -regime depicting the evolution of the periodic mesostructure ( $0.18 < q < 4 \text{ nm}^{-1}$ ), a second sample-detector length was employed providing information on structural features as large as  $\sim 300$  nm ( $0.018 < q < 0.6 \text{ nm}^{-1}$ ). The aim of these measurements was to correlate self-assembly processes and formation of the network and phase separation during sol-gel-synthesis.

1,4-Bis(tris-(2-hydroxyethoxy)silyl)benzene (bPhGMS) was prepared as described in Chapter 2.1.2 and used as silica precursor in aqueous medium under moderately acidic conditions ( $\text{pH}=2$ ) using Pluronic P123 as structure directing agent. Samples for *in-situ* measurements were filled into quartz capillaries, sealed immediately after homogenization and put into the beam. Gelation was followed by SAXS at least up to 15 min after mesostructure formation was observed in the SAXS-pattern. The phase separation mechanism was again checked by observing the colour change from transparent to white in a reference sample kept outside. The gels were kept at  $40^\circ\text{C}$  throughout the process.

Results from the time-resolved synchrotron SAXS measurements of a system with a concentration of bPhGMS(Si)/P123/ $10^{-2}$  M HCl = 48(4.9)/30/70 (w/w), further on denoted as system bPh490-A are shown in Figure 3.4.11. The two employed  $q$ -regions overlap. *In-situ* SAXS measurements on the gel kinetics were carried out directly after homogenization of the components. The given time data (x-axis) refer to the point of adding the silane to the surfactant/water mixture.

During the gel kinetic of this system, roughly three stages of development can be distinguished from the time-resolved SAXS curves shown in Figure 3.4.11 (a): For the first 15-35 minutes, a mixing and formation of new aggregates, respectively, is observable in the low  $q$ -regime ( $q$ -region I), as well as in the amplitude loss of the remaining liquid crystalline structure ( $q$ -region III:  $>0.2 \text{ nm}^{-1}$ ).

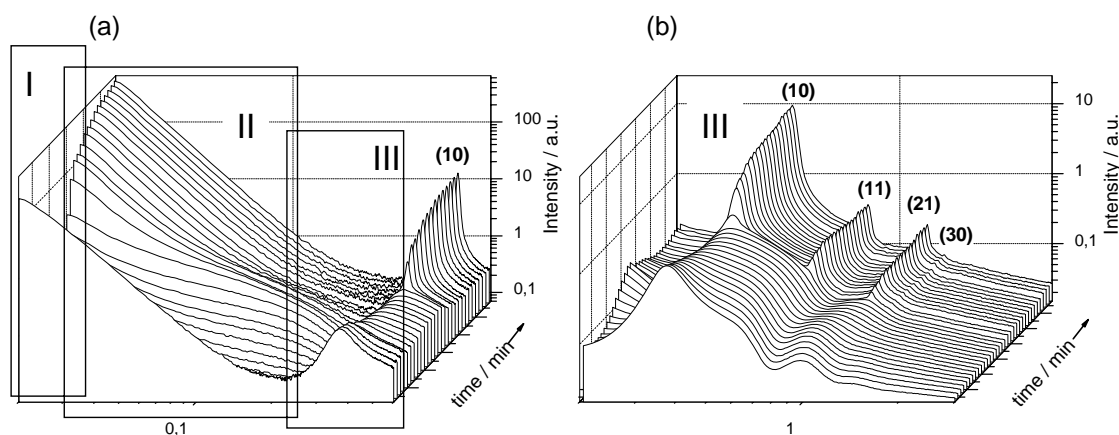


Figure 3.4.11. Time-resolved synchrotron SAXS patterns from a P123-mediated sol-gel-synthesis of the phenylene bridged silica-precursor leading to a macroporous network consisting of highly ordered, hexagonally arranged cylindrical mesopores. (a) SAXS-measurements carried out with a sample-detector distance of 10 m and (b) of 1.5 m.

From 40 to 65 min in time (prior and parallel to the mesostructure formation) the evolution of an “intermediate phase” is observed in the  $q$ -range smaller than  $0.2 \text{ nm}^{-1}$  ( $q$ -region II). In stage 3 the mesostructure develops (see Figure 3.4.11 (b)). In the following the results are presented in detail.

***LC-phase and mesostructure formation.*** Stage 1 ( $t \leq 35 \text{ min}$ ): At the beginning of the measurements (9 min after addition of the bPhGMS) the scattering pattern clearly shows rests of periodic order (Figure 3.4.11 (b)). The relation to the liquid crystalline phase of 30%(w/w) P123 in dilute HCl, consisting of hexagonally close-packed spheres (hcps) and cubic long range order of spherical micelles was already shown in Figure 3.4.1. Peaks corresponding to partially ordered P123 micelles are very broad, most likely due to a loss in the degree of periodicity. A possible explanation for this is the detaching of micelles (radius of  $\sim 8\text{-}9.5 \text{ nm}$ ) from the mixed liquid crystalline phase by interpenetration of  $\text{SiO}_2$ -oligomers into the hydrophilic region. The mixture is in a low viscous state, the network is not yet developed. However, it is very likely that the precursor molecules have been completely hydrolyzed and primary  $\text{SiO}_2$ -clusters from silicic acid have already been formed [157]. For the available  $q$ -range (down to  $0.018\text{-}4 \text{ nm}^{-1}$ ) structures (spheres, discs, rods) of dimensions up to 100 nm would be observable, as was checked with simulations of the corresponding form factor and is explained in more detail in Chapter 2.3.1. Shortly after mixing a Porod regime ( $\propto q^{-4}$ ) can be observed in the SAXS patterns, probably corresponding to the tail of a SAXS signal caused by large aggregates (dimensions larger than 100 nm) at low  $q$ . With time the amplitude of the Porod-fit decreases which may be explained by the growth of new aggregates rich in P123 and silica and dissolving of remaining LLC phase, respectively. This is shown in Figure 3.4.12 (a).

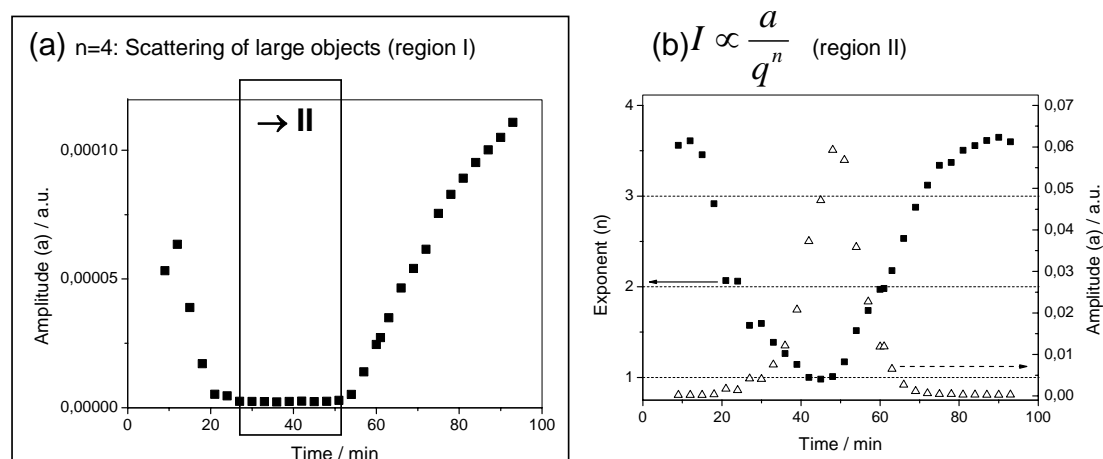


Figure 3.4.12 a) Amplitude of the Porod fit of system A is initially high, the decrease indicates dissolution of the components. The Porod regime shows some deviation due to the undefined surface between the phases. b) Fitting of region II reveals the evolution of smaller particles. A slope proportional to  $q^{-1}$  indicates cylindrical shapes.

Stage 2 (time = 35-75 min): A Guinier region evolves in q-region II (see Figure 3.4.11 (a) and Figure 3.4.12 (b)). The slope at small  $q$  is proportional to  $q^{-1}$ , which indicates cylindrically shaped particles. By subtracting the scattering from large aggregates (Porod scattering), the resulting slope of the particles more closely resembles the characteristic curve of spherical particles ( $I \propto q^0$ ). Therefore the corrected data were fitted with a Debye approximation (see Eq. 2.9). Fit results for the gel kinetic are plotted against time in Figure 3.4.13 (a). They describe the growth in number and size of spherical particles. The growth of the particles (silica/surfactant rich) continues up to a critical radius of  $\sim 11$  nm. The dashed line indicates the time at which the periodic mesostructure starts to evolve in the SAXS pattern. Time of mesostructure evolution and maximum of the particle radius seem to correlate, indicating interplay or arrival at a critical size or concentration of the particles, respectively. Figure 3.4.13 (b) demonstrates the good agreement of fit and experimental data, despite the rough approximation.

Stage 3 (time  $\geq 57$  min): At this point, the Bragg peaks of the periodical mesostructure start to evolve in q-region III (Figure 3.4.11 b). A sharp reflection appears at  $q=0.432 \text{ nm}^{-1}$  together with two less intense reflections at  $q=0.746 \text{ nm}^{-1}$  and  $q=1.146 \text{ nm}^{-1}$ , which can be indexed as (10), (11) and (21) reflections, associated with a  $p6mm$  hexagonal symmetry with a repeating unit distance of 14.5 nm, indicating the formation of highly ordered cylindrical mesopores (hexagonal). The (20) reflection is not visible at this point, as was also reported in [152] but is slightly visible after 108 min, as well as the (30) reflection, and is clearly existent in the scattering pattern of the aged and dried gel (see Figure 3.4.14).

This is due to the final wall thickness and the shrinkage of the cylinders which influences the form factor. Obviously, the wall has not yet developed fully at this stage of the synthesis.

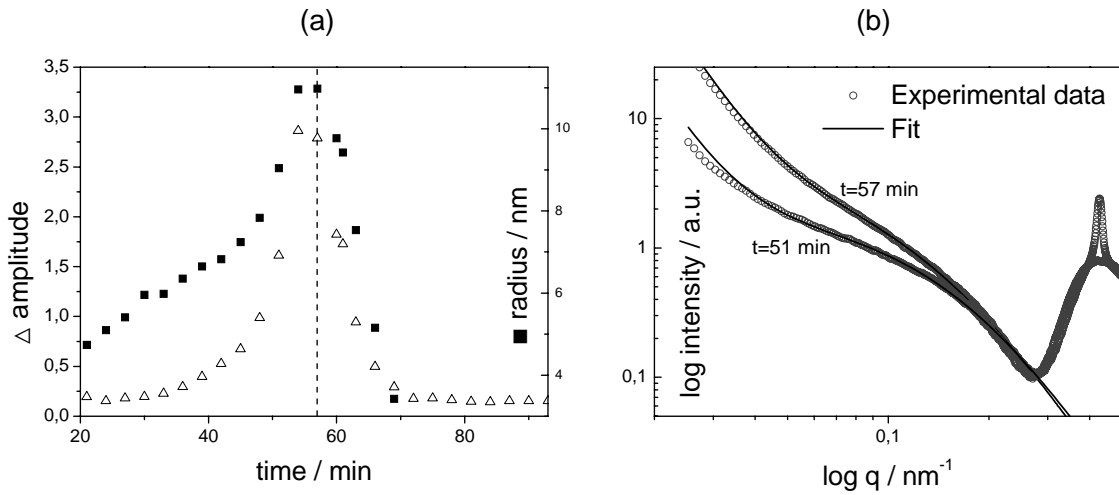


Figure 3.4.13. (a) Fit results of the *in-situ* SAXS curves reveal the growth of an intermediate phase prior to the formation of periodically arranged mesopores. As fit-function the form factor of spheres in Debye's approximation (Eq. 2.9) was applied to the experimental curves, leading to a good agreement as shown in (b).

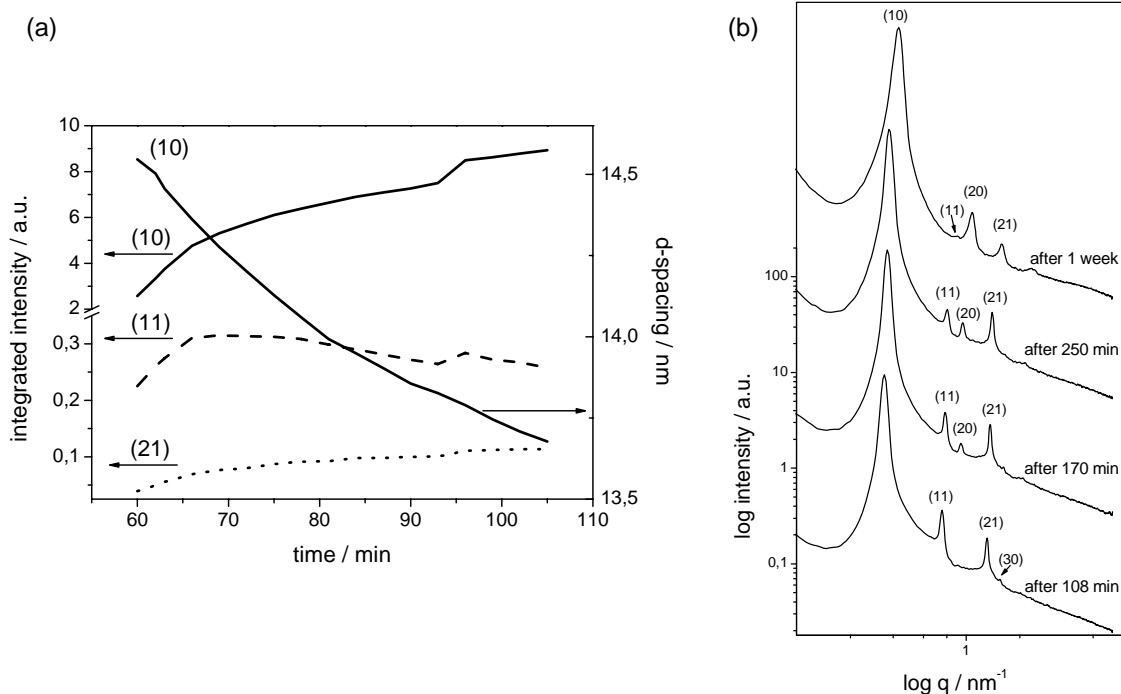


Figure 3.4.14 (a) depicts the time evolution of the  $d$ -spacing of the (10) reflection and the integrated intensities of the Bragg reflections of the periodic mesostructure. At the beginning of the formation process up to approximately 2 h only the (10), the (11) and the (21) reflection are clearly visible. (b) As seen in the presented SAXS curves this trend changes during the aging process. After one week, the (20) reflection has become much more pronounced.

The structure shrinks continuously with time (decrease of  $d$ -spacing, see Figure 3.4.14). The intensity of the (10) reflection increases with time, indicating an increase in the amount of ordered material. The same applies for the amplitude of the Porod regime (Figure 3.4.12), pointing towards a simultaneous development of mesostructure and macroscopic structure of the hybrid network. Unfortunately, the  $q$ -range available was not sufficient to follow the evolution of objects larger than 100 nm. The final dimension of the macrostructure is in the order of 250-5000 nm. The resulting macromorphology will be described in Chapter 3.4.6.

The observed intermediate phase, having its maximum (amplitude and also radius of the forming particles) at the moment the sharp Bragg-peak of the mesostructure starts to grow, may trigger, or is at least correlated to mesostructure formation. The Bragg reflections of the periodic mesostructure grow out of the broad peak of the surfactant/water liquid crystalline phase. The Porod-radius of the globular particles was determined for system A after 54 min (shortly before the Bragg peaks evolve) and yields a value of 9.1 nm. The scattering curve was also fitted with Guinier's law (see Eq. 2.3). The latter fit gives only a poor correlation and leads to a high value for the radius of gyration of  $R_g \sim 12$  nm ( $R_{Sphere} = \sqrt{5/3}R_g$ ). The corresponding radius ( $R_d$ ) obtained by fitting the curve with the Debye function given in Eq. 2.9, is 11 nm. The difference between values obtained by Debye and Guinier approximation is discussed in Appendix A. The position of the (10) Bragg reflection ( $q_{10} = 0.43 \text{ nm}^{-1}$ ) at the point of mesostructure formation yields a maximum radius (derived from the lattice parameters) for the forming cylinders of 8.5 nm. A possible explanation for this gap is that the evolving objects reach a critical size ( $R_d \sim 11$  nm in the Debye fit) and then collapse into cylinders. However, it is not possible to exclude the existence of single cylindrical micelles prior to the periodic arrangement.

From the scattering pattern, the point in time at which the Bragg peaks of the hexagonally arranged cylinders start to form can be determined as 57 min after mixing. The macroscopically observed gelation time is about 70 min.

Influence of relative volume fraction of “fluid” phase on gel kinetic and mesostructure formation.

Samples with various ratios of Pluronic P123 to  $10^{-2}$  M HCl were prepared. From sample bPh490-A (described in detail in the previous section) to sample bPh490-C, the ratio of silane to surfactant was kept constant with 48/30 by weight, whereas the fraction of dilute HCl in the sol was increased, resulting in silane/ $10^{-2}$  M HCl weight ratios of 48/70 (bPh490-A), 48/90 (bP490-B) and 48/110 (bP490-C). Concentrations of P123 in water in the case of B and C are situated in the micellar region of the phase diagram, even though close to region of cubic and HCPS lattice. All samples were prepared with the preassembled supramolecular template of 30%(w/w) P123/aq. HCl. Residual aq. HCl was added at the moment of mixing. All three compositions lead to monolithic, white gels. As the dilute hydrochloric acid content increases, the time, at which the evolution of the hexagonally ordered cylinders starts, decreases ( $t_{pm}$  see Table 3.6). For all three systems the observed time of phase separation ( $t_{ps}$ ) coincides approximately with  $t_{pm}$ , whereas gelation was observed afterwards. The time interval between  $t_{pm}$ ,  $t_{ps}$  and  $t_g$  grows larger at higher dilution.

Table 3.6. Composition, time of phase separation ( $t_{ps}$ , checked by color change), starting time of mesostructure evolution ( $t_{pm}$ ), gelation time ( $t_g$ ), radius for intermediate particles ( $R_d$ )\* at  $t_{pm}$ , lattice parameter of the 2D hexagonal structure ( $a$ , with  $a = 2/\sqrt{3}d_{10}$ ) at  $t_{pm}$  and after 1 week of aging at 40 °C.

Sample	bPhGMS (Si) / % (w/w)	P123 / % (w/w)	$10^{-2}$ M HCl / % (w/w)	$t_g$ / min	$t_{ps}$ / min	$t_{pm}$ / min	$R_d @ t_{pm}^*$ / nm	$a @ t_{pm}^{**}$ / nm	$a$ (aged gel) / nm
bPh490-A	48 (4.9)	30	70	70	54	54	10.98	17.0	13.9
bPh490-B	48 (4.9)	30	90	45	39	39	11.46	16.7	13.9
bPh490-C	48 (4.9)	30	110	>70	28	28	10.67	16.8	13.7

\*) Value from Debye-fit; \*\*)  $a=(4/3)^{1/2}d$ ;  $d=2\pi/q_{10}$

All three systems resulted in a periodic mesostructure with hexagonally arranged cylindrical mesopores as depicted in Figure 3.4.15 (top curves: resulting gels after aging). At the beginning of the measurements, it is clearly observable that in the more diluted systems reformation of the phases has already been achieved to a higher degree. This can be deduced from the first SAXS curves (bottom curves in Figure 3.4.15) as well as from the fit results for the Porod amplitude at low values of  $q$  which are depicted in Figure 3.4.16 (c).

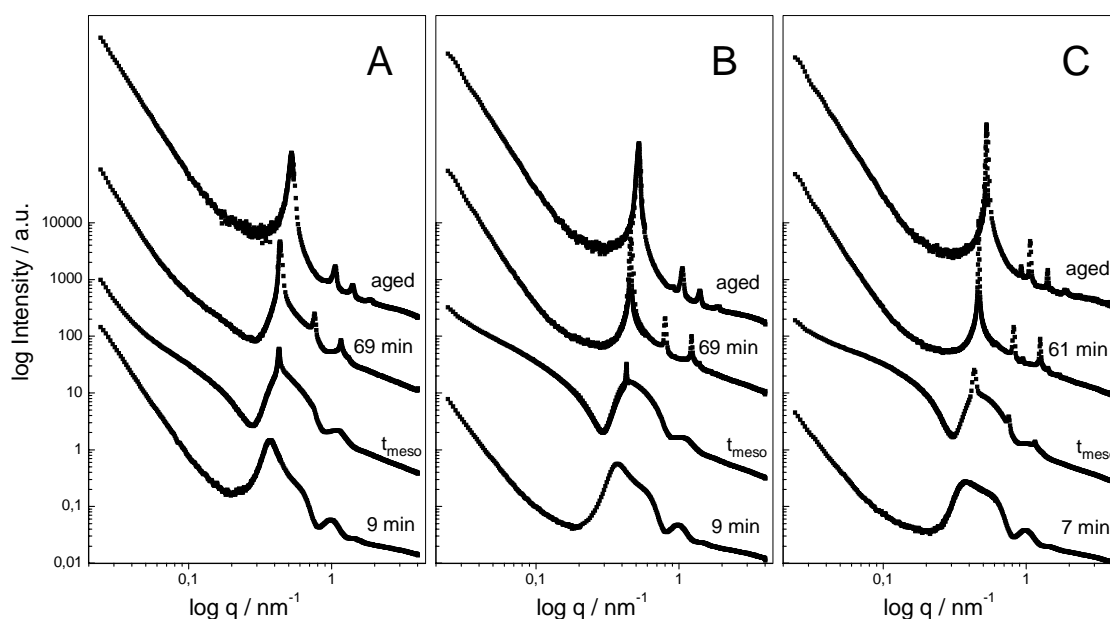


Figure 3.4.15 Scattering curves of the complete investigated  $q$ -range ( $0.024\text{--}4\text{ nm}^{-1}$ ) for system A, B and C at different stages of the synthesis, that is (from bottom to top): fairly at the beginning, at the phase transition to hexagonally ordered cylinders ( $t_{\text{meso}}$ ), after  $\sim 1$  h and after one week of aging at  $40^\circ\text{C}$ .

For all three systems a certain degree of structural ordering of a remaining liquid crystalline phase is observable after homogenisation, leading to the broad peaks at  $\sim q=0.38\text{--}1\text{ nm}^{-1}$ . Like with sample bP490-A, as described above, polydisperse objects start to evolve and grow with the more dilute compositions –B and –C, as can be seen in Figure 3.4.16 (b). Again this effect is observed shortly before/parallel to the evolution of the periodic mesostructure. The growth in diameter and amplitude reaches its maximum at  $t_{\text{pm}}$ . At this point the intermediate phase starts to vanish again in favour of the growth of the highly ordered mesophase. The obtained values for the maximum radius of the particles in Debye's approximation, as well as the lattice parameter at the beginning of the evolution, are very similar for all three compositions. This indicates that the forming micelles follow favourable dimension parameters, most likely for surface energy reasons.

Time-dependent results from Porod fit, Debye fit and fit of the periodic mesostructure are shown in detail in Figure 3.4.16 (a, b, c). The resulting radii from this procedure do not account for a core-shell model as was used, for example, by Soni et al. [13] for the hydrophobic core and the hydrophilic shell of P123 micelles, since we have a more complex system with interactions between silanol groups and the PEO chains of the surfactant. Most likely the radius of the observed objects is connected to the accumulated silica oligomers on the surface or in the shell of spherical P123 micelles that are not part of the original liquid crystalline assembly anymore.



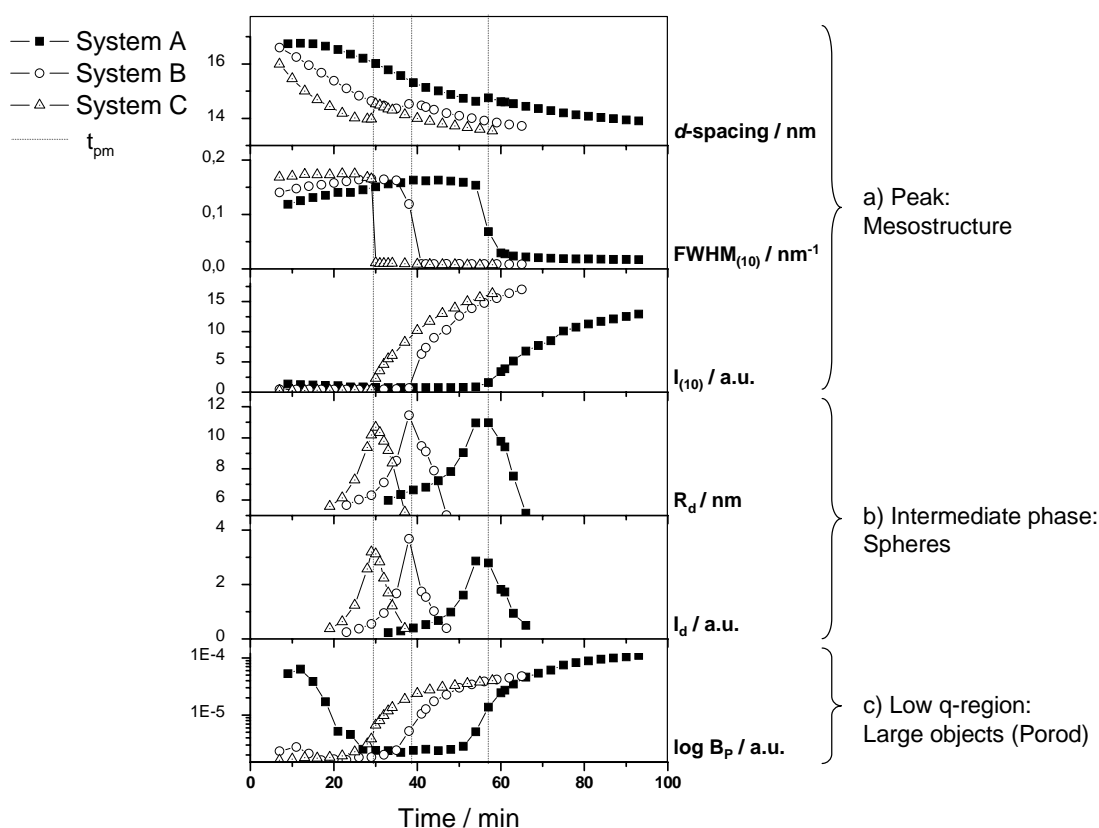


Figure 3.4.16. The time-dependence of best-fit parameters were evaluated for the three systems. Amplitude of the Porod-Fit ( $B_p$ ), amplitude and radius of form factor  $F(q)$  for spheres ( $I_d$ ,  $R_d$ ) and amplitude ( $I_{(10)}$ ), FWHM ( $\text{FWHM}_{(10)}$ ) and position of the “ $d_{10}$ ”-reflex fitted with a Gaussian function are shown from bottom to top. The vertical lines depict the corresponding times at which the periodic mesostructure starts to evolve ( $t_{pm}$ ) and are drawn as guidelines for the eye.

### 3.4.4 Extending the q-region in the scattering experiments: The pure silica network

The formation of a gel, derived from an ethylene glycol modified silane, was followed for a composition of EGMS(Si)/P123/1 M HCl = 48(4.7)/30/70 in the low q-region ( $0.018 < q < 0.6 \text{ nm}^{-1}$ ) at ID02/ESRF. Macroscopically, the system gelled after approximately 65 min. Phase separation, indicated by a colour change to white, was not observed for another 150 min. After aging for one week at 40 °C the gel exhibits three distinct Bragg reflections, which can be indexed according to (10), (20) and (30) and a (11) reflection that is very weak (Figure 3.4.17 (a)). The repeating unit distance,  $d$ , of the aged gel equals 11.74 nm.

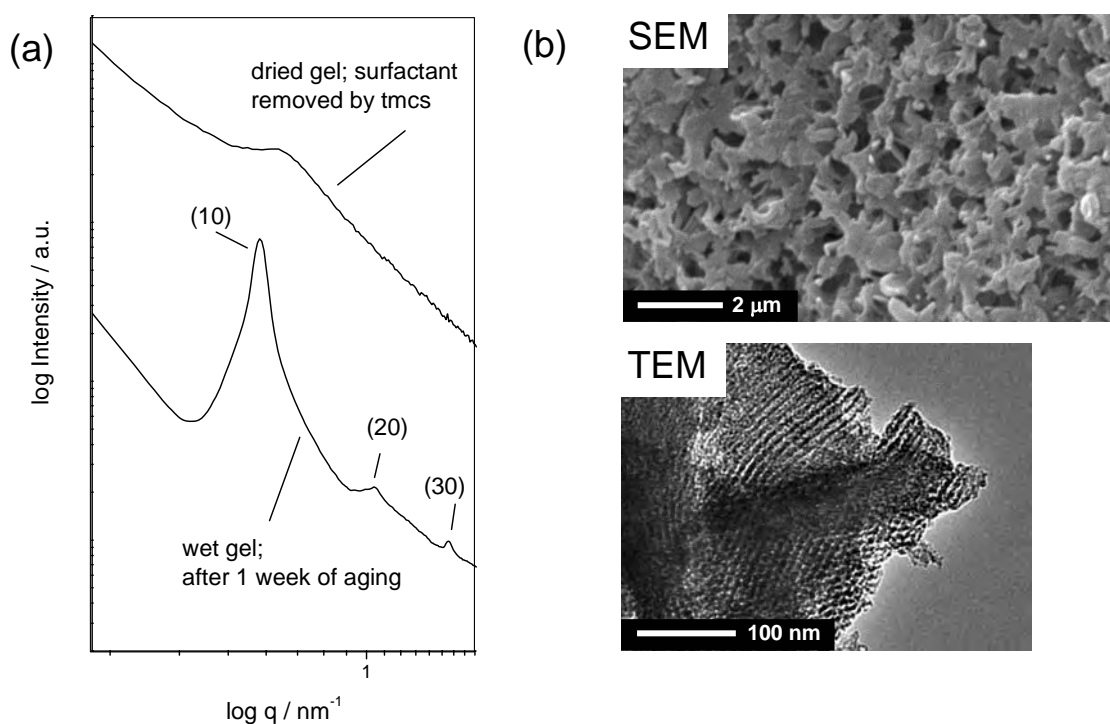


Figure 3.4.17. (a) Small angle X-ray scattering profiles for the dilute EGMS/P123/1 M HCl system after one week of aging and after surface silylation (tms) and drying. For the latter, only one broad reflection could be observed. (b) SEM images show the macroporous network of the dried gel. TEM images reveal regions with highly ordered periodic mesopores but also regions with unordered structure.

After treatment with trimethylchlorosilane, washing with petroleum ether, ethanol and slow heating, the long range order seems nearly destroyed, as can be seen in the SAXS curve of the dried gel (Figure 3.4.17 (a) upper curve). Only one weak peak corresponding to a repeating unit distance of 10.47 nm is visible. However, TEM investigations have shown that the material is inhomogeneous with small domains and regions with less pronounced ordering.

Time-resolved small angle X-ray profiles of the synthesis are depicted in Figure 3.4.18. The evolution of the porous network was followed during a time interval of 7 min up to 140 min after mixing the components, thus stopping prior to phase separation as well as long range order-formation. The broad peak(s) dominating the scattering pattern at the beginning of the measurement were fitted with two Gaussian functions, one for short range order and one for the slowly evolving long range order. The peak resulting in the first reflection of the periodic mesostructure is plotted in Figure 3.4.19 III. The fit data of the latter suggests an increase in intensity 65 to 75 min after homogenisation. This is in accordance with the gelation time of approximately 65 min. Parallel to the increase in intensity, a decrease in  $d$ -spacing and FWHM was observed as shown in Figure 3.4.19.

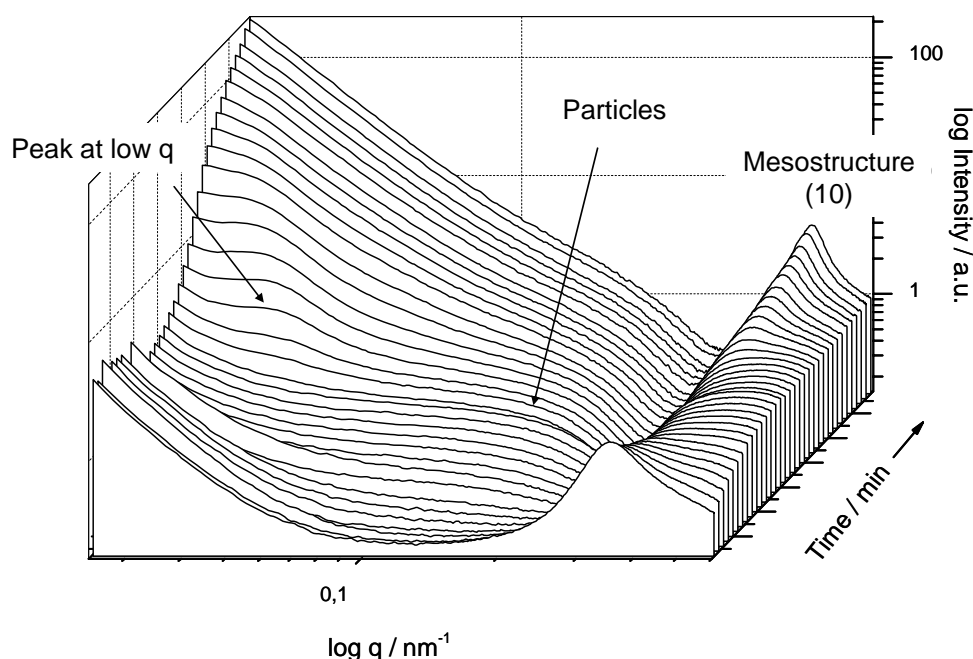


Figure 3.4.18. Time-resolved small angle X-ray scattering measurement of an EGMS/P123/1 M HCl system. Besides the evolution of a periodic mesostructure, again the formation of an intermediate phase is observed. In addition, a peak, respectively, a shoulder starts to evolve at low  $q$ , which shifts to even lower values of  $q$  throughout the synthesis (and leaves the investigated  $q$ -range).

Besides the formation of a periodic mesostructure, again an evolution of disordered objects was found in the SAXS-profiles, equivalent to the previously described intermediate phase in case of the phenylene-bridged precursor. That is, the first twenty minutes of synthesis can be described by a Porod regime and two independent overlapping broad peaks. The fit results depicted in Figure 3.4.19 I show the trend of the evolution of the Porod amplitude over time. The point of gelation is indicated with a dotted line. Parallel to gelation the contribution of large scattering objects starts to increase. After 20-25 min the evolving of a Guinier region with corresponding Porod region was observed in the scattering curves. The Guinier radius,  $R_g$ , estimated from the SAXS pattern at the starting point of the intermediate phase has a value of approximately 6 nm. The resulting fit parameters are plotted in Figure 3.4.19 II (void circles) together with exponent  $n$  of the characteristic slope ( $I \propto Bq^{-n}$ ; full quads). In contrast to the study of the phenylene-bridged system, the fit data does not support a maximum and subsequent dissolution of the phase. This is most likely due to the fact, that no spontaneous transition into periodically ordered cylindrical micelles had occurred at this stage of the synthesis. However, the observed shoulder is growing in intensity as well as dimension. Determination of the equivalent Porod radius,  $R_p$ , after 63 min gives a radius of 8.7 nm. After 58 minutes, an additional bump evolves at approximately  $q = 0.048 \text{ nm}^{-1}$ . This corresponds to a periodic unit distance of  $\sim 130 \text{ nm}$ .

Therefore, the fit of the curves measured 60 to 110 minutes after homogenization, were extended by an additional gaussian function. The fit results describing the shoulder at low values of  $q$  are displayed in Figure 3.4.19 III (void triangles). The position shifts to even lower  $q$  in the course of the experiment, leaving the observed  $q$ -range ( $d > 300$  nm) after approximately 90 min. The evolution of this maximum is a possible indication for the formation of macrostructure.

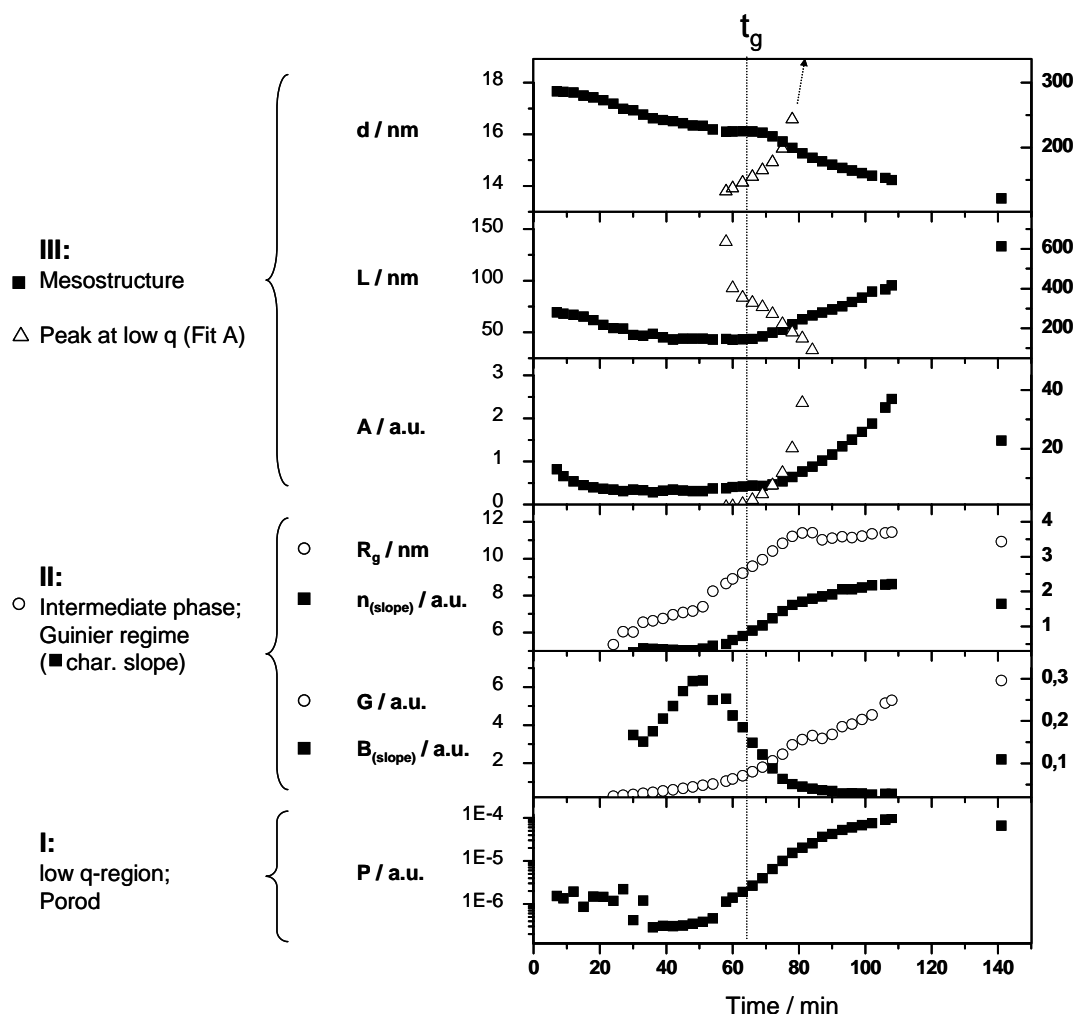


Figure 3.4.19. Fit results for the time resolved measurements of Figure 3.4.18. I: Porod amplitude (P) from the low  $q$ -region of the curves. II (o): Fit amplitude (G) and radius ( $R_g$ ) of the intermediate phase derived from Eq. 2.3). II (■): Fit parameters for the characteristic slope of the intermediate phase fitted according to  $I \propto Bq^n$ . III: Fit amplitude (A), coherence length (L) and repeating unit distance (d) of the peak resulting in the first reflection of the periodic mesostructure (■), and the peak observed at low  $q$  ( $\Delta$ ).

The shoulder evolving at low values of  $q$  after 60 min can also be approximated as second maximum of scattering obtained by spherical particles with a radius of about 132 nm. This attempt is shown in Figure 3.4.20. The experimental curve was taken 63 min after mixing of the components. Both shoulders are clearly visible. Fitting was performed by adding

two contributions of polydisperse spherical particles (Eq. 2.5 combined with Eq. 2.8) and a small Porod contribution. The assigned radii were  $R_1=12\pm 1$  nm and  $R_2=132\pm 20$  nm. The compliance between fit and measured curve is shown in Figure 3.4.20.

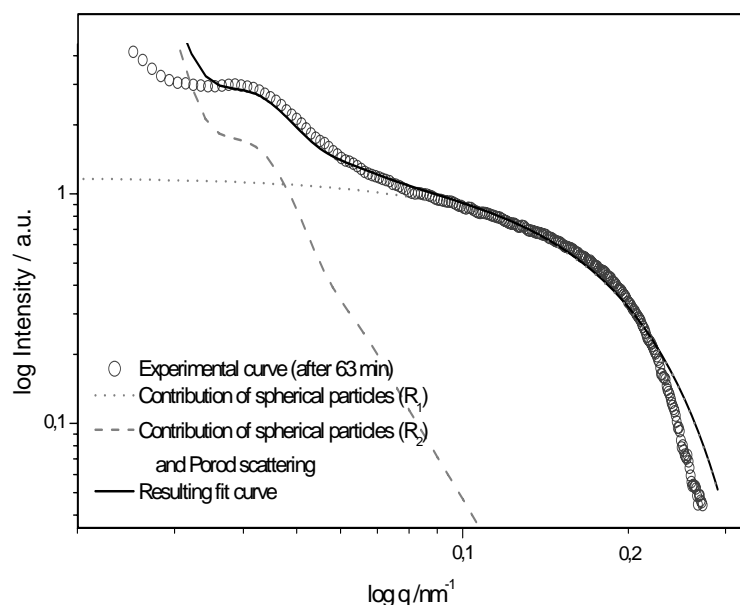


Figure 3.4.20. Experimental curve measured 63 minutes after mixing together with the estimated fit curve (full line). The measured curve was approximated by scattering contributions of two kinds of polydisperse spherical particles ( $R_1=12\pm 1$  nm,  $R_2=132\pm 20$  nm) which are depicted as dotted and dashed lines.

Further *in-situ* SAXS investigations on the low  $q$ -region of the EGMS system are necessary to draw definitive conclusions on the differences and similarities of the formation mechanism of the purely inorganic and the hybrid network. However, as was shown in these experiments, extending the studies to the USAXS-region provides crucial information on the interplay of mesostructure and macromorphology formation.

### 3.4.5 Interpretation

For interpretation of the results it is helpful to look at literature. Several attempts have been made to determine the mechanism of formation for the surfactant-assisted fabrication of mesoporous silicas. Initially, two possible pathways for the formation of M41S materials were proposed by the Mobil group [25, 26]. The first is the ‘(true) liquid crystal templating (TLCT) model’ based on the similarity of the final mesostructures and those of lyotropic liquid crystal phases of surfactant-water mixtures. In TLCT the inorganic material is supposed to enter the aqueous region of a preformed LLC phase, where it condenses, thus copying the organic template. However, most syntheses are carried out at low surfactant concentrations with no liquid crystal phase present in the initial mixture. For conventional

mesoporous silica films and powders initial concentrations of the amphiphiles are typically within the region of the micellar range ( $\sim 3\%$ (w/w) in water) [152, 158]. An exception is the investigation of Attard et al. [36] and, lately, Hanrahan et al. [159], who started with a high surfactant/water concentration already in the LC state. Even with this approach the liquid crystal structure was lost due to the release of alcohol during the hydrolysis of the conventional silica precursor and only reassembled subsequently.

The alternative proposed pathway for the fabrication of periodic mesoporous materials is the ‘micelle assembly model’ [160] or ‘cooperative assembly model’ [38, 161], [27, 162], [31]. Here, the inorganic species interact with the surfactant micelles in solution, in the end promoting a self-assembly into LC-like structures.

For dilute systems the steps proposed for the development of the 2D hexagonal silica-surfactant mesophases derived from non-ionic block copolymers are mainly agreed to be the following: a) hydrolysis of the silicon-alkoxide, b) attractive interaction between oligomeric siliceous species and surfactant molecules leading to the formation of silica-surfactant micelles, c) clustering of poorly condensed silica-surfactant hybrid micelles, d) elongation of the surfactant micelles and parallel formation of domains exhibiting hexagonal order, e) growth of the domains [163]. Yu et al. [33] proposed a colloidal phase separation mechanism for the formation of mesoporous materials, consisting of three phases; the cooperative self-assembly of inorganic/organic composites, secondly the formation of a new crystal-like phase, rich in aggregates of block copolymer/silica species, and thirdly a phase separation of this liquid crystal-like phase from the solution and further growth of solid mesostructures driven by further condensation of silica species. Regarding the gel formation mechanism of organically bridged precursors, first *in-situ* synchrotron SAXS/XRD studies of a mesoscopically ordered biphenylene-bridged organosilica powder with crystal-like pore wall using octadecyltrimethylammonium chloride (OTACl) as structure directing agent were reported by Morell et al. [45]. They found spherical hybrid micelles before nucleation and growth of the mesophase. Parallel to the formation of the mesostructure an ordering of the phenylene moieties in the walls was observed by WAXS.

The glycol-modified (organo-) precursors used in this work do not require a removing of alcohol, which would destroy the LC phase of the template. This allowed a full *in-situ* SAXS investigation on the bimodal pore formation in the monolithic mesoporous materials. For all investigated systems scattering from micelles and a faint structural relation were observed at the beginning of the measurements ( $\sim 3$  to 10 min after homogenization of the components). This is not surprising since the systems start with the structure-directing agent already in or close to the liquid crystalline phase (mixed phase of cubic and hexagonally close-packed spheres). Sattler et al [164] proposed a true liquid crystal pathway for the glycol-modified precursor. However, for the deployed

concentration the resulting materials showed a 2D hexagonal ordering of cylindrical mesopores, therefore the initial liquid crystal structure is not exactly reproduced. From the scattering at low  $q$  it can be concluded that at the beginning of the measurements the components of the system still reorder, the silane precursor molecules are hydrolyzed, water is consumed from the sol and ethylene glycol is released. Although ethylene glycol is compatible with the LC phases, the phase diagram is influenced and the long range order of the supramolecular assembly is partly destroyed. The size of the weakly ordered aggregates can be approximated by calculating the coherence length of the broad peak at approximately  $q=0.38 \text{ nm}^{-1}$  following Eq. 2.13 (lower limit), giving domain dimensions of  $\sim 55$  to  $70 \text{ nm}$  in case of the phenylene-bridged precursor. From investigating the low  $q$  Porod regime it can be assumed that the large building blocks are still dissolving into micellar clusters, micelles and free P123 molecules.

Following this dissolution process, a characteristic slope evolves in the measured SAXS curves, which can be interpreted as an intermediate phase, consisting of particles that are most likely spherical to cylindrical. Although the characteristic slope could not be monitored in detail for all systems, because of the  $q$ -range included in the measurements ( $q \geq 0.2 \text{ nm}^{-1}$ ), a corresponding increase in scattering intensity was observed at low  $q$  ( $\sim 0.22 \text{ nm}^{-1}$ ), not only for all investigated phenylene-bridged gels, but also in the case of the pure silica networks synthesized under acidic conditions. The characteristic slope may be explained by the formation of spherical particles with a maximum radius of  $11 - 12 \text{ nm}$ . The diameters of P123 micelles in the initial LC phase of P123 in water, which were calculated in Chapter 3.4.1 are approximately  $18.4 - 20 \text{ nm}$ , depending on pH. The size of the P123 micelles and the obtained values from fitting the scattering intensity of the intermediate phase are therefore very close. This suggests that the observed ‘particles’ correspond to a new kind of block copolymer micelles, which predate and induce the formation of the final long cylindrical micelles, respectively.

Furthermore, it can be concluded from the fits that these objects (intermediate phase) start to grow in number and diameter prior to the establishment of long range order of the evolving mesopores. In case of the phenylene-bridged systems the intensity and the fitted radii reached a maximum at the time the first reflection of the periodic 2D hexagonal structure starts to evolve.

One possible explanation is that P123-micelles dissociate from a residual LLC phase and Si-oligomers are subsequently adsorbed on the surface. However, the radius initially observed for the evolving structure ( $\sim 6 \text{ nm}$ ) seems very small compared with the radius of single P123 micelles in solution ( $8-9.5 \text{ nm}$ ) (compare Chapter 3.4.1, [13, 155]). A more plausible interpretation, supported by literature, is that the P123 molecules reorganize inside a newly formed P123/Si-oligomer-rich phase. It is known that there is a strong

attractive interaction between the silanol groups of partly condensed silica oligomers and the EO units of the block copolymer ([52, 154]. By bonding to the silanols with the ether oxygens, the surfactant molecules hinder Si-O-Si bond formation. Due to the high attraction between silica oligomers and EO units, it is very likely that a new phase forms, which is rich in silica and surfactant. This phase separation has been reported to proceed by spinodal decomposition. One feature of spinodal decomposition is that there is no distinct interface in the initial stages, and that the contrast in chemical composition develops continuously. This may explain the fact that no growth of silica/surfactant-rich regions was observed in the *in-situ* SAXS experiments in the low  $q$ -region. As the concentration of silica oligomers and surfactant micelles/molecules increases in the new phase, the system reaches the stage at which new surfactant micelles are formed (critical concentration), which are visible in the measurements as intermediate phase. These grow to a critical size of approximately 11-12 nm as phase separation proceeds, and finally, at a critical concentration and/or size, collapse into periodically arranged cylinders. At this point the macroscopic phase separation is already advanced in the phenylene-bridged system ( $t_{ps} < t_g$ ), and therefore, determines the size of the macroscopic domains.

Takahashi et al. [154] report that the radius of gyration can be interpreted as a measure of the degree of macroscopic phase separation. In this case the intermediate phase could denote fluctuations prior to spinodal decomposition, consisting of small Si-oligomers connected by P123 molecules via hydrogen bonds. After reaching a critical coherence length, the phase separation proceeds very fast, therefore no real “growth” of the macroscopic domains is observable.

### **3.4.6 Development of macromorphology in the phenylene-bridged network**

As described in Chapter 1.3.3, the macroporous network develops due to a phase separation into silica-surfactant rich and solvent-rich areas. At some point the system is frozen in by the sol-gel transition. The onset between these two processes as well as the concurring mesostructure evolution determines the final macromorphology of the network. For the investigated phenylene-bridged systems, bPh490-A to C, the colour changed from transparent to turbid ( $t_{ps}$  in Table 3.6) shortly before long-range order became visible in the SAXS measurements. In contrast to the systems investigated at Elettra (Chapter 3.4.2) gelation was observed after phase separation and mesostructure formation. The SAXS patterns of the wet gels prepared with different Si/ $10^{-2}$  M HCl ratios after one week of aging at 40 °C are shown in the topmost curves in Figure 3.4.15. In all three systems the peaks relate to a hexagonal ordering of the mesopores with a  $d_{10}$ -spacing of ~11.9 nm. A



lower limit for the coherence length  $L$  was estimated from the first reflections (sample detector distance of 10 m at ID02) according to Eq. 2.13.

In samples bPh490-A and bP490-B the coherence length for the liquid crystalline domains at the start of the kinetic measurements was found to be approximately 55-70 nm. The broadness of the peaks increases continuously until the point, where the periodic mesostructure starts to form. This transition results in large domains with hexagonally ordered cylindrical mesopores.

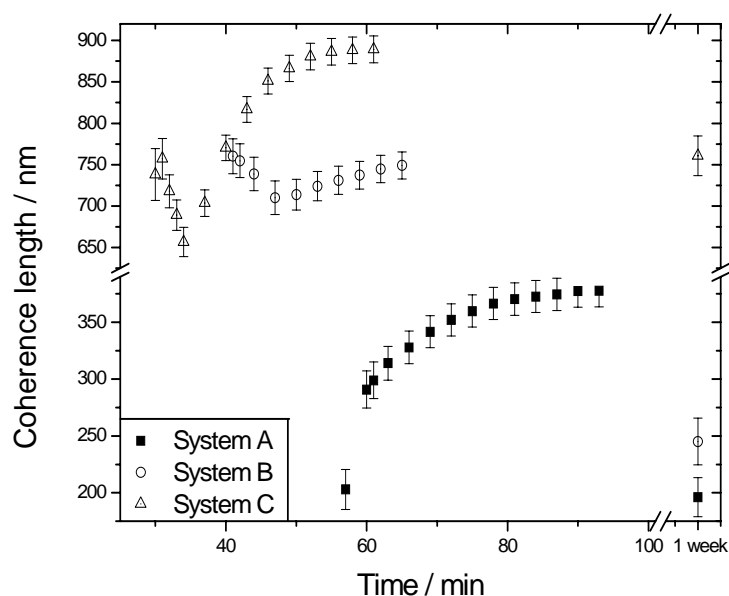


Figure 3.4.21. Calculated coherence lengths during the evolution of the mesostructured domains and the macroporous network taken from the *in-situ* data starting with the first appearance of the Bragg reflections, plus the values derived from the wet, aged gels (after 1 week).

From the estimated size of the coherent regions at the point of mesostructure formation, one can see that the domains exhibiting periodical arrangement are already very large at or shortly after phase transition. In system bPh490-A, where mesostructure evolution and sol-gel transition take place more slowly compared to the more diluted systems, the estimated domain size is approximately 200 nm at the beginning of structure formation and increases to as much as 380 nm during the following 30 min. In system bPh490-B and bPh490-C the contributing regions measure approximately 750 nm right from the start. The coherence length increases during the course of synthesis. This is shown in Figure 3.4.21. Fitting was performed using Mathematica. Surprisingly, we find much lower values for  $L$  in case of the aged gels. This is especially true for the system bPh490-B, where the loss in domain size is as large as 67%. In system bPh490-C a relatively small loss in coherence length (~15%) is found, which can be explained by shrinkage of the periodic structure from a

lattice parameter  $a=15.6$  nm, 55 min after mixing, down to  $a=13.7$  nm (12%) after one week of aging. The loss of domain size in the aged gels is probably caused by micro-cracks or boundary regions, respectively, and is most pronounced in system bPh490-A and bPh490-B, where the final network consists of smaller parts and therefore has more contact areas between different domains.

#### Macromorphology of the Resulting Dried Gels

Concerning the macrostructure we found in the SEM-images spherical to oblate structures with dimensions of 250 nm to 500 nm for bPh490-A, and disc like structures with dimensions of approximately 450 nm thickness and disc diameters up to 2  $\mu\text{m}$  for bPh490-B. For the even more diluted composition in case of bPh490-C, the thickness of the discs increases to approximately 550 nm and the diameters of the platelets become larger up to 5  $\mu\text{m}$ . Scanning and transmission electron microscopy images of the macromorphology of the aged and dried gels are shown in Figure 3.4.22.

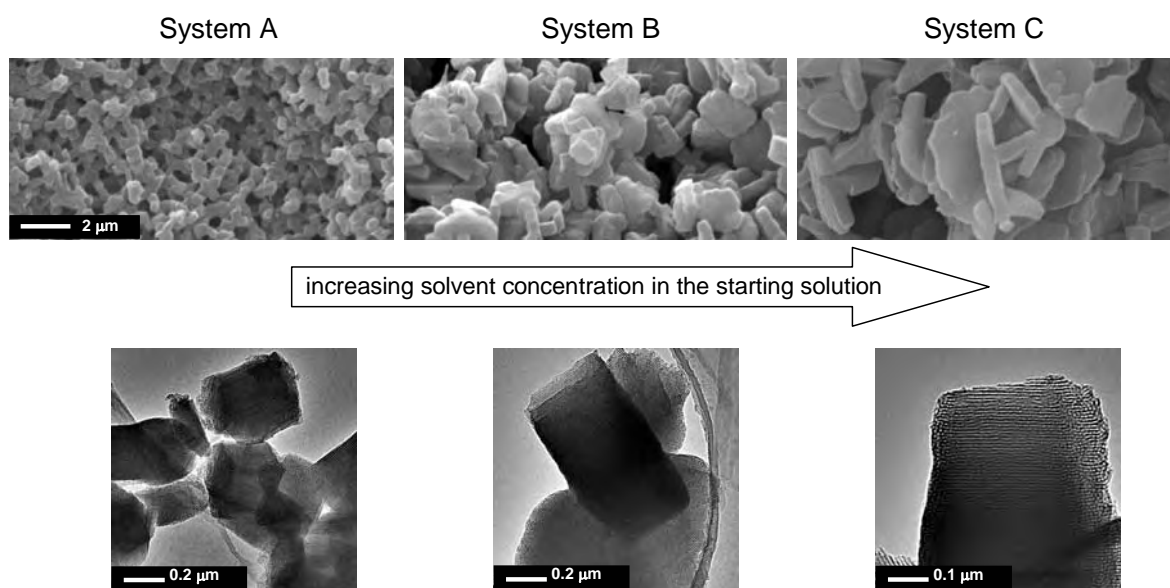


Figure 3.4.22. SEM and the corresponding TEM images of the three investigated phenylene-bridged systems. With increasing dilution, the interconnected parts building up the network become more and more disc-shaped. As the macroscopic dimensions (diameter of the discs) increase at larger dilution, the FWHM of the Bragg  $d_{10}$  reflection becomes smaller, in accordance with an increase in the mean size of coherent regions.

The morphologies of the mesoporous materials are developed after evolution of silica/surfactant-rich regions and are mainly influenced by the competition between the free energy of mesostructure self-assembly ( $\Delta G$ ) and the colloidal surface free energy ( $F$ ) [33]. When phase separation occurs quickly,  $\Delta G$  is dominant and the macrostructure of the mesoporous material is developed together with the formation of the mesostructure.

Therefore, resulting morphologies will have smaller curvatures, resulting in e.g. rods or platelets as found for the systems investigated in this work. Experimental conditions that increase the induction time for the phase separation such as lower temperature or smaller solvent content lead to morphologies with higher curvature (small surface) such as spheres (bPh490-A).  $F$  enforces the optimal trade-off between volume and surface of the resulting particles. Whether the final morphology is more spherical or more regular is furthermore governed by the balance between the polymerization of the inorganic species and the rate of the mesostructure formation [165]. Nevertheless, an internal structure with long range order, such as 2D hexagonal mesopores, will force the particles to adopt a corresponding form.

A further requirement for the formation of a highly ordered mesostructure is that the polymerization rate has to be slow compared to the self-assembly on the molecular level. For the hybrid networks derived from the phenylene-bridged precursor, the macroscopic network was found to consist of platelets with resemblance to hexagonal prisms. From sample bPh490 A to sample C the ratio between ‘diameter’ and thickness increased with increasing dilution.

#### *In-situ* SAXS observations on the macromorphology development

In principle, the process of network formation should be visible in the low- $q$ -range (USAXS). For the  $q$ -range ( $0.018 < q < 0.6 \text{ nm}^{-1}$ ) employed in the experiments on bPhGMS-systems at ESRF, no growth of macroscopic structures could be observed. This can be explained by a spontaneous phase separation into regions larger than 100 nm, respectively a spinodal phase separation, where suddenly a sharp interface/contrast is achieved. For the accessible  $q$ -range in the experiments, only objects with dimensions up to approximately 100 nm are identifiable through their characteristic Guinier slope. This was already shown in Chapter 2.3.1 for simple spherical, cylindrical and disc-shaped scattering objects. For polydisperse systems, the minima and maxima in the scattering curves are smeared out beyond recognition leaving only the characteristic slope in the low  $q$ -region and the following  $q^{-4}$ -decrease in the Porod region. This was demonstrated in Figure 2.3.2 (b) for discs (Eq. 2.7) with a mean thickness of 300 nm. Polydispersity is taken into account by assuming a Gaussian size distribution in Eq. 2.8.

Obviously the  $q$ -range observed in the experiments, did show a  $q^{-4}$ -behaviour, but did not include the Guinier regime of the macroporous network. Therefore, it is at the moment not possible to make any statements on the macroscopic structures during the formation of the macroporous network. Nevertheless, due to the emergence of minima and maxima in the low  $q$ -region during the formation process (pointing towards a very narrow size

distribution), it is possible to derive some conclusions, such as the dimensions of the scattering objects and their polydispersity.

The macrostructure of the dried gels is known from SEM and TEM investigations (see Figure 3.4.22). In systems bPh490-B and bPh490-C the resulting interconnected particles forming the macroporous network are very similar to discs, for which the radius,  $R$ , (or diameter, respectively) is large compared to the height,  $H$ . Therefore, the analytical expression for the form factor of bilayers (Eq. 2.7) was used for fitting [166], assuming that  $R$  is large and does not contribute. A Gaussian distribution was used to describe the polydispersity of thickness,  $H$ , and thus damping of the oscillations in the experimentally obtained scattering data of the platelets (see Eq. 2.8):

$$I(q) = A \frac{2\pi}{q^2} \int_{\bar{H}-3\sigma}^{\bar{H}+3\sigma} H \left( \frac{\sin(qH/2)}{qH/2} \right)^2 \frac{1}{\sqrt{2\pi}\sigma} \exp\left(-\frac{(H-\bar{H})^2}{2\sigma^2}\right) dH, \quad (\text{Eq. 3.4})$$

$\bar{D}$  is the mean thickness of the disc-shaped object and  $\sigma$  is the standard deviation.

The resulting values for thickness  $H$  are given in Table 3.7 for the aged gels, together with their size and the time of their first appearance during synthesis. During the kinetic measurements, periodic features in the low  $q$ -range of the SAXS data can be seen approximately 10 min after evolution of the sharp Bragg reflections of the hexagonally ordered cylindrical mesopores, but only in bPh490-B and bPh490-C. Thickness ( $H$ ), resulting from the fit according to Eq. 3.4, is already large with 585 nm or 593 nm for the two systems, respectively. The values obtained for bPh490-A have to be handled with care, because the periodic minima and maxima are very weak compared to the other two compositions. Furthermore, the structure is more spherical than disc-shaped. Periodic minima and maxima are most pronounced in the highly diluted system (-C), which consists of large platelets as already shown in the SEM images.

The estimation values for thickness are only rough due to idealistic assumptions of the model and do not fully agree with the dimensions found in the SEM and TEM images ( $H=450-550$  nm) of the dried gels. In accordance to the results of the SEM/TEM images, the platelets in system -C are thicker than in -B. The intensity increases upon aging, whereas  $\sigma$  becomes smaller. Deviation between fit results and the values evaluated from the SEM/TEM images of the final dried gels may furthermore be caused by shrinkage during the drying process. Larger differences are found for system -B due to the applied model, which is not fully accounted for ( $R \sim H$ ).

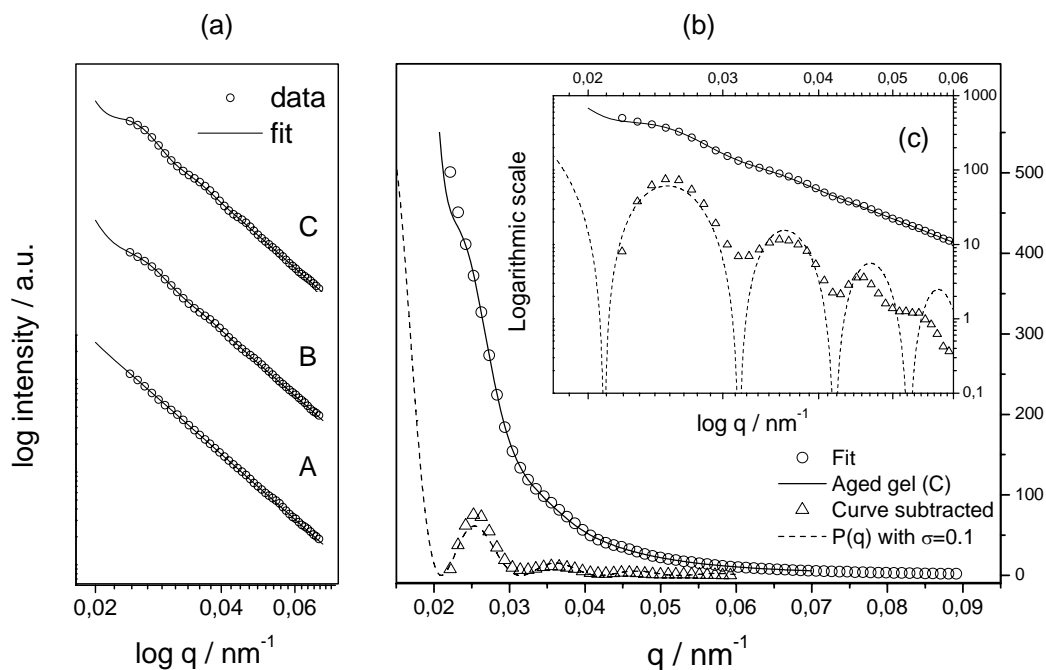


Figure 3.4.23. In the low  $q$ -region of the scattering curves, periodic minima and maxima were observed for the aged gels. This feature is most pronounced for bPh490-C and was assigned to the macroscopic parts forming the inorganic network. (a) Low  $q$  region of the aged, wet organo-bridged gels with periodic minima and maxima observable for system bPh490-C and bPh490-B. (b) Scattering curve of system bPh490-C with the corresponding fitted curve. For the dashed line  $a \cdot q^{-n}$  was subtracted from the original data to enhance the visibility of the “wiggles”. The overlaid triangular points correspond to the form factor for bilayers with a very small thickness-distribution ( $\sigma=0.1$  nm). (c) Both curves from (b) in logarithmic scale.

Table 3.7. Parameters obtained by fitting the form factor of discs to the aged, as well as, just synthesized P123/bPhGMS/ $10^{-2}$  M HCl systems (bPh490 A to C). The radius of the discs, with a thickness ( $H$ ) and a standard deviation ( $\sigma$ ), was assumed to be infinite. The appearance of the periodic features in the *in-situ* measurements was observed after the mesoscopic phase transition.

System	Aged gels			Evolution during sol-gel process			
	Amplitude (A)	Thickness (H) / nm	$\sigma$ / nm	Amplitude (A)	Thickness (H) / nm	$\sigma$ / nm	Evolution time after mesostructure formation (start) / min
(bPh490-A)*	0.0169	564	133	-	-	-	-
bPh490-B	0.01	570	83	0.0015	585	97	approx. 10 (53)
bPh490-C	0.0074	596	76	0.0012	593	84	approx. 10 (43)

\*) Results for the fit-parameters for system A have to be accepted with reservation since no distinct minima and maxima are observable. Also the macrostructure of the system does not exhibit the distinctive disc-shape.

The appearance of periodical features at small  $q$  observed in the synthesis of phenylene-bridged gels indicates a high monodispersity of the evolving macroporous network components. This effect is most pronounced in the diluted system bPh490-C, where the time between the evolution of first Bragg peaks of the periodic mesostructure and the observed gel time is longest.

### 3.5 Interplay of mesostructure and macromorphology

#### 3.5.1 Morphology derived from the ethylene glycol-modified precursor

Sample E802-C: The 3D inorganic spiderweb gel network of sample E802-C, with a composition of EGMS(Si)/P123/1 M HCl = 82(8)/30/110 (w/w), consists of rods that vary in length and diameter and spread radially from joints. The SEM and TEM images discussed in the following are representative for most samples obtained from the ethylene glycol-modified precursor in this work. As can be seen in the TEM-survey (Figure 3.5.1, right) the skeletal structure of these rather compact and straight rods is interspersed with thin, sometimes bent strands or thin rods, respectively.

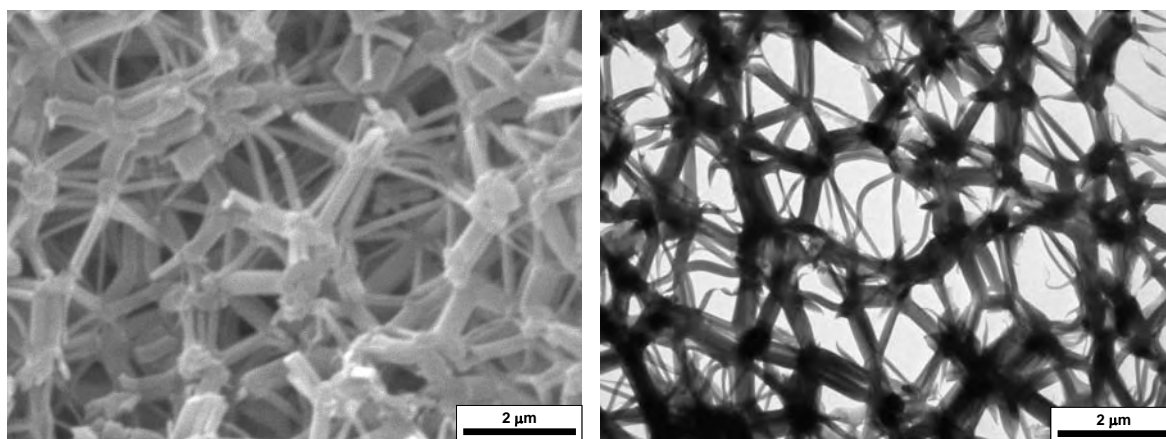


Figure 3.5.1. Scanning electron microscopy image of the inorganic, macroporous network of E802-C (left) and a transmission electron microscopy image of the same sample (right) depicting bent strands additionally connecting the joints.

Occasionally regions with huge junctions are found, with almost parallel rods emerging from the junctions. The length of the strands is as large as 1.9 μm and the thickest rod found has a diameter of about 640 nm. As seen in Figure 3.5.2 the rods, as well as the strands, consist of hexagonally bundled long cylindrical mesopores. The pore diameter from the TEM-images is 7.5 nm. N<sub>2</sub>-sorption/BJH measurements give a pore diameter of 9.5 nm in adsorption. Due to the hexagonal arrangement, one can observe rods with partly faceted cross-section. In all observed rods and strands the mesopores run parallel along the long axis. Most rods exhibit a non-mesoporous wall surrounding the periodically arranged cylindrical mesopores with a depth of approximately 17-20 nm (see Figure 3.5.2).

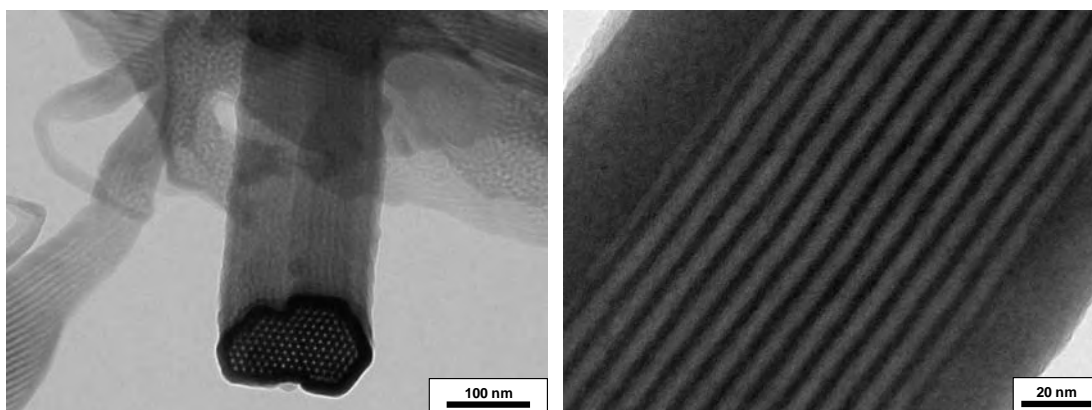


Figure 3.5.2. Hexagonal arrangement of the long cylinders perpendicular to the long axis of the rods.

At the joints, the pores are disordered, but possess a preferential orientation, as seen in the fast Fourier transform (FFT) (Figure 3.5.3). The joints consist of variable amount of converging rods (2 or more). Some rods seem to bend in the joint, without losing the pore distance and pore diameter (Figure 3.5.3 (b)). However, at the turning point the pores are disordered. A preferential orientation is only perceptible from the FFT. In conclusion, the final gel consists of long rods with high aspect ratio and disordered but textured worm-like mesopores at the junctions of the rods.

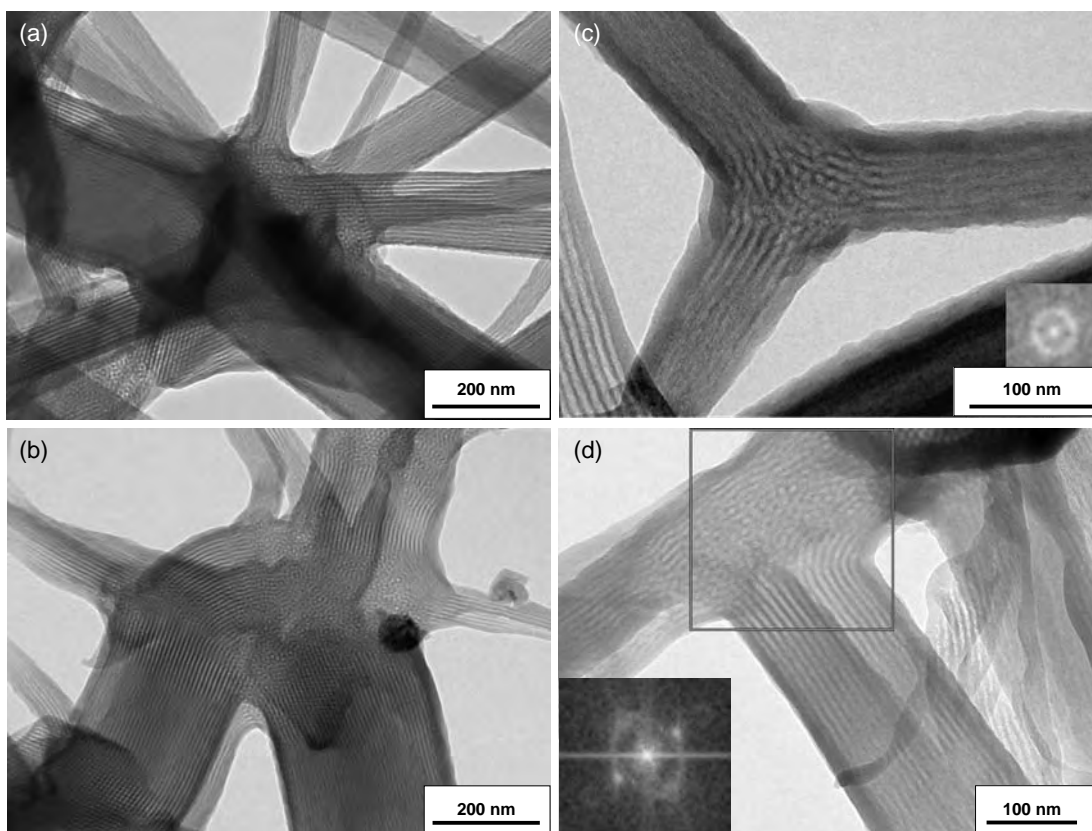


Figure 3.5.3. Different kinds of joints in the EGMS-derived rod-network.



### 3.5.2 Morphology in the phenylene-bridged systems

Figure 3.5.4 shows a typical macromorphology derived by the phenylene-bridged precursor (composition: bPhGMS03(Si)/P123/10<sup>-2</sup> M HCl = 83(5.8)/30/110), consisting of connected near spherical particles with sporadic strands in between different joints. Upon closer examination the near spherical particles from the SEM images turn out to be short thick rods with a diameter varying from 100 to 600 nm.

Sample bPh580-C:

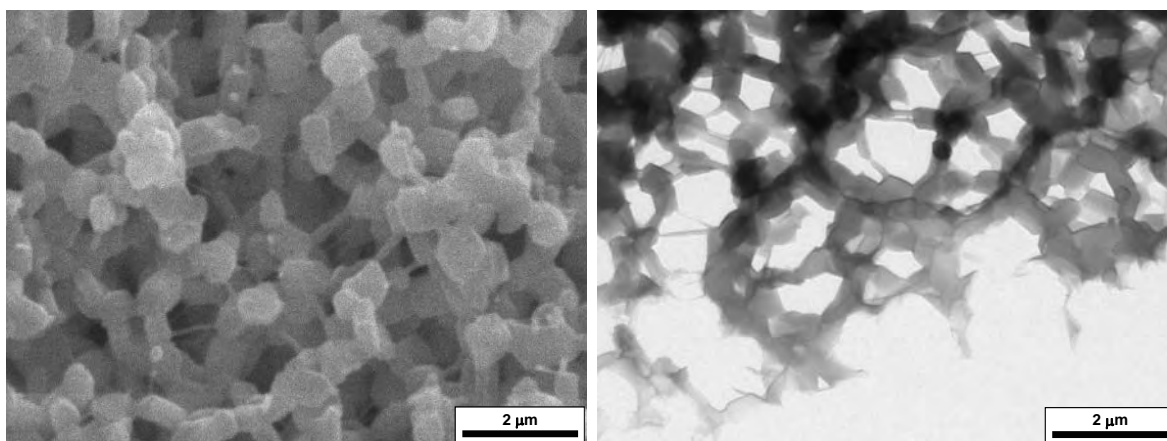


Figure 3.5.4. Typical macromorphology of the hybrid network derived from the phenylene-bridged glycol-modified precursor imaged by SEM (left) and TEM (right).

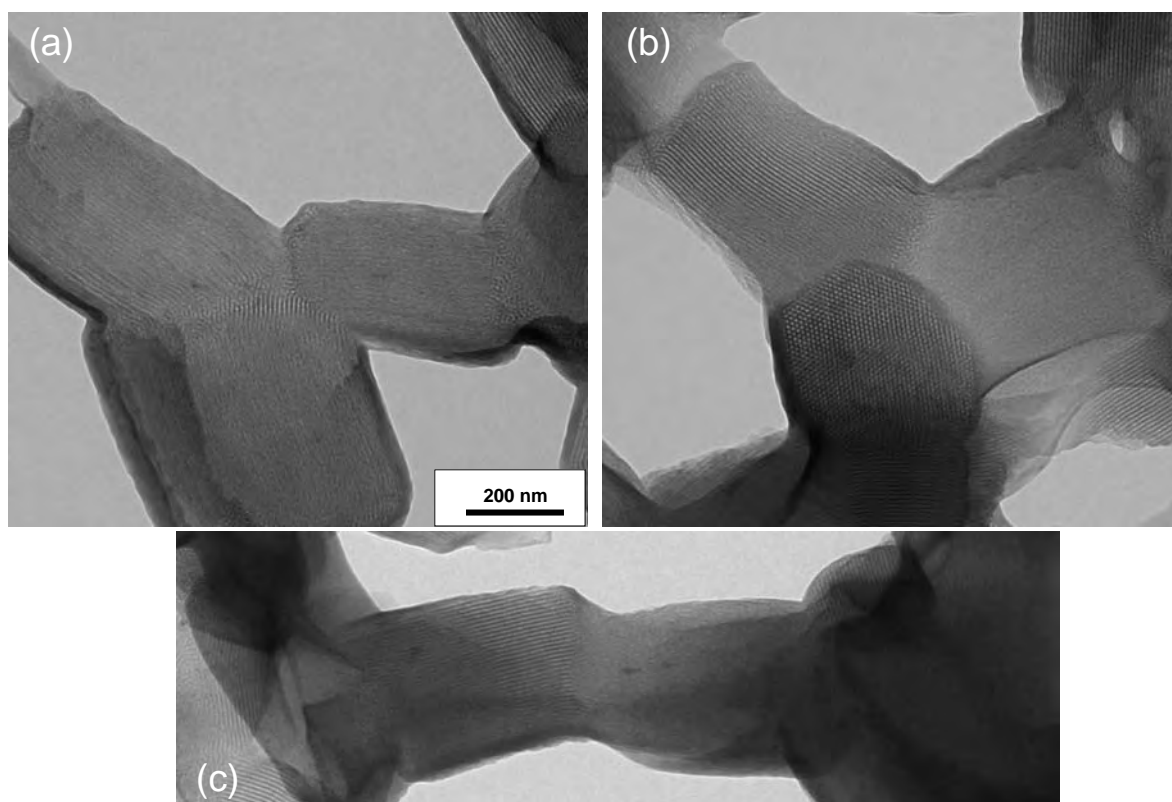


Figure 3.5.5. (a)-(c): Different joints observed in the phenylene-bridged network.

Again the cylindrical mesopores are arranged hexagonally and run along the long axis of the rods. Differently to the already described EGMS-rod structure, the hybrid network seems more particulate, also seen at the junctions which show displacement (e.g., Figure 3.5.5 (c)). This suggests that the rods form separately and join at a later stage. The mesopores at the joints may bend, turn by  $180^\circ$  (loops) or loose their organisation.

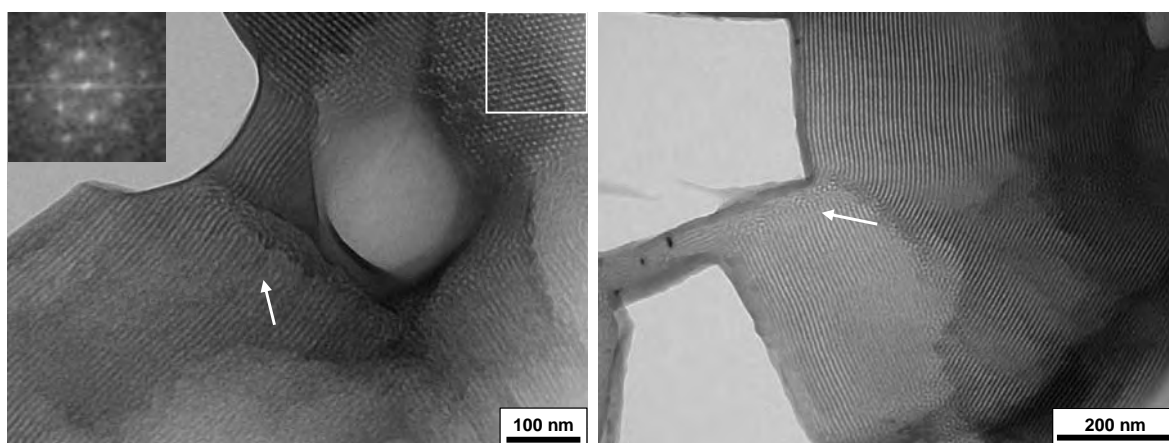


Figure 3.5.6. Interface between the particles forming the network. The arrows indicate the loops made by the mesopores at the end of the particles.

Sample bPh490-B (for structure evolution see Chapter 3.4.4):

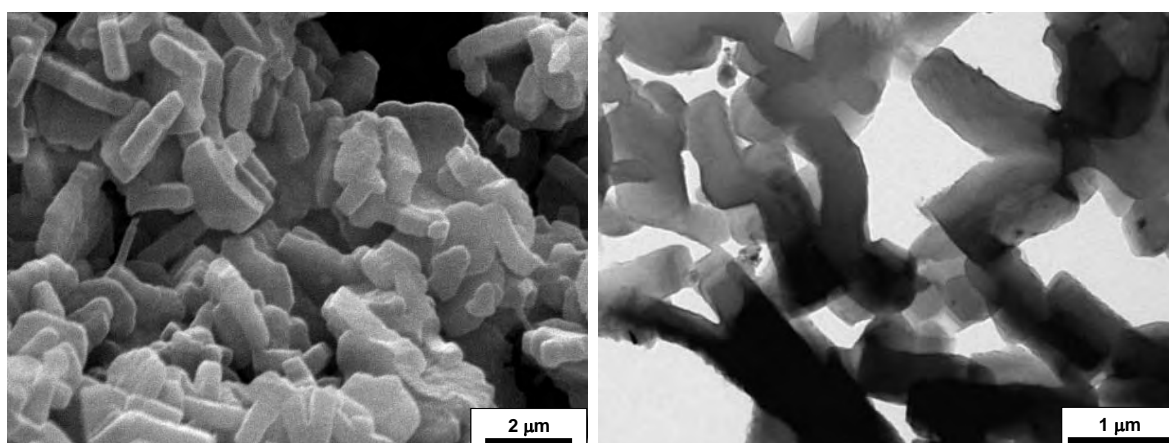


Figure 3.5.7. Hybrid network derived by the phenylene-bridged precursor consisting of interconnected disc-like particles.

As an example for the hybrid networks build-up of disc-shaped mesoporous particles investigated at the synchrotron facility ESRF, sample bPh490-B is shown in Figure 3.5.7 (composition: bPhGMS(Si)/P123/ $10^{-2}$  M HCl=48(4.9)/30/90). The platelets have a

thickness of approximately 330-440 nm ( $H_{\max} \sim 700$  nm) and are built-up of hexagonally arranged cylindrical mesopores oriented perpendicular to the disc-plane. Hereby, the diameter and the thickness of the platelets seem to be correlated (smaller diameter – smaller thickness and vice versa). The TEM images depict a high degree of periodicity and uniform pore structure. The platelets form hexagonal prisms. After inspection of the orientation of the mesopores within the platelets, we can conclude to the correspondence of structure and habit as in crystals (Figure 3.5.8 (a)).

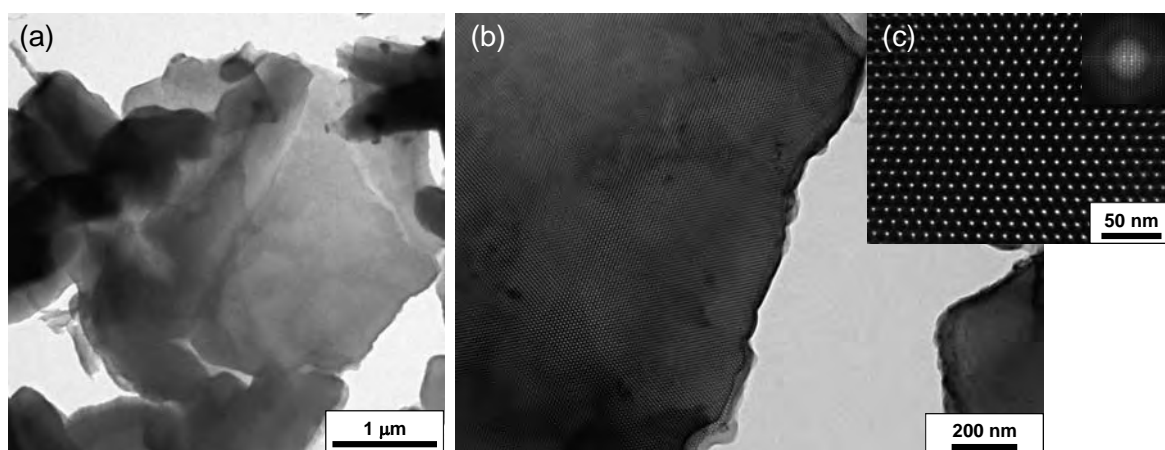


Figure 3.5.8. (a) The TEM overview of the platelet shows that its shape reminds of a regular hexagon; (b) and (c): At higher magnification the highly regular arrangement of the mesopores perpendicular to the disc-plane is clearly visible.

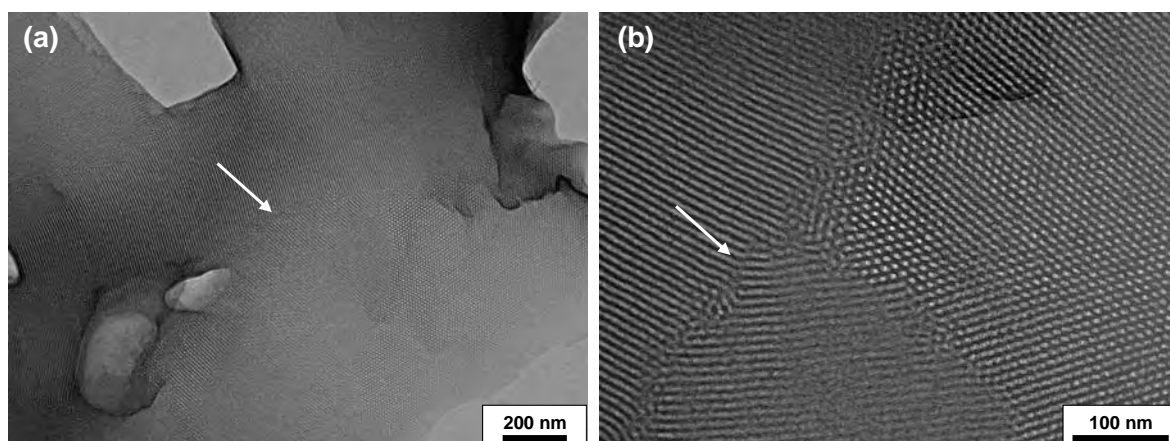


Figure 3.5.9. (a) In the network built up by discs comparatively sharp interfaces between the particles can be observed. The mesopores again make loops at the boundary. (b) However, also pores bending into the next disc are present.


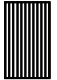

Concerning the junctions of the platelets the same applies as for sample bPh580-C, namely, the single plates seem to have developed separately. This is corroborated by the

rather sharp interface, although, as shown in Figure 3.5.9 (b) mesopores are also able to bend into the next disc. Large unstructured mesopore regions as found, e.g., in the joints of the EGMS-system (E802-C) cannot be seen.

### 3.5.3 Proposed growth model

All three with TEM investigated systems in principle form similar networks consisting of rods but with very different aspect ratios (given in Table 3.8). This leads to long thin rods (sample E802-C), short thick rods (sample bPh580-C) and disc-shaped “rods” (bPh490-B). The rods in turn are made of 2D hexagonally arranged cylindrical mesopores with their z-axis parallel to the “long” axis of the rods already indicating different growth models. Apart from the different aspect ratio, the junctions between the particles differ significantly between EGMS and bPhGMS samples. EGMS samples show interparticle junctions with a core of disordered but textured worm-like mesopores. The observation of worm-like mesopores is in agreement with Yu et al. [33] who report worm-like structures prior to periodic ordering. Phenylene-bridged samples show relative sharp interfaces. The lower the aspect ratio the lower was the content of disordered mesopores at the junctions.

Table 3.8. Lattice constant  $a$  (SAXS), mesopore diameter  $D^{\text{BJH}}$  ( $\text{N}_2$ -adsorption) and pore wall thickness  $t_{\text{wall}}$  of the investigated gels.

Sample	Formation			Mesostructure			Macromorphology
	$t_g /$ min	$t_{ps} /$ min	$t_{pm} /$ min	$a /$ nm	$D^{\text{BJH}} /$ nm	$t_{\text{wall}} /$ nm	Aspect ratio (spot checks from TEM)
E802-C	60- 70	90- 100	110	13.7	6.8	6.9	20:1 - 5:3 
bPh580-C	30- 40	30- 40	30- 40	12.5	7.5	5.0	7:1 - 1:1 
bPh490-B	45	39	39	12.9	7.7	5.2	1:5 - 1:6 

In Figure 3.5.10, the evolution of the structure formation process of a system very similar to E802-C (E802-B) and bPh490-B is shown measured with synchrotron SAXS (Elettra, ESRF). For better comparability the intensity of the (10)-reflection as well as the increase in intensity at  $q=0.22 \text{ nm}^{-1}$ , corresponding to the intermediate phase as was described in Chapter 3.4.3, is depicted over time. In both systems an increase and decrease of the latter intensity was observed. As discussed in Chapter 3.4.3, the slope visible at low  $q$  belongs to

the scattering contribution from disordered particles or fluctuations that accompany the mesostructure formation. This suggests that both materials grow from a disordered intermediate phase which dissolves at the moment of mesopore formation.

The time at which mesostructure starts to form is much longer in case of the EGMS-system. In the bPhGMS system phase separation, mesostructure formation and gelation take place much faster and more or less parallel, probably due to interactions of the phenylene moieties. This interplay leads to gel-networks with low aspect ratio such as thick rods (bP<sub>H</sub>580-C) or platelets (bPh490-B). The amount of worm-like pores at the particle junctions decreases with the aspect ratio, i.e. with the formation velocity.

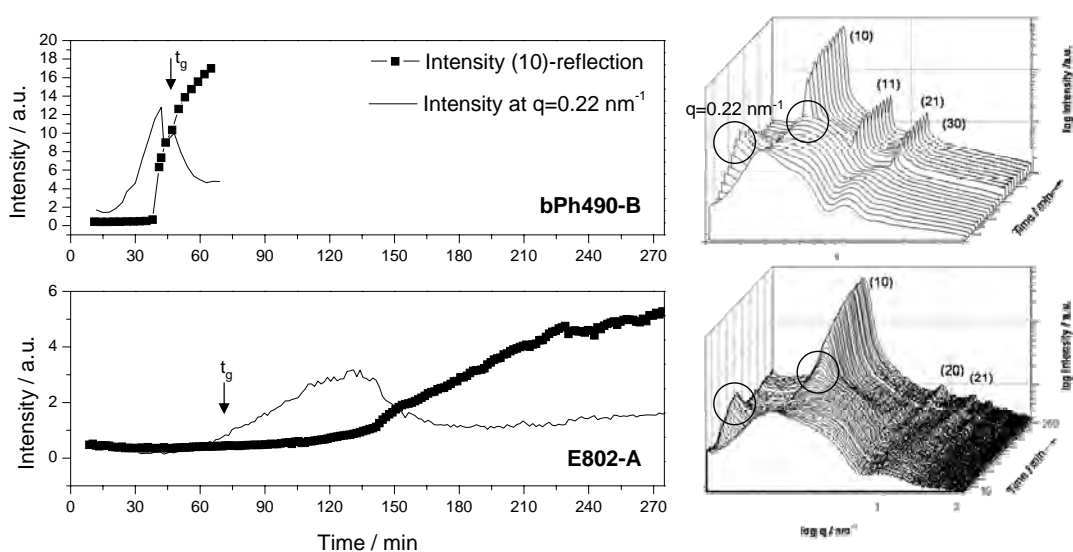


Figure 3.5.10 Comparison between structure formation of an EGMS-derived system (similar to E802-C; bottom) and a bPhGMS system (bPh490-B; top) from *in-situ* synchrotron SAXS investigation.

For the two examined systems, in the EGMS-system the relatively early time of gelation ( $t_g$ ) compared to mesostructure formation and phase separation is noticeable. This could provide a possible explanation for the interconnected mesopores in the junctions of the EGMS network, namely, that a loose-knit inorganic network is already present at the time the mesostructure evolves. In contrast, phase separation in the bPhGMS-system, noticeable as colour change from transparent to turbid, occurs prior or parallel to gelation, leading to a more particulate network. Furthermore, the increase in hydrophobicity of the precursor due to the bridging phenylene groups is likely to enhance phase separation and surface optimization to the point of lower aspect ratios and larger volumes. Whereas the macromorphology observed for the two precursors differs significantly, the mesostructure proved to be identical, aside from small deviations in pore diameter and wall thickness.

### 3.6 Mechanical properties of the hierarchically structured monolithic material

#### 3.6.1 Instrumented indentation tests

The mechanical stability of ordered mesoporous silica can be characterized by the elastic modulus and depends on the structure and on the silica consolidation in the pore walls. A more complete consolidation leads to a more rigid structure and is influenced by both the synthesis condition and the post-synthesis treatment, such as drying rates and temperature. The gels investigated in the following have been either silylated with trimethylchlorosilane (denoted as -tms) and slowly heated up to 120 °C, dried by supercritical fluid extraction with carbon dioxide or methanol as supercritical fluid (denoted as -scd(scf)) or dried in air (maximum temperature 55 °C, denoted as -d). The first two treatments extract the block copolymer template and allow for non-destructive drying. Depending on the post-synthesis treatment the condition of the gel surface as well as the condition of the pores is changed.

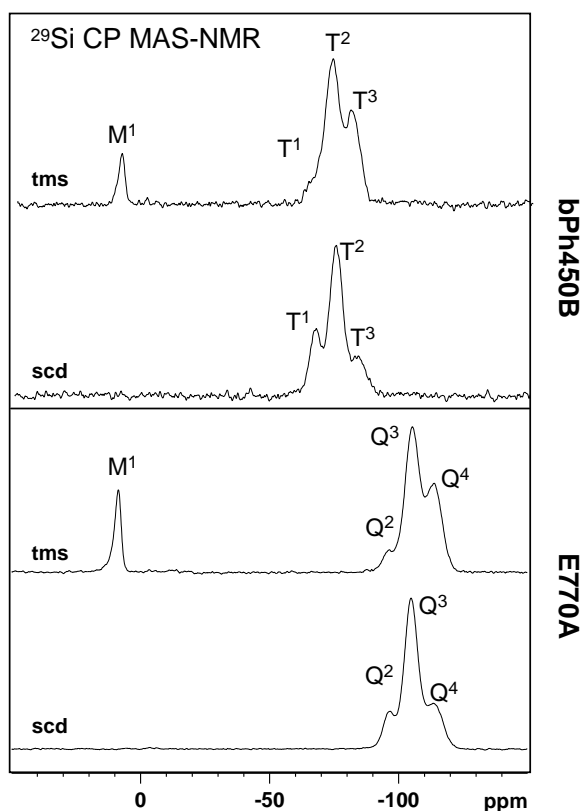


Figure 3.6.1.  $^{29}\text{Si}$  CP-MAS NMR spectra of the EGMS derived “pure” silica gel E800A and the bPhGMS-derived organo-silica hybrid gel bPh450B. Gels denoted with -tms were surface functionalized with trimethylchlorosilane.

In order to prove the intactness of the Si-O bonds after supercritical and ambient pressure drying by surface silylation in case of the phenylene-bridged gels,  $^{13}\text{C}$  CP- and  $^{29}\text{Si}$  CP-

MAS NMR investigations were undertaken. In the  $^{29}\text{Si}$  CP-MAS NMR spectrum of the hybrid material (bPh450-B) only T-signals with chemical shifts of -66.5, 74.6 and -83.0 ppm were detected except for the surface modified (-tms) sample, where an additional peak for M<sup>1</sup> peak from  $-\text{Si}(\text{CH}_3)_3$  was observed. In Figure 3.6.1 the  $^{29}\text{Si}$  CP-MAS NMR spectra of an organically bridged and a pure silica network are shown for comparison. Both drying methods leave the network of the gels intact. Instrumented hardness tests were performed on monolithic pieces of EGMS and bPhGMS03 (see Table 2.2) derived gels with bimodal pore structure. Mesopore structure was analyzed using SAXS and BET, macroporous structure was investigated with SEM. Detailed information on composition and structure is given in the Appendix (page 154).

### ***3.6.1.1 Bimodal porous silica monoliths prepared from EGMS***

In Figure 3.6.2 the network structure of a typical gel prepared from EGMS and P123 is shown together with the results from the nitrogen sorption studies after supercritical fluid extraction and ambient pressure drying after surface silylation, respectively. The sorption isotherm plots exhibit a defined step in the hysteresis loop as expected for the investigated materials. The specific surface area  $S^{\text{BET}}$  is as high as 891-1092  $\text{m}^2\text{g}^{-1}$  for the  $-\text{scd}(\text{CO}_2)$  material. Gels dried with supercritical methanol ( $-\text{scd}(\text{MeOH})$ ) have a lower specific surface area of 462-626  $\text{m}^2\text{g}^{-1}$ . The material consists of a macroporous network where the interconnected rod-shaped particles are built of 2D hexagonally arranged cylindrical mesopores of a repeating unit distance of approximately 10.5–12 nm, pore diameters of up to 9 nm and wall thicknesses of approximately 4-6 nm (compare Chapter 3.5.1). In addition to the mesopores a considerable amount of micropores contributes to the large surface areas in case of the -tms and especially the  $-\text{scd}(\text{CO}_2)$  specimen, as is known for mesoporous material templated with lyotropic phases of PEO-containing block copolymers. As shown in Figure 3.6.3 for sample E802A the modulus and the hardness are smallest for the fully dried surface-modified material (-tms) whereas the recovery is large compared to the same material after supercritical fluid extraction. The largest values for Young's modulus and hardness were found for the monoliths dried with supercritical methanol. The reason for this lies in the loss of microporosity in the pore walls of the mesostructure which leads to enhanced consolidation of within the pore walls as was confirmed by the  $\text{N}_2$ -sorption experiments.

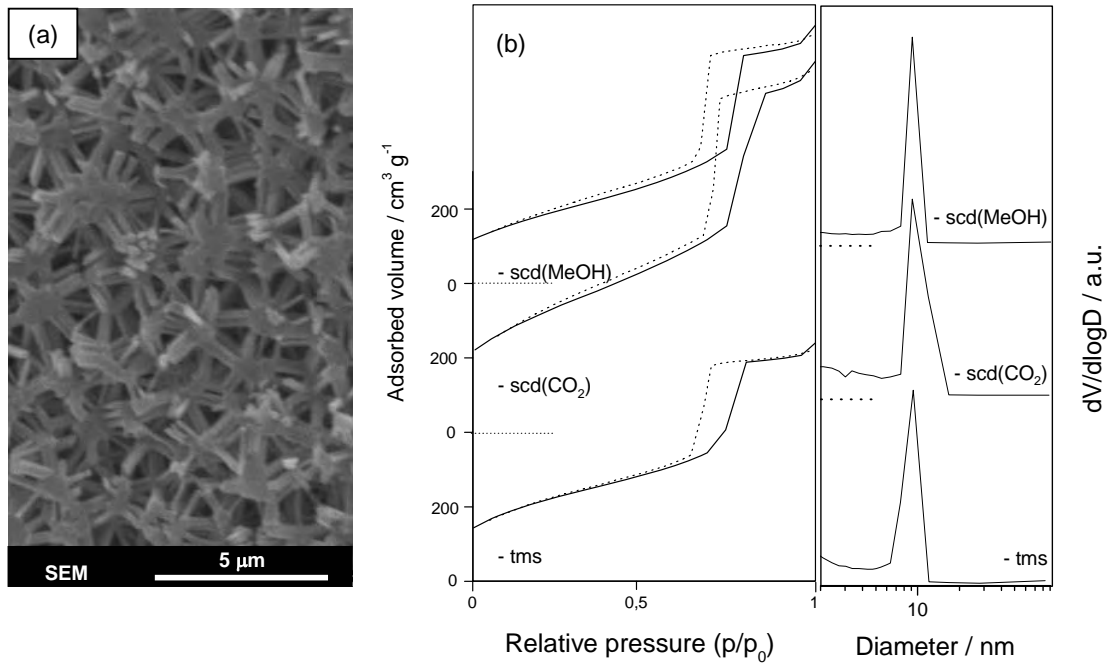


Figure 3.6.2. (a) Representative SEM image of sample E802A. The macroporous network consists of interconnected rods which are built of periodically ordered cylindrical mesopores arranged in a 2D hexagonal pattern. (b) Nitrogen sorption isotherm plots and the corresponding pore size distribution from the adsorption branch of the hierarchically organized material.

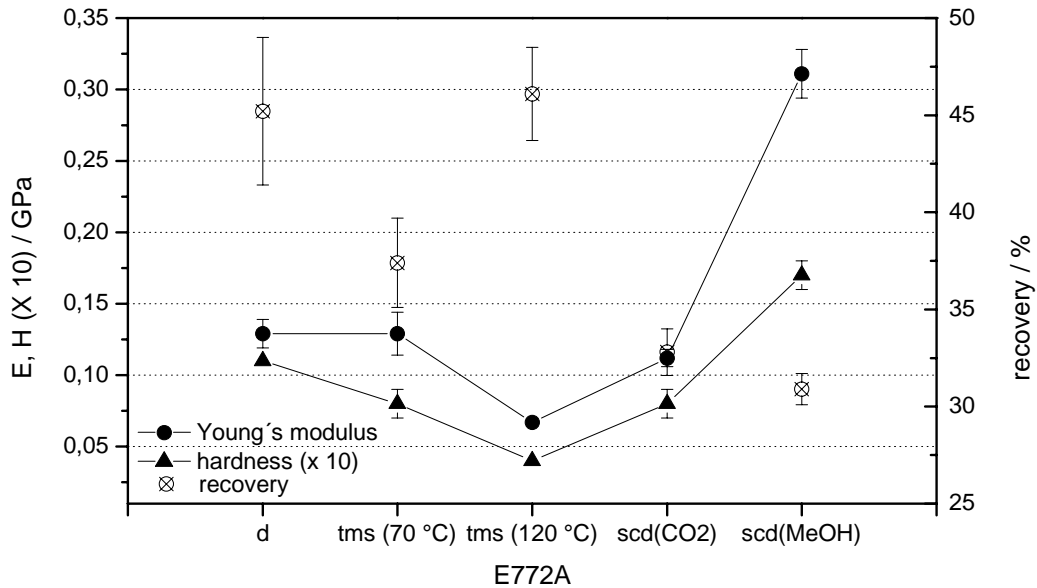


Figure 3.6.3 Results for Young's modulus, E, hardness, H, and recovery from instrumented indentation tests on gels derived from ethylene glycol-modified precursor and Pluronic P123 as structure directing agent (concentration of Si/P123/1 M HCl=8.0/30/70). Tests were performed after different post-synthesis treatment of the wet gel. Hardness was multiplied by a factor of 10 for better visibility.



For all samples with distinct 2D hexagonal periodic mesostructure derived from EGMS, the hardness of the material obtained by drying with supercritical carbon dioxide was higher than for the material after surface silylation with trimethylchlorosilane. The same trend applies for the obtained Young's modulus. The results from the instrumented indentation tests are listed in Table 3.9. The difference between the two drying/extraction methods is especially pronounced in the samples prepared at low acid concentrations of  $10^{-2}$  M HCl. The recovery is always larger for the silylated material. For EGMS-gels prepared with low precursor concentration (E450A, E452A) the trend between -scd and -tms is reversed. For E450A, due to a large shrinkage in the trimethylchlorosilane treated sample, the overall density is as high as  $0.45 \text{ g cm}^{-3}$ . Therefore the obtained values for Young's modulus and hardness are also high. It has to be noted, that the same material with lower density but complement macrostructure (rod-shaped particles) and highly ordered mesostructure (e.g., E800A-scd) succeeds to catch up concerning modulus and hardness.

Table 3.9. Obtained results from  $\text{N}_2$ -sorption and instrumented indentation experiments for the EGMS-derived material. Details for composition are found in Appendix C. Values for modulus (E), hardness (H) and recovery are the averaged values of at least four runs for each sample. \*Gels prepared from low precursor concentration leading to poorly ordered overall mesostructure.

Samples	$S^{\text{BET}} / \text{m}^2\text{g}^{-1}$		Density / $\text{gcm}^{-3}$		E / MPa		H / MPa		Recovery / %	
	-tms	-scd	-tms	-scd	-tms	-scd	-tms	-scd	-tms	-scd
E802A	732	1092	0.25	0.21	$67 \pm 1$	$112 \pm 6$	4	8	46	33
E802B	727	1054	0.19	0.19	$110 \pm 6$	$192 \pm 24$	7	9	38	22
E802C	1035	-	$\sim 0.13$	-	$42 \pm 4$	-	2	-	37	-
E452A*	716	-	-	-	$306 \pm 32$	-	27	-	62	-
E800A	769	627	n.s.	0.27	$91 \pm 5$	$334 \pm 27$	9	20	67	27
E450A*	575	935	0.45	0.2	$269 \pm 22$	$38 \pm 2$	19	3	53	37

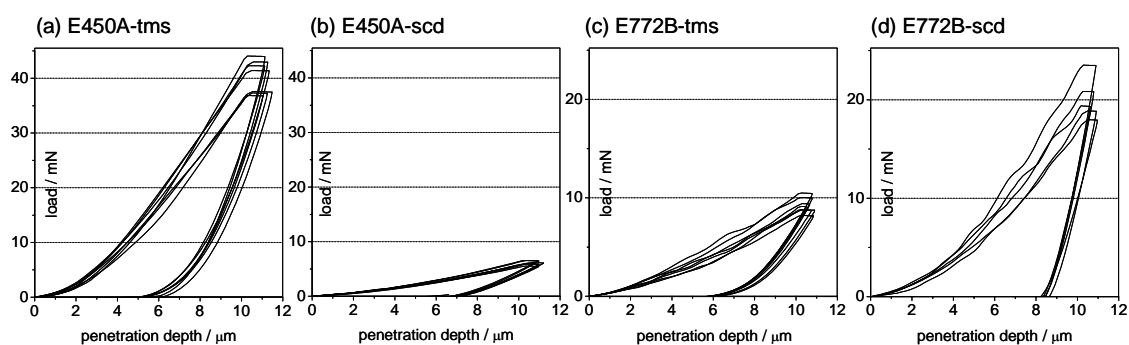


Figure 3.6.4. (a-b): Characteristic indentation curves for an EGMS gel (E450A) with low ordering of mesopores. (c-d): Typically EGMS gel with interplay in meso- and macrostructure. Both materials were investigated after treatment with trimethylchlorosilane and supercritical fluid extraction. For E450A-tms (a) the density was found to be as high as  $0.45 \text{ g cm}^{-3}$  resulting in a high modulus and hardness (see Table 3.9).

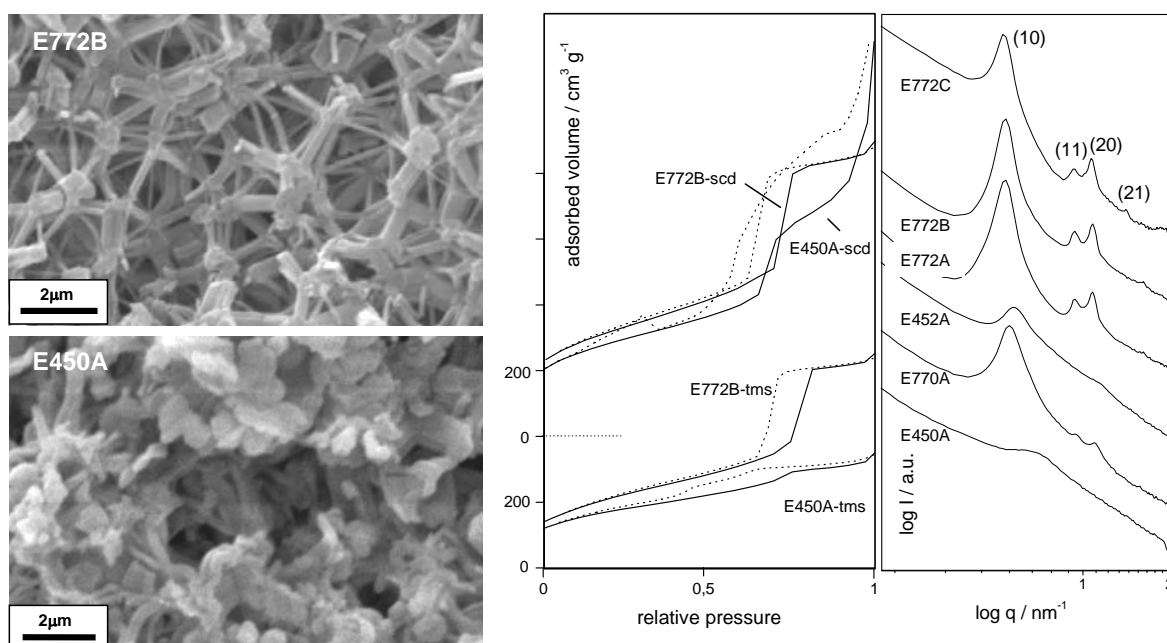


Figure 3.6.5. Left: Representative SEM images of the resulting macromorphology with different ratios of EGMS/P123 in the gel synthesis. Middle: Representative adsorption – desorption isotherms from nitrogen sorption for differently dried samples: E802B –tms and –scd and E450A –tms and –scd. Right: SAXS patterns for the gels outlined in Table 3.9.

In Figure 3.6.5 the difference between a typical highly organized hierarchically structured EGMS-gel templated with Pluronic P123 (E80) and a relatively disordered material (E45) derived from the same components is shown on the basis of SEM images as well as BET and SAXS results. In comparison with, e.g., E802B, in E450A the low silica content leads only to a fragmentary formation of periodic structure of the mesopores (see Figure 3.4.17 in Chapter 3.4.4). The sorption isotherms obtained for samples E450A reveal the presence of a multimodal pore structure with two relatively distinct pore diameters resulting from

templating with P123. Besides these mesopores, a second region of larger meso- and small macropores was found from the phase separation process for samples E450A after supercritical drying but not in case of the silylated material. Supercritically dried E450A and E802B have a similar overall density of 0.19–0.2 g cm<sup>-3</sup>. Here, E802B with a highly ordered periodic mesostructure has a five times higher modulus and three times higher value for the hardness than the mixed structure of E450A. The indentation load-displacement curves obtained for the material built-up of interconnected rod-shaped particles feature characteristic small horizontal steps (Figure 3.6.4 (a), (b)). A reason for this may be the voids between the mesoporous rods.

### 3.6.1.2 Bimodal porous organosilica monoliths prepared from bPhGMS

The results from instrumented indentation measurements on gels prepared with bPhGMS as precursor and Pluronic P123 as structure directing agent are listed in Table 3.10. For all investigated samples with Si<sup>bPhGMS</sup>/P123 ranging from 0.11–0.19 a periodically ordered mesostructure was observed in the SAXS patterns (Figure 3.6.6). The monolithic hybrid material has a slightly larger density than the pure silica monoliths described in the previous section. This may be one reason for the result that the organically bridged samples have on average higher values for Young's modulus and hardness compared to EGMS-gels with highly ordered mesostructure.

Table 3.10. Obtained results from N<sub>2</sub>-sorption and instrumented indentation experiments for the bPhGMS-derived material. All gels were templated with Pluronic P123 as structure directing agent. Macro-morphology and SAXS-patterns are depicted in Figure 3.6.6). Values are the averaged values of at least four runs for each sample.

Samples	S <sup>BET</sup> / m <sup>2</sup> g <sup>-1</sup>		Density / g cm <sup>-3</sup>		E / MPa		H / MPa		Recovery / %	
	-tms	-scd	-tms	-scd	-tms	-scd	-tms	-scd	-tms	-scd
bPh450A	488	-	0.39	-	281±19	-	38±3	-	80±3	-
bPh450B	292	327	0.34	0.36	321±32	199±6	31±4	15±1	61±4	74±1
bPh450C	412	569	0.27	0.33	161±15	122±15	13±1	9±2	61±2	63±4
bPh580C	564	622	0.24	0.33	90±3	122±8	7±1	11±1	60±3	70±2

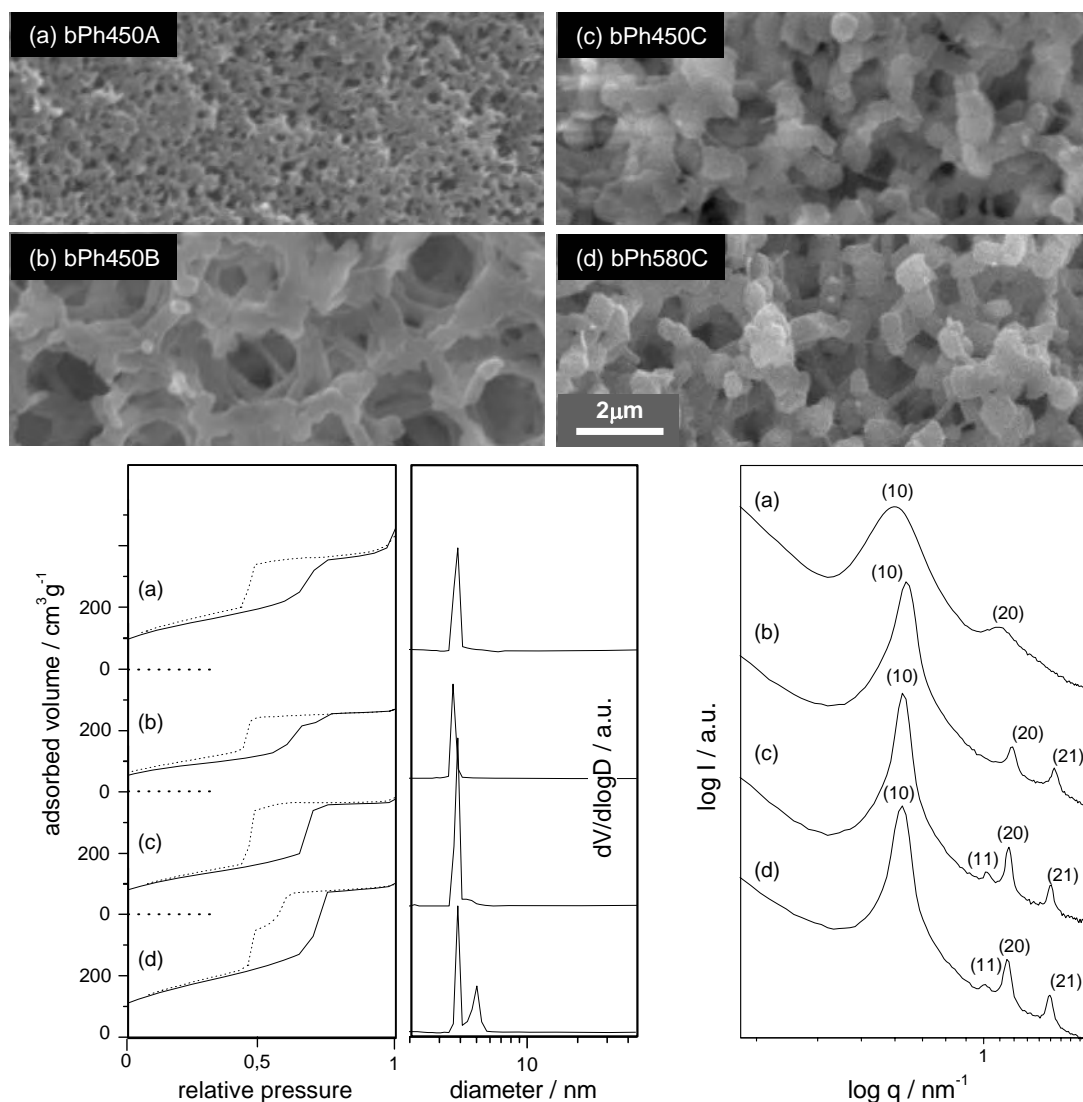


Figure 3.6.6. (a-d): Macromorphology of the investigated phenylene-bridged silsesquioxane gels imaged by SEM. (Bottom): Corresponding adsorption – desorption isotherms from nitrogen sorption and SAXS patterns.

Density is not the only cause for higher values as can be seen by comparing samples E802A-tms ( $0.25 \text{ g cm}^{-3}$ ) to bPh450C-tms ( $0.27 \text{ g cm}^{-3}$ ) or bPh580C-tms ( $0.24 \text{ g cm}^{-3}$ ). Compared to the EGMS-gel both bPhGMS-gels have higher values for Young's modulus and hardness. Also, compared to the pure silica monoliths the recovery obtained by the measurements tended to be higher for all investigated organically bridged gels.

Samples bPh450 A-C were prepared with increasing amount of  $10^{-2} \text{ M HCl}$  in the synthesis. By this, as can be seen in Figure 3.6.6 the macromorphology of the resulting gel is changed significantly at constant  $\text{Si}^{\text{bPhGMS}}/\text{P123}$  ratio, unlike for the EGMS-system (E802 A-C).

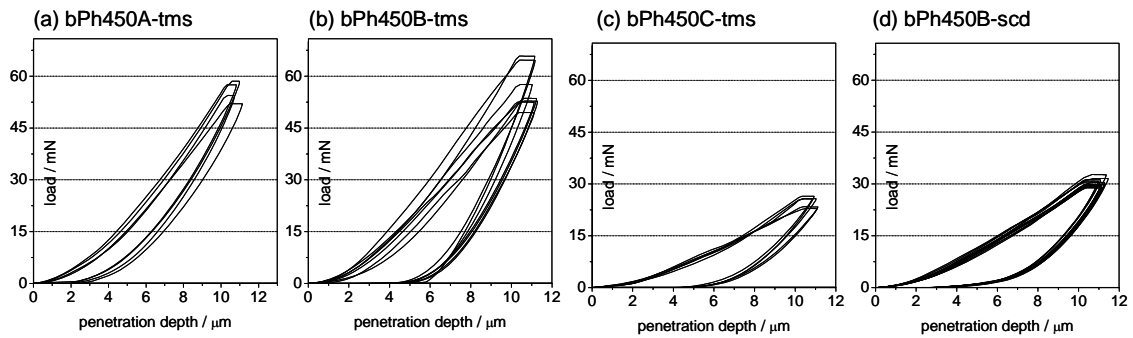


Figure 3.6.7. Characteristic indentation curves for phenylene-bridged silica material.

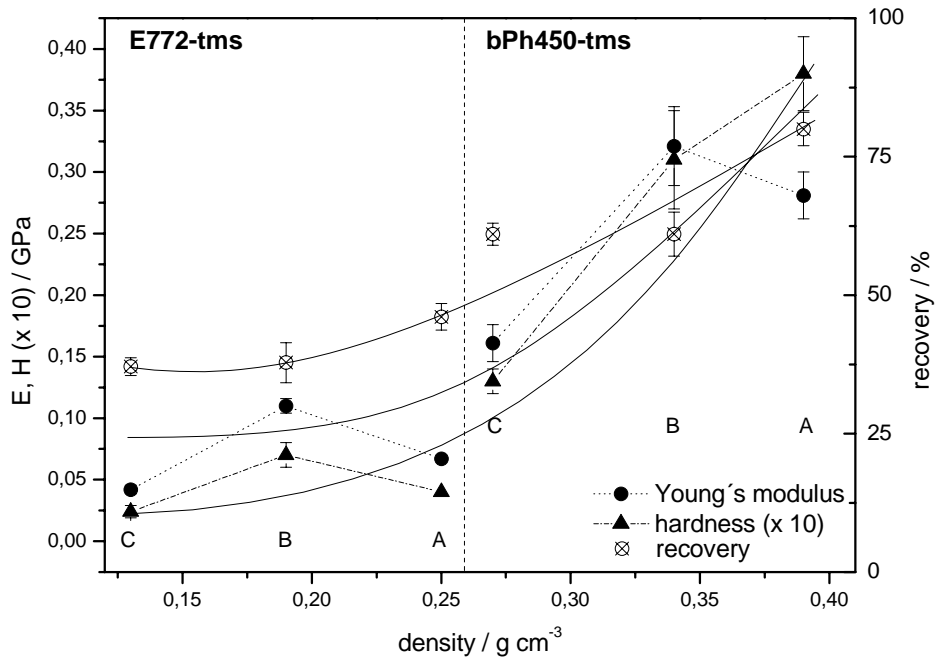


Figure 3.6.8. Result from instrumented indentation measurements for E802-tms and bPh450-tms with increasing aq. HCl amount in the starting composition. The hardness,  $H$ , has been multiplied with a factor 10 for better visibility. Full lines are drawn as guide to the eye.

For bPh450A the resulting morphology consists of a dense network with macropores of diameters smaller than 300 nm. For bPh450B and bPh450C a more particulate network with large macropores from phase separation is observed (diameters up to 2  $\mu\text{m}$ ). For the modulus as well as the hardness of the investigated samples in principle an increase with increasing overall density is observed.

Nevertheless, the results of the indentation experiments show a maximum for the modulus for samples prepared with a ratio of Si/P123/aq. HCl equally to (respective) Si/30/90 of the lyotropic mixture was found. For the EGMS-samples this may be explained by the relative large wall thickness of 6.1 nm (pore diameter of 7.4 nm) observed for samples B. For both samples A and C a wall thickness of 4.2 nm was calculated from combining BET and

SAXS results (mesopore diameters of  $\sim 9.3$ - $9.5$  nm). In case of the phenylene-bridged samples it is noticeable that for samples A and B modulus and hardness do not show the same behaviour. For samples A higher overall densities, and larger wall thickness (A: 8.2 nm, B: 6.5 nm) were obtained from the measurements. Even so, a higher modulus (but not a higher hardness) was observed for samples B, which has a comparable small  $S^{\text{BET}}$  (A:  $488 \text{ m}^2\text{g}^{-1}$ , B:  $492 \text{ m}^2\text{g}^{-1}$ , C:  $412 \text{ m}^2\text{g}^{-1}$ ). The recovery was highest for ratio A, at which also the highest density was observed within the respective series (A-C). Recovery did not change significantly going from B to C. From the load-penetration-curves obtained from the indentation experiments on the organically bridged silica material, samples bPh450A-tms with small macropores of 200-400 nm show especially large recovery.

### 3.6.2 Compressive tests on supercritically dried monoliths

Large, low density silica monoliths with a composition of EGMS(Si)/P123/1 M HCl of 82(8)/30/70 (E802A) were dried supercritically with either  $\text{CO}_2$  or MeOH as supercritical fluid following the procedure described in Chapter 2.1.3.1. By this, low shrinkage as well as mesopore-template extraction was achieved. The resulting monoliths had a cylindrical shape with a height of approximately 25 mm and a diameter of 9-10 mm. The obtained monoliths were tested under compression on a Zwick Z050. Two different experimental setups, which are described in Chapter 2.4.2, were employed to minimize errors due to friction and start-up behaviour.

In Table 3.11 the relevant sample characteristics are listed, including the density, which is between  $0.21$ – $0.27 \text{ g/cm}^3$  for the investigated material, the wall thickness of the mesopores, the pore diameter and the BET surface area. Samples that were dried with MeOH experienced a higher temperature ( $\sim 250$  °C) than samples dried with  $\text{CO}_2$  (only 40 °C). The higher temperature leads to a decrease of BET surface from  $891 \text{ m}^2/\text{g}$  to  $462 \text{ m}^2/\text{g}$ .

Table 3.11. Relevant data of the drying process and the resulting properties of the mesoporous gels. The d-spacing relates to hexagonally arranged mesopores inside the  $\text{SiO}_2$  network structure.

Supercritical fluid	$p_{\text{max}}$ (p_c) / bar	$T_{\text{max}}$ (T_c) / °C	Shrinkage / %	$\rho$ / $\text{g/cm}^3$	$d_{10}$ (SAXS) / nm	Wall thickness / nm	Pore diameter / nm	$S^{\text{BET}}$ / $\text{m}^2\text{g}^{-1}$
$\text{CO}_2$	173 (73.8)	40 (31)	10.4	0.21	12	4.8	9.1	891
MeOH	148 (80.9)	253 (240)	19.2	0.27	12	4	9.9	462

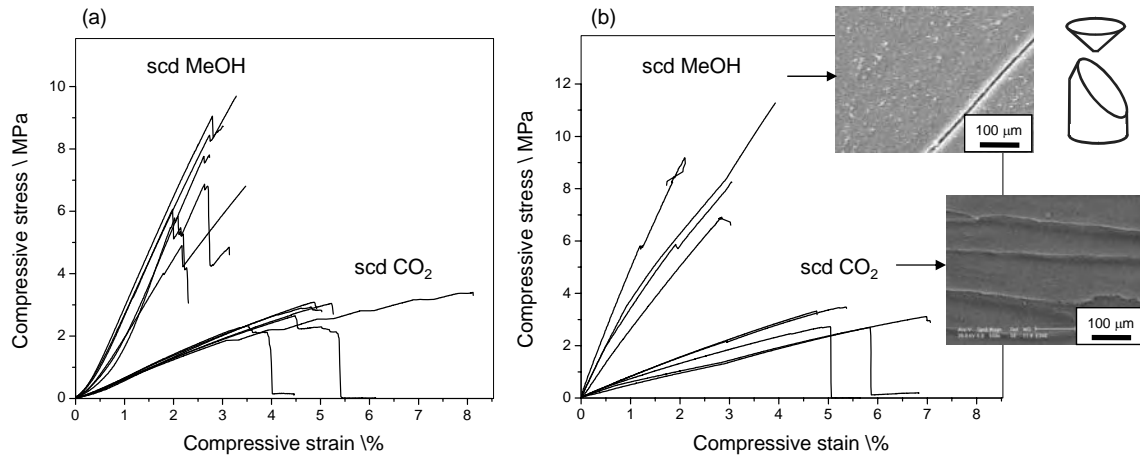


Figure 3.6.9 shows the resulting stress-strain curves of supercritically dried EGMS-gels during compression tests performed with (a) setup A, (b) setup B (for experimental details see Chapter 2.4.2). Higher temperature in the drying process results in higher Young's modulus and ultimate strength. SEM images depict that samples dried at ambient temperatures ( $\text{CO}_2$ ) buckle under the compression, whereas cracks are observed for the denser samples obtained with MeOH-drying. Schematic drawing of a monolith after failure.

Table 3.12. Result for Young's modulus ( $E$ ), ultimate strength ( $F_{\max}$ ) and compression at  $F_{\max}$  ( $\varepsilon-F_{\max}$ ) for cylindrical mesoporous  $\text{SiO}_2$ -monoliths in compression mode.

Setup	$\text{CO}_2$			MeOH		
	$E$ / MPa	$F_{\max}$ / MPa	$\varepsilon-F_{\max}$ / %	$E$ / MPa	$F_{\max}$ / MPa	$\varepsilon-F_{\max}$ / %
A	$72 \pm 4$	$2.8 \pm 0.3$	$4.6 \pm 0.7$	$338 \pm 52$	$7.7 \pm 1.4$	$2.9 \pm 0.5$
B	$70 \pm 13$	$3.1 \pm 0.3$	$5.6 \pm 0.9$	$387 \pm 88$	$8.9 \pm 1.8$	$3.0 \pm 0.8$

This is attributed to a loss in microporosity, in particular associated with increasing condensation of silanols ( $\text{Si-OH}$ ) to siloxane ( $\text{Si-O-Si}$ ) bonds. Thus, the pore diameter of the mesopores becomes larger, whereas the  $\text{SiO}_2$ -walls become more dense. Also a temperature of  $250\text{ }^\circ\text{C}$  enhances the macroscopic shrinkage of the monolithic gel bodies. To summarize, the overall density as well as the skeleton density is enhanced in the MeOH-dried samples. No change in the mesostructure takes place as was proven by the SAXS-measurements. Also the mesoporous network-structure of the material is conserved by both drying procedures.

In Figure 3.6.9 the obtained stress-strain curves are shown. The Young's modulus,  $E$ , was estimated to be in the range of 70 MPa for the  $\text{CO}_2$ -dried monoliths, gels and in the range of 300-400 MPa for the MeOH dried monoliths. Compared to the results obtained by instrumented hardness test ( $E_{\text{CO}_2}=112\text{ MPa}$ ,  $E_{\text{MeOH}}=310\text{ MPa}$ ) the value for the modulus of the  $\text{CO}_2$ -dried material is lower in compression. This can be explained by the fact, that the

viscous fraction plays a more important role in the compression test. Since the samples dried at lower temperature have a higher viscous fraction the difference in the results is more pronounced than for the measurements on the MeOH-dried samples. For the MeOH-samples an increase of compressive stress and at the same time a reduction of strain at failure could be observed. The denser material therefore is more brittle and has a higher strength at failure. The different failure modes are visible in the fractured surface investigated by SEM. For the more brittle MeOH-dried monoliths cracks were observed, whereas a more structured fracture surface, with characteristic buckling, was obtained for the CO<sub>2</sub>-samples. For all materials the monoliths flew in pieces after reaching the ultimate strength. One cone-shaped and one larger acuminated piece were left, schematically depicted in Figure 3.6.9.

#### Influence of the Porosity

As described in Table 3.11 the overall density of the investigated monolithic samples is between 0.21-0.27 g/cm<sup>3</sup>. The densities of the single samples can be correlated to the corresponding measured Young's modulus. In Figure 3.6.10 the Young's modulus of the compression tests is plotted against the density of the samples. The data is normalized by the Young's modulus ( $E_S=73$  GPa) and the density ( $\rho_S=2.2$  g/cm<sup>3</sup>) of fused silica. The lines depicted in the plot show fits according to Eq. 1.1.

The compact line takes  $E=E_S$ ,  $\rho=\rho_S$  and  $E=0$ ,  $\rho=0$  into account and leads to a scaling exponent  $n=2.6$ . Assuming that the Young's modulus of the solid,  $E_S$ , the density of the non-porous framework,  $\rho_S$ , and the structure of the differently dried samples are alike, the following scaling exponent was calculated according to Eq. 1.1:  $n \sim 5.9$  (lower limit:  $n=4$ ; upper limit:  $n=8.8$ ) for the samples measured with experimental setup A (dotted line).

Of course this result has to be handled with care. First, the density on the level of the mesopore walls is not identical for the two sample preparations, due to the loss of microporosity in the samples dried with MeOH. Second, an important geometric parameter for defining the stiffness and strength of a cellular material with given density is the connectivity, meaning the number of struts meeting in each node. Here also it is likely that samples dried at higher temperature exhibit stronger connections.

Third, the number and the thickness as well as the effective length of the struts, that is the distance between two nodes, play a significant role. Assuming that the principle morphology of the material is not changed during the drying procedure, the enhanced macroscopic shrinkage of the MeOH-dried samples suggests that the effective length of the struts building the macroscopic network has decreased.



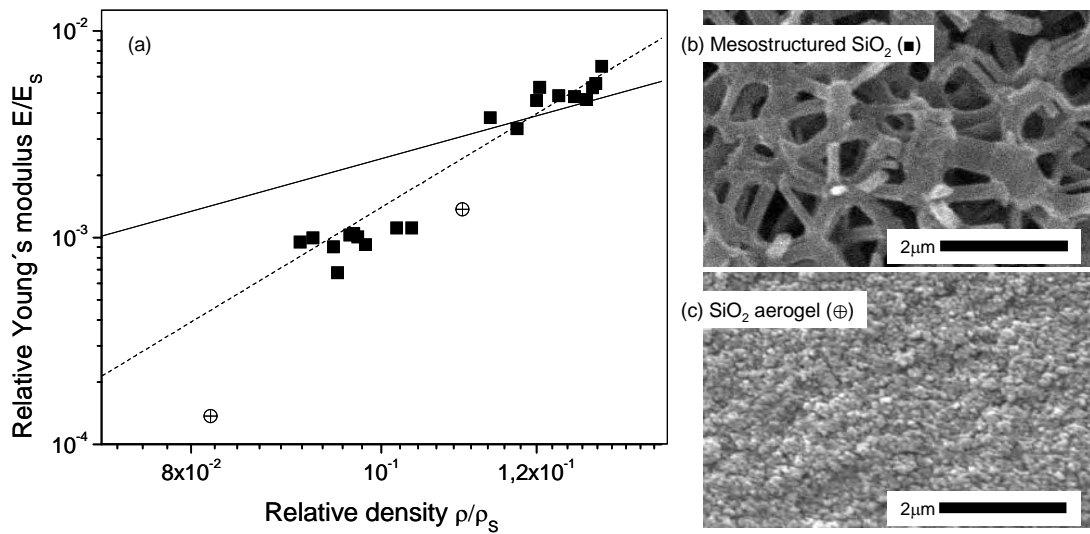


Figure 3.6.10. (a) The Young's modulus of  $\text{SiO}_2$  with a bimodal pore structure consisting of macropores and periodically arranged mesopores (b) plotted against density. The data is normalized by the Young's modulus ( $E_s=73$  GPa) and the density ( $\rho_s=2.2$  g/cm<sup>3</sup>) of fused silica. Additionally two points for a  $\text{SiO}_2$  aerogel without macroporosity and ordered mesoporosity (c) but of similar overall density measured with the resonant beam method [102] are shown for comparison. The compact and the dotted line are the fitting curves according to Eq. 1.1. The compact line takes the points  $E=E_s$ ,  $\rho=\rho_s$  and  $E=0$ ,  $\rho=0$  into account and leads to an exponent of  $n=2.6$ .

Highly porous gels are not completely mechanically connected and densification causes a greater portion of the structure to take the load. Woignier et al [101] report an increase of the elastic moduli of highly porous aerogels with  $\rho^n$ , where  $n$  lies between 3 and 4. They claim that the most important parameter is the connectivity which can be enhanced by temperature or isostatic pressure.

The determination of the elastic constants against temperature of a supercritically dried aerogel without ordered mesoporosity and a density of  $\sim 0.18$  g/cm<sup>3</sup> has been performed by the group of Herwig Peterlik [102] using the resonant beam method. This procedure gives values for the modulus of  $\sim 16$  MPa at RT and 100 MPa after being heated up to 700 °C (density change to 0.242 g/cm<sup>3</sup>). The results obtained by compression tests on monolithic samples in this work agree quite well with the published data for the non-ordered material.

This suggests that a compression test is a quite suitable method to gain information on the macroscopic materials properties. The modulus proves to be of the same order of magnitude for the hierarchical (Figure 3.6.10(b)) and the unordered porous material (Figure 3.6.10(c)). As long as the overall density is comparable, Young's modulus of the hierarchically material is even slightly less dependent on the apparent density.

## 3.7 Macroscopic Templating

The fabrication of sol-gel derived nanocomposites with a high degree of mesoscopic order in combination with tailored complex macroscopic morphologies and hierarchical build-up such as they are found in nature (e.g. bone), is rarely achieved. One reason is the difficulty encountered when making large monoliths, such as shrinkage and furthermore the general difficulty to bring mesostructured materials into complex 3D shapes. The approach mainly used is templating. Until now the final body structure of the monoliths is more or less limited to the shape of the preparation vessel. The fabrication of more complicated or undercut structures involves the usage of casts, which have to be removed afterwards. Mold removal usually involves high temperatures or solvents. The templating of organic/inorganic nanocomposites is a general challenge because of the temperature sensitivity of the organic phase that does not allow for calcination as a method for template removal. Rapid prototyping (RP) is a suitable method to build complex user-defined cellular structures. In this work RP was combined with new water- and organo-soluble photopolymers. The sacrificial molds built of the new resins could easily be dissolved at ambient temperatures and therefore offer to macroscopically shape materials derived by soft chemistry methods [112].

Still, there are some crucial points left in the templating process such as:

- inertness/stability of the polymeric mold during gelation and aging
- shrinkage of the gel and compatibility with the “rigid” mold
- dissolving
- influence of the presence of the polymer on the meso/macromorphology
- drying of the structured gel bodies

### 3.7.1 Water-soluble photopolymer molds

First experiments were performed with water-soluble sacrificial molds based on dimethylacrylamide (DMAA) and methacrylic acid (MA). Water-soluble molds in a simple geometry as depicted in Figure 3.7.1 (left) were placed in ethylene glycol (1), in water (2) and ethylene glycol modified silane (3). After two days in solvent (1), surface swelling was observed and the edges of the mold had become transparent. In component (2) the colour of the photopolymeric part changed from yellow to turbid white, accompanied by light swelling. The sample put in EGMS did not show any effect. Since the polymeric parts seemed to be sufficiently stable in the single components, gels with EGMS/Brij56/H<sub>2</sub>O in different ratios of precursor to surfactant and a fixed ratio of precursor to water of 40/60

were prepared with and without the presence of the water-soluble photopolymeric structures. Already after two days all molds were heavily macerated with no geometric structure identifiable. In Table 3.13 the different formulations of gels are listed with the according gel times.

Table 3.13. Gels prepared with ethylene glycol-modified silane and non-ionic block copolymer surfactant Brij 56 as structure directing agent for the mesostructure. Gels were prepared with and without of the presence of water-soluble polymeric molds fabricated by Rapid Prototyping.

EGMS (Si) / % (w/w)	Brij 56 / % (w/w)	H <sub>2</sub> O / % (w/w)	Gel time / min	Gel time with mold / min	Appearance of resulting gel
62.0 (6.3)	7	93	18	37	2-phases
57.3 (5.8)	14	86	22	33	2-phases
53.3 (5.4)	20	80	34	35	2-phases, mold dissolved, light yellow sticky mass
46.7 (4.7)	30	70	28	28	
40.0 (4.0)	40	60	18	18	Gel has become yellow, mold still structured

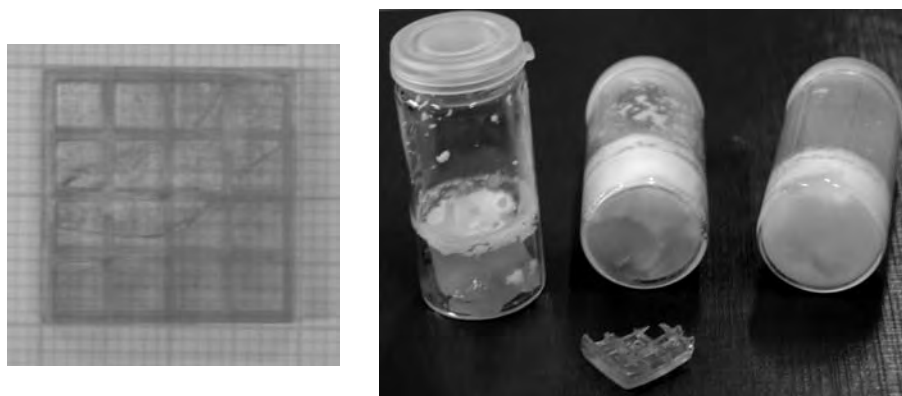


Figure 3.7.1. Left: Water-soluble molds with simple geometry were fabricated with stereolithography (Height=2 mm). Right: Gels prepared with EGMS/Brij56 and H<sub>2</sub>O (increasing ratio of surfactant to precursor from left to right).

The water-soluble polymeric molds employed in the experiments originally have a grid-like structure as shown in Figure 3.7.1 (left). The gel time seems to be influenced (delayed) by the presence of the water-soluble polymer, at least at low surfactant concentrations. In part of the samples the sol and gel separate into two differently coloured phases. In Figure 3.7.1 (right) EGMS/Brij56/H<sub>2</sub>O-gels with different ratios of precursor to surfactant after one week aging and vacuum drying are depicted. With decreasing surfactant concentration


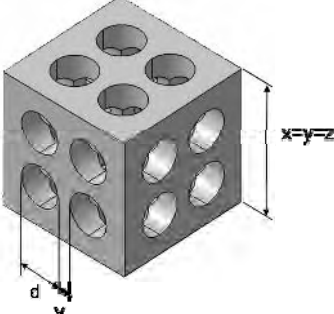
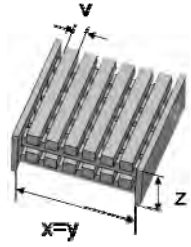
the polymer is dissolved in the gel phase. For the gel with lowest surfactant concentration (Figure 3.7.1 left: from left to right increasing surfactant concentration) the polymer structure has dissolved completely. A cut through the gels with high surfactant concentration reveals that the water-soluble structure is still existent, but highly damaged.

### 3.7.2 Organo-soluble photopolymer molds

#### 3.7.2.1 Design of the sacrificial molds and templating process

Whereas the applied water-soluble polymeric molds proved to be only insufficiently stable during the aging process, organo-soluble polymeric molds based on highly reactive acrylamides do not influence gelation and maintain their structure during one week (and even longer) in the wet gel. Molds with a composition as described in Chapter 2.2 were built following different designs depicted in Table 3.14. The designed parts all have more or less an open structure to allow an easy and thorough penetration of the sol as well as material exchange during the gelation process. The design of the sacrificial molds as depicted in Table 3.14 led to 3D net-structures with beams/macroscale pores of diameters down to 1 mm.

Table 3.14 Different designs for the photopolymeric molds used as templates.

Cylindrical	Cube <sup>1-3</sup>	3D-Grid
		
D = 7.3 mm	x=y=z=9.5 mm	x = y = 9 mm
d = 1.5 mm	d <sub>1</sub> =3 mm, d <sub>2</sub> =2.7 mm, d <sub>3</sub> =2.5 mm	z = 4 mm
v = 1.4 mm	v <sub>1</sub> =1 mm, v <sub>2</sub> =1.3 mm, v <sub>3</sub> =1.5 mm	v = 1 mm

In a typical procedure, the differently shaped organo-soluble photo-polymeric molds were filled with the sol of a composition of Si<sup>EGMS</sup>/P123/1 M HCl=8.0/30/70 (E802). The schematic casting procedure is depicted in Figure 3.7.2 (a).

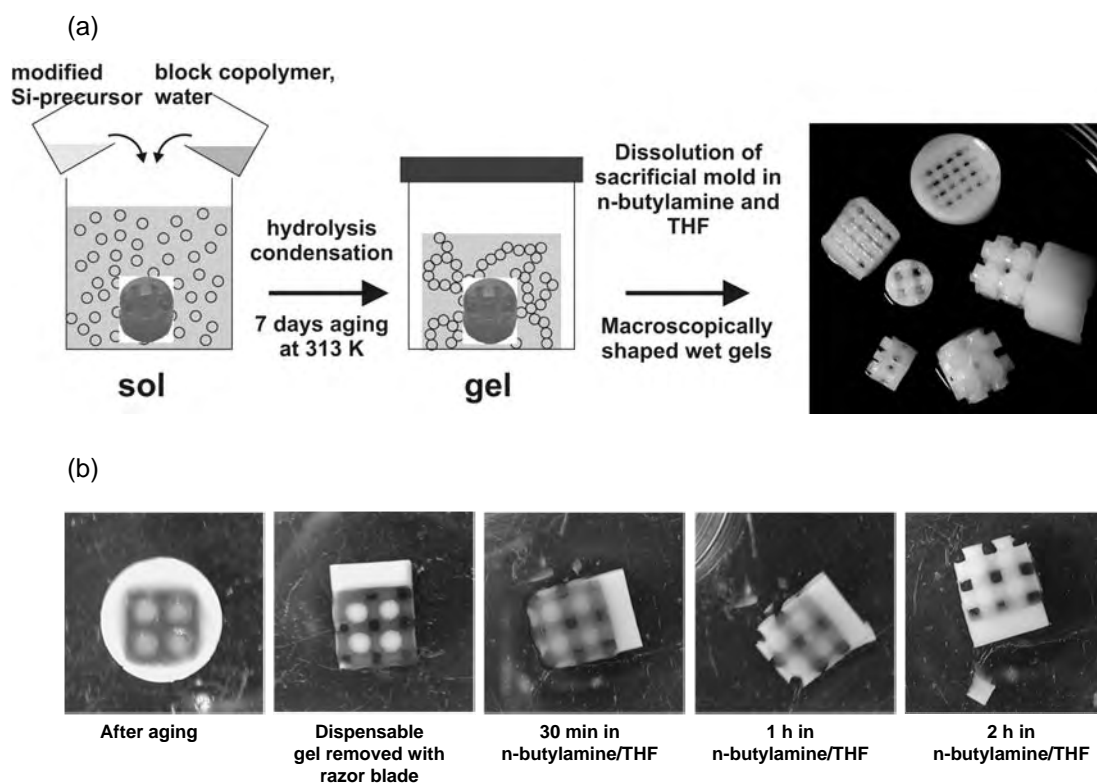


Figure 3.7.2. (a) Schematic process of macroscopic templating. (b) The sequence of images shows the dissolution of the polymeric mold in a solution of n-butylamine/THF ( $v/v=1/9$ ) at RT.

After mixing and homogenization of the reactants the aqueous sol was immediately transferred onto the RP-mold. Bubbles were avoided by short centrifugation or ultrasound, respectively. Self-assembly of the mesostructured silica/P123 composite took place inside the sacrificial mold. After aging of the gel for one week at 313 K in a closed vessel (standard procedure) the mold was removed by dissolving in THF/n-butylamine in a volume ratio of 9:1 at RT leaving the wet nanostructured gel. The dissolution took approximately 4 h at room temperature if the spare gel was cut away leaving a good contact surface as shown in Figure 3.7.2 (b). For parts mostly embedded in gel a dissolving was nevertheless possible but more time and solvent consuming.

The gel skeleton was washed several times in ethanol. The obtained gels depicted in the final step of Figure 3.7.2 (a) are well resolved negatives of the sacrificial polymeric structures described in Table 3.14. For higher stability the obtained macroscopic structured silica gels were subsequently treated in refluxing hydrochloric acid and ethanol for 6 hours. Afterwards the gel bodies were washed several times with methanol and supercritically dried with methanol as described in Chapter 2.1.3.1.

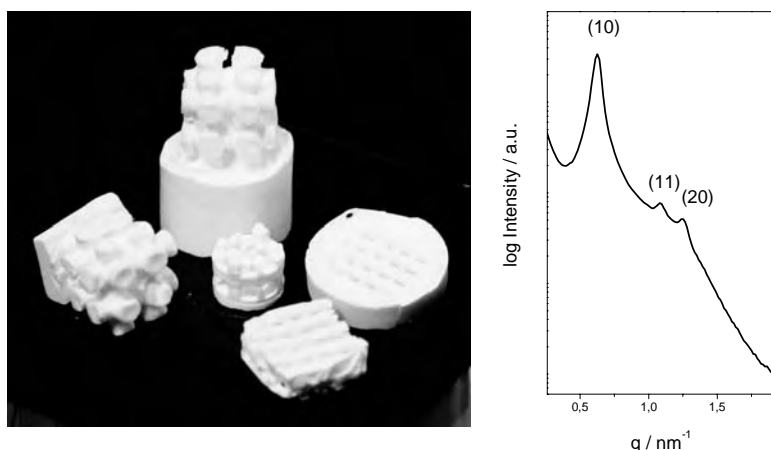


Figure 3.7.3. Left: Dry mesoporous gel parts with different macroscopic cellular architecture. Right: SAXS pattern of the gels confirm the periodical arrangement of the cylindrical mesopores.

Although the gels are exposed to high forces during the drying process, the macroscopic structure was maintained as well as the mesoporous structure. This was confirmed by SAXS measurements (Figure 3.7.3). The peak positions can be indexed according to a 2D hexagonal structure with (10), (11) and (20) with a  $d_{10}$ -spacing of 12 nm as for the not templated monolithic gel. The shrinkage obtained from the monolithic gel body was 19% for the MeOH-dried samples. Measurements on the macroscopically templated parts give shrinkage between 16-20%. This results in dimensions of 0.8 mm for the grid-like structure with the diameter of the resulting voids equally to the diameter of the struts.

Successful experiments were also performed with EGMS- and bPhGMS-derived gels in combination with supercritical fluid extraction with carbon dioxide. Gels were templated by the cubic design depicted in Table 3.14. The gels were prepared with a composition of EGMS(Si)/P123/1M HCl=82(8)/30/70 (w/w) and bPhGMS(Si)/P123/ $10^{-2}$ M HCl =48(5.3)/30/70 (w/w) leading to highly ordered hexagonally arranged cylindrical mesopores.

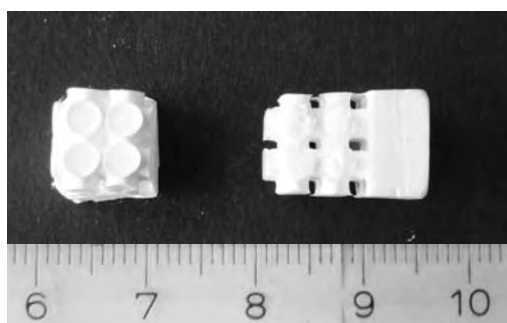


Figure 3.7.4. Phenylene-bridged gels with a designed hierarchy over 3-4 levels.

After removal of the polymer all samples stayed intact. The macroscopic structure reaches a scaffold porosity of 45-60 volume % (macroscopic void space in the scaffold resulting from the built-in channels). Figure 3.7.4 shows two gels derived from the phenylene-bridged glycol-modified precursor dried with supercritical CO<sub>2</sub>. The resulting macroscopic channels can be fabricated to diameters <1mm.

Not surprisingly, the overall dimension of the gel body shrinks during the washing and supercritical fluid extraction. Nevertheless, due to the fact that the gel is confined to the sacrificial mold during gelation and aging, the shrinkage of the structure is hindered until the removal. A shrinkage of ~6-7% was found for dimension x=y=z compared to a shrinkage of ~20% for EGMS-derived and ~29% for bPhGMS-derived reference gels.

A large scatter in the results is due to variations in the structure of the RP-mold. For the geometries obtained by the three different cubic structures defined in Table 3.14, following diameters, d, of gel beams and voids, v, where obtained for the EGMS (bPhGMS) gels:  $d_1/v_1=2.5/1.5$  mm resulted in  $d'_1/v'_1 \sim 2.2/1.4$  (2.1/1.4) mm and  $d_3/v_3=3.0/1.0$  mm resulted in  $d'_3/v'_3 \sim 2.9/0.45$  (2.8/0.5) mm.  $d_1$  was reduced by approximately 12% in case of the EGMS samples and 16% in case of the phenylene-bridged networks for  $d=2.5$  mm, lower shrinkage of the diameter d and increasing shrinkage of v was obtained for  $d>2.5$  mm,  $v<1.5$  mm. Results for samples dried slowly after surface silylation did not differ significantly; Equally well resolved gel parts were received for moderate heating rates (3 °C/2 h up to 60 °C, after that 10 °C/2 h).

### 3.7.2.2 Surface texture resulting from contact to the photopolymeric mold

Macroscopically structured gel bodies as shown in Figure 3.7.3 were investigated with SEM. On the surface of the resulting gel-body cladding is observed. The formed skin is thin, only weakly bound to the rest of the body and removed easily (depicted in Figure 3.7.5).

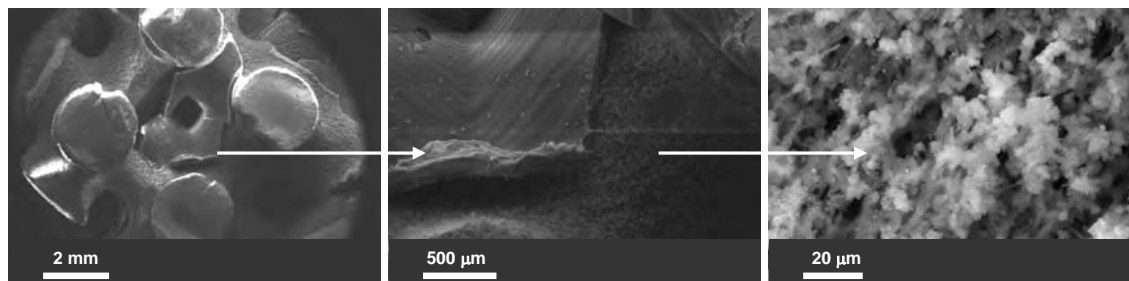


Figure 3.7.5. SEM images of the surface of the macroscopically structured, cellular gel part.

Below the dense film, a rather coarse 3D net-structure is observed that differs from the bulk structure. This effect is shown in detail in Figure 3.7.6. To compare the spider web structure close to the surface (and therefore close to the contact surface between gel and photopolymeric mold), a strut as schematically depicted in Figure 3.7.6 was removed carefully from the gel body. This leaves the socket with a cross-section from surface to bulk structure. As shown in the amplification, beneath the surface the net has larger macropores surrounded by composed and agglutinated struts. This suggests reactions at the interface of the sacrificial mold and the sol during gelation resulting in a further coarsening of the macroscopic gel network, most likely due to enhanced phase separation. The mesoscopic order of the nanostructure is not influenced by the presence of the RP part. Macropores up to diameters of 3-4  $\mu\text{m}$  were found in the region close to the dialkylacrylamide-based mold. The bulk region of the dismantled gel beam poses the same spider web structure as described earlier for E802 (A-C).

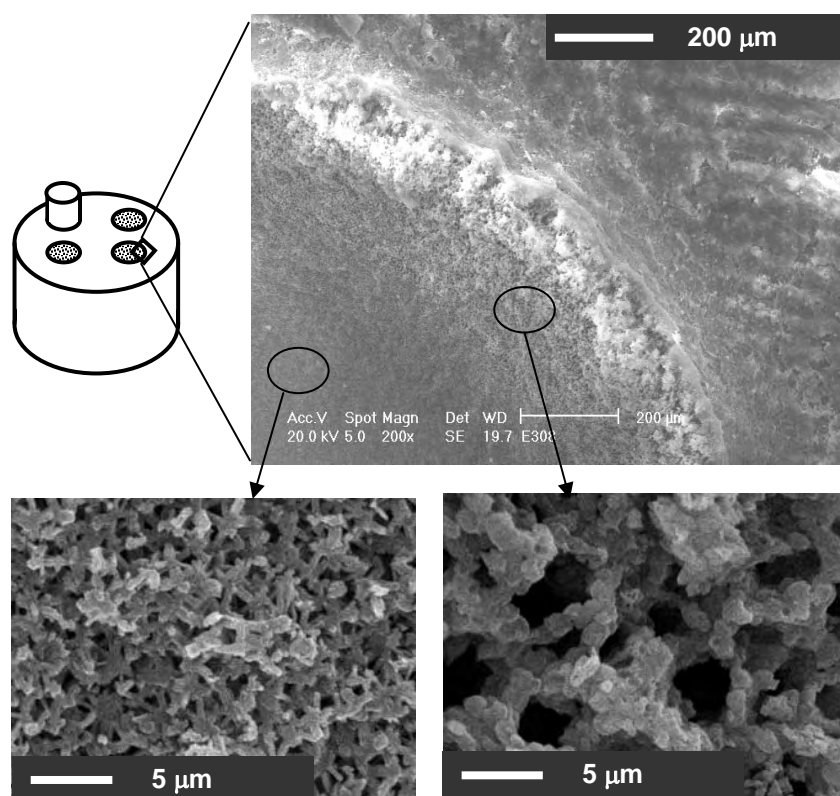


Figure 3.7.6. SEM images of the gel cast in the region close to the sacrificial polymeric mold and the macromorphology differences induced thereby.



### 3.7.2.3 Ambient pressure drying of the macroscopically shaped gels

A mixture of n-ethylamine and THF (v/v=1:9) proved equally appropriate to remove the sacrificial mold. Gels were prepared with EGMS as Si-precursor and Pluronic P123 as structure directing agent in acidic aqueous media (1 M HCl) in a composition of Si/P123/HCl (aq.) = 8/30/70 inside macroscopically shaped organo-soluble sacrificial structures. To find the most appropriate step for removal of the mold in the post-synthesis processing, the wet gel/photopolymer composite was exposed to n-ethylamine either prior or posterior to surface silylation with trimethylchlorosilane (tms). In Table 3.15 the different routes (step 1, step 2) are summarized for the experiments. In an additional step all samples were dried by slow heating ( $T_{\max}=150\text{ }^{\circ}\text{C}$ ) and finally calcined.

Table 3.15. Different investigated pathways to get rid of the sacrificial mold, surfactant and solvent.

Sample	1. Step	2. Step
RP-0	Silylation: - washing with tms/PE - 3x PE - 3x EtOH	
RP 1	Removal of photopolymer: - washing with n-ethylamine/THF - 3x THF	Silylation: - washing with tms/PE - 3x PE - 3x EtOH
RP-2	Silylation: - washing with tms/PE - 3x PE - 3x EtOH	Removal of sacrificial mold: - washing with n-ethylamine/THF - 3x THF
RP-3	Silylation: - washing with tms/PE - 3x PE	Removal of sacrificial mold: - washing with n-ethylamine/THF - 3x THF - 3x EtOH
RP-4	Removal of sacrificial mold: - washing with n-ethylamine/THF - 3x THF	

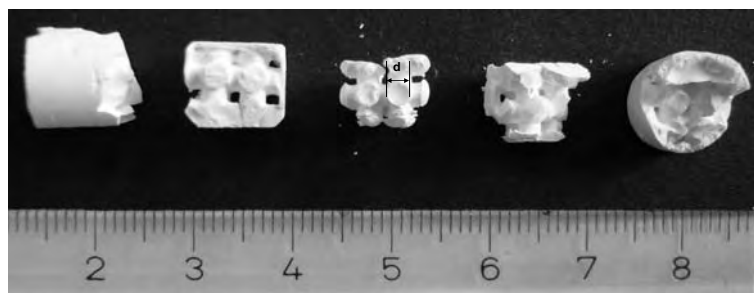


Figure 3.7.7. Calcined macroscopically templated silica gels with highly ordered mesostructure.

In Figure 3.7.7 the resulting morphologies are shown. For all samples the intended macroscopic structure is identifiable but except for sample RP-1 the gel body has been heavily deformed during the post synthesis treatment. Least shrinkage was observed for the gels first treated with n-ethylamine/THF (RP-1, RP-4). RP-1, which was first exposed to n-ethylamine/THF, washed with THF and afterwards silylated shows shrinkage of only 11% compared to gels processed by different routes (18-20%). From this it can be concluded that although the polymeric scaffold counteracts shrinkage of the geometric structure during aging, there is a ‘best moment’ to remove it in post processing of the wet gel.

Table 3.16 Results from BET, SAXS (for the gels slowly heated up to 150°C and the calcinated gels) and shrinkage during the washing and drying process for the different routes listed in Table 3.15.

Sample		Surface area / m <sup>2</sup> /g	Pore diameter / nm	Shrinkage: aged gel- dried (total) / %	q / nm <sup>-1</sup>	σ / nm <sup>-1</sup>
RP-0	150 °C	698	6.4	20	0.71	0.044
	calc.	320	4.0	11 (29)		
RP-1	150 °C	677	9.3	11	0.62	0.036
	calc.	663	7.6	8 (18)		
RP-2	150 °C	472	6.4	21	0.7	0.039
	calc.	748	5.5	6 (26)		
RP-3	150 °C	531	6.4	20	0.66	0.042
	calc.	536	6.4	5 (24)		
RP-4	150 °C	390	7.5	18	0.67	0.04
	calc.	414	7.6	6 (23)		

Nitrogen sorption measurements show that only the removal of the sacrificial structure with n-ethylamine/THF as first step combined with silylation with trimethylchlorosilane

(RP-1) possesses a surface area and a pore diameter (Table 3.16, Figure 3.7.8) comparable to the reference gel. Reversing the two steps (RP-3) still gives a high surface area, which is nevertheless significantly lower than for the reference gel. As shown in the results for RP-4 a much lower surface area was found, when the photopolymeric mold was removed without further silylation (or supercritical fluid extraction as shown previously).

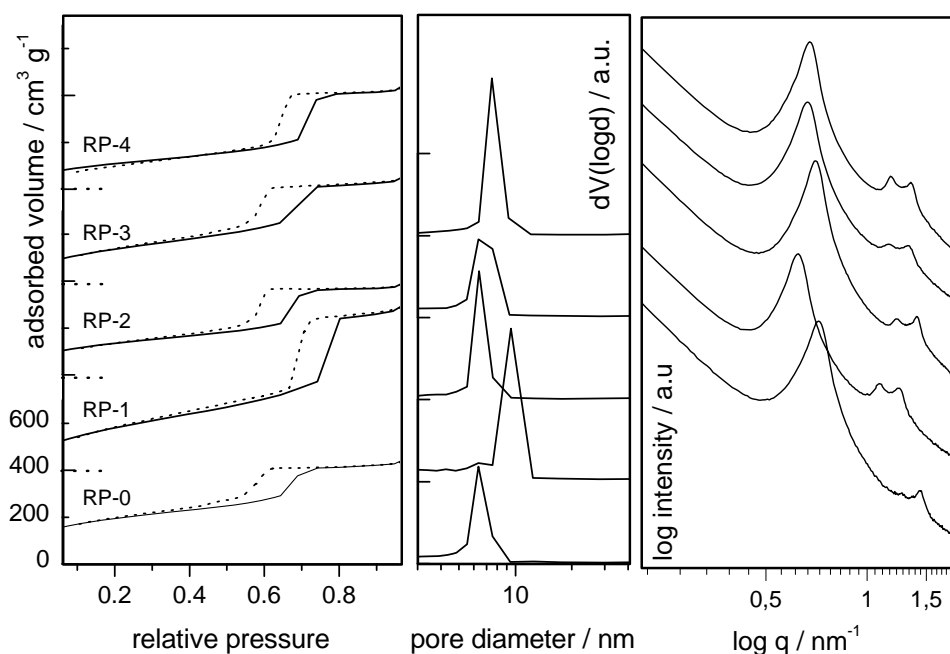


Figure 3.7.8. Nitrogen sorption isotherm plots, pore size distributions from the desorption branch and SAXS profiles of the macroscopically templated gel parts. Removal of the organic (surfactant and photopolymeric mold) was performed according to Table 3.15.

SAXS measurements confirm the high periodicity of the mesostructure in all gel casts (RP-1 to RP-4). Small differences in the wall structure can be seen from the intensities of the Bragg reflections. Calculating the wall thickness from the pore size and periodic distance derived by BET (adsorption branch) and SAXS investigations gives 2.4 nm for RP-1 and 3.8 nm for the reference gel. The highest value for the thickness of the mesopore walls was obtained for RP-4 (4.6 nm). Surprisingly for the gels prepared in the presence of the organo-soluble polymer, the specific surface area did not change significantly upon calcination, except for RP-2, where the specific surface area showed an increase.

One problem encountered in ambient pressure drying remains the removal of the solvent from the pores by temperature rising. The filigree cellular structure of the cast gels calls for a very cautious heating ramp. The samples shown in Figure 3.7.7 have been heated up in

steps of 20 °C/12 h (40-60-80-100-120, then 150 °C) which could also contribute to the damage of the cast material.

Concluding, best results in the fabrication of macroscopically shaped (hybrid) silica material with highly periodic arrangement of mesopores using glycolate-substituted silanes in combination with a liquid crystal templating approach in acidic aqueous media were obtained with organo-soluble polymeric molds based on diisobutyl acrylamide (DIBA). The removal of the sacrificial structure could be performed at room temperature, allowing for templating of organically modified silica gels. Truly hierarchical material was obtained with periodically ordered mesopores in the fashion of SBA-materials on the nanometer level, a macroporous framework on the micrometer level and deliberate cellular structure on the millimeter to centimeter level. The following processing route has proved to be optimal for the casting procedure:

- gelation inside the sacrificial polymeric mold
- aging of the gel
- removal of the sacrificial polymeric mold
- washing with THF
- washing with ethanol/methanol
- supercritical drying (CO<sub>2</sub>, MeOH)

Samples may also be prepared by ambient pressure drying after surface silylation but with higher risk of cracks and deformation. No loss in periodic mesostructure was observed, although the macroporous structure of the gels was influenced at the contact area.

## 4 Conclusions

In summary, this work presents detailed *in-situ* synchrotron small angle X-ray scattering (SAXS) studies on reordering effects of lyotropic liquid crystal (LLC) systems. Thorough SAXS investigations were also carried out to gain insight into the network formation mechanism in the fabrication of monolithic meso- and macroporous (bridged organo-) silica materials obtained by glycol-modified precursors and a preformed LLC phase. Furthermore, an additional hierarchical level was added to the meso- and macroporous material by a versatile macroscopic templating process, opening new potential applications for periodic mesoporous (organo-) silicas in the area of the life sciences. Extensive characterization of structure and mechanical properties was performed on the resulting materials.

The first part of this work deals with LLC systems and domain ordering effects. At ambient temperatures, the LC domains are usually randomly distributed. Heating the LLC systems over the anisotropic-isotropic phase transition and gradually cooling allows the molecules to rearrange with a higher degree of orientational order. *In-situ* small angle X-ray scattering (SAXS) measurements on the rearrangement of 2D hexagonal and lamellar LC systems were carried out to examine the alignment of the domains at surfaces as well as the alignment in external magnetic fields. Systems such as Triton X-45 showed a pronounced ordering effect of the lamellar LC domains parallel to the container walls after heating and cooling. Reorientation effects in external fields were observed for a highly alkaline lamellar silicate-surfactant system in a high magnetic field (7 T) and with very slow cooling rates. However, no influence of magnetic fields was achieved by low magnetic fields ( $\sim 1$  T) or fast cooling. All investigated LC systems proved to be sensitive to shear.

Lyotropic liquid crystals also play a central role in the synthesis of periodic mesoporous silica materials via the sol-gel route, since the amphiphiles serve as structure directing agents. Newly designed amphiphilic molecules with inflexible moieties, as candidates for alignment in external fields, and with polymerizable groups, as candidates for later crosslinking of the organic were analyzed with respect to their phase behaviour in aqueous media. One surfactant based on Brij 97, but with up to three double bonds in the hydrophobic alkyl chain, showed a very similar LLC phase behaviour. Due to the complex synthesis and extremely low yield, investigations on their templating abilities of inorganic structures were performed on a model surfactant. For low silica concentrations monolithic material with an ordered periodic mesostructure was obtained.

The poly(ethylene oxide)-based block copolymeric surfactant P123 is one of the non-ionic surfactants most commonly used as structure directing agent. Glycolate-substituted

(organo-) silanes templated by P123 give monolithic meso- and macroporous silica and organosilica materials with highly ordered pore structure. The high water solubility as well as the remarkable compatibility of the glycols with lyotropic phases in water, allows for a so-called “true-liquid crystal templating” (TLCT) approach. Here, a preformed lyotropic LC phase prepared with relatively high surfactant concentrations of typically  $\sim 30\%$ (w/w) in water is applied in the sol-gel process.

Extensive *in-situ* (synchrotron) SAXS investigations on the sol-gel transition of the glycol-modified precursors in combination with a P123-water template were carried out with focus on the evolution of meso- and macrostructure. Investigations started with a pre-assembled lyotropic liquid crystal phase of P123 in acidic aqueous media, consisting of a mixture of hexagonally close-packed spheres, HCPS ( $P6_3mmc$ ) and cubic arrangement of micelles ( $Fm3m$ ). The templating process resulted in 2D hexagonally ordered cylindrical mesopores ( $P6mm$ ). Due to the different structure in the final materials, it is not possible to speak of TLCT. During synthesis, the system phase separates, which results in a macroporous network. Compared to studies on more dilute systems reported in the literature, a residual order was observed in the SAXS-pattern prior to mesostructure formation. Sharp peaks derived from long range order of the cylindrical micelles were observed shortly after or together with phase separation. Prior and parallel to the observed long-range order the evolution of a characteristic slope was observed in the SAXS-profiles at low  $q$ , which was assumed to originate from disordered objects. A fit for spherical particles agreed well with the measured curves and showed an increase in number and diameter of the particles with a maximum at the point of mesostructure formation. This indicates a reordering process over a new intermediate phase, most likely consisting of inorganic-surfactant micelles that can be monitored by SAXS.

Additionally, the interplay between formation of mesopores and macroporous framework is highly interesting. Detailed transmission electron microscopy (TEM) studies on the network were performed with respect to the formation process. Whereas pure silica materials with highly ordered mesostructure always resulted in macroscopic networks consisting of interconnected rods, more diversified morphologies were found for the phenylene-bridged precursor. By raising the content of aqueous hydrochloric acid at constant ratio of surfactant to precursor, the aspect ratio of the interconnected particles changed from nearly spherical to large platelets.

As potential for technical applications increases, the study of the mechanical properties of monolithic periodic mesoporous (organo-)silica materials becomes more and more important. Therefore, another topic presented in this work is concerned with the mechanical properties of the monolithic material derived from the glycol-modified precursors. Compression tests and instrumented indentation tests on gels dried by

supercritical fluid extraction or by ambient pressure drying after surface silylation were performed. Naturally, Young's modulus and hardness derived from the measurements strongly depend on the density. Silica networks with phenylene-bridged walls were compared to pure silica material. Moduli of the samples ranged from approximately 0.04 to 0.4 GPa, hardness ranged from approximately 0.002 to 0.04 GPa. The drying method had a strong influence on the results. Highest values were found for the pure silica material dried with methanol as supercritical fluid. Here, the temperature involved in the drying process plays a crucial role, due to enhanced silica consolidation in the pore walls. Although the values for the Young's modulus are low compared to compact bone (~11 GPa), they are close to values reported for spongiosa. At least for the pure silica materials the mechanical properties may be fine-tuned by temperature treatment at the cost of low density and specific surface.

With possible applications in mind, silica and organo-silica monoliths with a hierarchical organisation of the pore structure have been successfully shaped by a simple casting process. Therefore, special water- and organo-soluble photopolymers based on dimethylacrylamide (DMAA) and diisobutyl acrylamide (DIBA) were used to fabricate cellular sacrificial molds with rapid prototyping. The (organo-) silica material with highly periodic arrangement of mesopores was prepared by using glycolate-substituted silane and phenylene-bridged triglycoxysilane in combination with a liquid crystal templating approach with P123 in acidic aqueous media. Whereas, not surprisingly, the water-soluble material did not show sufficient stability in the aqueous based sol-gel process, the organo-soluble photopolymers proved to be well suitable as mold materials and could easily be removed at ambient temperatures. Different processing routes to the final dried gel were investigated. The removal of the sacrificial molds after aging of the gels but prior to further post-synthesis treatment such as solvent exchange for supercritical fluid extraction or surface silylation with trimethylchlorosilane showed the best results concerning specific surface, shrinkage and final macroscopic structure. Since rapid prototyping (RP) allows the deliberate fabrication of structures with high geometric complexity and heavily undercut features the casting process introduced in this work will open new possibilities in the application of mesoporous materials derived by sol-gel synthesis, especially in the area of the life sciences. With these molds, it is possible to process 'bio-inspired' ceramic composites with a controlled architecture from the nanometer range up to the macroscopic scale.

## 5 References

1. Fratzl, P. and R. Weinkamer, *Nature's hierarchical materials*. Progress in Materials Science, 2007. **52**(8): p. 1263-1334.
2. Aizenberg, J., et al., *Skeleton of Euplectella sp.: Structural Hierarchy from the Nanoscale to the Macroscale*. Science (Washington, DC, United States), 2005. **309**(5732): p. 275-278.
3. Sumper, M., *A phase separation model for the nanopatterning of diatom biosilica*. Science, 2002. **295**(5564): p. 2430-2433.
4. Mann, S., et al., *Sol-Gel Synthesis of Organized Matter*. Chemistry of Materials, 1997. **9**(11): p. 2300-2310.
5. Brandhuber, D., *Hierarchically Structured (Organo-)Silica Monoliths*, in *Institute of Materials Chemistry*. 2005, University of Technology: Vienna.
6. Jönsson, B., et al., *Surfactants and Polymers in Aqueous Solution*. 1998.
7. Israelachvili, J.N., *Intermolecular and Surface Forces: With Applications to Colloidal and Biological Systems*. 1985. 296 pp.
8. Chandramani Singh, K., et al., *Phase diagram studies in two-surfactant ternary systems employing positron annihilation spectroscopy*. Journal of Colloid and Interface Science, 2005. **282**(1): p. 176-181.
9. Dimitrova, G.T., T.F. Tadros, and P.F. Luckham, *Investigations of the Phase Changes of Nonionic Surfactants Using Microscopy, Differential Scanning Calorimetry, and Rheology*. Langmuir, 1996. **11**: p. 1101-1111.
10. Forster, S., *Amphiphilic block copolymers for templating applications*. Colloid Chemistry 1, 2003. **226**: p. 1-28.
11. Fritscher, C., et al., *In situ SAXS study on cationic and non-ionic surfactant liquid crystals using synchrotron radiation*. Journal of Synchrotron Radiation, 2005. **12**(6): p. 717-720.
12. Nagarajan, R., *Solubilization of hydrocarbons and resulting aggregate shape transitions in aqueous solutions of Pluronic (PEO-PPO-PEO) block copolymers*. Colloids and Surfaces, B: Biointerfaces, 1999. **16**(1-4): p. 55-72.
13. Soni, S.S., et al., *Quantitative SAXS Analysis of the P123/Water/Ethanol Ternary Phase Diagram*. Journal of Physical Chemistry B, 2006. **110**(31): p. 15157-15165.
14. Wang, Z., et al., *Hexagonal Liquid Crystalline Phases Formed in Ternary Systems of Brij 97-Water-Ionic Liquids*. Langmuir, 2005. **21**(11): p. 4931-4937.
15. Wanka, G., H. Hoffmann, and W. Ulbricht, *Phase Diagrams and Aggregation Behavior of Poly(oxyethylene)-Poly(oxypropylene)-Poly(oxyethylene) Triblock Copolymers in Aqueous Solutions*. Macromolecules, 1994. **27**(15): p. 4145-9.
16. Hyde, S.T., *Identification of lyotropic liquid crystalline mesophases*. Handbook of Applied Surface and Colloid Chemistry, 2002. **2**: p. 299-332, 5 plates.
17. Liu, L.M., et al., *Shear-induced alignment and nanowire silica synthesis in a rigid crystalline surfactant mesophase*. Journal of the American Chemical Society, 2004. **126**(8): p. 2276-2277.
18. Melosh, N.A., et al., *Macroscopic shear alignment of bulk transparent mesostructured silica*. Journal of the American Chemical Society, 2001. **123**(6): p. 1240-1241.



19. Firouzi, A., et al., *Magnetic-field-induced orientational ordering of alkaline lyotropic silicate - surfactant liquid crystals*. Journal of the American Chemical Society, 1997. **119**(40): p. 9466-9477.
20. Tolbert, S.H., et al., *Magnetic field alignment of ordered silicate-surfactant composites and mesoporous silica*. Science, 1997. **278**(5336): p. 264-268.
21. Ku, A.Y., D.A. Saville, and I.A. Aksay, *Electric-Field-Induced Orientation of Surfactant-Templated Nanoscopic Silica*. Langmuir, 2007. **23**(15): p. 8156-8162.
22. Raimondi, M.E., et al., *Synthesis of direct templated aligned mesoporous silica coatings within capillaries*. Chemical Communications, 1997(19): p. 1843-1844.
23. Kimura, T., *Study on the effect of magnetic fields on polymeric materials and its application*. Polymer Journal, 2003. **35**(11): p. 823-843.
24. Schubert, U. and N. Huesing, *Synthesis of Inorganic Materials. Second, Revised and Updated Edition*. 2005: WILEY-VCH.
25. Beck, J.S., et al., *A New Family of Mesoporous Molecular-Sieves Prepared with Liquid-Crystal Templates*. Journal of the American Chemical Society, 1992. **114**(27): p. 10834-10843.
26. Kresge, C.T., et al., *Ordered Mesoporous Molecular-Sieves Synthesized by a Liquid-Crystal Template Mechanism*. Nature, 1992. **359**(6397): p. 710-712.
27. Bagshaw, S.A., E. Prouzet, and T.J. Pinnavaia, *Templating of mesoporous molecular sieves by nonionic polyethylene oxide surfactants*. Science (Washington, D. C.), 1995. **269**(5228): p. 1242-4.
28. Hoffmann, F., et al., *Silica-based mesoporous organic-inorganic hybrid materials*. Angewandte Chemie, International Edition, 2006. **45**(20): p. 3216-3251.
29. Soler-Illia, G., et al., *Block copolymer-templated mesoporous oxides*. Current Opinion in Colloid & Interface Science, 2003. **8**(1): p. 109-126.
30. Zhao, D.Y., et al., *Triblock copolymer syntheses of mesoporous silica with periodic 50 to 300 angstrom pores*. Science, 1998. **279**(5350): p. 548-552.
31. Zhao, D., et al., *Nonionic Triblock and Star Diblock Copolymer and Oligomeric Surfactant Syntheses of Highly Ordered, Hydrothermally Stable, Mesoporous Silica Structures*. J. Am. Chem. Soc., 1998. **120**: p. 6024-6036.
32. Flodstrom, K. and V. Alfredsson, *Influence of the block length of triblock copolymers on the formation of mesoporous silica*. Microporous and Mesoporous Materials, 2003. **59**(2-3): p. 167-176.
33. Yu, C., et al., *Morphology Development of Mesoporous Materials: a Colloidal Phase Separation Mechanism*. Chemistry of Materials, 2004. **16**(5): p. 889-898.
34. Behrens, P. and G.D. Stucky, *Ordered Molecular Arrays as Templates - a New Approach to the Synthesis of Mesoporous Materials*. Angewandte Chemie-International Edition, 1993. **32**(5): p. 696-699.
35. Wan, Y., Y. Shi, and D. Zhao, *Designed synthesis of mesoporous solids via nonionic-surfactant-templating approach*. Chemical Communications (Cambridge, United Kingdom), 2007(9): p. 897-926.
36. Attard, G.S., J.C. Glyde, and C.G. Goltner, *Liquid-Crystalline Phases as Templates for the Synthesis of Mesoporous Silica*. Nature, 1995. **378**(6555): p. 366-368.
37. Doshi, D.A., et al., *Peering into the self-assembly of surfactant templated thin-film silica mesophases*. Journal of the American Chemical Society, 2003. **125**(38): p. 11646-11655.
38. Huo, Q., et al., *Organization of Organic Molecules with Inorganic Molecular Species into Nanocomposite Biphase Arrays*. Chemistry of Materials, 1994. **6**(8): p. 1176-91.

39. Huo, Q.S., et al., *Generalized synthesis of periodic surfactant inorganic composite-materials*. Nature, 1994. **368**(6469): p. 317-321.
40. Flodstrom, K., et al., *In situ synchrotron small-angle X-ray scattering/X-ray diffraction study of the formation of SBA-15 mesoporous silica*. Langmuir: the ACS journal of surfaces and colloids, 2004. **20**(12): p. 4885-91.
41. Flodstrom, K., H. Wennerstrom, and V. Alfredsson, *Mechanism of mesoporous silica formation. A time-resolved NMR and TEM study of silica-block copolymer aggregation*. Langmuir FIELD Full Journal Title:Langmuir : the ACS journal of surfaces and colloids, 2004. **20**(3): p. 680-8.
42. Flodstrom, K., et al., *Time-resolved in situ studies of the formation of cubic mesoporous silica formed with triblock copolymers*. Langmuir: the ACS journal of surfaces and colloids, 2004. **20**(23): p. 10311-6.
43. Imperor-Clerc, M., et al., *New insights into the initial steps of the formation of SBA-15 materials: an in situ small angle neutron scattering investigation*. Chemical Communications (Cambridge, United Kingdom), 2007(8): p. 834-836.
44. Khodakov, A.Y., et al., *Characterization of the Initial Stages of SBA-15 Synthesis by in Situ Time-Resolved Small-Angle X-ray Scattering*. Journal of Physical Chemistry B, 2005. **109**(48): p. 22780-22790.
45. Morell, J., et al., *In situ Synchrotron SAXS/XRD Study on the Formation of Ordered Mesoscopic Hybrid Materials with Crystal-Like Walls*. Chem. Mater., 2004. **16**: p. 5564-5566.
46. Regev, O., *Nucleation Events during the Synthesis of Mesoporous Materials Using Liquid Crystalline Templating*. Langmuir, 1996. **12**(20): p. 4940-4944.
47. Ruthstein, S., et al., *Resolving Intermediate Solution Structures during the Formation of Mesoporous SBA-15*. Journal of the American Chemical Society, 2006. **128**(10): p. 3366-3374.
48. Nakanishi, K., *Pore Structure Control of Silica Gels Based on Phase Separation*. Journal of Porous Materials, 1997. **4**: p. 67-112.
49. Nakanishi, K., et al., *Formation of Hierarchical Pore Structure in Silica Gel*. Journal of Sol-Gel Science and Technology, 2000. **17**: p. 191-210.
50. Amatani, T., et al., *Monolithic Periodic Mesoporous Silica with Well-Defined Macropores*. Chemistry of Materials, 2005. **17**(8): p. 2114-2119.
51. Nakanishi, K., et al., *Spontaneous Formation of Hierarchical Macro-Mesoporous Ethane-Silica Monolith*. Chemistry of Materials, 2004. **16**(19): p. 3652-3658.
52. Nakanishi, K., *Sol-gel process of oxides accompanied by phase separation*. Bulletin of the Chemical Society of Japan, 2006. **79**(5): p. 673-691.
53. Deshpande, R., D.M. Smith, and C.J. Brinker, *Preparation of high-porosity xerogels by chemical surface modification*. 1994, (University of New Mexico, USA). Application: WO  
WO. p. 34 pp.
54. Smith, D.M., R. Deshpande, and C.J. Brinker, *Preparation of low-density aerogels at ambient pressure*. Materials Research Society Symposium Proceedings, 1992. **271**(Better Ceramics through Chemistry V): p. 567-72.
55. Smith, D.M., G.W. Scherer, and J.M. Anderson, *Shrinkage during drying of silica gel*. Journal of Non-Crystalline Solids, 1995. **188**(3): p. 191-206.
56. Smith, D.M., et al., *Preparation of low-density xerogels at ambient pressure*. Journal of Non-Crystalline Solids, 1995. **186**: p. 104-12.

57. Brandhuber, D., et al., *Cellular mesoscopically organized silica monoliths with tailored surface chemistry by one-step drying/extraction/surface modification processes*. Journal of Materials Chemistry, 2005. **15**(Advance Article).
58. Brandhuber, D., H. Peterlik, and N. Huesing, *Simultaneous drying and chemical modification of hierarchically organized silica monoliths with organofunctional silanes*. Journal of Materials Chemistry, 2005. **15**(35-36): p. 3896-3902.
59. Mammeri, F., et al., *Mechanical properties of hybrid organic-inorganic materials*. Journal of Materials Chemistry, 2005. **15**: p. 3787-3811.
60. Husing, N. and U. Schubert, *Porous inorganic-organic hybrid materials*. Functional Hybrid Materials, 2004: p. 86-121.
61. Asefa, T., et al., *Periodic mesoporous organosilicas with organic groups inside the channel walls*. Nature (London), 1999. **402**(6764): p. 867-871.
62. Asefa, T., et al., *New nanocomposites: putting organic function 'inside' the channel walls of periodic mesoporous silica*. Journal of Materials Chemistry, 2000. **10**(8): p. 1751-1755.
63. Burleigh, M.C., et al., *A versatile synthetic approach to periodic mesoporous organosilicas*. Colloid and Polymer Science, 2004. **282**(7): p. 728-733.
64. Inagaki, S., et al., *Novel Mesoporous Materials with a Uniform Distribution of Organic Groups and Inorganic Oxide in Their Frameworks*. Journal of the American Chemical Society, 1999. **121**(41): p. 9611-9614.
65. Melde, B.J., et al., *Mesoporous Sieves with Unified Hybrid Inorganic/Organic Frameworks*. Chemistry of Materials, 1999. **11**(11): p. 3302-3308.
66. Muth, O., C. Schellbach, and M. Froeba, *Triblock copolymer assisted synthesis of periodic mesoporous organosilicas (PMOs) with large pores*. Chemical Communications (Cambridge, United Kingdom), 2001(19): p. 2032-2033.
67. Rebbin, V., O. Muth, and M. Froeba, *Periodic mesoporous organosilicas (PMOs) with different organic bridging groups: synthesis and characterization*. Materials Research Society Symposium Proceedings, 2002. **726**(Organic/Inorganic Hybrid Materials--2002): p. 263-268.
68. Shea, K.J., D.A. Loy, and O. Webster, *Arylsilsesquioxane gels and related materials. New hybrids of organic and inorganic networks*. Journal of the American Chemical Society, 1992. **114**(17): p. 6700-10.
69. Shea, K.J., et al., *Bridged polysilsesquioxanes. Molecular-engineering nanostructured hybrid organic-inorganic materials*. Functional Hybrid Materials, 2004: p. 50-85.
70. Yoshina-Ishii, C., et al., *Periodic mesoporous organosilicas, PMOs: fusion of organic and inorganic chemistry 'inside' the channel walls of hexagonal mesoporous silica*. Chemical Communications (Cambridge), 1999(24): p. 2539-2540.
71. Brandhuber, D., N. Huesing, and H. Peterlik, *Inorganic-organic hybrid hierarchically structured methyl-modified silica monoliths*. Materials Research Society Symposium Proceedings, 2005. **847**(Organic/Inorganic Hybrid Materials--2004): p. 127-134.
72. Brandhuber, D., H. Peterlik, and N. Huesing, *Facile self-assembly processes to phenylene-bridged silica monoliths with four levels of hierarchy*. Small, 2006. **2**(4): p. 503-506.
73. Inagaki, S., et al., *An ordered mesoporous organosilica hybrid material with a crystal-like wall structure*. Nature (London, United Kingdom), 2002. **416**(6878): p. 304-307.

74. Kapoor, M.P., Q. Yang, and S. Inagaki, *Organization of Phenylene-Bridged Hybrid Mesoporous Silsesquioxane with a Crystal-like Pore Wall from a Precursor with Nonlinear Symmetry*. Chem. Mater., 2004. **16**: p. 1209-1213.
75. Mark, J.E., *Ceramic-reinforced polymers and polymer-modified ceramics*. Polymer Engineering and Science, 1996. **36**(24): p. 2905-2920.
76. Frisch, H.L. and J.E. Mark, *Nanocomposites Prepared by Threading Polymer Chains through Zeolites, Mesoporous Silica, or Silica Nanotubes*. Chem. Mater., 1996. **8**: p. 1735-1738.
77. Ji, X.L., et al., *Mesoporous silica-reinforced polymer nanocomposites*. Chemistry of Materials, 2003. **15**(19): p. 3656-3662.
78. Wang, N., M. Li, and J. Zhang, *Polymer-filled porous MCM-41: An effective means to design polymer-based nanocomposite*. Materials Letters, 2005. **59**(21): p. 2685-2688.
79. Summers, M. and J. Eastoe, *Applications of polymerizable surfactants*. Advances in Colloid and Interface Science, 2003. **100-102**: p. 137-152.
80. Freedman, H.H., J.P. Mason, and A.I. Medalia, *Polysoaps. II. Preparation of vinyl soaps*. Journal of Organic Chemistry, 1958. **23**: p. 76-82.
81. Eastoe, J., M. Summers, and R.K. Heenan, *Control over phase curvature using mixtures of polymerizable surfactants*. Chemistry of Materials, 2000. **12**(12): p. 3533-+.
82. Gin, D.L., et al., *Polymerized lyotropic liquid crystal assemblies for materials applications*. Accounts of Chemical Research, 2001. **34**(12): p. 973-980.
83. Hennaux, P. and A. Laschewsky, *Novel nonionic surfactants based on sulfoxides. 2. Homo- and copolymers*. Colloid and Polymer Science, 2003. **281**(9): p. 807-814.
84. Reppy, M.A., et al., *A new family of polymerizable lyotropic liquid crystals: Control of feature size in cross-linked inverted hexagonal assemblies via monomer structure*. Journal of the American Chemical Society, 2001. **123**(3): p. 363-371.
85. Samakande, A., P.C. Hartmann, and R.D. Sanderson, *Synthesis and characterization of new cationic quaternary ammonium polymerizable surfactants*. Journal of Colloid and Interface Science, 2006. **296**(1): p. 316-323.
86. Summers, M., J. Eastoe, and R.M. Richardson, *Concentrated Polymerized Cationic Surfactant Phases*. Langmuir, 2003. **19**(16): p. 6357-6362.
87. Yang, Y., et al., *Functional nanocomposites prepared by self-assembly and polymerization of diacetylene surfactants and silicic acid*. J Am Chem Soc, 2003. **125**(5): p. 1269-77.
88. Pindzola, B.A., J.Z. Jin, and D.L. Gin, *Cross-linked normal hexagonal and bicontinuous cubic assemblies via polymerizable gemini amphiphiles*. Journal of the American Chemical Society, 2003. **125**(10): p. 2940-2949.
89. Gray, D.H., et al., *Highly ordered polymer-inorganic nanocomposites via monomer self-assembly: In situ condensation approach*. Advanced Materials, 1997. **9**(9): p. 731-736.
90. Lu, Y.F., et al., *Self-assembly of mesoscopically ordered chromatic polydiacetylene/silica nanocomposites*. Nature, 2001. **410**(6831): p. 913-917.
91. Brinker, C.J., et al., *Evaporation-induced self-assembly. Nanostructures made easy*. Advanced Materials (Weinheim, Germany), 1999. **11**(7): p. 579-585.
92. McCaughey, B., et al., *Self-assembly of mesostructured conjugated poly(2,5-thienylene ethynylene)/silica nanocomposites*. Advanced Materials, 2003. **15**(15): p. 1266-1269.

93. Sellinger, A., et al., *Continuous self-assembly of organic-inorganic nanocomposite coatings that mimic nacre*. *Nature*, 1998. **394**(6690): p. 256-260.
94. Smarsly, B., et al., *Preparation and characterization of mesostructured polymer-functionalized sol-gel-derived thin films*. *Progress in Organic Coatings*, 2003. **47**(3-4): p. 393-400.
95. Gibson, L.J., *Biomechanics of cellular solids*. *Journal of Biomechanics*, 2005. **38**: p. 377-399.
96. Woesz, A., J. Stampfl, and P. Fratzl, *Cellular solids beyond the apparent density - an experimental assessment of mechanical properties*. *Advanced Engineering Materials*, 2004. **6**(3): p. 134-138.
97. Cassiers, K., et al., *A Detailed Study of Thermal, Hydrothermal, and Mechanical Stabilities of a Wide Range of Surfactant Assembled Mesoporous Silicas*. *Chemistry of Materials*, 2002. **14**(5): p. 2317-2324.
98. Gusev, V.Y., et al., *Mechanical Stability of Pure Silica Mesoporous MCM-41 by Nitrogen Adsorption and Small-Angle X-ray Diffraction Measurements*. *Journal of Physical Chemistry*, 1996. **100**(6): p. 1985-8.
99. Wu, J., X. Liu, and S.H. Tolbert, *High-Pressure Stability in Ordered Mesoporous Silicas: Rigidity and Elasticity through Nanometer Scale Arches*. *Journal of Physical Chemistry B*, 2000. **104**(50): p. 11837-11841.
100. Scherer, G.W., *Effect of drying on properties of silica gel*. *Journal of Non-Crystalline Solids*, 1997. **215**: p. 155-168.
101. Woignier, T., et al., *Different kinds of structure in aerogels: relationships with the mechanical properties*. *Journal of Non-Crystalline Solids*, 1998. **241**(1): p. 45-52.
102. Puchegger, S., et al., *Changing Poisson's ratio of mesoporous silica monoliths with high temperature treatment*. *Journal of Non-Crystalline Solids*, 2006. **352**(50-51): p. 5251-5256.
103. Puchegger, S., et al., *The dependence of the elastic moduli of reaction bonded alumina on porosity*. *Journal of the European Ceramic Society*, 2006. **27**(1): p. 35-39.
104. Kirsch, B.L., et al., *Probing the effects of nanoscale architecture on the mechanical properties of hexagonal silica/polymer composite thin films*. *Advanced Functional Materials*, 2005. **15**(8): p. 1319-1327.
105. Toivola, Y., A. Stein, and R.F. Cook, *Depth-sensing indentation response of ordered silica foam*. *Journal of Materials Research*, 2004. **19**(1): p. 260-271.
106. Fan, H., et al., *Modulus-density scaling behavior and framework architecture of nanoporous self-assembled silicas*. *Nature Materials*, 2007. **6**(6): p. 418-423.
107. Wang, Z., et al., *Effects of Hierarchical Architecture on Electronic and Mechanical Properties of Nanocast Monolithic Porous Carbons and Carbon-Carbon Nanocomposites*. *Chemistry of Materials*, 2006. **18**(23): p. 5543-5553.
108. Shinozaki, N., et al., *Strength and elasticity of bimodal porous silica prepared from water glass*. *Journal of Sol-Gel Science and Technology*, 2007. **43**(3): p. 275-282.
109. Takahashi, R., et al., *Bending strength of silica gel with bimodal pores*. *Materials Research Bulletin*, 2007. **42**(3): p. 523-531.
110. Limpanuphap, S. and B. Derby, *Manufacture of biomaterials by a novel printing process*. *Journal of Materials Science-Materials in Medicine*, 2002. **13**(12): p. 1163-1166.
111. Stampfl, J., et al., *Fabrication and moulding of cellular materials by rapid prototyping*. *International Journal of Materials & Product Technology*, 2004. **21**(4): p. 285-296.

112. Stampfl, J., et al., *Water soluble, photocurable resins for Rapid Prototyping applications*. Macromolecular Symposia, 2004. **217**: p. 99-107.
113. Vallet-Regi, M., *Revisiting ceramics for medical applications*. Dalton Transactions, 2006(44): p. 5211-5220.
114. Vallet-Regi, M., *Ordered mesoporous materials in the context of drug delivery systems and bone tissue engineering*. Chemistry--A European Journal, 2006. **12**(23): p. 5934-5943.
115. Vallet-Regi, M., et al., *Revisiting silica based ordered mesoporous materials: medical applications*. Journal of Materials Chemistry, 2006. **16**(1): p. 26-31.
116. Yan, X., et al., *Highly ordered mesoporous bioactive glasses with superior in vitro bone-forming bioactivities*. Angewandte Chemie, International Edition, 2004. **43**(44): p. 5980-5984.
117. Vasiliev, P.O., et al., *Meso/Macroporous, Mechanically Stable Silica Monoliths of Complex Shape by Controlled Fusion of Mesoporous Spherical Particles*. Chemistry of Materials, 2006. **18**(20): p. 4933-4938.
118. Smått, J.-H., S. Schunk, and M. Lindén, *Versatile Double-Templating Synthesis Route to Silica Monoliths Exhibiting a Multimodal Hierarchical Porosity*. Chem. Mater., 2003. **15**: p. 2354-2361.
119. Maekawa, H., et al., *Meso/macroporous inorganic oxide monoliths from polymer foams*. Advanced Materials, 2003. **15**(7-8): p. 591-596.
120. Liang, C., S. Dai, and G. Guiochon, *Use of gel-casting to prepare HPLC monolithic silica columns with uniform mesopores and tunable macrochannels*. Chem. Commun., 2002: p. 2680-2681.
121. Fan, H.Y., et al., *Rapid prototyping of patterned functional nanostructures*. Nature, 2000. **405**(6782): p. 56-60.
122. Yoon, K.B., B.-S. Bae, and M. Popall, *Fabrication of Low-Loss Waveguides Using Organic-Inorganic Hybrid Materials*. Journal of Nonlinear Optical Physics & Materials, 2005. **14**(3): p. 399-407.
123. Chu, T.M.G., et al., *Hydroxyapatite implants with designed internal architecture*. Journal of Materials Science: Materials in Medicine, 2001. **12**(6): p. 471-478.
124. Khimyak, Y.Z. and J. Klinowski, *Formation of mesoporous silicates using Triton XN surfactants in the presence of concentrated mineral acids*. Journal of Materials Chemistry, 2000. **10**(8): p. 1847-1855.
125. Firouzi, A., et al., *Alkaline lyotropic silicate-surfactant liquid crystals*. Journal of the American Chemical Society, 1997. **119**(15): p. 3596-3610.
126. Mehrotra, R.C. and R.P. Narain, *Reactions of tetramethoxy- and triethoxysilanes with glycols*. Indian Journal of Chemistry, 1967. **5**(9): p. 444-8.
127. Huesing, N., et al., *Influence of supercritical drying fluid on structure and properties of organically modified silica aerogels*. Journal of Non-Crystalline Solids, 1995. **186**: p. 37-43.
128. Schuster, M., et al., *Evaluation of biocompatible photopolymers I: photoreactivity and mechanical properties of reactive diluents*. Journal of Macromolecular Science, Part A: Pure and Applied Chemistry, 2007. **44**(5): p. 547-557.
129. Infuehr, R., et al., *3D lithography of organo-soluble mold materials for sol-gel nanocomposites*. RadTech Europe 05: UV/EB--Join the Winning Technology, [Conference Proceedings], Barcelona, Spain, Oct. 18-20, 2005, 2005. **2**: p. 489-494.

130. Inführ, R., *Entwicklung von Photopolymeren für Rapid Prototyping zur Herstellung von zellulären organolöslichen Abformmaterialien*, in *Institute of Applied Synthetic Chemistry*. 2005, Vienna University of Technology: Vienna.
131. Liska, R., et al., *Water-soluble photopolymers for rapid prototyping of cellular materials*. *Journal of Applied Polymer Science*, 2005. **97**(6): p. 2286-2298.
132. Guinier, A. and G. Fournet, *Small-Angle Scattering of X-rays*. 1955. 268 pp.
133. Kasai, N., M. Kakudo, and Editors, *X-Ray Diffraction by Macromolecules*. 2005.
134. Lindner, P., T. Zemb, and Editors, *Neutron, X-Ray, and Light Scattering: Introduction to an Investigative Tool for Colloidal and Polymeric Systems. Proceedings of the European Workshop on Neutron, X-ray and and Light Scattering as an Investigative Tool for Colloidal and Polymeric Systems, Bombannes, France, 27 May - 2 June, 1990*. 1991. 375 pp.
135. Pedersen, J.S., *Analysis of small-angle scattering data from colloids and polymer solutions: modeling and least-squares fitting*. *Advances in Colloid and Interface Science*, 1997. **70**: p. 171-210.
136. Peterlik, H. and P. Fratzl, *Small-Angle X-Ray Scattering to Characterize Nanostructures in Inorganic and Hybrid Materials Chemistry*. *Monatshefte fuer Chemie*, 2006. **137**(5): p. 529-543.
137. Förster, S., et al., *Scattering Curves of Ordered Mesoscopic Materials*. *J. Phys. Chem. B*, 2005. **109**: p. 1347-1360.
138. Narayanan, T., *Synchrotron small-angle X-ray scattering, in Soft Matter: Scattering, Imaging and Manipulation*, ed. E.R.B.a.R. Pecora. Vol. 3. 2007: Springer.
139. Glatter, O. and O. Kratky, *Small Angle X-ray Scattering*. 1982, London, New York: Academic Press.
140. Emmerling, A., et al., *Relationship between optical transparency and nanostructural features of silica aerogels*. *Journal of Non-Crystalline Solids*, 1995. **185**(3): p. 240-8.
141. Svergun, D.I. and L.A. Feigin, *X-ray and Neutron Low-Angle Scattering*. 1986. 278 pp.
142. Hammersley, A.P., *Synchrotron Rad. News*, 1989. **2**: p. 24-26.
143. Schüth, F., K.S.W. Sing, and J. Weitkamp, *Handbook of Porous Solids*. 2002: Wiley-VCH.
144. Oliver, W.C. and G.M. Pharr, *An Improved Technique for Determining Hardness and Elastic- Modulus Using Load and Displacement Sensing Indentation Experiments*. *Journal of Materials Research*, 1992. **7**(6): p. 1564-1583.
145. Jager-Lezer, N., et al., *Influence of the chemical nature of various geometries on the rheological behavior of a lamellar lyotropic phase*. *Journal of Rheology (New York)*, 1999. **43**(5): p. 1067-1081.
146. Zimmermann, A., *Funktionelle Tenside als Template für Sol-Gel Prozesse*, in *Institute of Applied Synthetic Chemistry*. 2006, Vienna University of Technology: Vienna.
147. Arnaud, A., et al., *Aqueous supramolecular polymer formed from an amphiphilic perylene derivative*. *Angewandte Chemie, International Edition*, 2004. **43**(13): p. 1718-1721.
148. Bagshaw, S.A., *Bimodal pore systems in non-ionically templated [Si]-MSU-X mesoporous silica through biomimetic synthesis in weakly ionic solutions*. *Chemical Communications (Cambridge)*, 1999(18): p. 1785-1786.

149. Michaux, F., J.L. Blin, and M.J. Stebe, *Design of Ordered Bimodal Mesoporous Silica Materials by Using a Mixed Fluorinated-Hydrogenated Surfactant-Based System*. Langmuir, 2007. **23**(4): p. 2138-2144.
150. Hüsing, N., et al., *Periodically Mesostructured Silica Monoliths from Diol-Modified Silanes*. Chem. Mater., 2003. **15**: p. 2690-2692.
151. Sattler, K., et al., *Influence of surfactant on the gelation of novel ethylene glycol esters of silicic acid*. Berichte der Bunsen-Gesellschaft, 1998. **102**(11): p. 1544-1547.
152. Flodström, K., et al., *In Situ Synchrotron Small-Angle X-ray Scattering/X-ray Diffraction Study of the Formation of SBA-15 Mesoporous Silica*. Langmuir, 2004. **20**: p. 4885-4891.
153. Rubio, J. and J.A. Kitchener, *The mechanism of adsorption of poly(ethylene oxide) flocculant on silica*. Journal of Colloid and Interface Science, 1976. **57**(1): p. 132-42.
154. Takahashi, R., K. Nakanishi, and N. Soga, *Aggregation Behavior of Alkoxide-Derived Silica in Sol-Gel Process in Presence of Poly(ethylene oxide)*. Journal of Sol-Gel Science and Technology, 2000. **17**: p. 7-18.
155. Yang, B., et al., *Effect of Acid on the Aggregation of Poly(ethylene oxide)-Poly(propylene oxide)-Poly(ethylene oxide) Block Copolymers*. Journal of Physical Chemistry B, 2006. **110**(46): p. 23068-23074.
156. Brandhuber, D., et al., *Glycol-modified silanes in the synthesis of mesoscopically organized silica monoliths with hierarchical porosity*. Chemistry of Materials, 2005. **17**(16): p. 4262-4271.
157. Meyer, M., A. Fischer, and H. Hoffmann, *Novel ringing silica gels that do not shrink*. Journal of Physical Chemistry B, 2002. **106**(7): p. 1528-1533.
158. Flodström, K., et al., *Time-Resolved in Situ Studies of the Formation of Cubic Mesoporous Silica Formed with Triblock Copolymers*. Langmuir, 2004. **20**: p. 10311-10316.
159. Hanrahan, J.P., et al., *In situ studies of order-disorder phenomena in the synthesis of mesoporous silica*. Journal of Non-Crystalline Solids, 2007. **353**(52-54): p. 4823-4829.
160. Chen, C.Y., et al., *Studies on mesoporous materials. II. Synthesis mechanism of MCM-41*. Microporous Materials, 1993. **2**(1): p. 27-34.
161. Firouzi, A., et al., *Cooperative organization of inorganic-surfactant and biomimetic assemblies*. Science, 1995. **267**(5201): p. 1138-1143.
162. Tanev, P.T. and T.J. Pinnavaia, *A Neutral Templating Route to Mesoporous Molecular-Sieves*. Science, 1995. **267**(5199): p. 865-867.
163. Linden, M., et al., *In situ SAXS/XRD on mesoscopically ordered surfactant-silica mesophases; what can we learn?* Materials Research Society Symposium Proceedings, 2005. **847**(Organic/Inorganic Hybrid Materials--2004): p. 495-505.
164. Sattler, K. and H. Hoffmann, *A new glycol precursor for template synthesis and its interaction with a surfactant*. Chemie Ingenieur Technik, 2000. **72**(5): p. 487-490.
165. Chan, H.B.S., P.M. Budd, and T.d.V. Naylor, *Control of mesostructured silica particle morphology*. Journal of Materials Chemistry, 2001. **11**(3): p. 951-957.
166. Lindner, P. and T. Zemb, eds. *Neutrons, X-rays and Light: Scattering Methods Applied to Soft Condensed Matter*. 2002, Elsevier.



## Appendix

### A. Considerations on the limitations of the obtained numerical values

#### Fitting of spherically shaped particles

The intermediate phase seen in the SAXS pattern prior and parallel to the mesostructure formation was assumed to originate from particles being formed by surfactant and condensing silica species. In a first approximation these particles were assumed to be spherical. Since the characteristic slope is accessible only in a small  $q$ -region and moreover obscured by other scattering contributions, no precise conclusion is possible. As shown in Figure 3.4.13 and Figure 3.4.19 the characteristic slope changes in the course of the *in-situ* experiments, equivalent to a change in the shape of the particles. Since the phase seems to trigger the evolving mesostructure, a transformation from spherical to cylindrical structures is likely. No oscillations of the scattered intensity are observed in the Porod regime because of the polydispersity of the particles. As approximation in case of the phenylene bridged precursor a Debye function was used [140], where the constant  $\sqrt{2/3}$  provides an asymptotic approach to the form factor of a perfect sphere for large scattering vectors. In an other attempt the radius was approximated using Guinier's law. The obtained radius of gyration,  $R_g$ , is linked to the radius of spheres by  $R_{g,spheres} = \sqrt{5/3}R_g$ . Examples for both fits are shown in Figure 3.7.1 for the EGMS/P123/1 M HCl system. The radii resulted in  $R_d=5.2$  nm, respectively,  $R_g=7.8$  nm ( $R_{g,sphere}\sim 10$  nm).

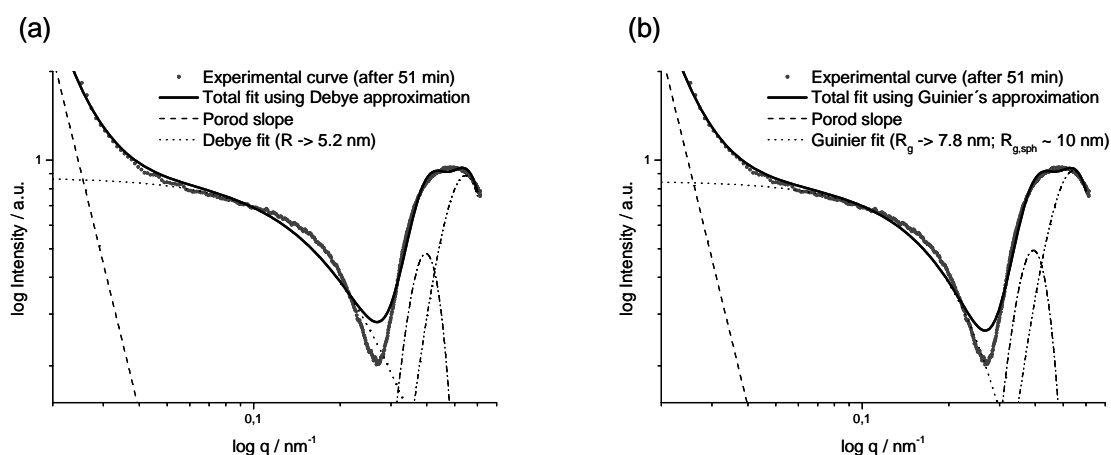


Figure 3.7.1. Experimental scattering curve of the EGMS/P123/1 M HCl synthesis, 50 minutes after mixing the components, and the corresponding fit curves (a) Debye, (b) Guinier approximation.

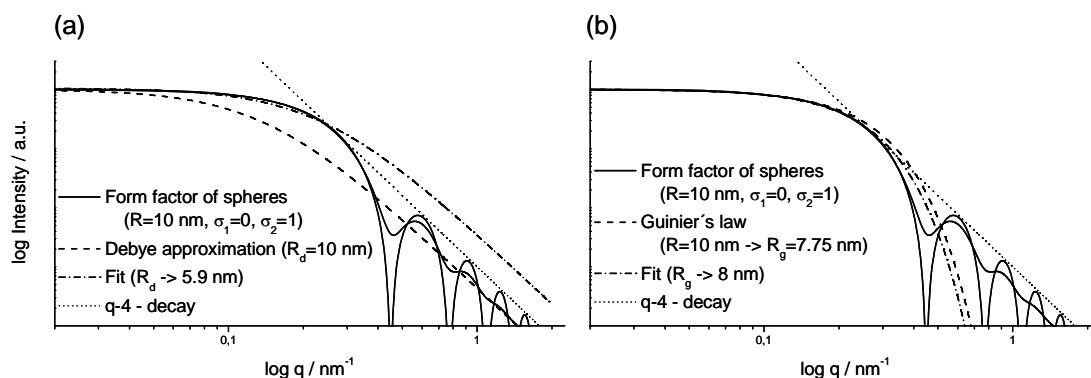


Figure 3.7.2. Form factor for monodisperse and polydisperse spheres with the corresponding (a) Debye curve and (b) Guinier curve.

In Figure 3.7.2 (a) the scattering intensity for monodisperse and slightly polydisperse spheres ( $\sigma=1$  nm) with a radius of 10 nm is plotted together with the corresponding Debye function for spheres. Additionally, the curve derived by fitting the scattering from the monodisperse spheres is shown. The same approach is plotted in Figure 3.7.2 (b) applying Guinier's law. In case of the Debye approximation it is clearly visible, that the function underestimates the exact solution [136]. In the fits of the experimental scattering curves, the obtained radii are smaller than the expected ones. The opposite applies for the Guinier fit.

For better understanding of the fitted radii obtained by using Guinier's law ( $R_g$ ), respectively, Debye's approximation ( $R_d$ ) in the kinetic measurements, scattering curves of spherical particles were simulated with different radii. The values chosen are comparable to the expected values (range of 5 nm–12 nm). Scattering profiles were generated using the classical expressions for the form factor of spheres (Eq. 2.5) and a size distribution function to smear out the minima/maxima ( $\sigma=pR$ ) (Eq. 2.8). The resulting curves were then fitted with the Debye approximation for spherical particles and Guinier's law in the region accessible to the experiment as well as for a larger  $q$ -range (0.01 to 3 nm<sup>-1</sup>).

In Figure 3.7.3 the scattering curve for polydisperse spherical particles with radius  $R=9.9$  nm and a standard deviation of  $\sigma=0.4 R$  is shown together with the obtained fit curves. For the experimentally investigated  $q$ -regime both approximations agree well, but give different radii, namely,  $R_d=7.5$  nm and  $R_g=10.5$  nm (leading to a radius for spheres of 13.6 nm). Both obtained radii differ significantly from the employed radius  $R=9.9$  nm. Despite the observed deviation, the fit values follow the behaviour of the "true" radius, as is shown in Figure 3.7.4 a), and therefore give information about growth/shrinkage of the particle diameter.

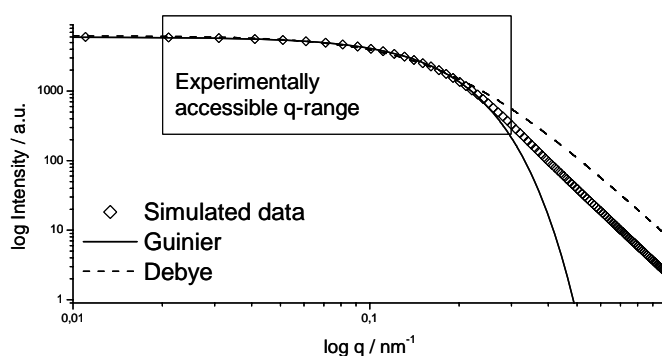


Figure 3.7.3. Simulated curve with radius  $R=9.9$  nm and polydispersity  $p=0.4 R$  and the corresponding fits following Eq. 2.3 (Guinier's law) and Eq. 2.9 (Debye approximation). The  $q$ -range which was investigated in the experiment is highlighted and was also used as data in the fits. Both fits optically agree quite well with the smeared form factor of spheres, although they lead to differing radii.

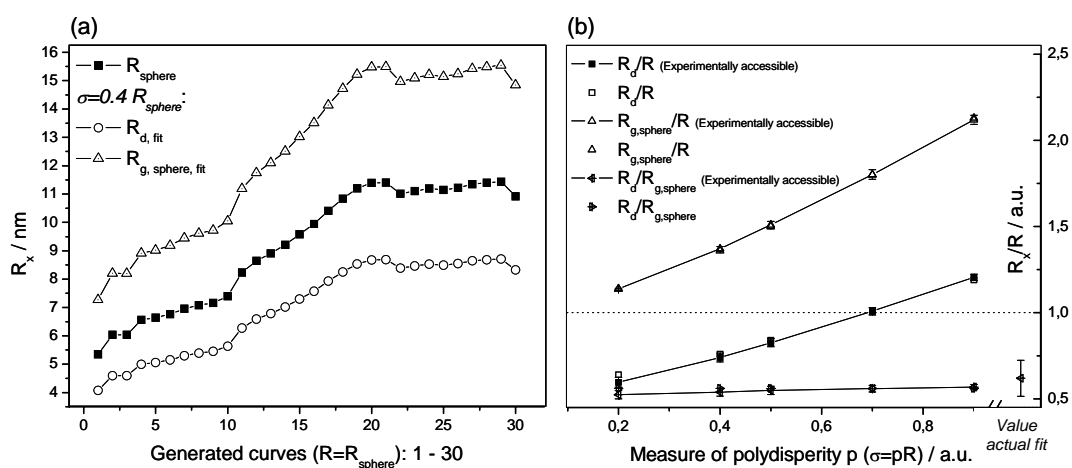


Figure 3.7.4. (a) Resulting fit values for thirty simulated curves.  $R_{\text{sphere}}$  is the radius used in the simulation. (b) Ratios of the obtained values for  $R_d$  (Debye) and  $R_{g, \text{sphere}}$  (Guinier) from fitting the curves generated from different  $R$ , plotted against polydispersity. Fits were performed on the experimentally accessible  $q$ -range as well as a  $q$ -range ranging from  $0.01$  to  $3 \text{ nm}^{-1}$ . A sample curve is shown in Figure 3.7.3. The values have been averaged over thirty curves. Fitting was performed with Mathematica.

From the normalized fit results of the simulated scattering curves of spherical particles, shown in Figure 3.7.4 (b), one can see that polydispersity has an influence on the deviation of the obtained values. Radius  $R_{g, \text{sphere}}$  which is derived from the Guinier fit is always larger than the “real” mean radius  $R$ . The factor between the values for the radii obtained by Debye and Guinier approximation ( $R_d/R_{g, \text{sphere}}$ ) was found to be approximately  $0.56 \pm 0.02$  in the simulated curves with tendency to increase with higher polydispersity of the particles. The value derived from the fits of the experimentally obtained scattering curves for the EGMS-kinetic gives a factor of  $0.62 \pm 0.1$ . In conclusion the approximation functions such as Eq. 2.9 (Debye) and Eq. 2.3 (Guinier) can not give the exact values but both reflect the tendency of particle evolution equally well.

## B. Experimental details on supercritical drying

### MeOH supercritical drying (ICMAB):

- Pressurization till 52 bar in 11 min
- Increase T:

time (min)	p (bar)	T (°C)
0	52	23
10	58	26
20	74	46
30	90	70
40	104	99
50	112	120
60	122	150
70	132	181
80	144	212
90	149	241
100	146	256
110	140	264

- 4 h at high pressure-high temperature
- 1h 10min depressurization
- natural cooling

### CO<sub>2</sub> supercritical drying (ICMAB)

- Pressurization till 100 bar in 23 min (T=22 °C)
- 4 h MeOH-CO<sub>2</sub> exchange at 3-4 kg/h
- Increase T:

time (min)	p (bar)	T (°C)
0	100	19
10	126	24
20	159	33
31	173	40

- 1 h at supercritical conditions
- 50 min depressurization

### C. Samples for mechanical testing

Samples were prepared from EGMS (TGA: Si 9.7%(w/w)) and bPhGMS03 (TGA: Si 7%(w/w)) with a relative high amount of residual ethanol.

Table 5.1. Synthesis conditions and gelation times ( $t_g$ ) of samples prepared from EGMS and bPhGMS for instrumented indentation testing (production series H).

Composition / weight fraction						
Samples	$c_{\text{HCl}} / \text{M}$	Si	EGMS	P123/HCl (aq.)	$t_g / \text{min}$	Resulting macroporous structure
E802A	1	8.0	82	30/70	60	spiderweb
E452A	1	4.5	48	30/70	65	sponge-like
E802B	1	8.0	82	30/90	80	spiderweb
E802C	1	8.0	82	30/110	70	spiderweb
E800A	$10^{-2}$	8.0	82	30/70	240 (60)	spiderweb
E450A	$10^{-2}$	4.5	48	30/70	> 180	sponge-like
Samples	$c_{\text{HCl}} / \text{M}$	Si	bPhGMS	P123/HCl (aq.)	$t_g / \text{min}$	
bPh450A	$10^{-2}$	4.5	64	30/70	80	sponge-like
bPh450B	$10^{-2}$	4.5	64	30/90	70	comb
bPh450C	$10^{-2}$	4.5	64	30/110	65	short struts
bPh580C	$10^{-2}$	5.8	83	30/110	30	close to plates

#### Samples dried at ambient temperature after surface silylation:

Prior to drying, the wet gels were reacted by immersing the whole monolith body in a solution of 10%(w/w) of trimethylchlorosilane in petroleum ether (PE) for 24 h. The silylated gels were then washed with petroleum ether three times (within 12 hours) and with ethanol five times (within 24 h) to remove unreacted silane species. Drying was performed by slowly heating to 70 °C (3 °C/2 h) and further heating to 120 °C.

Table 5.2. SAXS and BET results for the surface silylated materials..

Samples	Apparent density / $\text{g cm}^{-3}$	$d_{10}^{\text{SAXS}}$ (w) / nm (%)	$S^{\text{BET}}$ / $\text{m}^2\text{g}^{-1}$	$V_{\text{max}}^{N_2}$ / $\text{m}^2\text{g}^{-1}$	C	$D^{\text{BJH}}$ / nm	$t_{\text{wall}}$ / nm
E802A-tms	0.25	11.7 (1.5)	732	644	67	9.3	4.2
E452A-tms	-	10.8 (1.8)	716	465	75	6.4	6.1
E802B-tms	0.19	11.7 (1.3)	727	667	62	7.4	6.1
E802C-tms	0.13*	11.9 (1.3)	1035	1030	135	9.5	4.2
E800A-tms	-	11.3 (1.8)	769	701	54	9.3	3.7
E450A-tms	0.45	9.4 (2.9)	575	367	126	3/9.5	7.9/1.4
bPh450A-tms	0.39	11.3 (2.9)	488	495	74	4.8	8.2
bPh450B-tms	0.34	10.5(1.0)	292	278	63	5.6	6.5
bPh450C-tms	0.27	10.7 (0.8)	412	387	82	4.7	7.7
bPh580C-tms	0.24	10.8 (1)	564	511	68	7.5	5

Table 5.3. Mechanical properties obtained by instrumented indentation testing for the surface silylated materials.

Samples	Macroscopic shrinkage / %	Number of runs	E / MPa	Hardness / MPa	Recovery / %
E802A-tms	21	8	$67 \pm 1$	4	$46.1 \pm 2.4$
E452A-tms	43	10	$306 \pm 32$	27	$61.6 \pm 1.8$
E802B-tms	17	8	$110 \pm 6$	7	$37.8 \pm 3.6$
E802C-tms	18	7	$42 \pm 3.5$	2	$37.1 \pm 1.6$
E800A-tms	-	7	$91 \pm 5$	9	$66.9 \pm 3.2$
E450A-tms	43	7	$269 \pm 22$	19	$53.3 \pm 4.1$
bPh450A-tms	28	4	$281 \pm 19$	38	$80 \pm 3$
bPh450B-tms	21	7	$321 \pm 32$	31	$61 \pm 4$
bPh450C-tms	36	5	$161 \pm 15$	13	$61 \pm 2$
bPh580C-tms	31	5	$90.4 \pm 3.4$	7	$60 \pm 3$

Samples dried by supercritical fluid extraction:

The pore fluid of the wet gels was first exchanged to methanol. Supercritical drying was performed with carbon dioxide as supercritical fluid, except sample E802A-scd<sub>MeOH</sub> which was dried with supercritical methanol.

Table 5.4. BET results of samples dried by supercritical fluid extraction.

Samples	Apparent density / g cm <sup>-3</sup>	$d_{10}^{SAXS}$ (w) / nm (%)	$S^{BET}$ / m <sup>2</sup> g <sup>-1</sup>	$V_{max}^{N_2}$ / m <sup>2</sup> g <sup>-1</sup>	C	$D^{BJH}$ / nm	$t_{wall}$ / nm
E802A-scd	0.21	11.9 (1.9)	1092	1006	77	9.2	4.5
E802A-scd <sub>MeOH</sub>	0.27	12 (1.9)	626	699	49	9.2	4.7
E802B-scd	0.19	-	1054	916	176	5.8	-
E800A-scd	0.27	-	627	601	106	7.8	-
E450A-scd	0.2	-	935	1541	202	6.5	-
bPh450B-scd	0.36	-	327	289	53	5.5	-
bPh450C-scd	0.33	-	569	460	285	5.6	-
bPh580C-scd	0.33	-	622	471	353	5.6	-

Table 5.5. Mechanical properties obtained by instrumented indentation testing.

Sample	Macroscopic shrinkage / %	Number of runs	E / MPa	Hardness / MPa	Recovery / %
E802A-scd	16	8	112 ± 6	8 ± 1	32.8 ± 1.2
E802A-scd <sub>MeOH</sub>	24	8	311 ± 17	17 ± 1	30.9 ± 0.8
E802B-scd	19	5	192 ± 24	9 ± 1	22.3 ± 1.6
E800A-scd	23	4	334 ± 27	20 ± 2	26.7 ± 0.4
E450A-scd	26	6	38 ± 2	3	37.2 ± 1.4
bPh450B-scd	25	13	199 ± 6	15 ± 1	74 ± 1
bPh450C-scd	27	6	122 ± 15	9 ± 1	62.6 ± 4
bPh580C-scd	29	11	122 ± 8	11 ± 1	70.2 ± 2

# Curriculum Vitae

**Christina Fritscher**

---

Johann Straußgasse 36/16, A-1040 Vienna, Austria

Born on the 28<sup>th</sup> of July 1977 in Salzburg, Austria

Austrian Citizenship

---

## Higher Education

11/2003 - 08/2008     **Studies for the PhD degree in Technical Sciences, Mechanical Engineering and Science of Management** at the Vienna University of Technology (TU Vienna), Austria.

**PhD thesis** on cooperative self-assembly and structure formation in (organo-)silica materials with hierarchical pore structure and on the mechanical properties of these materials, elaborated at the Institute of Materials Science and Technology and the Institute of Materials Chemistry, TU Vienna, Austria, under the guidance of Privatdoz. Helga Lichtenegger and Prof. Nicola Hüsing (now Department of Inorganic Chemistry I, University of Ulm, Germany).

10/1995 – 03/2003     **Studies for the Diploma Program in Technical Physics** at the TU Vienna with focus on solid state physics.

**Diploma Thesis: “Die atomare Struktur von Fe-Ni-Oberflächen nahe der Invar-Zusammensetzung“.**

Elaborated at the Institut für Allgemeine Physik, TU Vienna, supervised by Prof. Michael Schmid.

## School Education

09/1991 – 06/1995     High school, BG Braunau/Inn, Austria.

09/1987 – 06/1991     High school, BG Rainergasse, 1050 Vienna, Austria.

09/1983 – 06/1987     Elementary school, Graf-Starhemberg-Gasse, 1040 Vienna, Austria.



## Professional Experience

- 09/2007 – to date      **Test Engineer** at IRM Integriertes Ressourcen Management GmbH, Vienna, Austria.
- 11/2003 – 08/2008      **Scientific Coworker** (wissenschaftlicher Mitarbeiter in Ausbildung) and **Project Assistent** at the TU Vienna, Austria.
- 11/2005                      **Research stay** at the Institut de Ciència de Materials de Barcelona, Barcelona, Spain (3 weeks).
- During 2004 -2006      Several (short) projects at the synchrotron facilities Elettra, Trieste, Italy and ESRF, Grenoble, France.
- 08/2003 – 10/2003      **Employee** at Christoph Sator/SPIRIT GmbH in the field of public relation.
- 07/2000 – 09/2000      **Summer Internship**, quality control / transmission electron microscopy, Siemens AG, Zentralabteilung Technik, München-Perlach, Germany.
- 07/1999                      **Summer Internship**, quality assurance, Wacker-Chemie GmbH, Burghausen, Germany.
- 07/1998 – 08/1998      **Summer Internship**, quality assurance, Wacker-Chemie GmbH, Burghausen, Germany.
- 08/1997 and  
07/1996 – 08/1996      **Summer Internship**, Atomic Institute of the Austrian Universities, Vienna, Austria.

---

## Publications

### Articles

C. Fritscher, N. Hüsing, S. Bernstorff, D. Brandhuber, T. Koch, S. Seidler, H. Lichtenegger, Journal of Synchrotron Radiation, 2005, 12, 717 - 720. *In-situ SAXS study on cationic and non-ionic surfactant liquid crystals using synchrotron radiation.*

R. Supplit, N. Hüsing, C. Fritscher, P. Jakubiak, V. G. Kessler, G. A. Seisenbaeva, S. Bernstorff. Mat. Res. Soc. Symp. Proc. 2005, 847, 177-182. *Iron oxide - doped mesostructured silica films.*

R. Infuehr, R. Liska, H. Lichtenegger, C. Fritscher, J. Stampfl, N. Hüsing. RadTech Europe, 2005, Conference Proceedings Volume II, 489-494. *3D lithography of organo-soluble mold materials for sol-gel nanocomposites.*

M Ondracek, F. Maca, J. Kudrnovsky, J. Redinger, A. Biedermann, C. Fritscher, M. Schmid, P. Varga. Physical Review B: Condensed Matter and Materials Physics, 2006, 74(23), 235437/1-7. *Chemical ordering and composition fluctuations at the (001) surface of the Fe<sub>64</sub>Ni<sub>36</sub> Invar alloy.*

### **Project Reports (published)**

C. Fritscher, N. Hüsing, S. Bernstorff, D. Brandhuber, T. Koch, S. Puchegger, S. Geist, J. Geserick, S. Hartmann, S. Seidler, H. C. Lichtenegger. Annual report 2006, Austrian SAXS beamline at Elettra, 2006, 110-111. *In-situ Investigation on the Formation of Periodically Ordered Mesostructures in Silica and Organosilica Gels synthesized with Glycol-Modified Silanes and Organosilanes.*

C. Fritscher, N. Hüsing, S. Bernstorff, D. Brandhuber, T. Koch, S. Geist, S. Seidler, H. C. Lichtenegger. Annual report 2005, Austrian SAXS beamline at Elettra 2005, 120-121. *In-situ SAXS investigation of mesostructure evolution in a nanocomposite derived by sol-gel chemistry.*

C. Fritscher, N. Hüsing, S. Bernstorff, D. Brandhuber, T. Koch, S. Seidler, H. C. Lichtenegger. Annual report 2004, Austrian SAXS beamline at Elettra, 2004, 102-103. *In-situ SAXS investigations on the phase behaviour of selected non-ionic surfactant liquid crystalline systems.*

### **Talks**

Hierarchisch strukturiertes Siliziumdioxid und seine mechanischen Eigenschaften.

C. Fritscher, H. C. Lichtenegger, J. Stampfl, N. Hüsing, R. Liska, R. Inführ, T. Koch, S. 2. Wiener Biomaterialsymposium 2006, Vienna, Austria.

3-Dimensional Mesoporous Silica Monoliths and their Structural and Mechanical Properties.

C. Fritscher, H. C. Lichtenegger, J. Stampfl, N. Hüsing, R. Liska, R. Inführ, T. Koch, S. Seidler, Polymerwerkstoffe 2006, Halle/Saale, Germany.

Sol-Gel-Synthese: Ein Weg zu bioinspirierten Materialien.

C. Fritscher, H. C. Lichtenegger, J. Stampfl, N. Hüsing, R. Liska, S. Bernstorff, T. Koch, D. Brandhuber, S. Seidler, 1. Wiener Biomaterialsymposium 2004, Vienna, Austria.

### ***Poster Presentations***

Templating of Organic/Inorganic Hybrid Materials.

C. Fritscher, H. Lichtenegger, J. Stampfl, N. Hüsing, R. Liska, EMRS Spring Meeting 2005, Strasbourg, France.

Nanostructured Silica/Polymer-Monoliths.

C. Fritscher, H. Lichtenegger, J. Stampfl, N. Hüsing, R. Liska, S. Seidler, ISOS XIV 2005, Würzburg, Germany.

Fabrication of Bio-Inspired Ceramic Composites Using Soluble Photopolymers as Mold Materials.

R. Inführ, Ch. Fritscher, R. Liska, H.C. Lichtenegger, J. Stampfl, N. Hüsing, EuroMat 2005, Prag, Czech Republic.

3D Lithography of organo-soluble mold materials.

R. Inführ, H. Lichtenegger, C. Fritscher, J. Stampfl, R. Liska, 7<sup>th</sup> Austrian Polymer Meeting 2005, Graz, Austria.

Fabrication of Bio-inspired Silica Composites.

C. Fritscher, H. C. Lichtenegger, J. Stampfl, N. Hüsing, R. Liska, S. Bernstorff, T. Koch, D. Brandhuber, S. Seidler, MRS Fall Meeting 2004, Boston, USA.

Fabrication of Bio-inspired ceramic composites.

C. Fritscher, H. Lichtenegger, J. Stampfl, N. Hüsing, R. Liska, S. Seidler, Junior Euromat, Lausanne 2004, Switzerland (Short oral presentation and poster presentation).

Fabrication of bio-inspired ceramic composites.

C. Fritscher, H.C. Lichtenegger, J. Stampfl, N. Hüsing, R. Liska, S. Seidler, Micro-Mechanical Properties of Biomaterials 2004, Tomar, Portugal.